

2007-08-17

# Osmotic- and Stroke-Induced Blood-Brain Barrier Disruption Detected by Manganese-Enhanced Magnetic Resonance Imaging

David G. Bennett  
*Worcester Polytechnic Institute*

Follow this and additional works at: <https://digitalcommons.wpi.edu/etd-dissertations>

---

## Repository Citation

Bennett, D. G. (2007). *Osmotic- and Stroke-Induced Blood-Brain Barrier Disruption Detected by Manganese-Enhanced Magnetic Resonance Imaging*. Retrieved from <https://digitalcommons.wpi.edu/etd-dissertations/349>

This dissertation is brought to you for free and open access by [Digital WPI](#). It has been accepted for inclusion in Doctoral Dissertations (All Dissertations, All Years) by an authorized administrator of Digital WPI. For more information, please contact [wpi-etd@wpi.edu](mailto:wpi-etd@wpi.edu).

# **Osmotic- and Stroke-Induced Blood-Brain Barrier Disruption Detected by Manganese-Enhanced Magnetic Resonance Imaging**

A dissertation submitted to the faculty of  
Worcester Polytechnic Institute  
in partial fulfillment of the requirements for the degree of Doctor of Philosophy in  
Biomedical Engineering  
by

---

David G. Bennett

June 2007

Approved:

---

Christopher H. Sotak, Ph.D.

Major Advisor

Professor

Department of Biomedical Engineering  
Worcester Polytechnic Institute

---

George D. Pins, Ph.D.

Associate Professor

Department of Biomedical Engineering  
Worcester Polytechnic Institute

---

Karl G. Helmer, Ph.D.

A. A. Martinos Center for Biomedical Imaging  
Charlestown, Massachusetts

---

Yitzhak Mendelson, Ph.D.

Professor and Interim Head

Department of Biomedical Engineering  
Worcester Polytechnic Institute

---

Peter Grigg, Ph.D.

Professor

Department of Physiology  
University of Massachusetts Medical School

# ACKNOWLEDGEMENTS

As I look back on my time at WPI it is apparent that I owe a debt of gratitude to several individuals who assisted me in good times and bad. First and foremost, I am thankful for having the support of my wonderful wife Alexia and close friends of ours. Alexia is a woman of seemingly infinite patience and love. She stood steadfast by my side during summer weekend imaging trials, periods of frustration, and months of writing. Alexia's support and encouragement helped make this work possible. Thank you for everything my love. I love you.

My start to a career in MRI began with the generous support of TJ and Maura McCartney back in 1994. Maura, you started me on this career path with your generous assistance and I wish I could celebrate and thank you in person now. You truly came to me at a decisive time in my life and for this I am humbly grateful. My memory of you is crystal clear and my affections have not changed over the years since your passing. I hope to see you again. May God bless you.

I am very thankful for having been a part of Prof. Christopher Sotak's lab. Through his wealth of scientific knowledge and demand for scientific rigor Chris provides a rich research environment that is demanding yet open to new ideas. Chris, you are well aware of my successes and failures and through each of these I have grown as a person and as a scientist. I sincerely thank you for your efforts in steering me towards success. As another member of Chris' lab during my time at WPI, Dr. Karl Helmer was a key resource for scientific and personal advice. Karl, since your parting from the lab I have missed our discussions, both scientific and political! Thank you for all forms of your support during my time at WPI.

I very much enjoyed the time I spent with Dr. Yitzhak Mendelson, both in the classroom and in informal discussions. Dr. Mendelson's friendly demeanor made it easy to talk about graduate student life in general and he provided perspective from someone with a background similar to mine. Dr. Nils Henninger and James Bouley provided invaluable surgical assistance

during my experiments. Nils, your scientific skepticism was most appreciated and motivated me further towards experimental rigor. And Nils please remember, it's manganese, not magnesium! I thank you very much for everything and I am glad to consider you both a friend.

I am grateful for the efforts of my dissertation committee members; Drs. Chris Sotak, Karl Helmer, Yitzhak Mendelson, Peter Grigg, and George Pins. I appreciate their time spent reading my dissertation and attending committee meetings. I also appreciate their suggestions during my defense discussion and I will strive to reach their level of scientific achievement and personal success.

I thank Dr. Erica Henning for starting me on the MEMRI experiments, answering my questions via email while she was at the NIH and for all of our conversations, scientific or otherwise-oriented. I also thank Dr. Jeremy Wellen for his help and advice before he left the lab. I wish we had had the opportunity to work together more. And for Siva, Govind, Salman, Pallavi, and Ronn; thank you all for the conversations and comic relief. I will miss you all and I will leave you with yet another lecture: write often and early!

# TABLE OF CONTENTS

Abstract	v
Chapter 1 - Basic Principles of MRI	1
1.0 Basic Physical Principles of Nuclear Magnetic Resonance	1
1.1 Introduction	1
1.2 Electromagnetic Wave Theory	1
1.2.1 The Electric and Magnetic Field	1
1.2.2 Generation of an Electromagnetic Wave	3
1.3 Nuclear Energy States	5
1.4 The Free Induction Decay Signal	13
1.4.1 Sampling the MR Signal	14
1.5 Relaxation in the MR Experiment	16
1.5.1 Mechanism of Spin-Lattice ( $T_1$ ) and Spin-Spin ( $T_2$ ) Relaxation	16
1.5.2 The Spin-Echo RF Pulse Sequence	20
1.6 Measurement of Relaxation Times	23
1.6.1 $T_1$ Relaxation Measurement Techniques	23
1.6.2 $T_2$ Relaxation Measurement by Carr-Purcell-Meiboom-Gill Pulse Sequence	25
2.0 Magnetic Resonance Imaging	27
2.1 Spatial Localization of a MR Signal	27
2.1.1 Magnetic Field Gradients for MRI	27
2.1.2 The Fourier Transform	29
2.1.3 Basic Properties of the Fourier Transform	31
2.1.4 Slice Select Gradients and the RF Excitation Pulse	32
2.1.4.1 Slice Dephasing	33
2.2 Spatial Encoding of the MR Signal	35
2.2.1 Phase-Encoding	36
2.2.2 Frequency-Encoding	37
2.3 Spin-Echo MRI	38
2.3.1 Spin-Echo MRI Pulse Sequence	38
2.4 The Gradient-Echo and Gradient-Echo (GRE) MRI	42
2.5 Image Contrast Based on Tissue $T_1$ and $T_2$ Relaxation Times	45
2.6 Multi-Slice Spin-Echo MRI	49
2.7 Echo-Planar Imaging	51
2.7.1 Echo-Planar Imaging Methods for Traversing k-space	52
2.8 Diffusion-Weighted Imaging	55
2.8.1 Diffusion of Water	56
2.8.2 Stejskal-Tanner Diffusion-Weighted Pulse Sequence	57
2.8.3 Quantification of Diffusion-Weighted Images: The ADC Map	58
References	59
Chapter 2 – Characteristics and Manipulation of the Blood-Brain Barrier (BBB)	61
2.1 Blood-Brain Barrier (BBB) Background	61
2.2 Anatomy of the BBB	61

2.2.1	Brain Capillary Epithelium	62
2.3	Techniques to Determine BBB Permeability	65
2.3.1	Quantification of BBB Permeability Using the Brain-Perfusion Technique	65
2.3.2	A Semi-Quantitative Measure of BBB Permeability Using Evans Blue (EB) Dye	67
2.4	Hyperosmotic Disruption of the BBB	68
2.4.1	Characteristics of Reversible Osmotic BBB Disruption	69
2.4.2	Mannitol and Arabinose as Hyperosmolar Infusates for BBB Disruption	71
2.5	The BBB and Cerebral Edema	76
2.6	MRI Detection of BBB Disruption	79
2.6.1	Gd-DTPA Used to Detect Regions of Pathological BBB Disruption	80
	References	81
<b>Chapter 3 – Theory and Application of Manganese-Enhanced Magnetic Resonance Imaging (MEMRI)</b>		<b>85</b>
Introduction		85
3.1	Magnetic Resonance Contrast Agent Physics	85
3.1.1	Effect of Contrast Agents on MR Parameters	86
3.1.2	Relaxation Effects of Paramagnetic Ion Metal Complexes	87
3.2	Manganese as a Calcium ( $\text{Ca}^{2+}$ ) Analog	90
3.2.1	Neurotransmission in Brain: The Role of Calcium Channels	91
3.2.2	$\text{Mn}^{2+}$ Passage into Cells via Voltage-Gated Calcium Channels	92
3.3	Manganese Toxicity and Cellular Effects of Manganese	96
3.3.1	$\text{Mn}^{2+}$ <i>In Vivo</i> After Intravenous (I.V.) Infusion	100
3.4	$\text{Mn}^{2+}$ Transport Across the BBB	104
3.5	$\text{Mn}^{2+}$ as MR Contrast Agent – $\text{Mn}^{2+}$ -Enhanced Magnetic Resonance Imaging (MEMRI)	105
3.5.1	MEMRI with Mn-DPDP	105
3.5.2	MEMRI with $\text{MnCl}_2$	107
3.5.2.1	A Review of Experiments in Brain Imaging with $\text{MnCl}_2$	108
	References	118
<b>Chapter 4 – Nonspecific <math>T_1</math>-Weighted Manganese Enhancement in Rat Brain Correlates with Evans Blue Staining After Osmotic Blood-Brain Barrier Disruption</b>		<b>123</b>
Abstract		124
4.1	Introduction	125
4.1.1	Challenges in MEMRI	125
4.1.2	Evans Blue as a Marker for Osmotic BBB Disruption	127
4.1.3	Co-Infusion of $\text{MnCl}_2$ and Evans Blue (EB) Dye as a Qualitative Method for Validating $\text{MnCl}_2$ Distribution in Brain	128
4.1.4	Experimental Design to Test Mechanisms of Nonspecific MEMRI Signal-Enhancement	129
4.1.5	Relevance of Experiments to Future Work	129
4.2	Methods	130
4.2.1	Animal Preparation	130
4.2.2	Osmotic BBB Disruption and $\text{MnCl}_2$ +Evans Blue (EB) Administration	131
4.2.3	Timing of Drug Administration	132
4.2.4	Level of Anesthetic During $\text{MnCl}_2$ +EB Infusion	132

4.2.5	EB Stain Histology	132
4.2.6	MRI Measurements	133
4.2.7	Data Analysis	133
4.2.8	Statistical Analysis	135
4.3	Results	135
4.3.1	MEMRI Signal-Enhancement	135
4.3.2	Evans Blue (EB) Stain	138
4.3.3	Correlation Between Regions of MEMRI Signal-Enhancement and Evans Blue (EB) Staining	142
4.4	Discussion	145
4.4.1	Isoflurane and Halothane Level and Nonspecific MEMRI Signal-Enhancement	146
4.4.2	Nonspecific $T_1$ -Enhancement after Osmotic BBB Disruption	147
4.4.3	Cellular Uptake of $MnCl_2$ +Evans Blue (EB) Dye after Osmotic BBB Disruption	149
4.4.4	Limitations	150
4.4.5	Conclusions	151
	References	152
<b>Chapter 5 – Brain Damage and Mismatch Between Manganese-Enhanced MRI (MEMRI) and Diffusion-Weighted MRI in the Absence of Specific Neuronal Stimuli: Potential Pitfalls in MEMRI After Osmotic BBB Disruption</b>		154
Abstract		155
5.1	Introduction	156
5.1.1	MEMRI Background	156
5.1.2	Side Effects of Osmotic BBB Disruption	156
5.2	Methods	158
5.2.1	Animal Preparation	158
5.2.2	Osmotic BBB Disruption and $MnCl_2$ +EB Administration	159
5.2.3	MRI Measurements	160
5.2.4	EB and 2,3,5 TriphenylTetrazolium Chloride (TTC) Histology	161
5.2.5	Data Analysis	162
5.2.6	Statistical Analysis	167
5.3	Results	167
5.3.1	Animal Physiology	167
5.3.2	Brain Edema	169
5.3.3	MEMRI Signal-Enhancement	171
5.3.4	ADC Deficit	174
5.3.5	TTC Lesion Area	177
5.3.6	MEMRI-DWI Mismatch	182
5.3.7	Correlation of MEMRI-DWI Mismatch to TTC Lesion Area	185
5.4	Discussion	187
5.4.1	Nonspecific MEMRI Signal-Enhancement: Relation to Anesthesia and Blood Gases	187
5.4.2	Brain Edema After Osmotic BBB Disruption	188
5.4.3	Is MEMRI Signal-Enhancement Indicative of Tissue Damage?	190
5.4.4	Brain Damage Verified by TTC Lesion	191
5.4.5	MEMRI-DWI Mismatch	192
	References	197

Chapter 6 – Blood-Brain Barrier Disruption in Embolic Stroke Detected by Manganese-Enhanced Magnetic Resonance Imaging (MEMRI)	200
Abstract	201
6.1 Introduction	202
6.1.1 Stroke Background	204
6.1.2 Stroke and the BBB	205
6.1.3 The Embolic Stroke Model and Associated BBB Injury	207
6.1.4 Intracellular Calcium Level Increase During Stroke – Implications for MEMRI	209
6.2 Methods	210
6.2.1 Animal Preparation	210
6.2.2 Embolic Middle Cerebral Artery Occlusion (eMCAO)	211
6.2.3 MR Imaging	212
6.2.4 MnCl <sub>2</sub> + Evans Blue (EB) Infusion Protocol	212
6.2.5 EB and 2,3,5 TriphenylTetrazolium Chloride (TTC) Histology	213
6.2.6 Data Analysis	213
6.3 Results	216
6.3.1 MEMRI Signal-Enhancement	216
6.3.2 ADC Deficit	217
6.3.3 MEMRI-DWI Mismatch & Match	218
6.3.4 MEMRI Signal-Enhancement and ADC Correlation With Evans Blue and TTC Histology	219
6.4 Discussion	223
6.4.1 MEMRI Signal-Enhancement: Detection of Hemorrhagic Transformation During Acute Stages of Embolic Stroke?	223
6.4.2 MEMRI Signal-Enhancement in Stroke: Mechanisms Related to Cell Calcium Uptake	225
References	228
Chapter 7 – Summary	231
Appendix	
I. The Author’s Curriculum Vitae	
II. Select Conference Proceedings	



# ABSTRACT

Manganese ( $\text{Mn}^{2+}$ ) has recently gained acceptance as a magnetic resonance imaging (MRI) contrast agent useful for generating contrast in the functioning brain. The paramagnetic properties of  $\text{Mn}^{2+}$ , combined with the cell's affinity for  $\text{Mn}^{2+}$  via voltage-gated calcium channels, makes  $\text{Mn}^{2+}$  sensitive to cellular activity in the brain. Compared with indirect measures of brain function, such as blood oxygenation level dependent (BOLD) functional MRI, manganese-enhanced MRI (MEMRI) can provide a direct means to visualize brain activity.

MEMRI of the brain typically involves osmotic opening of the blood-brain barrier (BBB) to deliver  $\text{Mn}^{2+}$  into the interstitial space prior to initiation of a specific neuronal stimulus. This method assumes that the BBB-disruption process itself does not induce any apparent stimuli or cause tissue damage that might obscure any subsequent experimental observations. However, this assumption is often incorrect and can lead to misleading results for particular types of MRI applications.

One aspect of these studies focused on characterizing the confounding effects of the BBB-opening process on MRI measurements typically employed to characterize functional activity or disease in the brain (Chapters 4 and 5). The apparent diffusion coefficient (ADC) of tissue water was found to decrease (relative to the undisrupted contralateral hemisphere) following BBB opening, obscuring similar ADC changes associated with ischemic brain tissue following stroke. Brain regions exhibiting reduced ADC values following osmotic BBB disruption also experienced permanent tissue damage, as validated by histological measures in the same vicinity of the brain. Non-specific MEMRI-signal enhancement was also observed under similar conditions and was found to be correlated to regions with BBB opening as verified by Evans Blue histological staining.

In this case, MEMRI may prove to be a useful alternative for monitoring BBB-permeability changes *in vivo*.

MEMRI was also investigated as a method for visualizing regions of BBB damage following ischemic brain injury (Chapter 6). BBB disruption following stroke has been investigated using gadolinium-based MRI contrast agents (e.g., Gd-DTPA). However, as an extracellular MRI contrast agent, Gd-DTPA is not expected to provide information regarding cell viability or function as part of MR image contrast enhancement. By comparison, brain regions with ischemia-induced BBB damage, and blood-flow levels sufficient to deliver  $Mn^{2+}$ , show MEMRI-signal enhancement that correlates to regions with tissue damage as verified by histological staining. This approach should allow us to better understand the factors responsible for ischemia-induced BBB damage. Furthermore, MEMRI should be a useful tool for monitoring therapeutic interventions that might mitigate the damage associated with BBB disruption following stroke.

# CHAPTER 1

## Basic Principles of MRI

### Basic Physical Principles of MR

Electromagnetic Wave Theory

Nuclear Energy States

The Free Induction Decay Signal

Relaxation in the MR Experiment

Measurement of Relaxation Times

### Magnetic Resonance Imaging

Spatial Localization of a MR Signal

Spatial Encoding of the MR Signal

Spin-Echo MRI

The Gradient-Echo and Gradient-Echo (GRE) MRI

Image Contrast Based on T<sub>1</sub> and T<sub>2</sub> Relaxation Times

Multi-Slice Spin-Echo MRI

Echo-Planar Imaging

Diffusion-Weighted Imaging

## 1.0 Basic Physical Principles of Nuclear Magnetic Resonance

### 1.1 Introduction

This chapter is an introduction to the basic theory of magnetic resonance imaging (MRI). The topics covered include the MR theory and methods that pertain specifically to the research described in this dissertation. The MR theory is discussed at a depth that should provide a basic understanding of spin-echo, gradient echo, echo-planar and diffusion-weighted MR imaging.

### 1.2 Electromagnetic Wave Theory

The electromagnetic wave is of fundamental importance for the generation of a magnetic resonance image. A brief discussion of the basic components of an electromagnetic wave, the electric and magnetic field, and what portions of the wave are important to magnetic resonance imaging (MRI) are presented here.

#### 1.2.1 The Electric and Magnetic Field

##### *Generation of the electric and magnetic field by charged particles*

The concept of a 'field' can be described with a common force that surrounds us: gravity. To every point in space we can assign a vector  $\mathbf{g}$  that represents the force  $\mathbf{F}$  exerted on some mass  $m$  by earth's gravity. The gravitational field is then written as  $\mathbf{g} = \mathbf{F}/m$ . In a similar fashion we can talk of a vector  $\mathbf{E}$  that represents the force  $\mathbf{F}$  that a positive electric charge  $q$  experiences when placed near a charged rod. The electric field is then described as  $\mathbf{E} = \mathbf{F}/q$ . The direction of the vector  $\mathbf{E}$  is the same as  $\mathbf{F}$ ; it is the direction the stationary positively-charged particle would accelerate towards the rod. The electric field, therefore, is representing the force of one electrically-charged particle on another. Can it then be said that the magnetic field is a representation of a magnetically-charged particle on

another? The answer to date is no, i.e., there are no known magnetic charges. It is the moving electrical charge that generates a magnetic field.

### *Properties of the Magnetic Field*

A charged particle moving in the presence of a magnetic field  $B$  does not experience acceleration but can have its direction changed. The magnetic field deflects a moving charge by a force  $F_B$  maximally when the charged particle is moving perpendicular to the direction of the magnetic field:  $F_B = qvB\sin(\theta)$  where  $\theta$  is the angle between the direction of the moving particle and the direction of the magnetic field,  $q$  is the measure of electric charge, and  $v$  is the velocity of the charge. The measure of magnetic field strength is the newton / (ampere \* meter) or more simply and more commonly referred to as the Tesla ( $1 \text{ T} = 1 \text{ N}/(\text{A} * \text{M})$ ) (1). As reference a small toy magnet (refrigerator magnet) has a magnetic field strength of  $\sim 10^{-2} \text{ T}$ , the magnetic field at the surface of the earth is  $\sim 10^{-4} \text{ T}$  and a clinical MRI scanner is at 1.5 T. Figure 1.1 shows an example of the magnetic-field profile of a bar magnet.

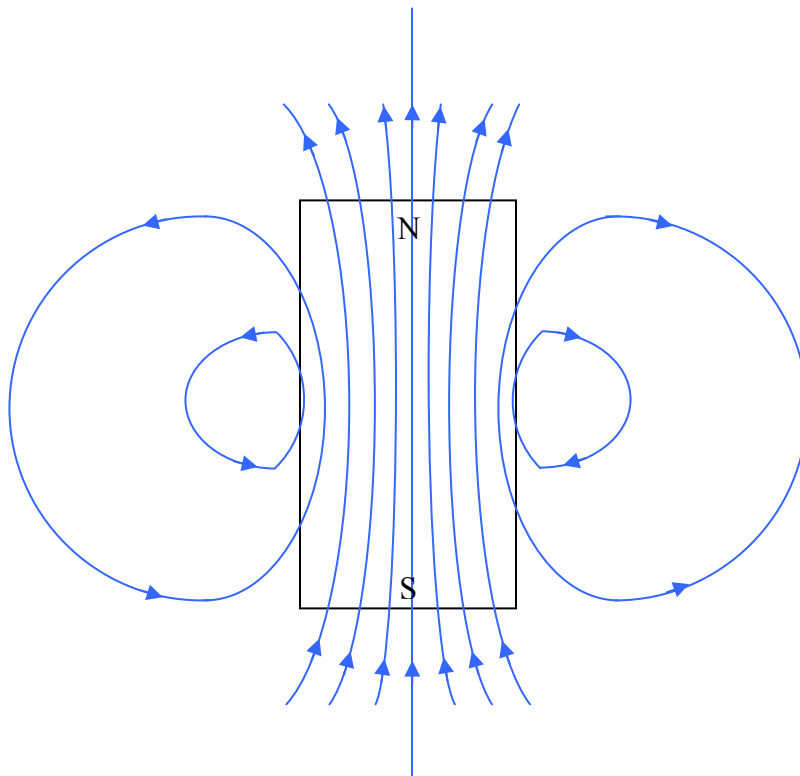


Figure 1-1: Magnetic field lines for a typical bar magnet. Note the linearity of the field in the middle of the magnet; this is an important characteristic of magnets for magnetic resonance imaging and will be discussed later.

### 1.2.2 Generation of an Electromagnetic Wave

Electric and magnetic fields can be generated by point charges and bar magnets, respectively, as discussed in the previous section. What is required to generate a magnetic resonance image is a propagating magnetic field (which moves in a direction perpendicular to the main magnetic field of the MRI scanner). A convenient way to generate a relatively small and switchable magnetic field is by passing an electric current through a small loop of wire that surrounds the sample we are interested in imaging. The small loop of wire and the circuit that completes it is referred to as a LC oscillator.

#### *Induced Magnetic Field in Wire Loop*

For a single loop of wire carrying a current  $I$ , a fairly homogenous magnetic field is generated near the center of the loop as shown in Figure 1-2:

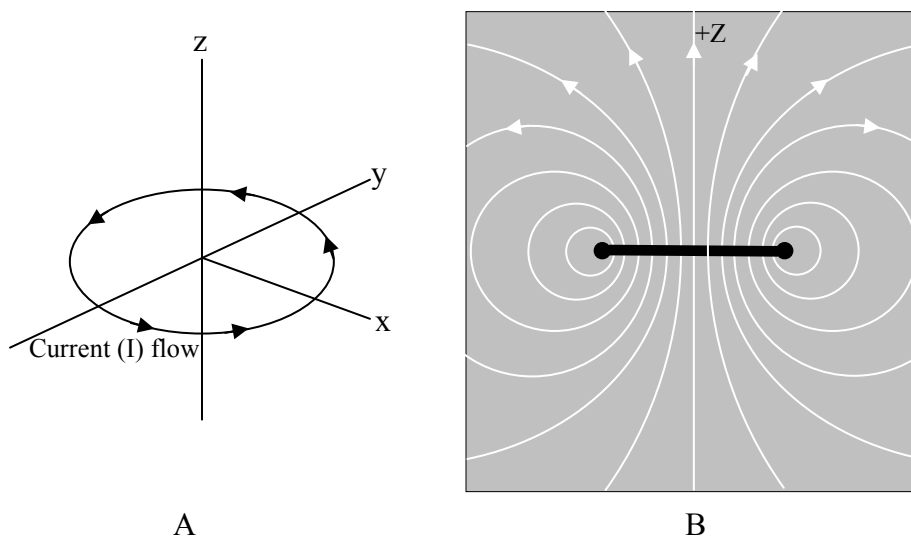


Figure 1-2: Current flow in single loop of wire (A) and a side view of resultant magnetic field lines (B).

*The LC Oscillator*

The electric charge and current in the LC oscillator circuit fluctuates at a particular frequency given by  $\omega = 1/\sqrt{LC}$  where L and C are the inductance and capacitance values in the circuit. The oscillation frequency of the LC circuit is more commonly named the resonant frequency. For MRI applications the frequency of oscillation of the magnetic field needed for MR signal generation is in the radio-frequency (RF) range. Therefore, the ‘coil’ (or coils) used to generate MR images are commonly referred to as RF coils. When an LC oscillator (or resonator) is used to acquire images in a 2 Tesla MR scanner, the resonant frequency of the LC circuit must be tuned to 2 Tesla \* 42.57 MegaHertz/Tesla (MHz/T) or  $\sim 85$  MHz. The special constant, 42.57 MHz/T, will be discussed later in this chapter.

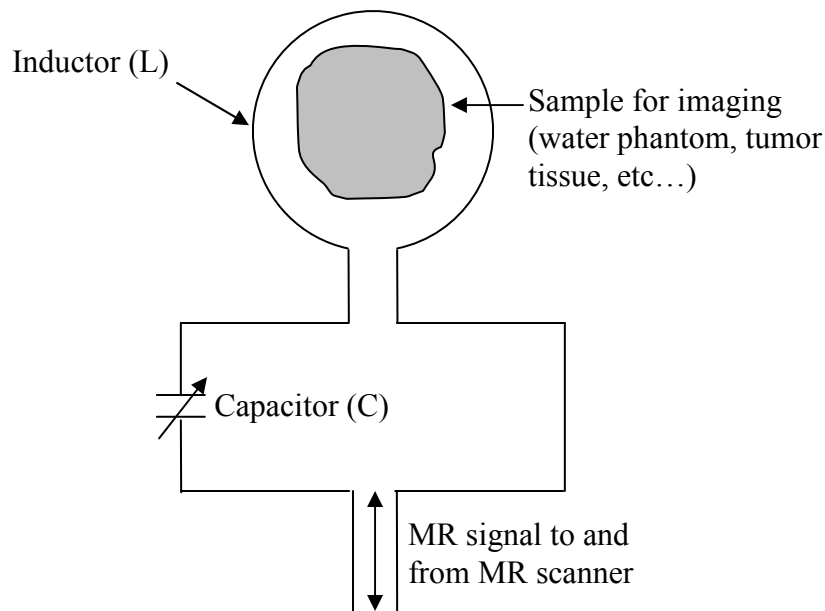


Figure 1-3: LC oscillator circuit. The capacitor shown is adjustable to allow the user to tune the coil to an exact frequency (the resonant frequency of the coil can change due to stray capacitance values in the sample among several other variables). The inductor shown is a single loop of copper wire. In this form the RF coil is referred to as a ‘surface coil’.

The single loop of wire shown in Figure 1-3 is one of many ways of generating a resonating magnetic field within a tissue of interest. Multiple loops of wire wound tightly together (solenoid) are also commonly used with the advantage of a highly homogeneous magnetic field produced

within the diameter of the coil. The transfer of energy from the coil to the tissue (sample) of interest (via the magnetic field produced by the coil) is the primary goal of the LC oscillator and all RF coils used for MRI. Water molecules within the tissue of interest become 'excited' by the magnetic energy produced by the coil. The means by which the tissue becomes excited is the subject of the next section.

### 1.3 Nuclear Energy States

#### *Atomic structure and angular momentum*

Atomic structure is defined by an atom's nuclear configuration and its orbiting electron(s). The nucleus of the atom consists of protons (charge =  $+e$ , where  $e$  is the charge of an electron:  $-1.60 \times 10^{-19}$  Coulomb) and neutrons (charge = 0); both of which are referred to as nucleons. The electron(s) that orbit(s) the nucleus are each negatively charged and possess both spin and orbital angular momentum. The angular momentum associated with a charged particle generates a magnetic field (referred to as the magnetic dipole moment or MDM) which is a vector quantity with both magnitude and direction. The magnetic field associated with electrons is referred to as the electron MDM. Since nuclei can also possess spin and orbital angular momentum and are positively charged, the associated magnetic field is referred to as the nuclear MDM. For MRI, the MDM of the  $^1\text{H}$  isotope of hydrogen is simply that associated with the single proton in the nucleus (Figure 1-4). The proton MDM is the fundamental physical property that is exploited to generate an MR image.



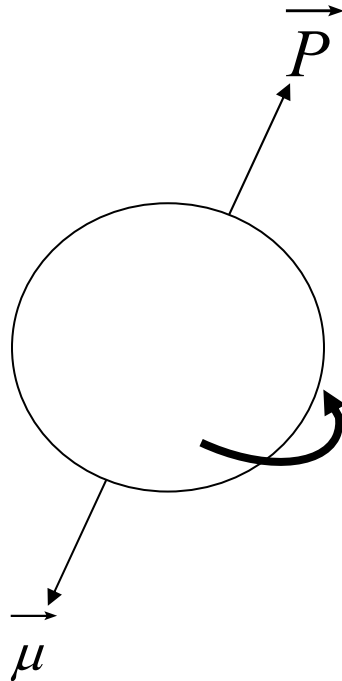


Figure 1-4: Single proton ( $^1\text{H}$  isotope of hydrogen) showing the angular momentum vector ( $\mathbf{P}$ ) and the antiparallel nuclear MDM ( $\boldsymbol{\mu}$ ) vector that is created by the moving positive charge associated with the proton.

A convenient way to represent the relationship between the nuclear MDM and its angular momentum is to consider the ratio of the two quantities. This ratio is referred to as the magnetogyric (or gyromagnetic) ratio and is written as  $\gamma = \mu/P = -(e/2m_e)$ , where  $e$  and  $m_e$  are the charge and mass of the proton, respectively, when considering the  $^1\text{H}$  isotope of hydrogen.

#### *The 'spin' of a nucleus*

The laws of quantum mechanics require that the angular momentum of the proton shown in Figure 1-4 be quantized, i.e., the magnitude of the nuclear spin angular momentum can only be represented by specific discrete values:

$$\vec{P} = \eta[I(I + 1)]^{1/2} \quad (1.1)$$

where  $\eta = h/2\pi$  ( $h = \text{Planck's constant} = 6.63 \times 10^{-34} \text{ kg}\cdot\text{m}\cdot\text{s}^{-1}$ ) and  $I$  is the nuclear spin quantum number. The value of  $I$  depends on the structure of the nucleus; specifically, the number of protons and neutrons. Each proton and neutron has an associated spin of  $1/2$ . In the nucleus, the pairing of two protons (or two neutrons) results in a cancellation of the spin from each partner. Consequently, the net spin of a particular nucleus is determined by the number of unpaired protons and/or neutrons in the nucleus. For example, the  $^{13}\text{C}$  nucleus has six protons and seven neutrons. The six protons form three pairs whose spins cancel. The seven neutrons form three spin pairs and with one neutron remaining unpaired. As a result, the net spin associated with the  $^{13}\text{C}$  isotope is simply that contributed by the single unpaired neutron (i.e.,  $I = 1/2$ ), as shown in Figure 1.5.

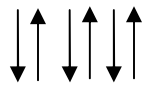
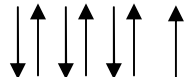
$^{13}\text{C}$ Nuclear Config.	Spin Pairs	Resulting Spin ( $I$ )
6 Protons		0
7 Neutrons		$1/2$

Figure 1-5: Spin pairs for the  $^{13}\text{C}$  nucleus. Paired protons and neutrons result in a net zero spin for each pair. It is the unpaired neutron that gives  $^{13}\text{C}$  a spin of  $I = 1/2$ .

### *Nuclei in an external magnetic field*

For nuclei with a non-zero value of  $I$ , the nuclear MDM can adopt certain orientations with respect to the direction of an applied external magnetic field. For spin- $1/2$  nuclei, such as  $^1\text{H}$  or  $^{13}\text{C}$ , the nuclear MDM can be oriented in a 'spin-up' or 'spin-down' state which corresponds to the nuclear MDM being either parallel or antiparallel to the external magnetic field, respectively. In the absence of an applied external magnetic field, the two spin states have the same energy (i.e., they are said to be *degenerate*). However, in the presence of an applied external magnetic field – usually designated as  $B_0$  – the energy associated with each state is different and given by:

$$E_i = -m_i(\gamma\hbar B_0 / 2\pi) \quad (1.2)$$

where  $\gamma$  is the magnetogyric ratio,  $h$  is Planck's constant,  $B_0$  is the external magnetic field strength, and  $i$  is the particular spin state (either  $+\frac{1}{2}$  or  $-\frac{1}{2}$  in the case of  $^1\text{H}$ ). Equation 1.2 indicates that the energy of the proton MDM is quantized in units of  $\gamma h B_0 / 2\pi$  and varies with the external magnetic field strength  $B_0$ . Figure 1-6 shows the two energy levels associated with the proton MDM in the absence and presence of the  $B_0$  field.

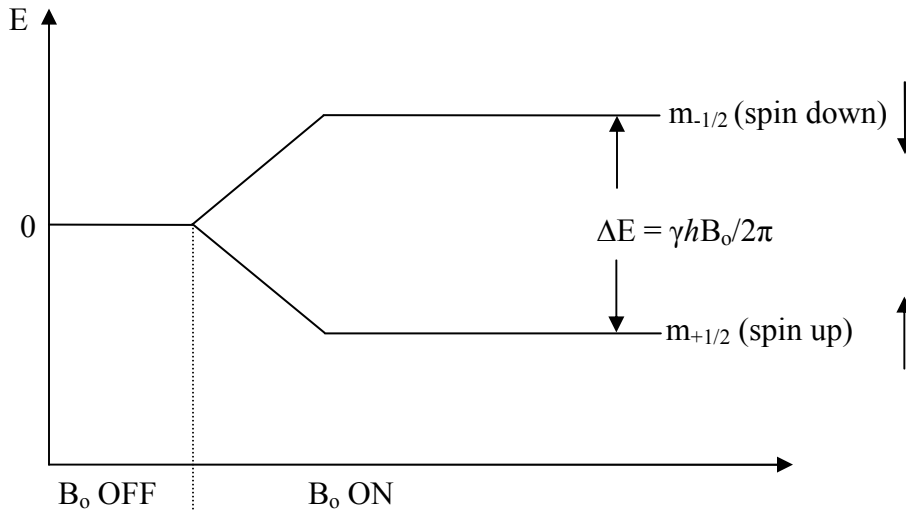


Figure 1-6: Energy of the proton ( $^1\text{H}$ ) MDM in the absence and presence of an external magnetic field  $B_0$ . The quantization of the proton MDM implies that the MDM can occupy only one of two possible energy states.

When a sample containing spin- $\frac{1}{2}$  nuclei is placed into an external magnetic field, the nuclei will distribute themselves between the two energy states according to the Boltzmann distribution. The number of nuclei in a particular energy state,  $N_I$ , is given by:

$$N_I = e^{\frac{-E_I}{KT}} \quad (1.3)$$

where  $E_I$  is the energy of state  $I$ ,  $K$  is the Boltzmann constant ( $1.38 \times 10^{-23}$  Joules/Kelvin), and  $T$  is temperature (Kelvin scale). The ratio of nuclei in each state is given by:

$$N_{-1/2} / N_{1/2} = \frac{e^{-E_{-1/2}/KT}}{e^{-E_{1/2}/KT}} = e^{-\Delta E/KT}, \quad (1.4)$$

where  $N_{-1/2}$  and  $N_{1/2}$  are the populations of nuclei in the upper and lower states, respectively, and  $\Delta E$  is the energy difference between the two states. Writing the total population of nuclei as  $N_T = N_{-1/2} +$

$N_{1/2}$ , the difference in population between the two states as  $\Delta N = N_{1/2} - N_{-1/2}$ , and using the Taylor series approximation  $e^{-E_{-1/2}/KT} \sim 1 - \Delta E/KT$ , the difference in population between the two energy states,  $\Delta N$ , can be written as:

$$\Delta N = \frac{N_T \Delta E}{2KT} . \quad (1.5)$$

**For an MRI experiment, the MR signal is directly proportional to the population difference,  $\Delta N$ , between the two states.** The population difference can be expressed in terms of the net nuclear magnetization vector,  $M$ , which is defined as the sum of all the individual nuclear magnetic moments,  $\mu$ :

$$M = \sum_{m=-I}^I N_m \vec{\mu}_{zm} , \quad (1.6)$$

where  $N_m$  is the number of nuclei in state  $m$  and  $\mu_{zm}$  is the z-component of all the nuclear magnetic moments in state  $I$ . If the system is at the Boltzmann equilibrium, then the net nuclear magnetization vector is designated as  $M_0$ , where the subscript denotes the equilibrium condition.

From a quantum-mechanical point of view, the MRI experiment involves transitions between energy states. For spin- $1/2$  nuclei, transitions from the lower to the higher energy state are induced by applying energy [in the form of radiofrequency (RF) radiation] that exactly equals the difference in energy between the two states (i.e.,  $\Delta E = \gamma \hbar B_0 / 2\pi$ ). Since the difference in energy between the two states is also given by  $\Delta E = h\nu$ , where  $\nu$  is the frequency of electromagnetic radiation (in this case RF), then the RF frequency that satisfies the “resonance” condition is given by:

$$\nu = \gamma B_0 / 2\pi . \quad (1.7)$$

Equation 1.7 can be thought of as the quantum-mechanical version of the magnetic resonance equation.

### *Classical Description of MR*

The net nuclear magnetization,  $M$  (from Eq. 1.6), can be depicted in the classical sense using vector diagrams. Figure 1-7 shows a vector diagram for a single nuclear MDM and a diagram for a collection of nuclear MDMs that give rise to the net magnetization vector,  $M$ , in the laboratory frame of reference. If the system is at the Boltzmann equilibrium, then the net nuclear magnetization vector is designated as  $M_0$ , where the subscript denotes the equilibrium condition.

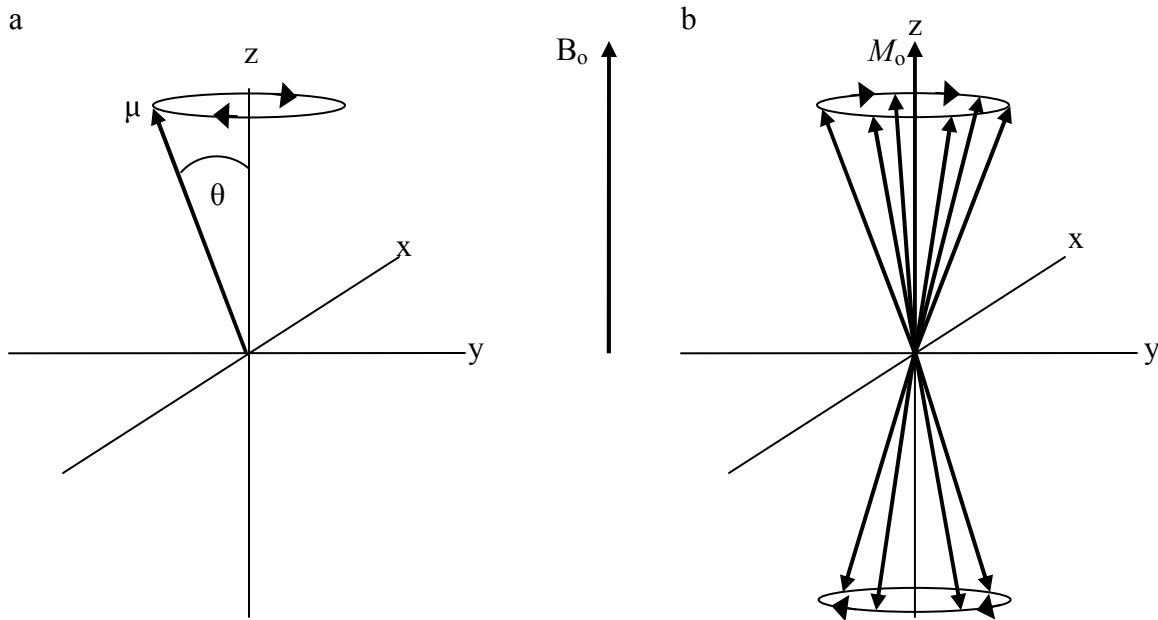


Figure 1-7: a) A single nuclear magnetic dipole moment (MDM),  $\mu$ , in the presence of the external magnetic field,  $B_0$ . The  $B_0$  field exerts a force on  $\mu$ , resulting in a precessional motion of  $\mu$  about  $B_0$ . b) A collection of nuclear MDMs precessing about  $B_0$  with an excess population (of two) oriented in the  $B_0$  direction. Although the transverse (x-y) components of the MDMs cancel each other out, there is a net z-component of magnetization,  $M_0$  (if the system is at the Boltzmann equilibrium), which corresponds to the population difference between the two orientations. The Cartesian-coordinate system is defined in this case as the ‘laboratory’ frame of reference.

In the presence of an external magnetic field,  $B_0$ , aligned along the z-direction of a Cartesian coordinate reference frame, individual nuclear MDMs will precess about  $B_0$  as a result of the force exerted on them by  $B_0$ . The precessional frequency,  $\omega$  (in rad/s), is given by the Larmor equation:

$$\omega = \gamma B_0. \quad (1.8)$$

Notice that the Larmor equation has a form analogous to the resonance equation (Eq. 1.7) derived from the quantum-mechanical model.

In the presence of a radiofrequency field,  $B_1$ , that is perpendicular to the main magnetic field,  $B_0$ , and to  $M$ , the motion of  $M$  in the laboratory frame of reference (a fixed frame of reference with respect to the laboratory surroundings) can be described by a set of differential equations known as

the Bloch equations (2). The Bloch equations also include the relaxation parameters  $T_1$  and  $T_2$  (more on these parameters in Section 1.4) which account for the motion of the  $M_z$  and  $M_{xy}$  components of  $M$ , respectively, during their return to the Boltzmann equilibrium (after the RF field is turned off). By considering first the single magnetic moment (Figure 1-7a), the rate of change of  $\mu$  with respect to time is given by:

$$\frac{d\vec{\mu}}{dt} = \gamma(\vec{\mu} \times B_0), \quad (1.9)$$

which describes the precessional motion of  $\mu$  around  $B_0$ . An analogous Bloch equation can also be written for the net magnetization vector  $M$  as:

$$\frac{d\vec{M}}{dt} = \gamma(\vec{M} \times B_0) \quad (1.10)$$

By adding the contributions that describe the behavior of the magnetization under the influence of the  $B_1$  field as well as relaxation, the full Bloch equations for each component of  $M$  are summarized as follows:

$$\frac{dM_x}{dt} = \gamma B_0 M_y + \gamma B_1 \sin \omega t M_z - \frac{M_x}{T_2} \quad (1.11)$$

$$\frac{dM_y}{dt} = -\gamma B_0 M_x + \gamma B_1 \cos \omega t M_z - \frac{M_y}{T_2} \quad (1.12)$$

$$\frac{dM_z}{dt} = -\gamma B_1 (\sin \omega t M_x + \cos \omega t M_y) - \frac{(M_z - M_0)}{T_1} \quad (1.13)$$

In this form the Bloch equations are tedious to solve. However, the task is made easier by a coordinate system transformation into a frame of reference that is rotating at the precessional frequency of the nuclei (i.e., a rotating reference frame). For example, consider a spinning merry-go-round with several children aboard. To the observer standing next to the merry-go-round, the children would appear to be spinning at the rotational frequency of the ride. However, if the observer were to then jump on the merry-go-round with the children, the children would not appear to be moving (i.e., they would appear to be stationary) in that frame of reference. Similarly, if the magnetization vector  $M$  is observed from a frame of reference rotating at the precessional frequency of the nuclei, then  $M$  will also appear to be stationary in that rotating frame of reference. In other words, observing  $M$  in the rotating reference frame effectively removes the contribution of the precessional term (i.e.,  $\gamma B_0 M_y$  or  $-\gamma B_0 M_x$ ) from the Bloch equations (e.g., Eqs. 1.11 and 1.12,

respectively). Transforming to the rotating frame of reference ( $x'$ ,  $y'$ ,  $z'$ ) from the fixed laboratory frame of reference ( $x$ ,  $y$ ,  $z$ ) requires the following definitions for the Cartesian components of magnetization in the rotating reference frame:

$$M_{x'} = M_x \cos(\omega t) - M_y \sin(\omega t) \quad (1.14)$$

$$M_{y'} = M_x \sin(\omega t) + M_y \cos(\omega t) \quad (1.15)$$

$$M_{z'} = M_z. \quad (1.16)$$

The Bloch equations can then be re-written as:

$$\frac{dM_{x'}}{dt} = (\omega_0 - \omega)M_{y'} - \frac{M_{x'}}{T_2} \quad (1.17)$$

$$\frac{dM_{y'}}{dt} = -(\omega_0 - \omega)M_{x'} - \frac{M_{y'}}{T_2} + \gamma \vec{B}_1 M_z \quad (1.18)$$

$$\frac{dM_z}{dt} = -\left(\frac{M_z - M_0}{T_1}\right) - \gamma \vec{B}_1 M_{y'}, \quad (1.19)$$

and solved in this form to predict how the different components of magnetization behave under a particular set of experimental conditions.

Figure 1-8 shows the observed path of  $M$  in the presence of an RF magnetic field,  $B_1$ , oscillating at the Larmor frequency for an observer in the laboratory frame of reference (Figure 1-8a) and in the rotating frame of reference (Figure 1-8b). The RF coil in Figure 1-8 is positioned such that when alternating current is passed through the coil, an oscillating magnetic field,  $B_1$ , is generated according to Ampere's law. The  $B_1$  field is perpendicular to  $B_0$  and to  $M$  and exerts a torque on  $M$  such that  $M$  tips away from  $B_0$ . The 'tip angle'  $\theta$  can be adjusted by controlling the amplitude of the  $B_1$  field and the duration,  $t$ , of the RF pulse that is applied to the coil. For a nucleus with a gyromagnetic ratio  $\gamma_n$ , the flip angle  $\theta$  is given by:

$$\theta = \gamma_n B_1 t. \quad (1.20)$$

The purpose of the  $B_1$  field then is to convert the z-component of magnetization ( $M_z$ ), which is not directly observable, into detectable transverse components of magnetization (i.e.,  $M_{xy}$ ). As shown in Figure 1-8b, a  $90^\circ$  RF pulse creates the maximum transverse component of magnetization which in turn yields the largest MR signal intensity.

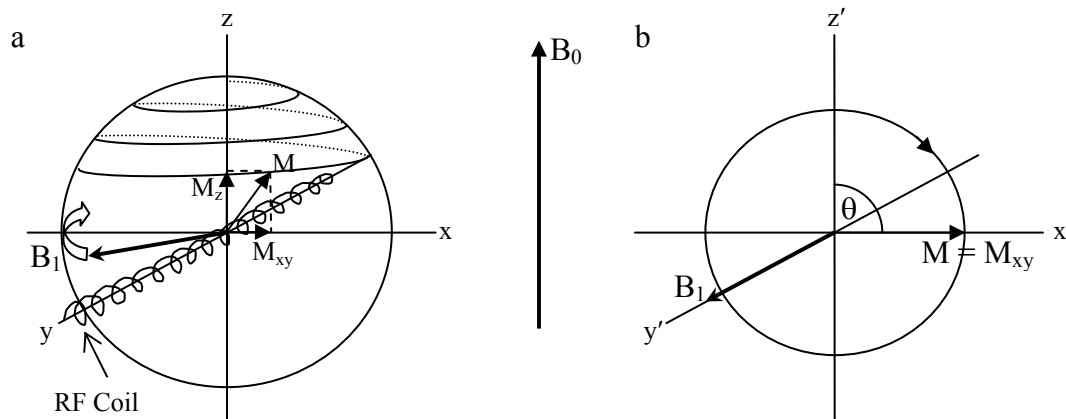


Figure 1-8: a) The RF magnetic field  $B_1$  and  $M$  in the fixed or laboratory frame of reference containing  $B_0$ . In this frame of reference, the  $B_1$  field rotates at the Larmor precessional frequency of  $M$ . The effect of  $B_1$  and  $B_0$  together forces  $M$  to tip away from the  $z$ -axis as well as precess about  $B_0$  at the same time (resulting in the complex spiral motion indicated in the figure). At the time point shown in the figure,  $M$  has two nonzero components;  $M_z$  (longitudinal) and  $M_{xy}$  (transverse) magnetization. b) The RF magnetic field  $B_1$  and  $M$  in the rotating frame of reference. In this frame of reference, the  $B_1$  field now appears stationary and the effect of the  $B_0$  field on  $M$  is effectively removed. Consequently, in the rotating reference frame,  $M$  only experiences the effect of the  $B_1$  field and is confined to rotate about  $B_1$  in the  $x', z'$  plane. At the time point shown in the figure,  $M$  has rotated through  $90^\circ$  and thus has only a transverse component,  $M_{xy}$ .

## 1.4 The Free Induction Decay Signal

As long as the external magnetic field  $B_1$  is applied, the net magnetization vector  $M$  will continue to precess about the  $B_1$  axis (in the rotating frame of reference). When the  $B_1$  field is removed (or no longer oscillates at the Larmor frequency),  $M$  begins to return to the Boltzmann equilibrium state. The MR signal can then be detected during this period. From Faraday's law of induction, an oscillating magnetic field – in this case  $M_{xy}$  – generates (or induces) an electromotive force (emf) in the RF coil (that has a geometry and orientation to specifically detect transverse components of magnetization). The small emf oscillating in the RF coil is referred to as the free induction decay (FID). 'Free' refers to the process being free of any applied forces, 'induction' refers to the emf induced in the coil, and 'decay' refers to the fact that the amplitude of the induced emf decays over time. The FID is amplified and then digitized for subsequent signal processing (e.g., Fourier transformation) to extract the frequency components of the signal. A typical FID and the corresponding RF detection coil arrangement in the laboratory frame of reference are shown in Figure 1-9.



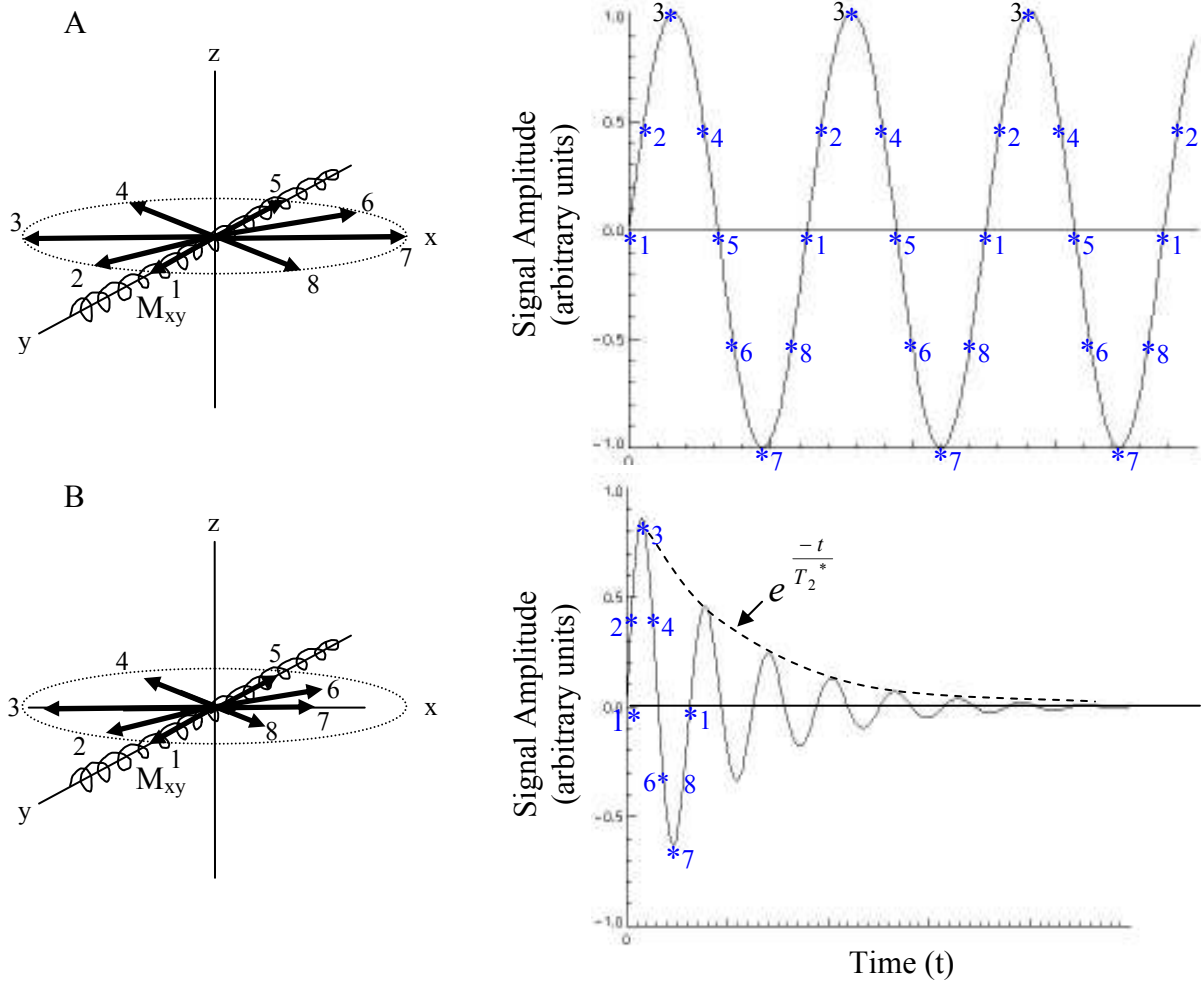


Figure 1-9: Detection of transverse magnetization,  $M_{xy}$ . The Cartesian coordinate systems depict  $M_{xy}$  vectors at different time points in the absence (A) or presence (B) of transverse magnetization decay. The graphs depict the corresponding amplitude of  $M_{xy}$  (in terms of signal intensity) as a function of time. The phase of the signal depicted by numbered points on graphs depends on the initial position of the  $M_{xy}$  vector in the transverse plane relative to the position of the RF detection coil. The decaying  $M_{xy}$  signal is referred to as the free induction decay (FID). The FID shape is the result of a sinusoid multiplied by an exponential. The decay rate is dependent on  $T_2^*$  relaxation (more on  $T_2^*$  relaxation in Section 1.4.1).

### 1.4.1 Sampling the MR Signal

The MR signal is a continuous signal (i.e., analog) while signals that computers deal with are discrete or digital signals. Therefore, MR signals must be sampled and stored digitally (i.e., digitized) before the FT can be applied to generate a MR image. A minimum sampling rate is necessary for correct digitization of the MR signal (and any time-domain signal) and is determined

according to the Nyquist Sampling Theorem. The Nyquist Sampling Theorem states that to correctly digitize a signal the sampling rate must be twice the highest frequency contained within the signal. This concept is shown graphically in Figure 1-10:

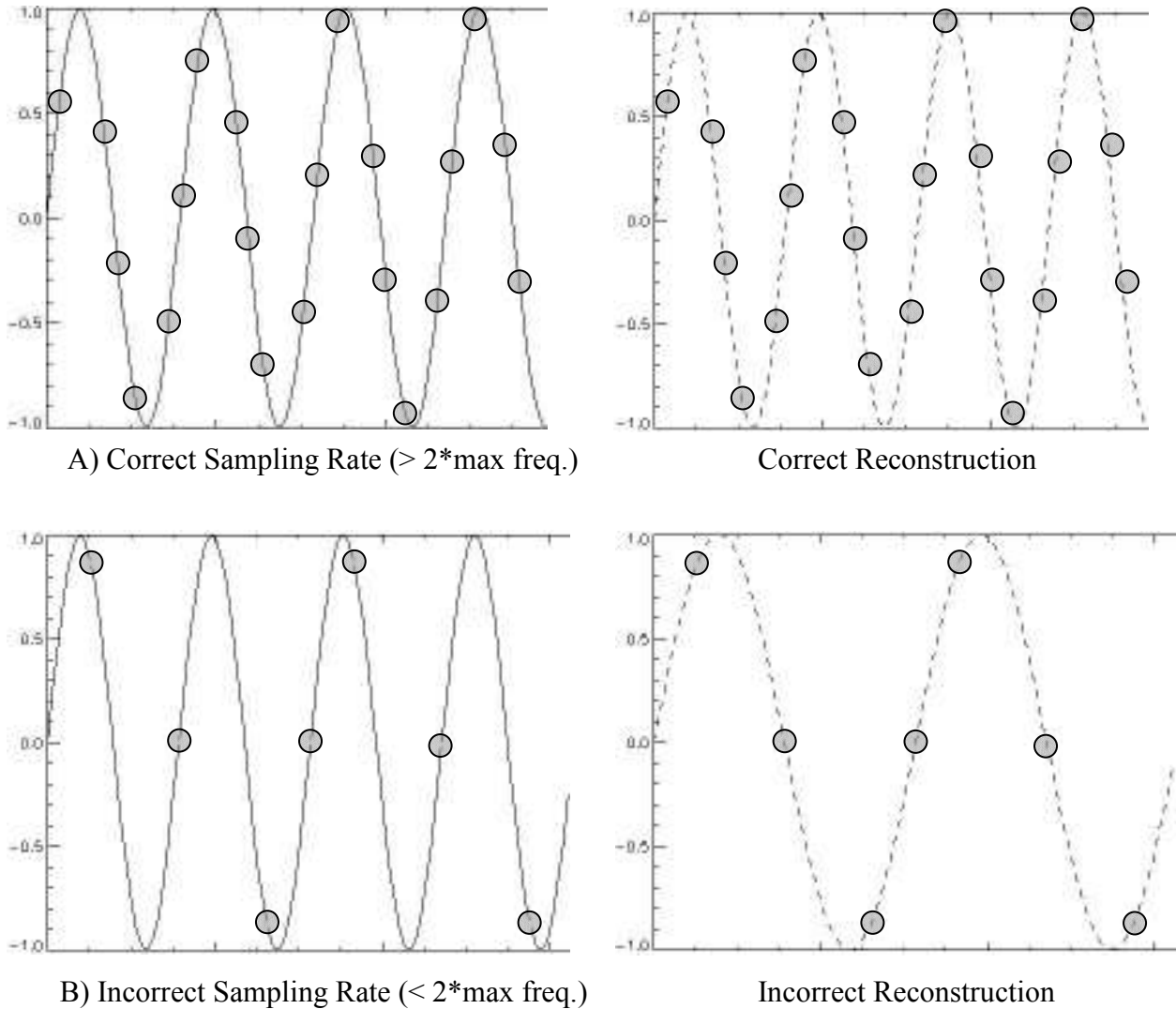


Figure 1-10: Examples of correct and incorrect sampling of a time domain signal. Sample rate in A) is greater than twice the highest frequency component in the signal and the resulting reconstruction (digitization) of the signal is accurate. Sample rate in B) is less than twice the highest frequency component in the signal and the resulting digitization of the signal does not accurately represent the original signal. In this example (B), the frequency of the reconstructed signal is exactly half of the sampled signal.

## 1.5 Relaxation in the MR Experiment

A complete description of the Bloch equations includes a basic understanding of the MR relaxation parameters  $T_1$  (spin-lattice relaxation) and  $T_2$  (spin-spin relaxation).  $T_1$  and  $T_2$  depend on the biological sample and the magnitude of the main magnetic field ( $B_0$ ) and are the primary contributing factors to the contrast seen in most magnetic resonance images.

### 1.5.1 Mechanism of Spin-Lattice ( $T_1$ ) and Spin-Spin ( $T_2$ ) Relaxation

To perturb the equilibrium nuclear magnetization vector  $M_0$  towards the transverse plane (i.e., which is equivalent to exciting the nuclei from the ground state to the excited state) requires RF stimulation supplied by the RF transmitter (via the RF coil) of the spectrometer. Similarly, recovery of the longitudinal component of magnetization (i.e.,  $M_z$ ) back to the Boltzmann equilibrium state (or, from a quantum-mechanical point of view, nuclei in the excited state to returning to ground state) also involves RF stimulation; albeit from a very different source: the nuclei's surroundings or 'lattice'. Each water molecule contains two protons, each with their own individual nuclear MDM. Given the magnitude of the proton MDM and the close proximity of the water protons to each other, each proton experiences the dipolar field of its neighbor – the so-called lattice field – in addition to the main magnetic field  $B_0$ . As the water molecule rotates and/or translates, the local magnetic field experienced by each proton then fluctuates at the rotational/translational frequency of the water molecule. Water molecules rotating and/or translating at a frequency that is at or near the Larmor frequency create effective coupling between the nuclei and the lattice. Under these circumstances, energy can be efficiently dissipated from the nuclei to the lattice which in turn allows excited nuclei to return to the lower (ground) energy state.

For example, bulk water has a relatively long spin-lattice ( $T_1$ ) relaxation time since the rotational frequency of the water molecules is much faster than the Larmor frequency; resulting in poor coupling between the molecules and the lattice and thus inefficient energy dissipation. On the other hand, water in biological tissues has  $T_1$  relaxation times on the order of hundreds of milliseconds. In this case, a fraction of the water molecules are bound to macromolecules and membranes in the tissue, reducing their rotational frequency in the bound state to that of the slower-moving macromolecules. Since water molecules are in fast exchange between the bulk phase and the bound state, the average rotational frequency of the tissue water molecules are reduced. As the

average rotational frequency of the water molecules approaches the Larmor frequency, the molecules will couple more effectively to the lattice; resulting in more efficient energy transfer from the excited protons to their surroundings and thus reduced  $T_1$  relaxation times. The rotational rate and, therefore, the  $T_1$  relaxation time of bound water depends on the size of the macromolecule involved as shown in Figure 1-11.

The theory of Bloembergen, Purcel, and Pound (3) provides a quantitative estimate of  $T_1$  and  $T_2$  relaxation times based on the correlation time ( $\tau_c$ ) of the molecule. The correlation time is defined as the time required for a molecule to rotate through  $1/2\pi$  of a cycle (i.e., 1 radian or  $57.3^\circ$ ) or the “average” time between molecular collisions. The  $R_1$  ( $1/T_1$ ) and  $R_2$  ( $1/T_2$ ) relaxation rates also depend on the Larmor resonant frequency ( $\omega_0$ ) of the nuclei as well as a number of other nuclear parameters as given by:

$$\frac{1}{T_1} = K \left[ \frac{\tau_c}{1 + \omega_0^2 \tau_c^2} + \frac{4\tau_c}{1 + 4\omega_0^2 \tau_c^2} \right] \quad (1.21)$$

$$\frac{1}{T_2} = \frac{K}{2} \left[ 3\tau_c + \frac{5\tau_c}{1 + \omega_0^2 \tau_c^2} + \frac{2\tau_c}{1 + 4\omega_0^2 \tau_c^2} \right], \quad (1.22)$$

where  $K = \frac{3\mu^2 \eta^2 \gamma^4}{160\pi^2 r^6}$ ,  $\mu$  = the MDM of the particular nucleus,  $\hbar = h/2\pi$  = Planck's constant divided by  $2\pi$ ,  $\gamma$  = the gyromagnetic ratio of the nuclear species, and  $r$  = the separation between the protons in the water molecule (i.e., the dipole-dipole separation).

Figure 1-11 shows the relationship between molecular correlation times and  $T_1$  and  $T_2$  relaxation times for various sized molecules. Note that as the molecular size increases (i.e., decreasing  $\tau_c$ ) the  $T_1$  relaxation time decreases and attains a minimum where the average rotational/translational frequency of the molecules ( $1/\tau_c$ ) matches the Larmor frequency. As the molecular size increases further, the  $T_1$  relaxation time also increases due to the increasing mismatch between the average molecular rotational/translational frequency and the Larmor frequency. In the case of the transverse relaxation time,  $T_2$  also decreases with increasing molecular size. However, the additional  $3\tau_c$  term in Eq. 1.22 (as compared to Eq. 1.21 for  $T_1$ ) causes the  $T_2$  relaxation time to continue to decrease (rather than increase as seen for  $T_1$ ) as the molecular size continues to increase.

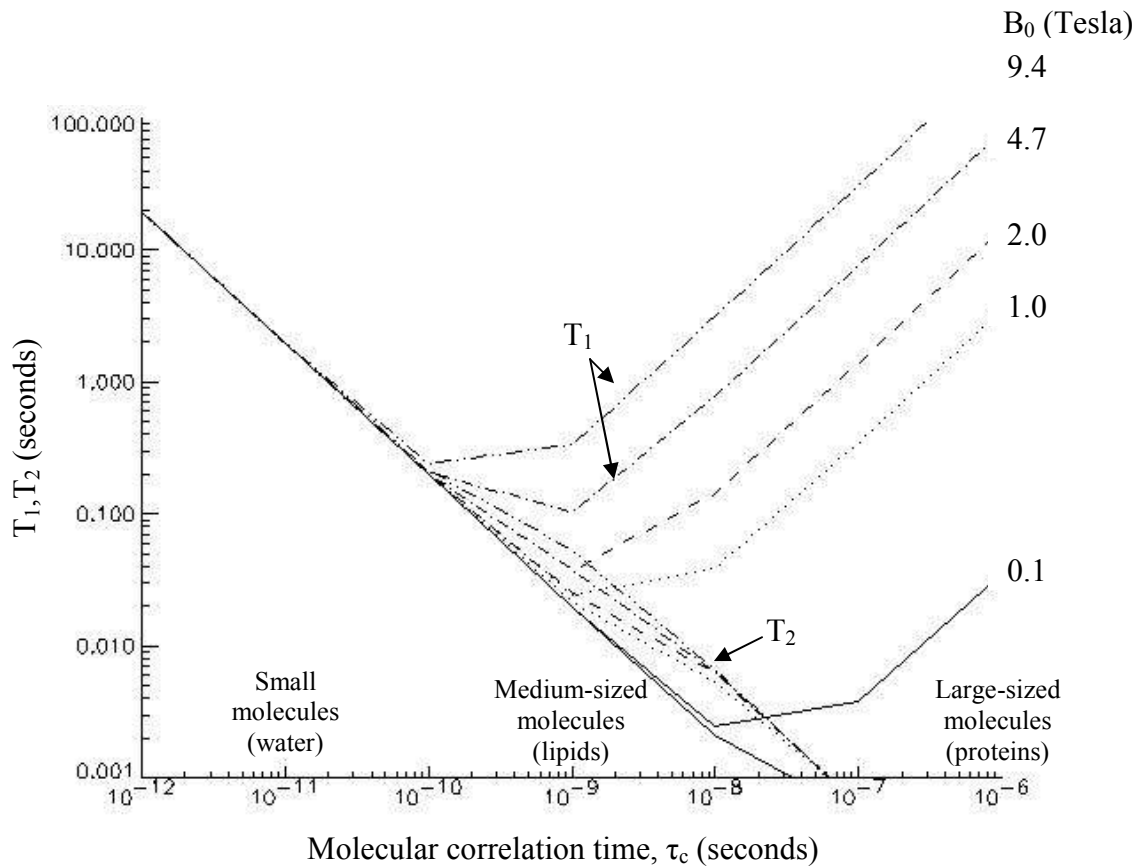


Figure 1-11: Plot of  $T_1$  and  $T_2$  relaxation times versus molecular correlation time ( $\tau_c$ ) (from Eqs. 1.21 and 1.22). Note that for bulk water the  $T_1$  and  $T_2$  relaxation times are nearly identical (this is the so-called ‘extreme narrowing’ regime) while for larger molecules, such as lipids and proteins,  $T_1$  and  $T_2$  differ significantly. The dependency of  $T_1$  on the main magnetic field strength,  $B_0$ , is clearly demonstrated for medium-sized and large molecules. The minimum in the  $T_1$  curves is the point at which the rotational frequency of the molecules (i.e.,  $1/\tau_c$ ) equals the Larmor frequency.

The transverse or spin-spin relaxation time,  $T_2$ , characterizes the rate of decay of the  $M_{xy}$  magnetization that is created following the rotation of  $M_z$  magnetization into the transverse plane following the application of an RF pulse. In the case of an FID, the time constant associated with the decay of the transverse magnetization is denoted by  $T_2^*$ , which contains contributions from a variety of sources. The  $R_2^*$  relaxation rate (i.e.,  $1/T_2^*$ ) is given by:

$$\frac{1}{T_2^*} = \frac{1}{T_{2(\text{INTRINSIC})}} + \frac{1}{T_{2(\text{INHOMOGENEOUS})}} + \frac{1}{T_{2(\text{SUSCEPTIBILITY})}} + \frac{1}{T_{2(\text{DIFFUSION})}} \quad (1.23)$$

In addition to the intrinsic fields that contribute to  $T_2$ , inhomogeneities in the main magnetic field  $B_0$ , local magnetic field inhomogeneities arising from differences in magnetic susceptibility (e.g., at air-tissue interfaces), and molecular diffusion in the presence of magnetic field inhomogeneities all result in loss of phase coherence among the individual nuclear MDMs as they precess in the transverse plane. Ideally, it would be desirable to have  $T_2^*$  dominated by intrinsic field effects (i.e., only the first term on the right-hand side of Eq. 1.23). Although the other terms in Eq. 1.23 can often contribute significantly to the decay of the transverse magnetization, there are compensatory measures that can be taken to mitigate their effects (discussed in the next section). The effect of  $T_2^*$  on the FID signal is shown in Figure 1-12.

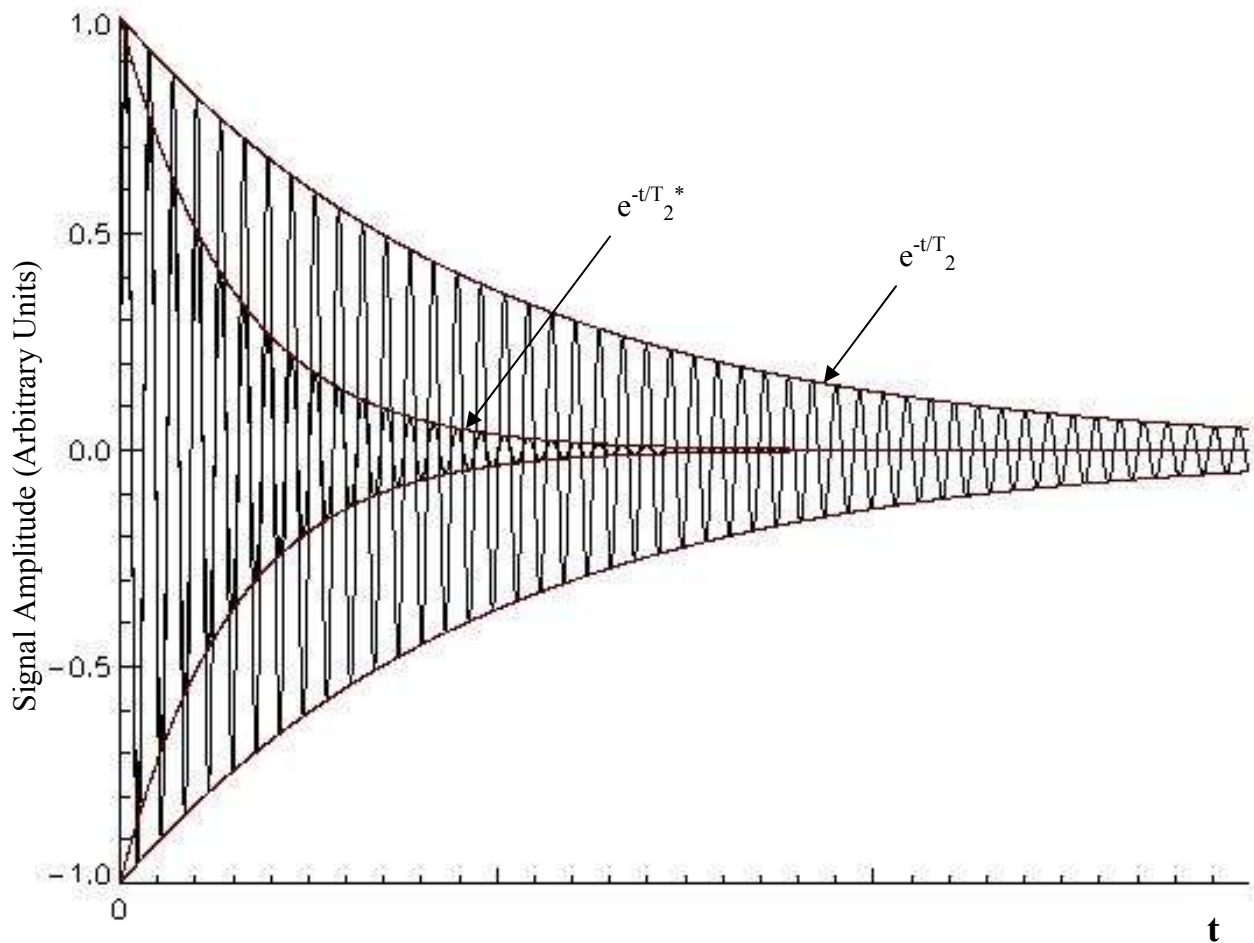


Figure 1-12: Two FID envelopes, one with a decay envelope dominated by  $T_2$  effects (spin-spin interactions) only, the other dominated by  $T_2^*$  effects (spin-spin interactions, magnetic field inhomogeneities, susceptibility, and diffusion).

### 1.5.2 The Spin-Echo RF Pulse Sequence

There are no experimental methods for removing the intrinsic-field effects from the decay of the transverse magnetization. However, magnetic field inhomogeneities can be corrected using the spin-echo RF pulse sequence. Magnetic field inhomogeneities arise from imperfections in the main  $B_0$  field as well as local (within the sample) magnetic field inhomogeneities that are due to differences in magnetic susceptibility at the interface of two dissimilar materials (e.g., at air/tissue interfaces).

To understand how the spin-echo RF pulse sequence works, consider a race-track analogy with four runners of varying abilities (Runner #4 > #3 > #2 > #1). Before the start of the race, the runners position themselves at the appropriate starting positions and can be considered to be 'in phase' with each other. At the sound of the starter's gun the runners are off. After 15 seconds, the runners are given a signal to turn around and head back to the starting line, running at the same speed as they were during the first 15-second interval. After another 15 seconds, the runners return to exactly the same starting positions (i.e., they return to their 'in phase' positions). This mock race is depicted in Figure 1-13:

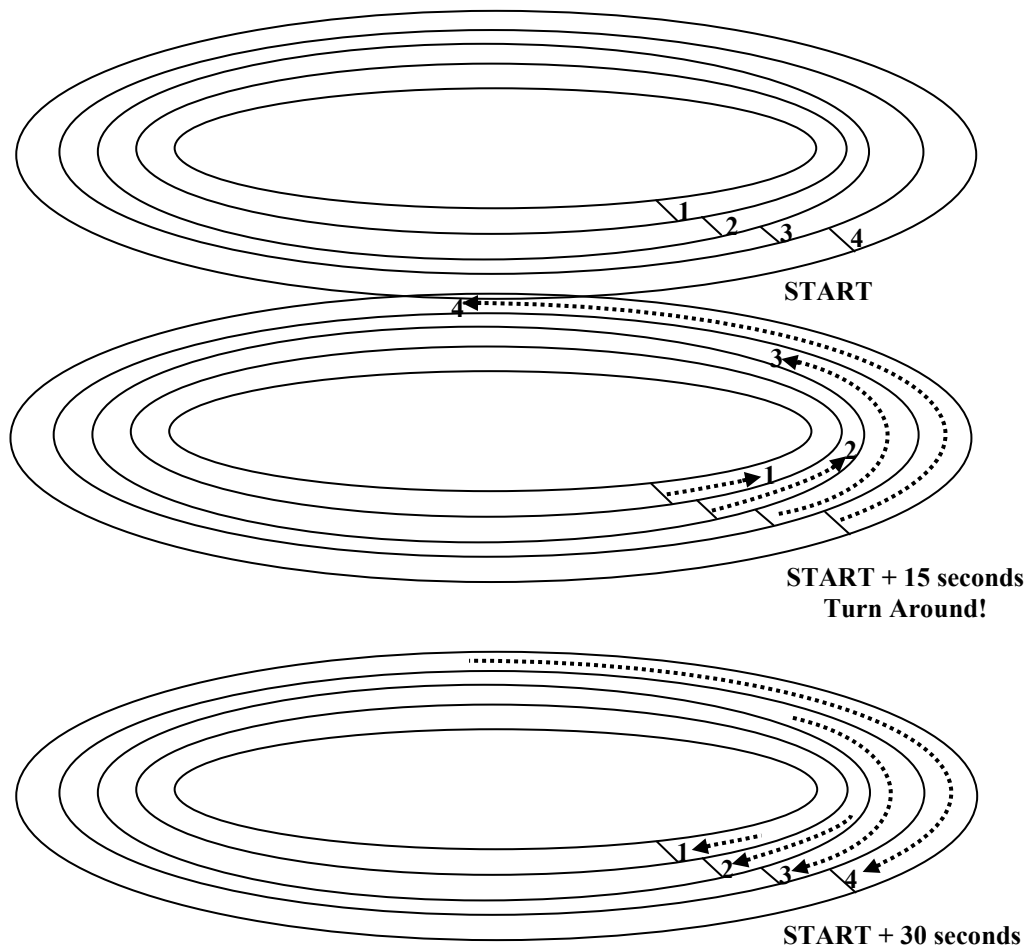


Figure 1-13: Mock foot race of four runners of varying abilities (Runner #4>#3>#2> #1). The runners are “in phase” with each other at the start of the race. Fifteen seconds into the race, the runners are given a signal to turn around and head back to the starting line. Fifteen seconds later, the runners are back “in phase” with each other at their original starting positions.

The mock foot race depicted in Figure 1-13 can be extended to the transverse magnetization vector created after a  $90^\circ$  pulse is applied to  $M_0$  (i.e.,  $M_z$  is moved completely into the transverse plane leaving only  $M_{xy}$ ) in the rotating frame of reference. Following the  $90^\circ$  pulse, the in-phase  $M_{xy}$  magnetization vector begins to precess in the transverse plane. As individual nuclear MDMs within the spin ensemble experience small magnetic field differences, some precess faster than others resulting in a loss of phase coherence due to  $T_2^*$  effects. After a time  $(TE/2)$ , the analogous foot race ‘turn around!’ signal is given to the dephasing nuclear MDMs in the form of a  $180^\circ$  RF pulse. The



RF pulse rotates each nuclear MDM  $180^\circ$  about the  $x'$  axis, effectively reversing the relative positions of the nuclear MDMs. After another  $TE/2$  time period, all of the nuclear MDMs come back into phase producing a 'spin-echo' signal. The spin-echo signal looks similar to two FIDs back to back. At this point, the transverse magnetization vector is only attenuated by the intrinsic  $T_2$  relaxation effects. The process of spin-echo formation is shown graphically in Figure 1-14 using vectors in the rotating frame of reference:

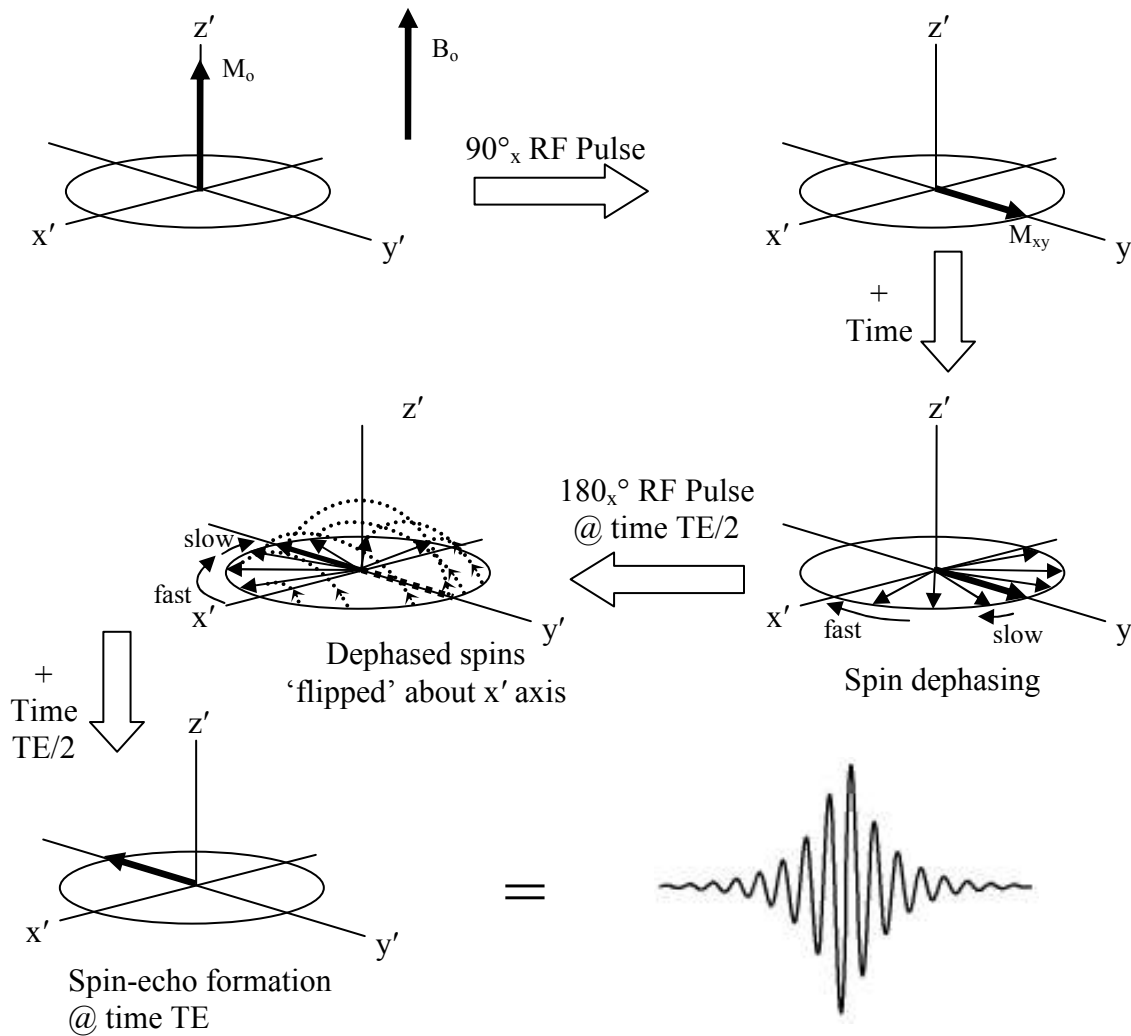


Figure 1-14: Formation of the spin-echo by a sequence of  $90^\circ$  -  $180^\circ$  RF pulses. This experiment was first performed by Hahn and colleagues in 1950 (4).

## 1.6 Measurement of Relaxation Times

Measurement of  $T_1$  and  $T_2$  relaxation times can be accomplished using several methods. Inversion recovery and the Carr-Purcell-Meiboom-Gill pulse sequence for  $T_1$  and  $T_2$  measurements, respectively, are very robust and commonly used methods for relaxation measurements.

### 1.6.1 $T_1$ Relaxation Measurement Techniques

Measurement of the  $T_1$  relaxation time requires that a series of data is acquired at various time intervals and then fitted to a model equation to estimate the  $T_1$  relaxation time constant. The model fitting equation can be derived by solving the Bloch equation for the longitudinal ( $M_z$ ) component of magnetization under a particular set of experimental conditions. For example, recall that the Bloch equation describing the  $T_1$  relaxation time (Eq. 1.19) is as follows:

$$\frac{dM_z}{dt} = -\left(\frac{M_z - M_0}{T_1}\right) - \gamma \vec{B}_1 M_y.$$

Solving this equation for the case where the  $M_z$  magnetization recovers from zero (i.e., immediately following a  $90^\circ$  RF pulse) for a system that was initially at the Boltzmann equilibrium yields the following expression:

$$M_z(t) = M_0 \left(1 - e^{-\frac{t}{T_1}}\right), \quad (1.24)$$

where  $M_z(t)$  is the magnitude of the longitudinal magnetization at some time,  $t$ , following the application of the  $90^\circ$  RF pulse,  $M_0$  is the Boltzmann equilibrium magnetization, and  $T_1$  is the longitudinal relaxation time constant. The recovery of the longitudinal magnetization is a first-order rate process and thus is well-modeled by an exponential function. Consequently, one way to think of  $T_1$  is that it is the time required for the longitudinal magnetization to recover 63% of its original equilibrium value after perturbation by an RF pulse. A plot of the longitudinal magnetization as a function of time under these experimental conditions is shown in Figure 1-15.

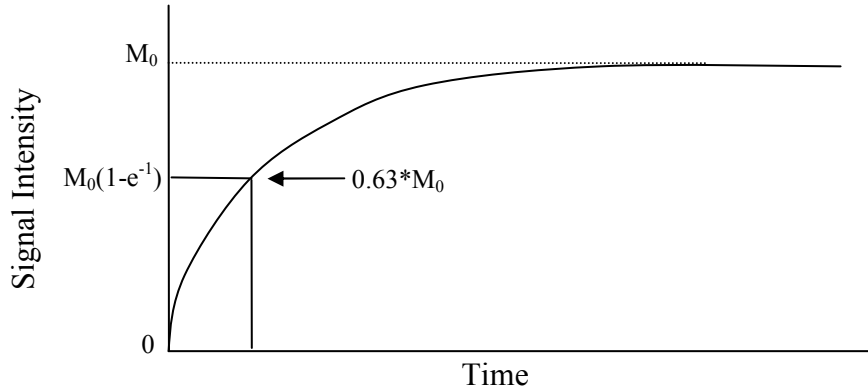


Figure 1-15: Recovery of longitudinal magnetization after the rotation of  $M_0$  into the  $xy$  plane by a  $90^\circ$  RF pulse as modeled by Eq. 1.24. The  $T_1$  ‘time’ is the time at which longitudinal magnetization recovers to 63% of its original value.

Alternatively, if Eq. 1.19 is solved for the case where the  $M_z$  magnetization recovers from  $-M_0$  (i.e., immediately following a  $180^\circ$  inversion RF pulse) for a system that was initially at the Boltzmann equilibrium, then the model equation is slightly different from that in Eq. 1.24. In this case, an additional factor of 2 precedes the exponential term as shown in the following expression:

$$M_z(t) = M_0(1 - 2e^{-\frac{t}{T_1}}). \quad (1.25)$$

A plot of the longitudinal magnetization as a function of time under these experimental conditions is shown in Figure 1-16.

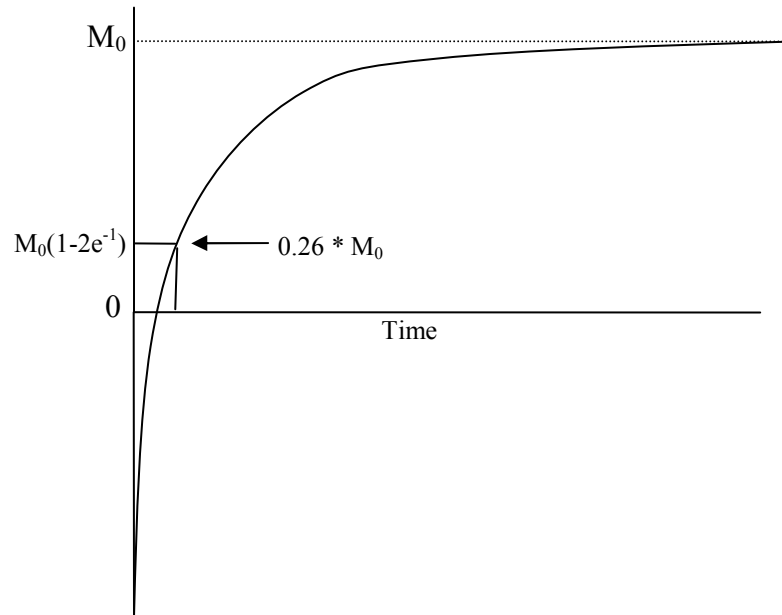


Figure 1-16: Recovery of longitudinal magnetization after rotation by a  $180^\circ$  RF pulse onto the  $-z$  axis as modeled by Eq. 1.25. In this case, the  $180^\circ$  RF pulse ‘inverts’ the magnetization; hence the term ‘inversion recovery’.

### 1.6.2 $T_2$ Relaxation Measurement by Carr-Purcell-Meiboom-Gill Pulse Sequence

Application of successive  $180^\circ$  RF pulses following a  $90^\circ$ - $180^\circ$  pulse sequence will result in a train of spin-echoes whose amplitudes decay exponentially after each  $180^\circ$  RF pulse. The decay rate of each individual echo is governed by  $T_2^*$  effects while the decrease in amplitude of each successive echo is governed by intrinsic  $T_2$  effects. The echo train depicted in Figure 1-17 was first demonstrated by Carr and Purcell in 1954 (5).

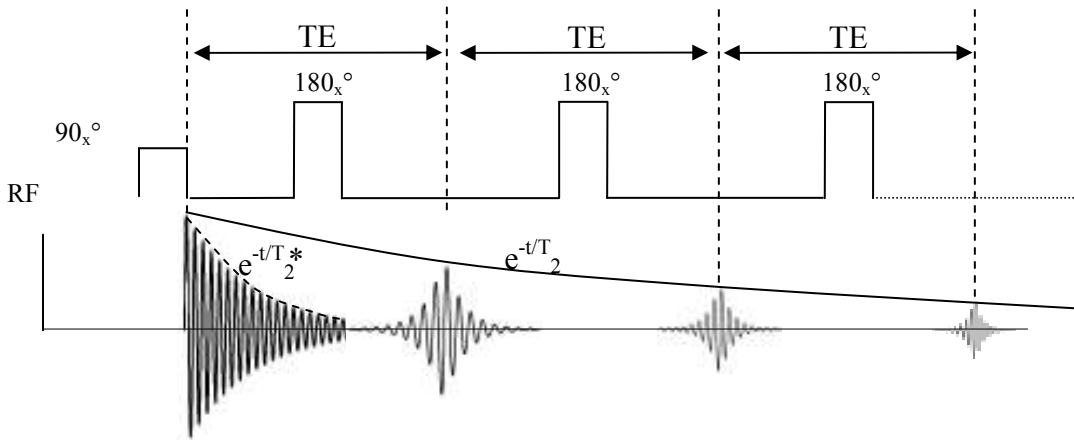


Figure 1-17: After an initial  $90^\circ$  and  $180^\circ$  RF pulse one spin-echo is formed at time TE after the  $90^\circ$  pulse. Continued application of successive  $180^\circ$  pulses, at time intervals equal to TE after the initial  $180^\circ$  pulse, results in a train of spin-echoes each of which reforms and decays according to the  $T_2^*$  of the sample. The decrease in amplitude in each successive spin-echo is attributable to the intrinsic  $T_2$  relaxation and, in some cases, to  $T_2$  relaxation combined with molecular diffusion effects.

The echo train length in a Carr-Purcell echo train is determined by the  $T_2$  of the sample and the magnitude of the signal is given by:

$$S(t) = e^{\left(\frac{-2\tau}{T_2}\right)} e^{\left(\frac{-2\gamma^2 G(t) D \tau^3}{3}\right)} \quad (1.26)$$

where  $G(t)$  is any magnetic field gradient that affects the nuclear magnetic moments in the sample,  $D$  is the self-diffusion coefficient of the sample, and  $\tau = TE/2$  (as shown in Figure 1-17). To reduce the effects of diffusion (more on this topic in Section 2.7), the time  $\tau$  should be minimized (on the order of 500-1000  $\mu\text{sec}$ ) to ensure the decaying signal amplitude of each echo in a Carr-Purcell echo train is due mostly to the intrinsic  $T_2$  relaxation time.

One disadvantage of the Carr-Purcell sequence is that imperfections in the applied  $180^\circ$  RF pulses can give erroneous estimates for the  $T_2$  relaxation time. This issue was addressed by Carr and Purcell in 1958, however, a more elegant solution was proposed by Meiboom and Gill in the same year (6). By changing the phase of the  $180^\circ$  RF pulse so that the  $B_1$  field is oriented along the y-axis

(rather than the x-axis as shown in Figure 1-17), flip-angle errors associated with imperfections in the  $180^\circ$  RF pulses are compensated for by the even-order echoes. Consequently, the Carr-Purcell Meiboom-Gill (CPMG) pulse sequence is the preferred method for accurately measuring the intrinsic  $T_2$  relaxation times.

## 2.0 Magnetic Resonance Imaging

### 2.1 Spatial Localization of a MR Signal

To obtain an MR image from biological samples requires encoding of the spatial information into the MR signal. Within the plane of the image, spatial encoding in two dimensions is required. The two most common methods of spatially encoding the MR signal are the so-called frequency-encoding and phase-encoding schemes. Frequency- and phase-encoding in MRI requires the application of linear magnetic field gradients across a particular region of interest (or field of view) within the sample. The linear magnetic field gradients allow the spatial location of nuclei in the sample to be uniquely encoded into the frequency and phase of the measured MRI signal.

#### 2.1.1 Magnetic Field Gradients for MRI

The magnetic field gradients used for MR imaging are created by unique sets of copper coils mounted on a former within the bore of a (typically) superconducting MRI magnet. MR images can be generated in any plane of a 3-D sample by separately controlling currents in each of the X,Y, or Z gradient coils. The typical geometries of the gradient coils are shown in Figure 1-18:

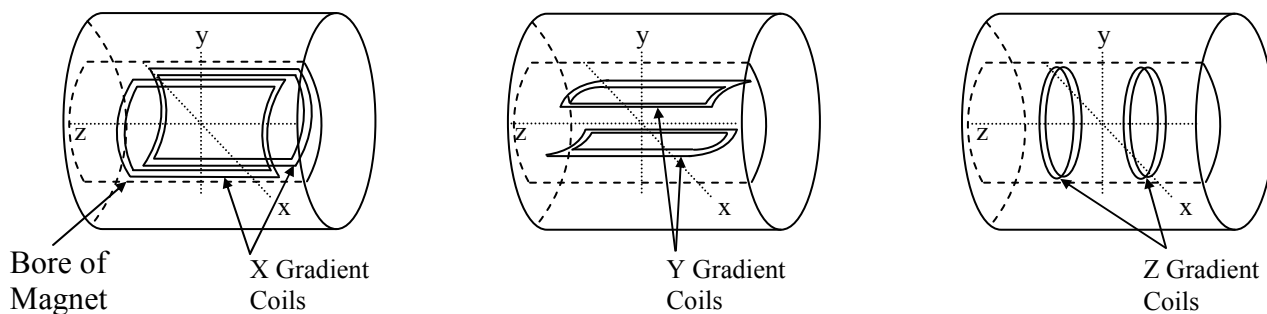


Figure 1-18: Typical geometries and orientations of copper conducting bands (or ‘coils’) that, when energized, produce linear magnetic field gradients in the X,Y, and Z directions, respectively. Depending on the imaging sequence used, electric current in the gradient coils can be (for very short periods of time) as high as 30 Amperes (and higher for echo-planar imaging applications) in order to create linear gradients with strengths of approximately 10-30 mT/m.

The magnetic field gradient produced by each of the gradient coils shown in Figure 1-18 is superimposed on the main  $B_0$  field to create a magnetic field that varies linearly in strength as a function of distance from the center of the magnet. Consequently, in the presence of a magnetic field gradient, the nuclei placed within the bore of the magnet will have precessional frequencies that vary linearly with respect to their position within the magnet. A ‘steeper’ gradient will allow for a greater difference in precessional frequencies for nuclei that are closely spaced; allowing for higher spatial resolution in MR images. In addition to encoding spatial information in the phase and frequency of the MR signal, RF pulses – applied in concert with magnetic field gradients – can be used to selectively excite nuclei within a particular region of the sample. This approach essentially provides the 3<sup>rd</sup> dimension of spatial localization for the MR image (with frequency and phase encoding providing spatial localization in the 2-dimensional plane of the image). “Slice selection” is achieved by applying amplitude-modulated RF pulses in conjunction with a linear magnetic field gradient. The ‘bandwidth’ (BW) of the RF pulse together with the slope of the gradient determines the thickness of the desired MR image ‘slice’. The co-dependency of MR image slice thickness, gradient slope, and RF BW is shown in Figure 1-19.

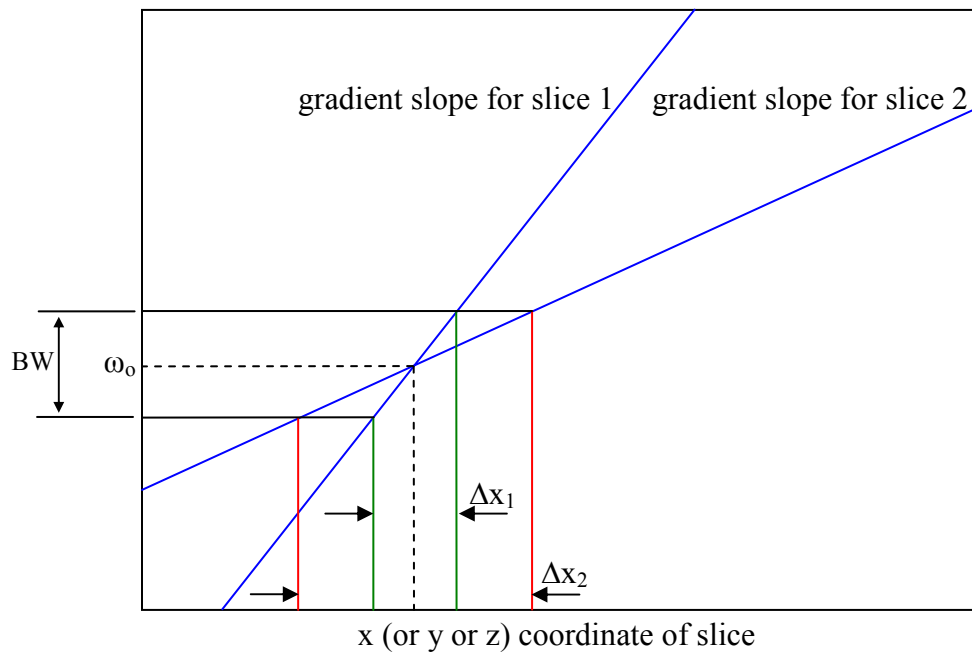


Figure 1-19: The MR slice thickness can be adjusted by varying the slope (i.e., strength) of the magnetic field gradient (blue lines) for a given RF excitation bandwidth (BW). Adjustment of  $\omega_0$ , the resonant (Larmor) frequency, controls the position of the slice. The slice thicknesses that arise from the two different gradient strengths are given by  $\Delta x_1$  and  $\Delta x_2$ , respectively. Note that slice thickness is also dependent on RF pulse bandwidth (BW).

As can be seen in Figure 1-19, the slice profiles defined by  $\Delta x_1$  and  $\Delta x_2$  are rectangular in shape. To excite a rectangular bandwidth in the “frequency domain” requires that the RF pulse be amplitude modulated based on the Fourier equivalent in the “time domain” (where the RF pulse is generated). In this case, the Fourier transformation can be used to determine the specific functional form of the RF amplitude modulation needed to excite the desired bandwidth of frequencies.

### 2.1.2 The Fourier Transform

The Fourier transform (FT), named after the French mathematician Jean Baptiste Joseph Fourier (1768-1830), is a mathematical operation that transforms a time-domain signal into its equivalent frequency-domain representation. Consider a signal in the time domain oscillating at only one frequency; the FT of this signal has a peak at that particular frequency. If a time-domain signal oscillates at two or more frequencies, the FT of the signal will have peaks at the unique frequencies in the signal. The amplitude of the FT peaks provides information about the strength of the time-domain signal at that particular frequency. Figure 1-20 and 1-21 show examples of the FT of two basic time-domain signals (sinusoids).



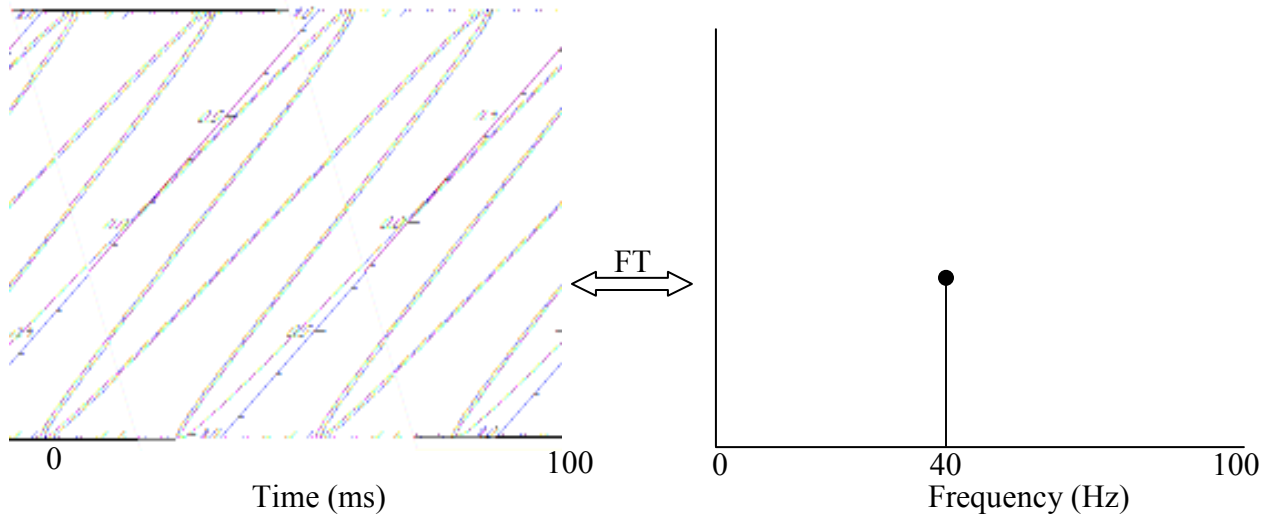


Figure 1-20: Oscillating time domain signal with a period of 25 ms and its corresponding Fourier transform (FT).

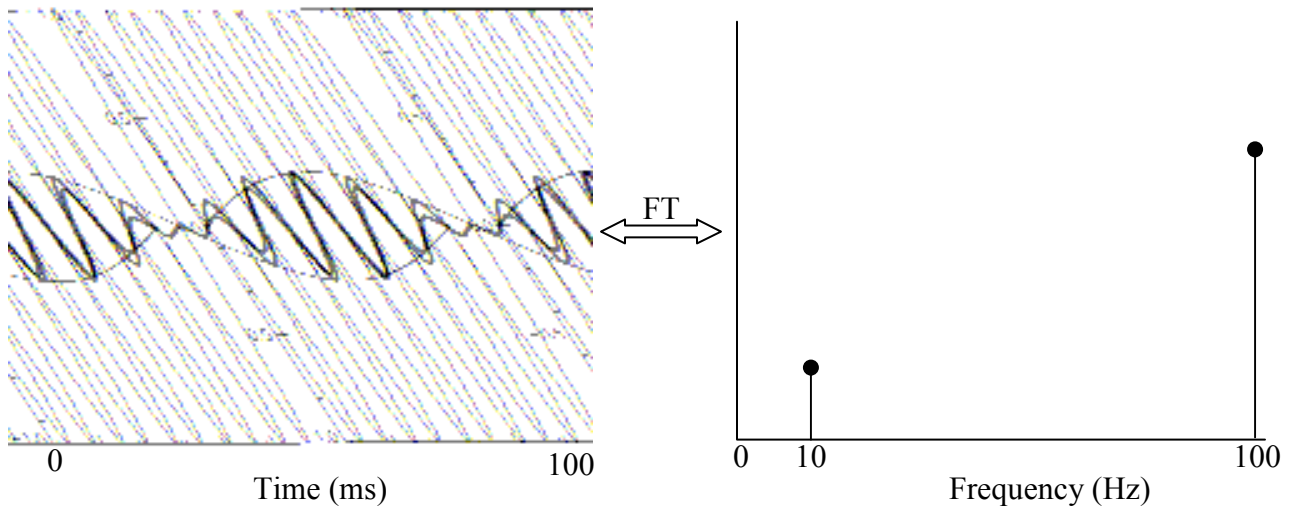


Figure 1-21: Combination (multiplication) of two oscillating time-domain signals with periods of 10 ms and 100 ms. The signal with the dark line is the combined signal for which the FT is shown in the adjacent figure. Note the difference in amplitude in the two peaks of the FT and the difference in amplitude of the two time-domain signals (the amplitudes of the FT representation are not exact but are qualitative for display purposes).

The FT is used in a wide array of signal processing applications, but, for the purposes of this thesis (and for basic MR theory), it is sufficient to look at a limited number of FT properties. The interested reader is referred to Oppenheimer and Schaffer (7) for a more detailed description of the FT (DFT, FFT) and its properties and applications to digital signal processing.

### 2.1.3 Basic Properties of the Fourier Transform

Consider the function  $f(t)$  and its FT  $F(k)$ . The two functions  $f(t)$  and  $F(k)$  are referred to as FT pairs. The term ‘pair’ is appropriate because the function  $f(t)$  can be retrieved from the function  $F(k)$  by using the *inverse* FT (IFT). In other words, the IFT undoes the operation of the FT as follows:

$$IFT(FT(f(t))) = f(t) \quad (1.27)$$

A FT pair that is very important for the understanding of MR image formation is the FT pair that relates a rectangular (RECT) function in the time domain to its frequency-domain equivalent, the  $\sin x/x$  (SINC) function as shown in Figure 1-22:

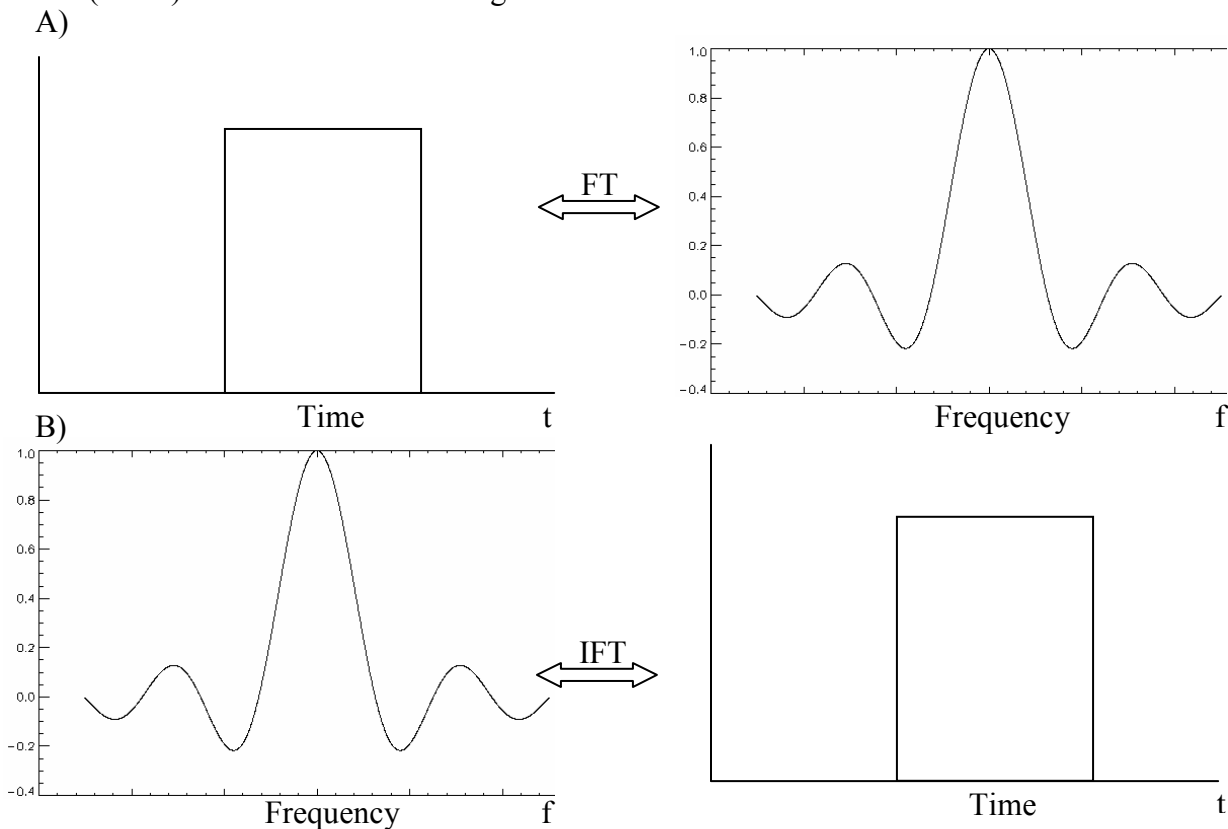


Figure 1-22: A generalized view of the relationship between a rectangular function in the time-domain and its frequency-domain counterpart. The time waveform in A) and B) is commonly referred to as a RECT function and the frequency-domain waveform is referred to as a SINC function. Note that the relationships shown above hold if the RECT function is in the frequency domain and if the SINC function is in the time domain. A time-domain SINC function is used in MR for rectangular frequency-domain excitation.

Based on the FT properties discussed above, to excite a rectangular region of frequency space requires that a SINC-shaped RF pulse be applied in the time domain together with a linear magnetic

field gradient of the appropriate strength. MR hardware can approximate the SINC function in the time domain by using a series of short ‘hard’ or rectangular pulses as shown in Figure 1-23:

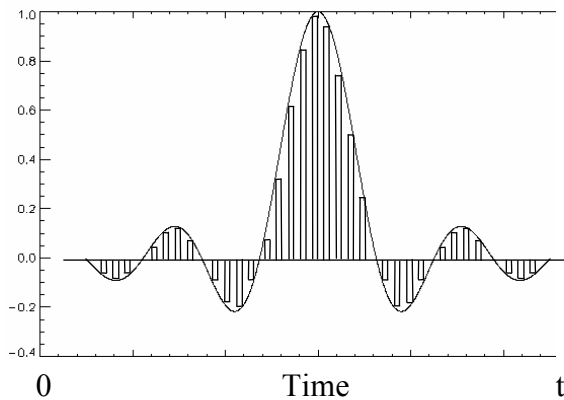
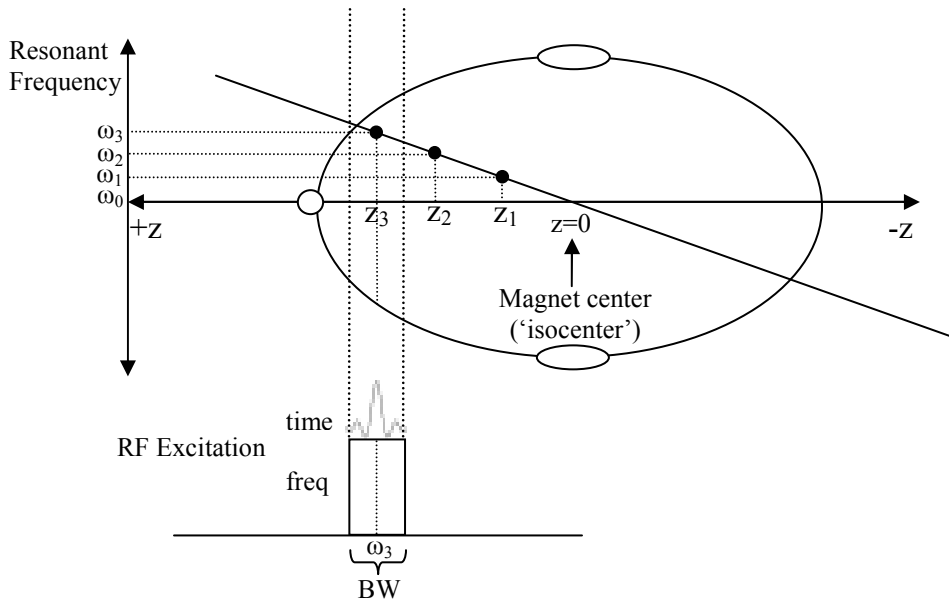


Figure 1-23: Narrow rectangular pulses of varying amplitude and polarity can be combined to approximate a SINC function in the time-domain. A perfect rectangular pulse in the frequency-domain is not possible because a SINC pulse in the time domain must be truncated to a finite length.

#### 2.1.4 Slice Select Gradients and the RF Excitation Pulse

The function of slice-select gradients is to change the Larmor frequency of spins across the sample in a position dependent manner as shown in Figure 1-24. Slice-select gradients change the Larmor frequency of spins across the sample to allow a RF excitation pulse to transfer energy to one particular slice. The slice-select gradient and RF excitation pulse are typically applied simultaneously during slice selection.

A) Selection of one slice of a particular thickness in a hypothetical human head.



B) Typical pulse sequence diagram for slice selection and excitation.

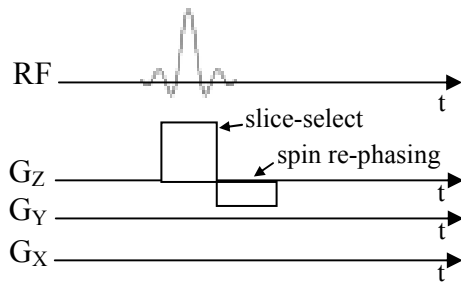


Figure 1-24: A) Schematic of slice-select gradient and RF excitation pulse in hypothetical human head. When the RF excitation pulse is generated with a center frequency at  $\omega_3 \pm BW/2$ , the spins within a slice at a particular location along the z-axis are excited. B) A pulse-sequence diagram indicating the timing of the RF pulse and the slice-select gradient. The need for a 're-phasing' gradient is discussed in Section 2.1.4.1.

### 2.1.4.1 Slice Dephasing

Ideally, after application of a  $90^\circ$  RF excitation pulse, all nuclear MDMs are precessing at the same frequency in the transverse plane and are in phase with each other. In the case of a slice selection pulse, however, this is not true. As the  $90^\circ$  RF excitation pulse begins to rotate magnetization into the transverse plane, the nuclei experience a large magnetic field inhomogeneity from the slice selection gradient since it is being applied at the same time. The result is that the nuclear MDMs quickly dephase; significantly reducing the amount of transverse magnetization available for subsequent spatial encoding and signal detection. Fortunately, the dephasing effect of the slice-selection gradient can be reversed by applying an additional magnetic field gradient pulse immediately following the  $90^\circ$  RF excitation pulse. In order to rephase all of the nuclei within the

slice, the 're-phasing' gradient must be of opposite polarity and have an area equal to half of that of the slice-selection gradient. Figure 1-25 demonstrates the idea of slice dephasing.

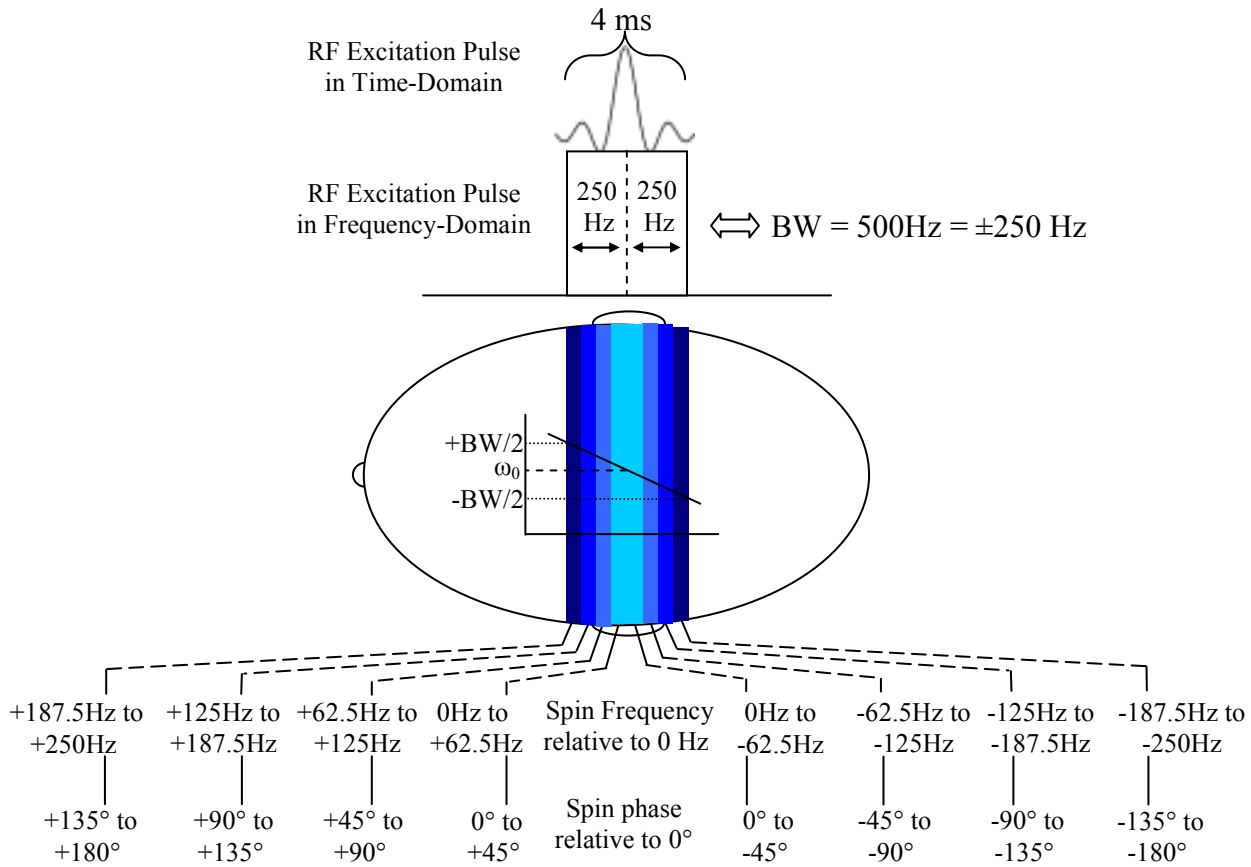


Figure 1-25: De-phasing within a slice (within a hypothetical human head) during application of a 90° slice-selective RF excitation pulse. The dephasing of all nuclear MDMs within the slice can be rephased after the RF excitation by application of a re-phasing gradient (Figure 1-26).

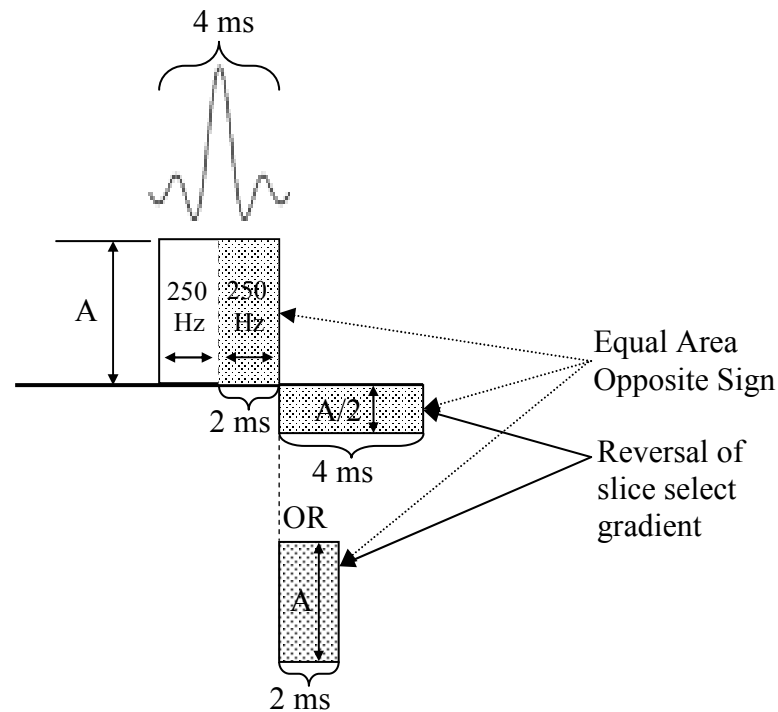


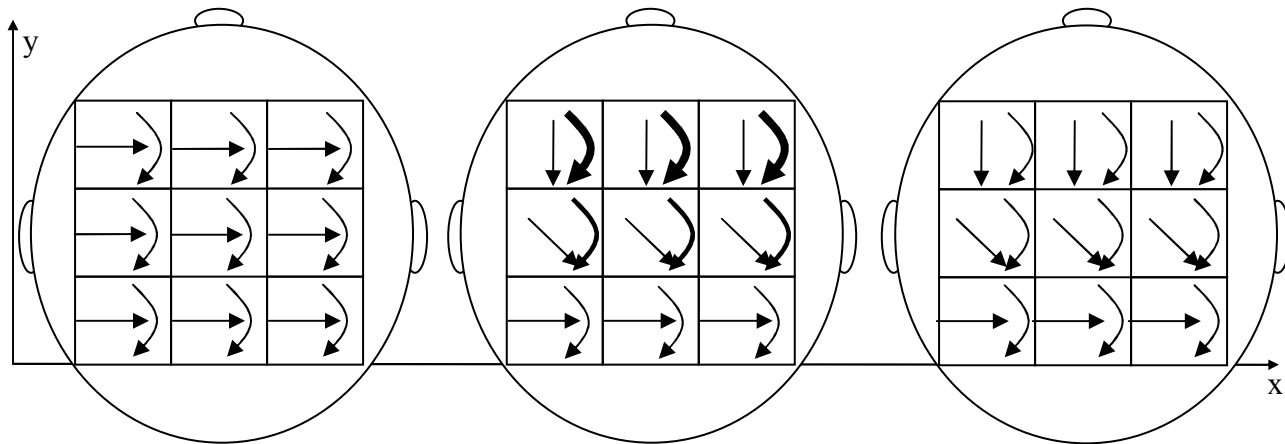
Figure 1-26: Slice-selection re-phasing gradient used to restore the phase coherence of the transverse magnetization following de-phasing due to the slice-selective RF pulse. For complete restoration of phase coherence, the re-phasing gradient must have an amplitude-duration product (area under curve) equal to half that of the slice-selective RF excitation pulse. Note that the re-phasing gradient can have any shape (not necessarily rectangular) as long as the amplitude-duration product is equal to the amplitude-duration product of half of the slice-selective RF pulse.

## 2.2 Spatial Encoding of the MR Signal

The MR signal received by the RF coil includes the vector sum of all signals from all voxels within a particular FOV. The problem arises then as to how to make the signal from each voxel spatially distinct in order to create a two-dimensional image. Considering that all time-domain signals have associated amplitude, frequency, and phase, a means of encoding spatial information into some of these parameters is needed for MRI. Since the amplitude of the signal is used to create signal-intensity contrast between different regions of the image, only the frequency and phase of the MR signal are available for spatial encoding.

### 2.2.1 Phase-Encoding

After slice-selective excitation and re-phasing of nuclei within a particular slice, the phase and frequency of the transverse magnetization can then be used to encode the 2-dimensional spatial information in the plane of the slice. If a magnetic field gradient is applied for a short period of time in a different direction (relative to that of the slice-selection gradient), the nuclei will begin to precess at different rates depending on their position along that gradient direction. When the gradient is turned off, the nuclei will return to their original precession frequency. However, the relative phase between the precessing nuclei will be different, depending upon their relative position along the phase-encoding-gradient direction. Consider a hypothetical slice through a human head immediately following slice selection perpendicular to the z-gradient direction. The plane of the slice is divided into rows and columns which represent individual volume elements (or voxels) within the plane of the image. At Time 1 in Figure 1-27, all spins are in-phase and are precessing (or are about to precess) at the same frequency. At Time 2, a phase-encoding gradient is applied along the y-axis for a finite period of time, producing a phase shift among the nuclei in various voxels, the magnitude of which depends upon their relative position along the phase-encoding gradient direction. At Time 3, immediately after the phase-encoding gradient has been turned off, the spins resume the same precessional frequency they had at Time 1, however, the phase imparted to the nuclei by the phase-encoding gradient is retained and measured during the detection period.



Time Point 1: immediately after slice-selective RF excitation and re-phasing; all nuclei in each voxel precess at the same rate.

Time Point 2: phase-encoding gradient ( $y$ ) applied for finite time period; nuclei in each voxel have different precession rates based on relative position along gradient axis.

Time Point 3: phase-encoding gradient off; nuclei in each voxel return to original precession rates but retain relative phase differences accumulated during the phase-encoding period.

Figure 1-27: Phase-encoding of nuclei in a sample based on position along a gradient in the  $y$ -direction. A phase-encoding gradient is applied for a finite time period, causing the nuclei to acquire a phase-shift that is unique to their particular position along the magnetic field gradient direction (Time Point 2). At Time Point 3, the phase-encoding gradient is turned off, however, the nuclei retain their respective phase shifts acquired during the second time period.

### 2.2.2 Frequency-Encoding

Just as the  $y$ -gradient was used for phase-encoding in the previous section, the  $x$ -gradient can be used to spatially encode the remaining dimension of information. The concept of frequency-encoding is similar to phase-encoding and can be demonstrated again using Figure 1-27. Observation of Time Point 2 in Figure 1-27 reveals a difference in spin frequency between rows as a result of the brief  $y$ -gradient. To make each *voxel* unique in phase and frequency it is clear that a gradient along the  $x$ -axis (Figure 1-27) will also change the frequency of precession within each voxel as a function of position along the  $x$ -gradient axis. For generation of an MR image, the frequency-encoding gradient must be 1) applied in a direction perpendicular to the phase-encoding gradient and 2) applied in concert with the acquisition (digitization) of the MR signal (the frequency-encode gradient is therefore sometimes referred to as the *read or readout* gradient). To generate a MR image, phase- and frequency-encoding can be used together with slice-selective RF pulses in a carefully timed manner. The timing of the slice-selective RF pulses and the phase and frequency-



encoding gradients can be diagrammed using a so-called *pulse sequence*. The spin-echo pulse sequence is described in the next section.

## 2.3 Spin-Echo MRI

The MR spin-echo method is one of the most commonly-used methods for generating MR images. The RF and gradient pulses needed to create the spin-echo are played out at specific time intervals diagrammed by a pulse sequence. The MR signals generated and acquired during the execution of the pulse sequence are stored in a 2-dimensional matrix commonly referred to as the *k-space* (or time-domain) representation of the raw data.

### 2.3.1 Spin-Echo MRI Pulse Sequence

The spin-echo pulse sequence shown in Figure 1-28 represents the timing diagram necessary to generate a MR signal that will be stored in one 'row' in 'k-space,' which is the time-domain representation of the image data. Most of the components of Figure 1-28 are those discussed in previous sections. The portions of Figure 1-28 that have not been mentioned are 1) the gradient representation along the ' $G_Y$ ' axis and 2) the positive gradient pulse applied along the x direction before the  $180^\circ$  refocusing pulse. The amplitude of the phase-encoding gradient pulse shown along the ' $G_Y$ ' axis changes each time the pulse sequence is repeated (typically 128 or 256 times for an image with  $128 \times 128$  or  $256 \times 256$  matrix size, respectively). The positive  $G_X$  gradient pulse in Figure 1-28A serves the same function as the re-phasing portion of the slice-selection gradient. In this case, however, the re-phasing gradient compensates for de-phasing that will occur during the subsequent acquisition of the signal during the frequency-encoding (i.e., readout) period; when the frequency-encoding gradient is being applied. The polarity of the de-phasing gradient is the same as that of the frequency-encoding gradient when the de-phasing gradient precedes the  $180^\circ$  refocusing pulse (since the  $180^\circ$  pulse effectively reverses the precessional direction of the de-phasing gradient), as shown in Figure 1-28A. If the de-phasing gradient pulse immediately precedes the frequency-encoding period (as shown in Figure 1-28B), then its polarity is opposite that of the gradient applied during the frequency-encoding period. When the area under the de-phasing gradient pulse is half that of the frequency-encoding-gradient pulse, the nuclei will come back into phase (i.e., refocus) resulting in a gradient-echo (which is also the same point at which the RF spin-echo is formed). The MR signal receiver is turned on at the beginning of the readout-gradient period in order to acquire the entire

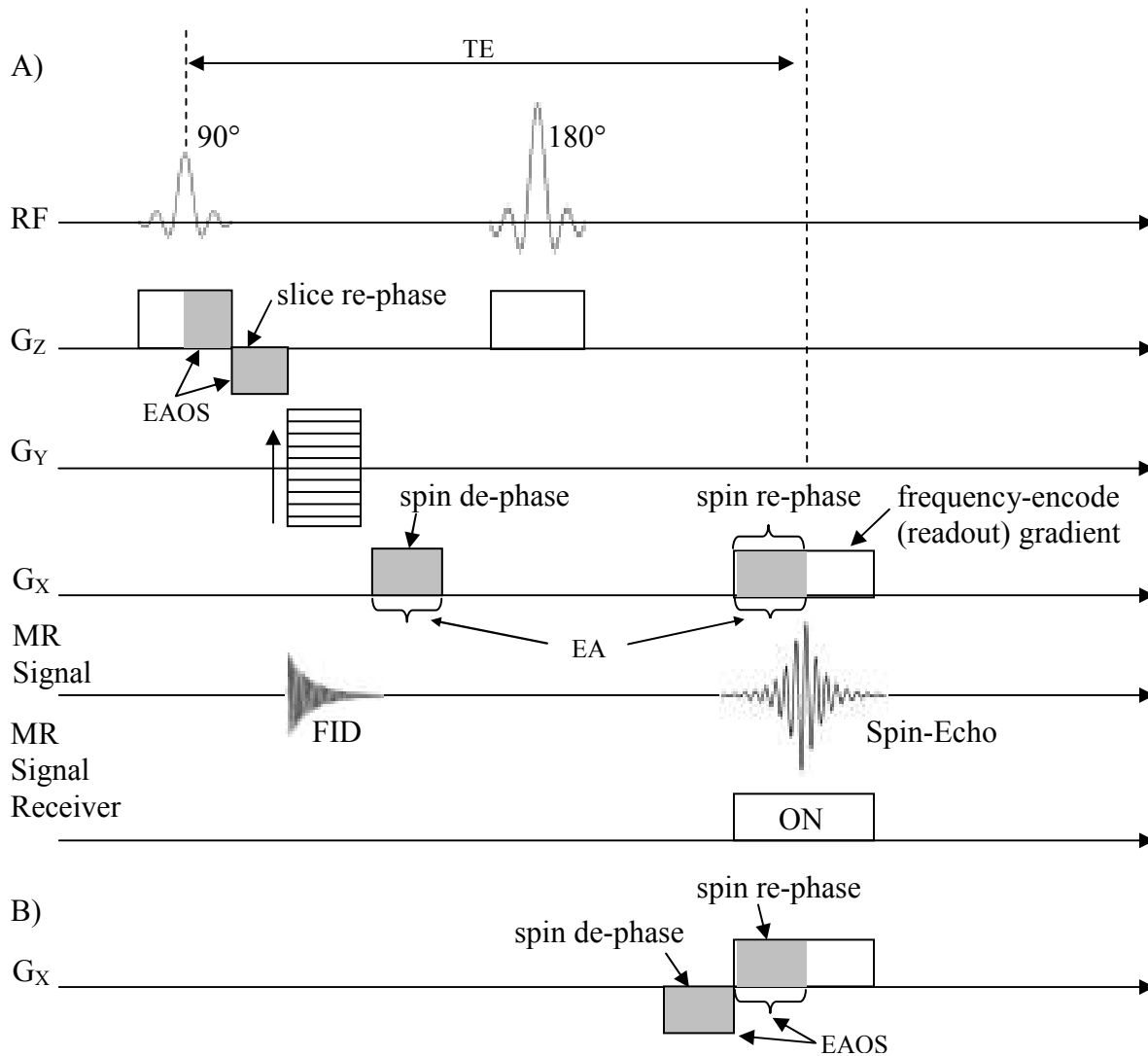


Figure 1-28: A) Timing diagram of the spin-echo MR pulse sequence. A slice-selective 90° RF pulse creates transverse magnetization within the selected slice. The amplitude of the phase-encoding gradient ( $G_Y$  in this case) is varied incrementally between successive repetition time (TR) intervals as a part of creating a 2-dimensional k-space representation of the raw time-domain data (one row at a time). The second dimension of spatial information in the plane of the image is obtained by acquiring the spin-echo signal in the presence of a frequency-encoding gradient. In A), the de-phasing gradient for the frequency-encoding period is applied before the 180° refocusing pulse. Note that the FID generated after the slice rephase gradient ( $G_Z$ ) is not measured at that point so as to allow for subsequent phase- and frequency-encoding of the measured spin-echo signal. The time between the middle of the 90° slice-selective RF pulse and the apex of the spin-echo signal is referred to as the time to echo or TE time. EAOS = Equal Area Opposite Sign, EA = Equal Area. B) The spin-echo pulse sequence can also be implemented by applying a de-phasing gradient just prior to the frequency-encoding period; however, in this case, the polarity must be opposite to that of the readout gradient.

echo. The digitized spin-echo signal for a particular value of the phase-encoding gradient is used to fill one row of k-space. The sequence is then repeated, incrementally varying the amplitude of the phase-encoding gradient, until the desired number of k-space rows has been acquired.

To better understand how the entire k-space acquisition process works; consider the series of spin-echo pulse sequences in Figure 1-29. The time between each  $90^\circ$  RF pulse is referred to as the repetition time or TR. Each new TR period begins with a  $90^\circ$  RF pulse and the only difference from one TR interval to the next is a change in the amplitude of the phase-encoding gradient (e.g.,  $G_Y$  in Figure 1-29). For the first TR period in the series, the phase-encoding gradient amplitude is typically at its most extreme (negative or positive) value. At the end of the first TR interval, the data acquired during the readout-gradient period is stored as the outer-most (in this case 'bottom') row or line of k-space. During each subsequent TR interval, a new line of k-space is filled which corresponds to the particular value of the phase-encoding-gradient amplitude during that interval. This process continues until the desired image resolution in the phase-encoding direction has been achieved. For example, a spin-echo image with a  $256 \times 256$  matrix will have 256 different phase-encoding steps (requiring 256 TR intervals), with the spin-echo signal being digitized with 256 points during the frequency-encoding period of each TR interval. Note in Figure 1-29 that the amplitude of the received MR signal increases as the phase-encoding-gradient amplitude decreases. This is because the phase-encoding-gradient pulse, just like any other gradient, causes de-phasing of the signal (proportional to the area of the pulse) and a concomitant reduction in signal amplitude. The outer lines of k-space contain the high-spatial-frequency information (e.g., sharp edges) in the image. The center lines of k-space contain the low-spatial-frequency and signal-intensity information within the image (e.g., general shapes in the image (8)).

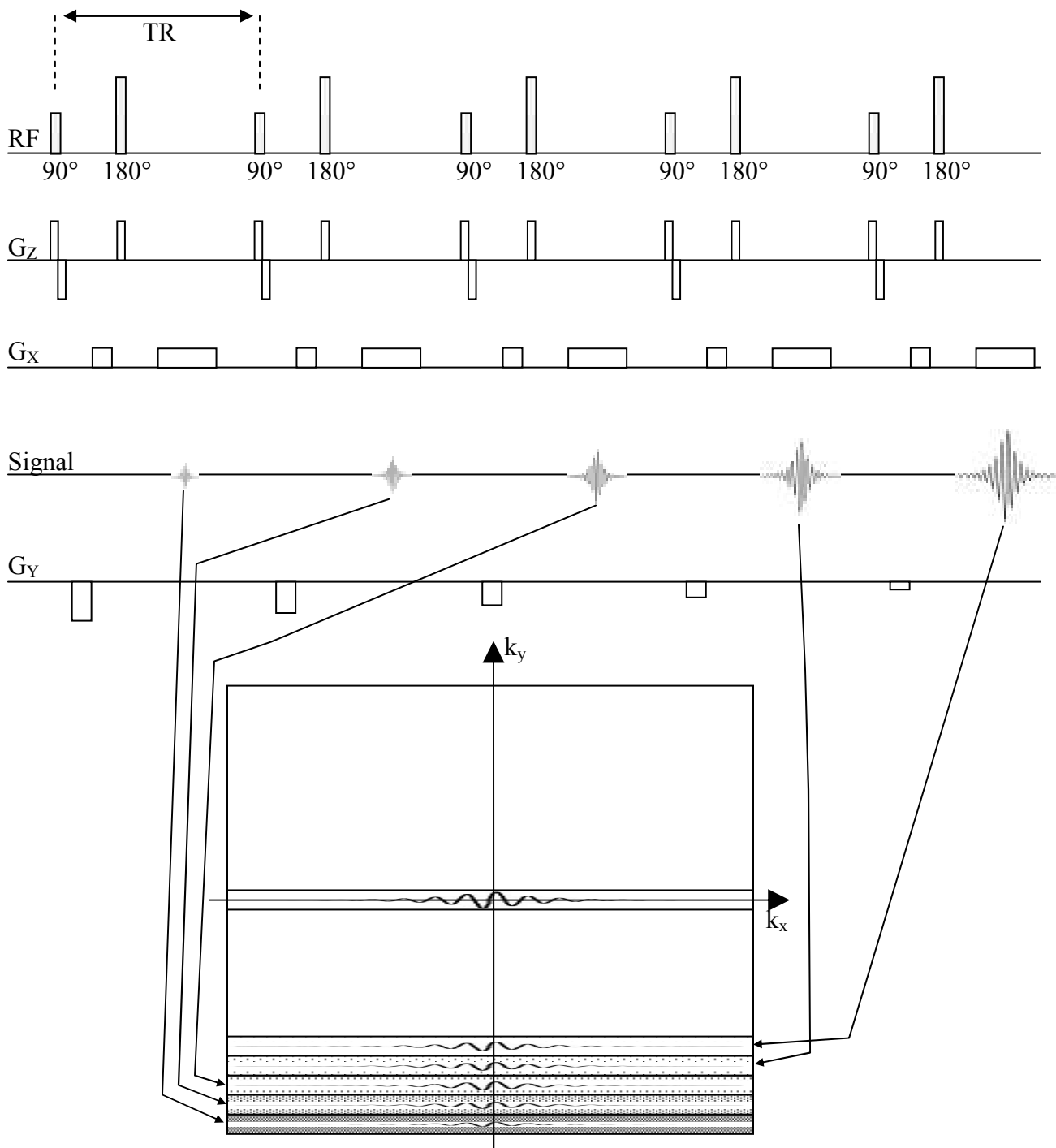


Figure 1-29: Spin-echo MRI pulse sequence and placement of raw-data into k-space as a function of the phase-encoding-gradient amplitude. Each line (row) of k-space corresponds to a particular value of the phase-encoding-gradient amplitude during the respective TR interval. Large phase-encoding-gradient amplitudes result in progressively smaller MR signals due to the increased de-phasing of the transverse magnetization during the phase-encoding period. Consequently, the center lines of k-space, where the phase-encoding-gradient is low, contain the low-spatial-frequency and signal-intensity information in the image whereas the high-spatial-frequency information is contained in the outer lines of k-space.

The MR data acquired in k-space are the 2-dimensional time-domain representation of the data. The k-space data are then converted into the spatial (i.e., frequency) domain via a 2-dimensional Fourier transformation in order to create the MR image. The k-space data acquired in a typical MRI experiment can be represented as shown Figure 1-30. Raw data acquired during each step of the phase-encoding process (e.g., during the acquisition/readout period of a TR interval) comprise a row of complex data points from the digitized spin-echo signal. The real ('Re') and ('Im') part of each complex data point arise from the fact that the signal is measured in quadrature; using two channels that are 90° out of phase with each other.

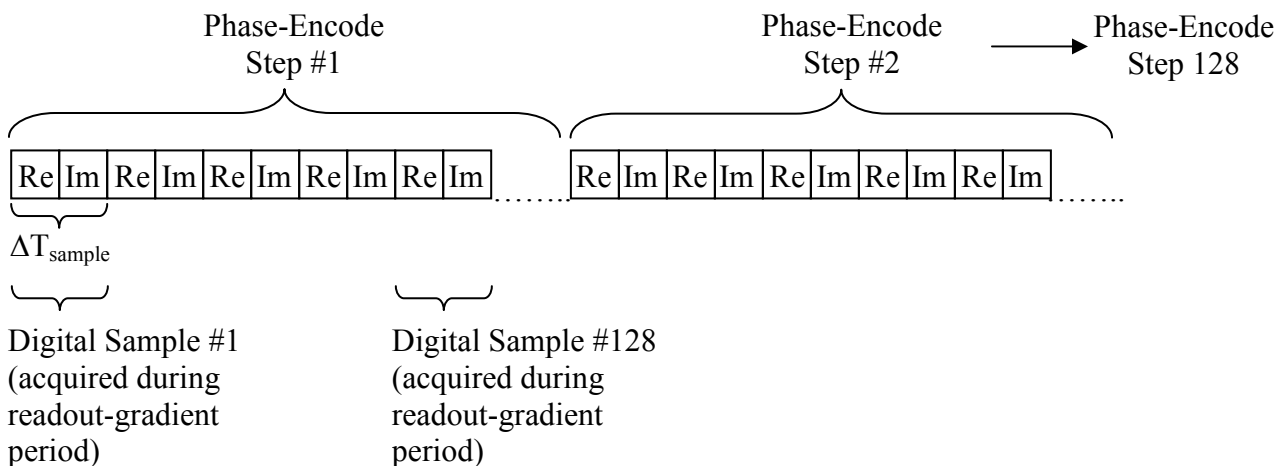


Figure 1-30: Raw MR data storage format typically used during the acquisition of 2-dimensional k-space data for a 128X128 image. Each data point is acquired using quadrature detection (i.e., two receiver channels that are 90° out of phase with each other) and stored as a complex (real and imaginary) pair. A complex 2-dimensional Fourier transform is then used to convert the k-space data into the spatial (i.e., frequency) domain.

Following a complex 2-dimensional Fourier transformation, each point in the MR image is still represented as a complex pair. However, for display purposes, the real and imaginary parts of the data are separated and only the real part is used for image display.

## 2.4 The Gradient-Echo and Gradient-Echo (GRE) MRI

The gradient-echo (GRE) method is frequently used for MRI applications that require fast imaging times. Formation of a GRE has already been discussed to some extent (e.g., in the context of Figure 1-28B), but will be revisited here for clarity. Consider Figure 1-31, where an echo is shown forming after de-phasing and re-phasing of nuclei using a magnetic field gradient. Note that the echo is formed at the point where the duration-amplitude product (area) of the de-phasing

gradient pulse is equal to the duration-amplitude product (area) of the first half of the readout (or, in this case, re-phasing) gradient pulse.

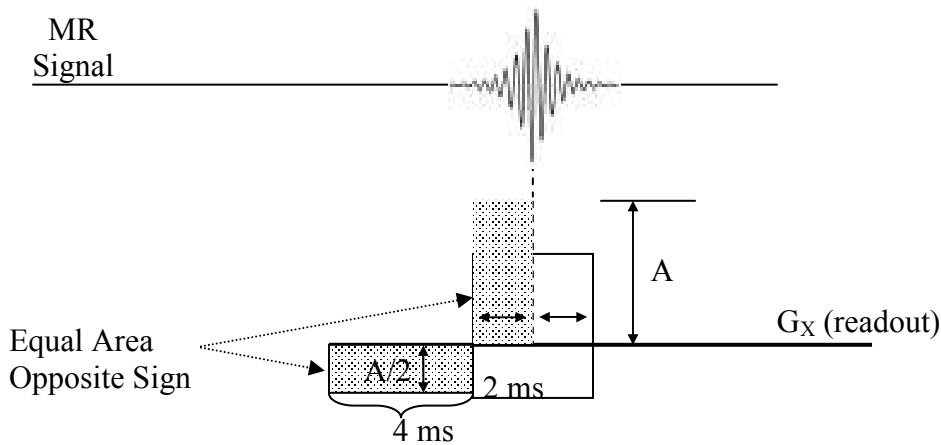


Figure 1-31: Formation of a gradient echo (GRE) by reversing the gradient polarity. A GRE is formed when the duration-amplitude product of the de-phasing gradient is equal to the duration-amplitude product of the first half of the readout gradient pulse.

Since the GRE imaging pulse sequence does not use a  $180^\circ$  RF pulse to refocus transverse magnetization, the echo time (i.e., TE) of the imaging sequence can be significantly reduced. To further minimize the TE time, the re-phasing gradient pulses for both slice-selection and frequency-encoding can be applied simultaneously in the phase-encoding-gradient period. To reduce the imaging time by decreasing the repetition time (TR), the RF pulses used for GRE imaging typically do not rotate longitudinal magnetization completely into the transverse plane (i.e., the flip angle –  $\alpha$  in Figure 1.32 – is generally much less than  $90^\circ$ ). As a result, a substantial fraction of the longitudinal magnetization remains along the z-axis. In this case, the longitudinal magnetization does not require as much time to recover to the Boltzmann equilibrium (relative to a  $90^\circ$  RF pulse) and successive applications of the reduced-tip-angle pulse can be applied more frequently.

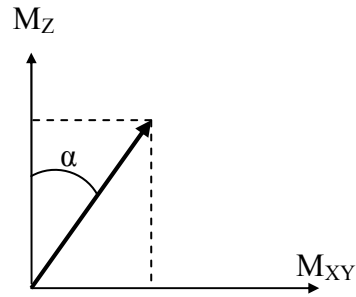


Figure 1-32: The flip angle ' $\alpha$ ' of the RF pulse in a GRE imaging pulse sequence is usually less than  $90^\circ$  to allow for significant magnetization to be available following each repetition time (TR) interval.

Selection of the optimal flip angle for a GRE excitation pulse is commonly based on the ratio of the repetition time (TR) to the  $T_1$  relaxation time. The flip angle that maximizes the MR signal [for sequences that do not establish a steady-state transverse magnetization (9)] is given the Ernst-angle,  $\alpha_E$ , equation:

$$\cos(\alpha_E) = e^{\frac{-TR}{T_1}} . \quad (1.31)$$

A typical pulse sequence for GRE imaging is shown in Figure 1-33. Note that the re-phasing gradient pulses for both slice-selection and frequency-encoding are applied simultaneously in the phase-encoding-gradient period. This is possible since each gradient has a separate effect on the transverse magnetization which can be distinguished from those of the other gradients. Although these spatial-encoding gradients could also be applied sequentially, the TE time would be increased unnecessarily.

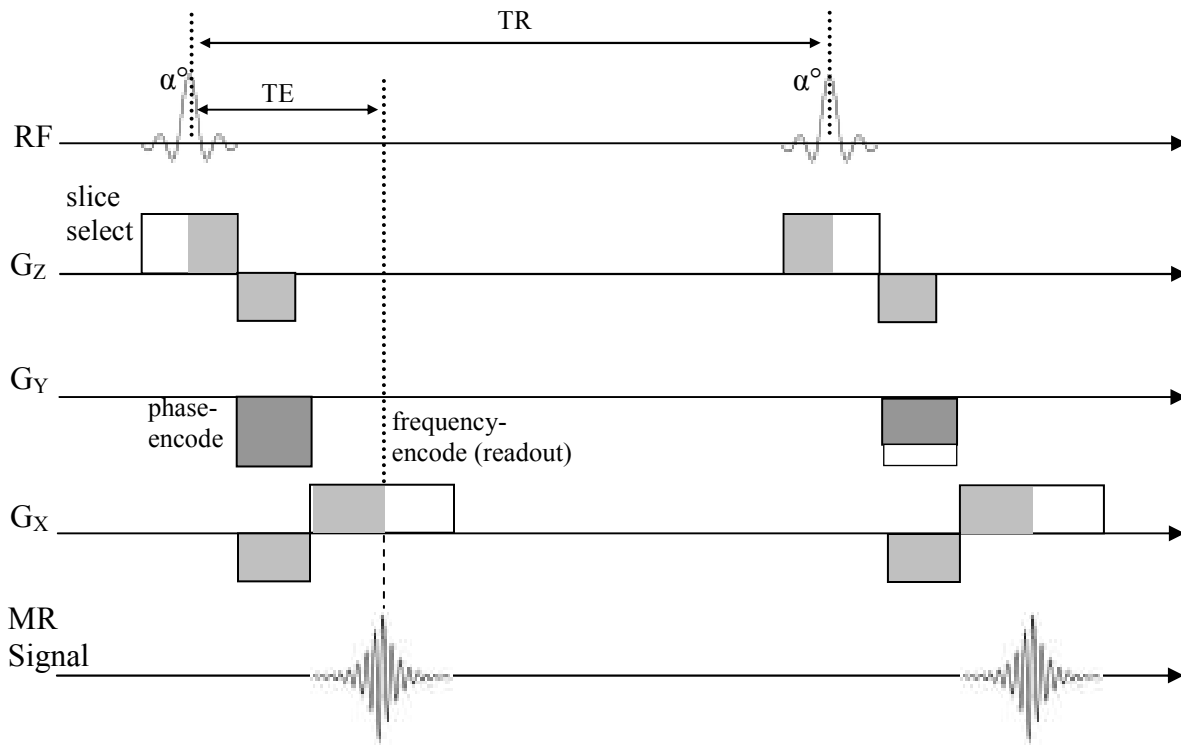


Figure 1-33: Gradient-echo (GRE) MRI pulse sequence. The flip angle,  $\alpha$ , of the slice-selective RF pulse is typically less than  $90^\circ$  so that the residual longitudinal magnetization can recover to the Boltzmann equilibrium in a shorter period of time. As a result, the repetition time (TR) can be shortened, significantly reducing the total imaging time.

### 2.5 Image Contrast Based on Tissue $T_1$ and $T_2$ Relaxation Times

Most tissue contrast in MR images is derived from differences in tissue proton density ( $N(H)$ ) and the  $T_1$  and  $T_2$  relaxation times. MR images with tissue contrast (i.e., signal-intensity differences) based on relative differences in  $N(H)$ ,  $T_1$ , or  $T_2$  are referred to as  $N(H)$ -weighted,  $T_1$ -weighted, or  $T_2$ -weighted images, respectively. For spin-echo MRI, the signal intensity in a voxel,  $S(TE, TR)$  in Eq. 1.32, is dependent on the user-adjustable MRI parameters TE and TR as well as tissue  $N(H)$ ,  $T_1$  and  $T_2$  (10):

$$S(TE, TR) = \underbrace{N[H]}_{\text{Spin Density Factor}} \underbrace{\left(1 - e^{-\frac{(TR-TE)/2}{T_2}} + e^{-\frac{TR}{T_1}}\right)}_{T_1 \text{ Factor}} \underbrace{e^{-\frac{TE}{T_2}}}_{T_2 \text{ Factor}}. \quad (1.32)$$



$T_1$ - and  $T_2$ -weighted spin-echo imaging is commonly used for neurological applications in the brain due to the large differences among  $T_1$  and  $T_2$  relaxation times between tissues. For example, the  $T_1$  value of white matter, gray matter and cerebrospinal fluid (CSF) in the brain is  $\sim 780$  ms,  $\sim 920$  ms, and  $\sim 4000$  ms, respectively, at 1.5T (11,12). The significant difference in  $T_1$  relaxation times between brain white and gray matter makes it possible to differentiate between these tissues in a  $T_1$ -weighted MR image. Consider the  $T_1$  recovery curves in Figure 1-34. To optimize the  $T_1$ -weighted MRI contrast between the two tissues, a TR value is chosen that maximizes the signal-intensity difference between the two curves. For the case shown in Figure 1-34 the optimal TR time is 850 ms based on the TR that coincides with the apex of the signal-intensity difference curve. The optimal TR, in this case, is also equal to the average of the tissue  $T_1$  values.

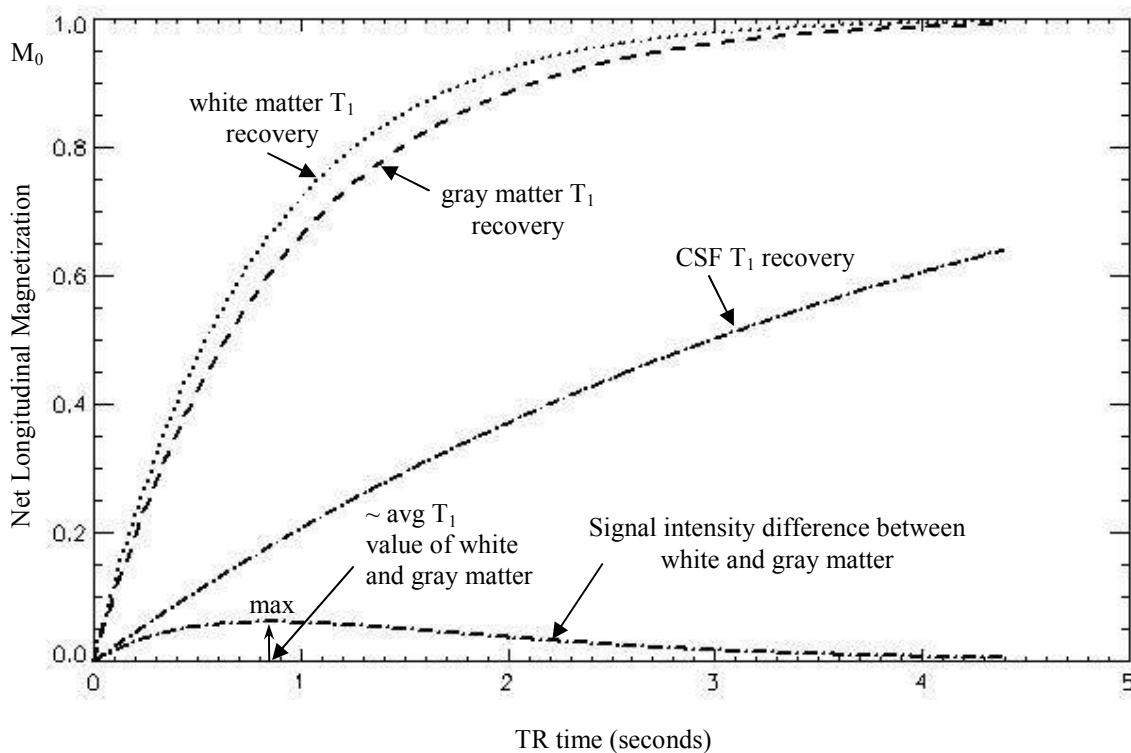


Figure 1-34:  $T_1$  recovery for white and gray matter in the human brain and difference in signal intensity between white matter and gray matter as a function of TR. To produce the highest contrast between white and gray matter in a MR image, a TR is chosen that maximizes the signal intensity difference between the two tissues. In this case, the TR that maximizes the signal intensity difference between white and gray matter is also equal to the average value of the tissue  $T_1$  values (850 ms).

For a visual example, consider the images of human brain in Figure 1-35. In this case the TR values were varied from 400 ms (leftmost image) to 6000 ms (rightmost image) while the TE value was held constant at 20 ms. Contrast between white and gray matter is evident at TR/TE = 800/20 ms. At TR/TE = 6000/20 ms the white/gray matter contrast appears reversed compared to the white/gray matter contrast at TR/TE = 800/20 ms. MR images of brain acquired at TR/TE = 800/20 ms (and 400/20 ms) are primarily  $T_1$ -weighted and at TR/TE = 6000/20 ms MR images are primarily N(H)-weighted.

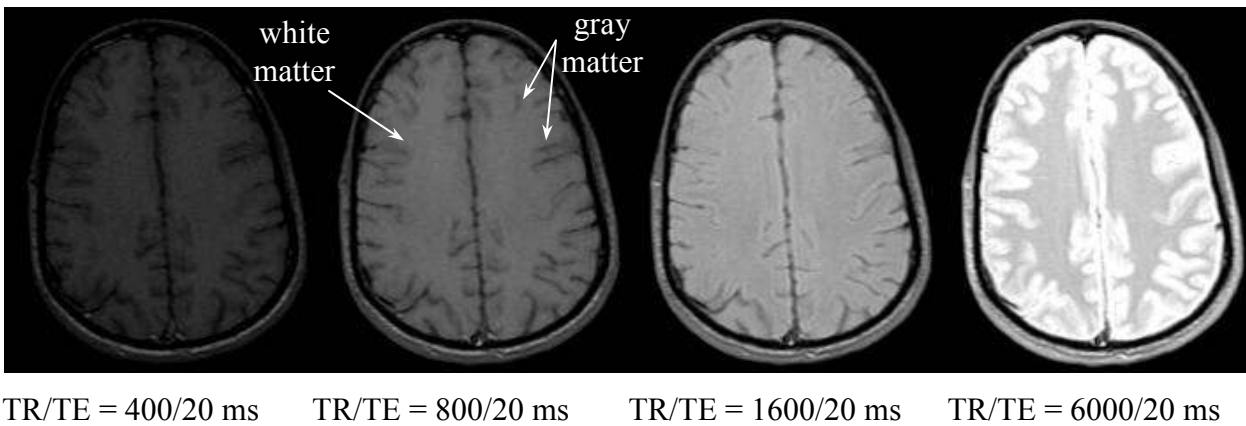


Figure 1-35: Series of adult human brain images to demonstrate changes in contrast between white and gray matter (and CSF) as TR is changed (TE constant at 20 ms). The leftmost image (TR/TE = 400/20 ms) is primarily  $T_1$ -weighted while the rightmost image (TR/TE = 6000/20 ms) is primarily N(H)-weighted. In  $T_1$ -weighted adult human brain images white matter appears white (or relatively bright) and gray matter appears gray (or relatively dark). There is considerable contrast between white and gray matter (as well as CSF) in the rightmost image due to differences in proton density between the two tissue brain tissues as well as CSF. Images here were acquired using a 1.5T clinical scanner and have resolution of approximately 940  $\mu\text{m}$ .

To acquire  $T_2$ -weighted spin-echo images, it is important to use long TR values to minimize the effect of  $T_1$ -weighting on the image. For example, notice that as the TR value approaches a value on the order of  $5T_1$ , the “ $T_1$  factor” term in Eq. 1.32 approaches one. In that case, the MR signal intensity within each voxel will depend primarily on the N(H) and  $T_2$  relaxation time of the tissue as well as the TE value used in the spin-echo MRI pulse sequence as:

$$S(TE, TR) = N[H](1)e^{\frac{-TE}{T_2}} \quad (1.33)$$

Inspection of Eq. 1.33 also reveals that a N(H)-weighted spin-echo MR can be acquired by maximizing TR ( $\sim 4-5T_1$ ) and minimizing the TE value (e.g., 5-10 ms); the right-most image in Figure 1-35 being a good example.

For  $T_2$ -weighted spin-echo MRI, TE is typically long (on the order of 80-100 ms). The  $T_2$ -relaxation-time values for white matter, gray matter and cerebrospinal fluid (CSF) in the human brain are 67, 77, and 180 ms, respectively. The N(H) values are 0.61, 0.69 and 1.00, respectively (11), normalized relative to CSF, which has the maximum value. By minimizing  $T_1$ -relaxation-time effects (i.e., using Eq. 1.33), the MRI signal-intensity-decay curves, as a function of the TE value, are as shown in Figure 1-36.

As with  $T_1$ -relaxation-time recovery curves, the  $T_2$ -relaxation-time decay curves indicates that for optimal contrast between tissues based on differences in the  $T_2$  relaxation times, a TE value is chosen that maximizes the MRI signal-intensity differences between the respective tissues and/or CSF.

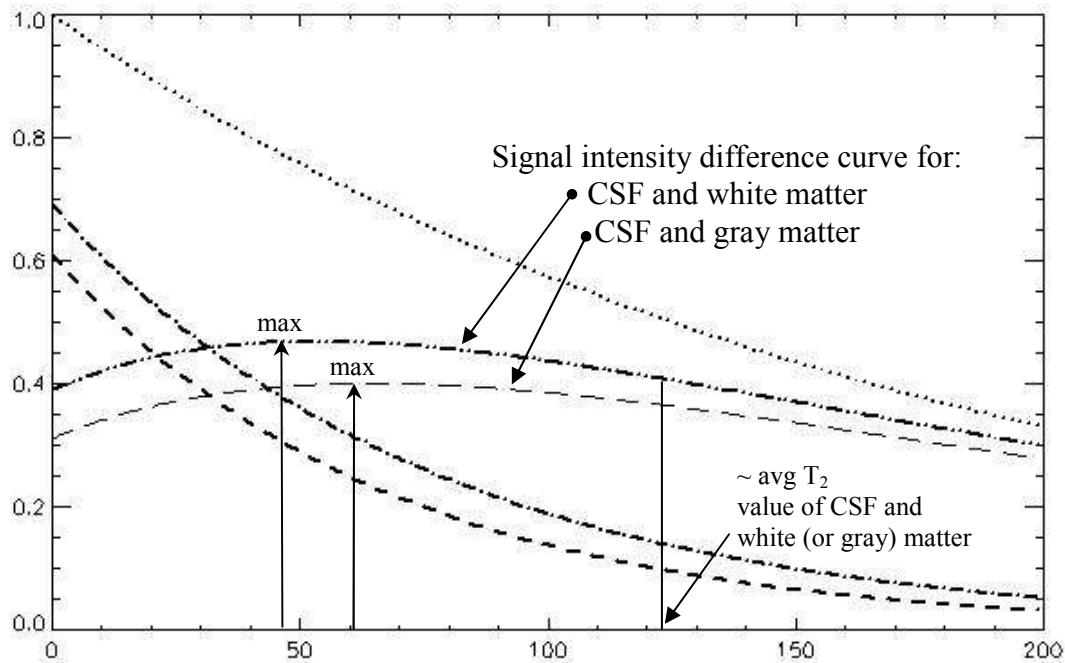
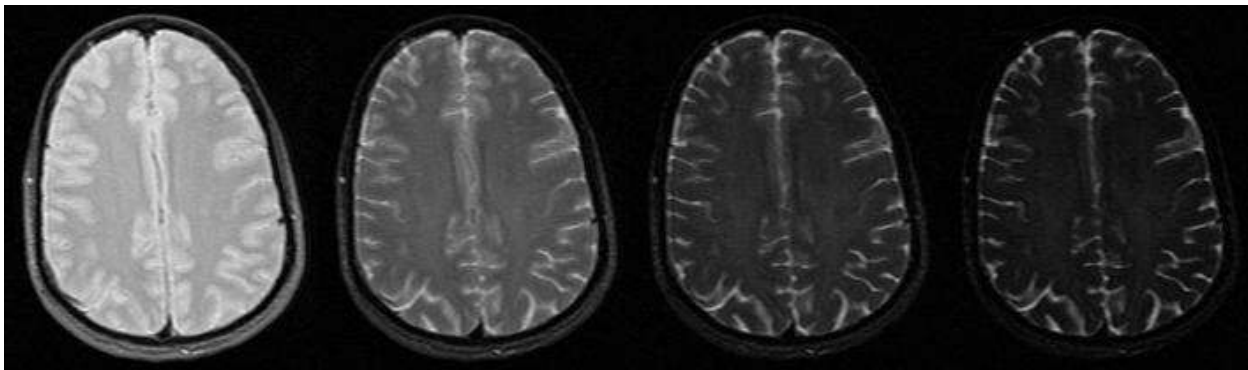


Figure 1-36:  $T_2$  decay curves for cerebral spinal fluid (CSF), and white and gray matter in the human brain. The long  $T_2$  relaxation time of CSF, relative to those of white and gray matter, results in higher CSF signal intensity relative to white and gray matter on  $T_2$ -weighted brain MR images. The optimal TE time to maximize contrast between white and gray matter and CSF is the TE time that maximizes the signal intensity difference between white matter and gray matter and CSF ( $\sim 51$  ms and  $\sim 65$  ms respectively as indicated on the graph). In this case the TE times that maximize contrast

between white and gray matter and CSF do not coincide with the average  $T_2$  value ( $\sim 125$  ms) of CSF and white (or gray) matter.

For a visual example, consider the human brain images in Figure 1-37. Here, the TE values were varied from 50 ms to 200 ms while TR was held constant at 3000 ms. In Figure 1-37 the change in contrast between white (and gray) matter and CSF is apparent as TE increases. As TE increases signal from CSF is stronger relative to surrounding brain matter as predicted by the  $T_2$  decay curves in Fig. 1-36.



TR/TE = 3000/50 ms

TR/TE = 3000/100

TR/TE = 3000/150

TR/TE = 3000/200

Figure 1-37: Series of adult human brain images to demonstrate changes in contrast between CSF and white and gray matter as TE is changed (TR constant at 3000 ms). The leftmost image (TR/TE = 3000/50 ms) is primarily proton-density-weighted while the rightmost image (TR/TE = 3000/200 ms) is primarily  $T_2$ -weighted. Note the sharp decline in white and gray matter signal intensity as TE becomes longer as predicted by  $T_2$  decay curves in Fig. 1-36. CSF signal intensity remains strong relative to white and gray matter providing excellent contrast between CSF and brain tissue at TE = 100-200ms. Images here were acquired using a 1.5T clinical scanner and have resolution of approximately 940  $\mu\text{m}$ .

## 2.6 Multi-Slice Spin-Echo MRI

Consider a spin-echo MRI pulse sequence with TR/TE of 250/11 milliseconds and a desired matrix size of 256x256. The time needed to acquire such an image (assuming no averaging of slice data) is  $250 \text{ ms} * 256 = 128$  seconds (1 minutes and 4 seconds). If it was desired to acquire 8 slices at different positions (for example, through the human brain), and each slice was acquired sequentially, then the imaging time increases by a factor of 8 to 512 seconds (8 minutes 32 seconds). As an alternative, the imaging time can be reduced significantly using a multi-slice, spin-echo MRI pulse sequence, where additional slices are obtain at other positions within the brain

during the residual portion of the TR interval following the acquisition of the first slice. Consider the timing diagram of the spin-echo MRI pulse shown in Figure 1-38. If the TE value and the data acquisition period are such that the first slice is acquired in 50 ms, then the residual time left in the TR interval is 200 ms before the  $90^\circ$  RF pulse is applied again at the same slice position (for example, to acquire the next line of k-space for that slice).

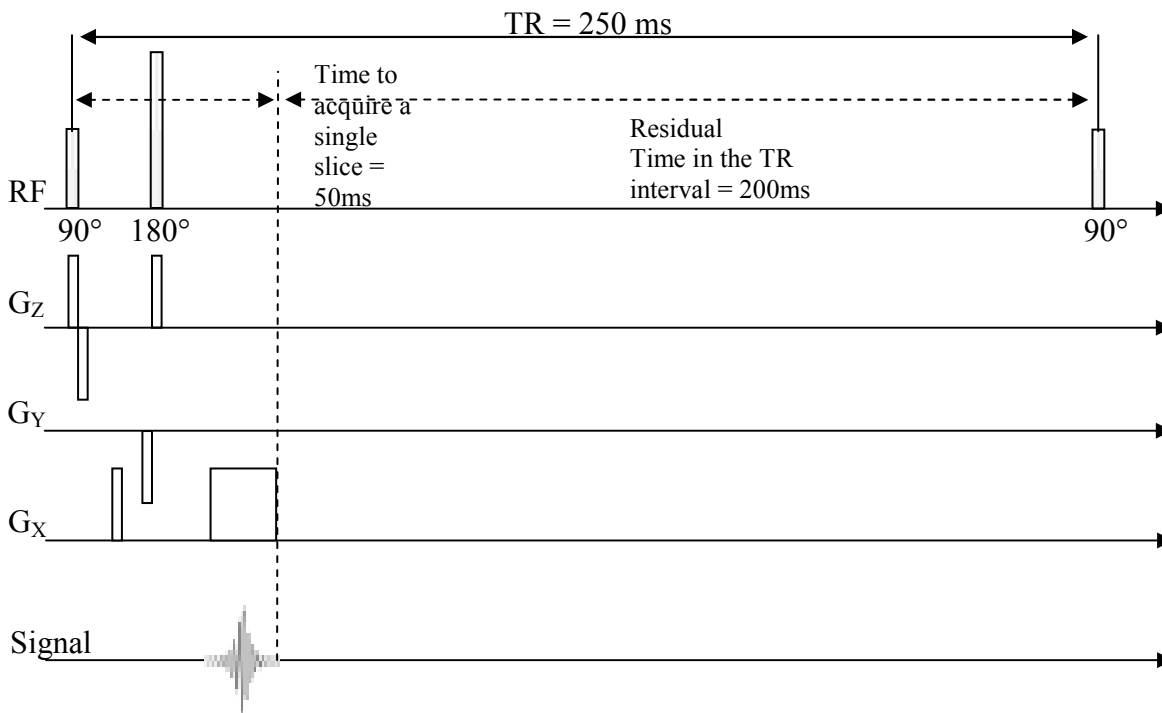


Figure 1-38: Timing diagram for a spin-echo MRI pulse sequence showing the time needed to acquire a single slice and the residual time in the TR interval before the  $90^\circ$  RF pulse is applied again at the same slice position (for example, to acquire the next line of k-space for that slice).

During the residual 200 ms in the TR interval shown in Figure 1-38, several other slices (up to four) at different slice positions could be excited. Usually, all slices in a multi-slice scan have the same thickness requiring the same RF excitation bandwidth and the same slice-select gradient. Therefore, for a multi-slice spin-echo imaging pulse sequence, the RF excitation pulses that select the other slices must have a different center frequency with respect to each other. Figure 1-38 can now be redrawn (Figure 1-39) to include four additional  $90^\circ$  RF excitation pulses during the residual TR period. The center frequency of each  $90^\circ$  RF excitation pulse is usually chosen to provide an interleaved acquisition of the slices (e.g., a slice order of 1, 3, 5, 2, and 4 in this case). This interleaved scheme reduces “cross-talk” between adjacent slices.

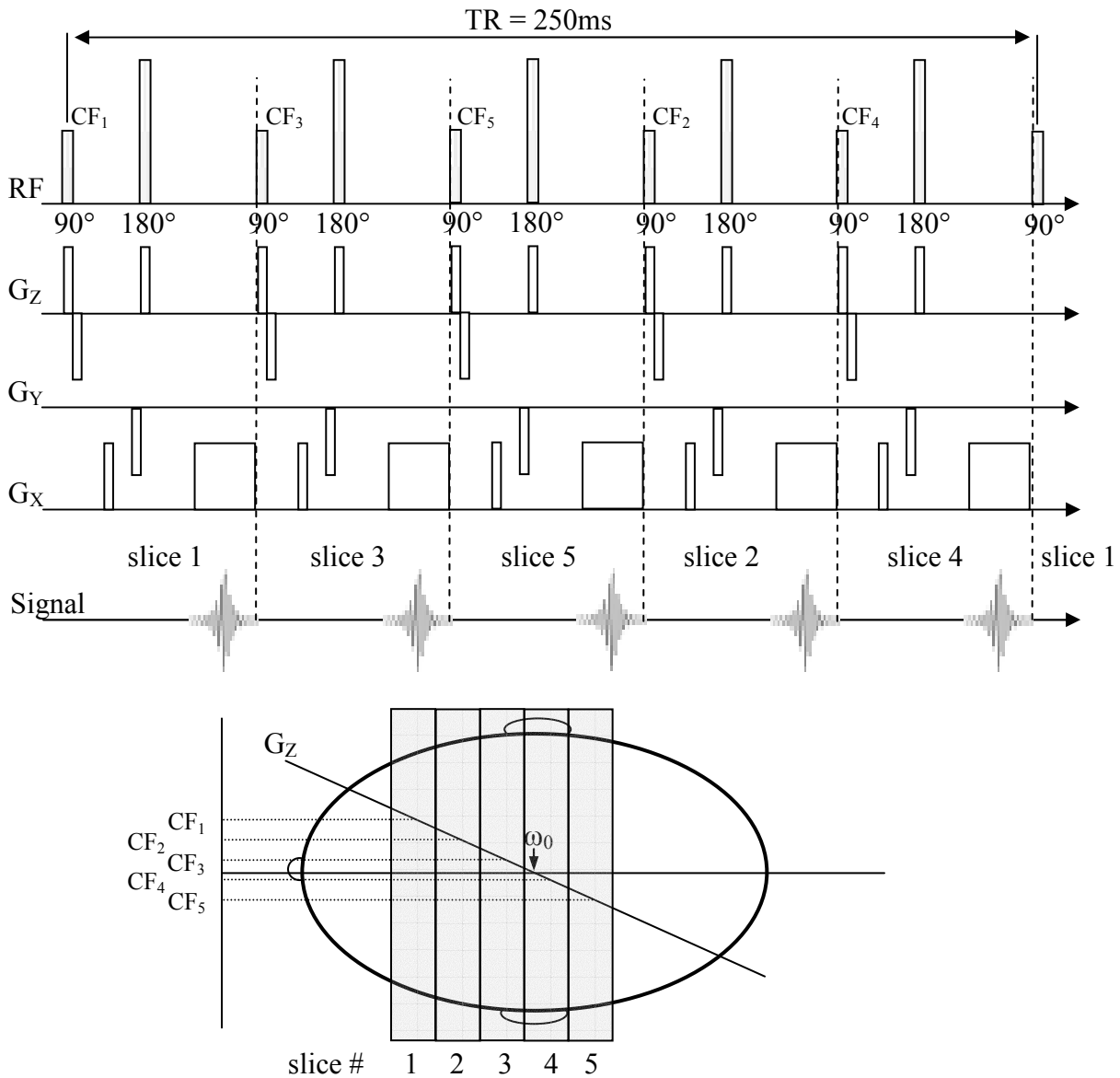


Figure 1-39: One repetition time (TR) interval of a multi-slice spin-echo MRI pulse sequence (the time to acquire a single slice is 50 ms and TR – 250 ms). By acquiring five slices within one TR period, the total imaging time is reduced by a factor of five. The slice positions are determined by the respective center frequencies, ‘CF’, of the corresponding RF excitation pulses.

## 2.7 Echo-Planar Imaging

In 1977, Sir Peter Mansfield recognized that k-space could be filled completely following a single RF excitation (13), eliminating the need to fill k-space one line at a time (or one line per TR period). Using the echo-planar imaging (EPI) technique, images could potentially be acquired in 30 to 100 ms (14). Unfortunately, however, the MRI hardware required to implement the pulse sequence was not available at the time and it took a number of years before EPI became a practical reality. By 1991, Stehling et al. (14) reported various uses for EPI such as flow imaging, water diffusion imaging, brain imaging, and functional brain imaging.

### 2.7.1 Echo-Planar Imaging Methods for Traversing k-space

To traverse k-space in a “single shot,” EPI employs a number of data acquisition strategies that differ from the trajectory path employed by more conventional MRI methods (e.g., spin-echo or GRE MRI).

#### *Gradient-echo EPI (GRE EPI)*

Figure 1-40 compares the conventional k-space trajectory with that of the GRE EPI implementation. The k-space trajectory for a conventional MRI pulse sequence is shown in Figure 1-40a. For each line of k-space, following the RF excitation pulse, a single echo is acquired at a particular value of the phase-encoding-gradient amplitude. During the intervening TR interval, the phase-encoding-gradient amplitude is incremented, and then the next line of k-space is acquired. In the case of GRE EPI, however, following the acquisition of the first echo, the phase-encoding-gradient amplitude is incremented and then a second echo (i.e., line of k-space) is acquired in the same “TR” interval. This process is then repeated until all of the lines of k-space are acquired during a single data acquisition interval. After the initial RF excitation pulse, the GRE EPI pulse sequence forms a “train” of gradient echoes by rapidly switching the polarity of the readout gradient and digitizing the signal at the same time. During the switching time between each echo acquisition, a “blipped” phase-encoding gradient is applied to advance to the next line of k-space (Figure 1-40b). The entire k-space dataset can typically be acquired in 30-100ms (15). The GRE EPI pulse sequence used to traverse k-space as shown in Figure 1-40b is shown in Figure 1-41.

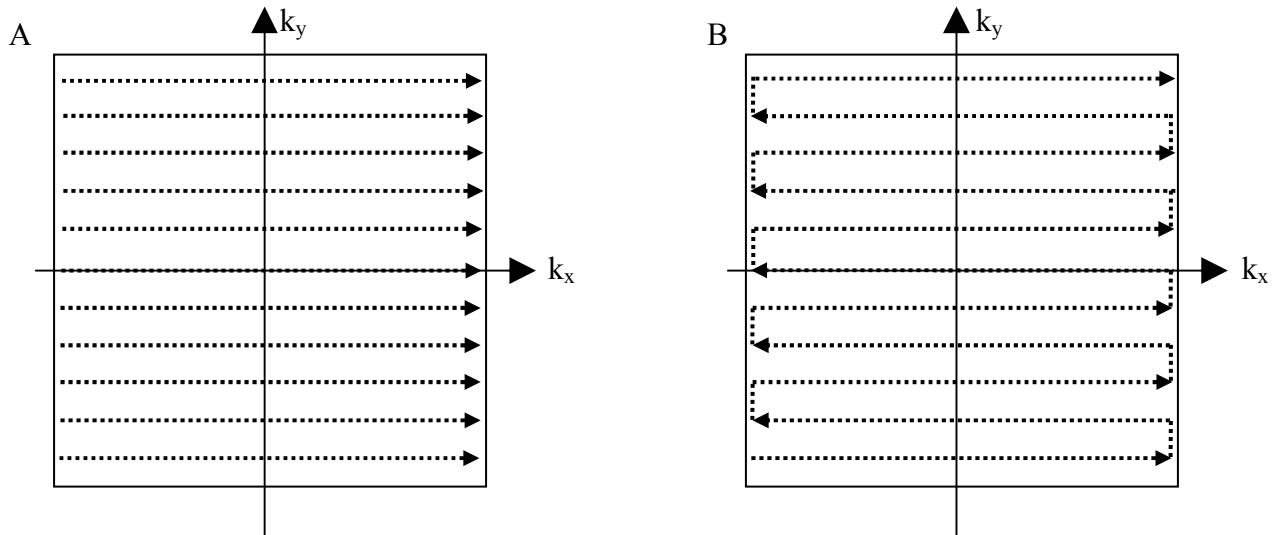


Figure 1-40: A) Conventional 2D-FT MRI k-space trajectory; acquisition of each line of k-space requires a separate RF excitation and TR period. B) GRE EPI k-space trajectory; following a single RF excitation, all lines of k-space are acquired in a “single shot.”



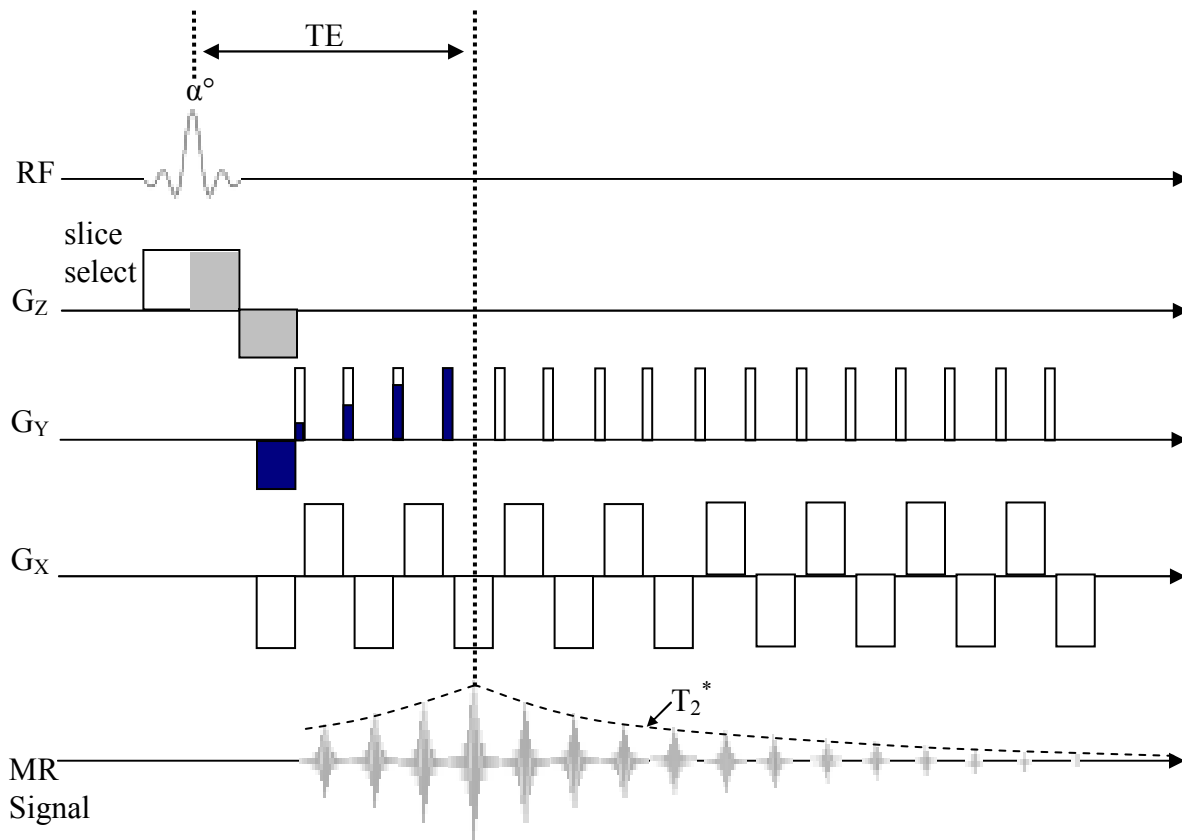


Figure 1-41: GRE EPI MRI pulse sequence. The echo time (TE) for the sequence occurs at a time when the duration-time product of the positive-going “blipped” phase-encoding–gradient pulses ( $G_y$ ) is equal to the duration-time product of the initial  $G_y$  de-phasing gradient pulse. The successive accumulation of gradient duration-time product by positive-going  $G_y$  pulses is represented by the first four positive-going  $G_y$  pulses. All of k-space is filled before complete signal dephasing due to  $T_2^*$  effects (~30-100ms).

### *Spin-echo EPI (SE EPI)*

The spin-echo EPI MRI pulse sequence is essentially the same as the GRE EPI method except that a  $180^\circ$  RF refocusing pulse applied at a time TE/2 after the initial  $90^\circ$  RF excitation pulse. Phase and frequency-encoding is SE EPI, as shown in Figure 1-42, is the same as for GRE EPI.

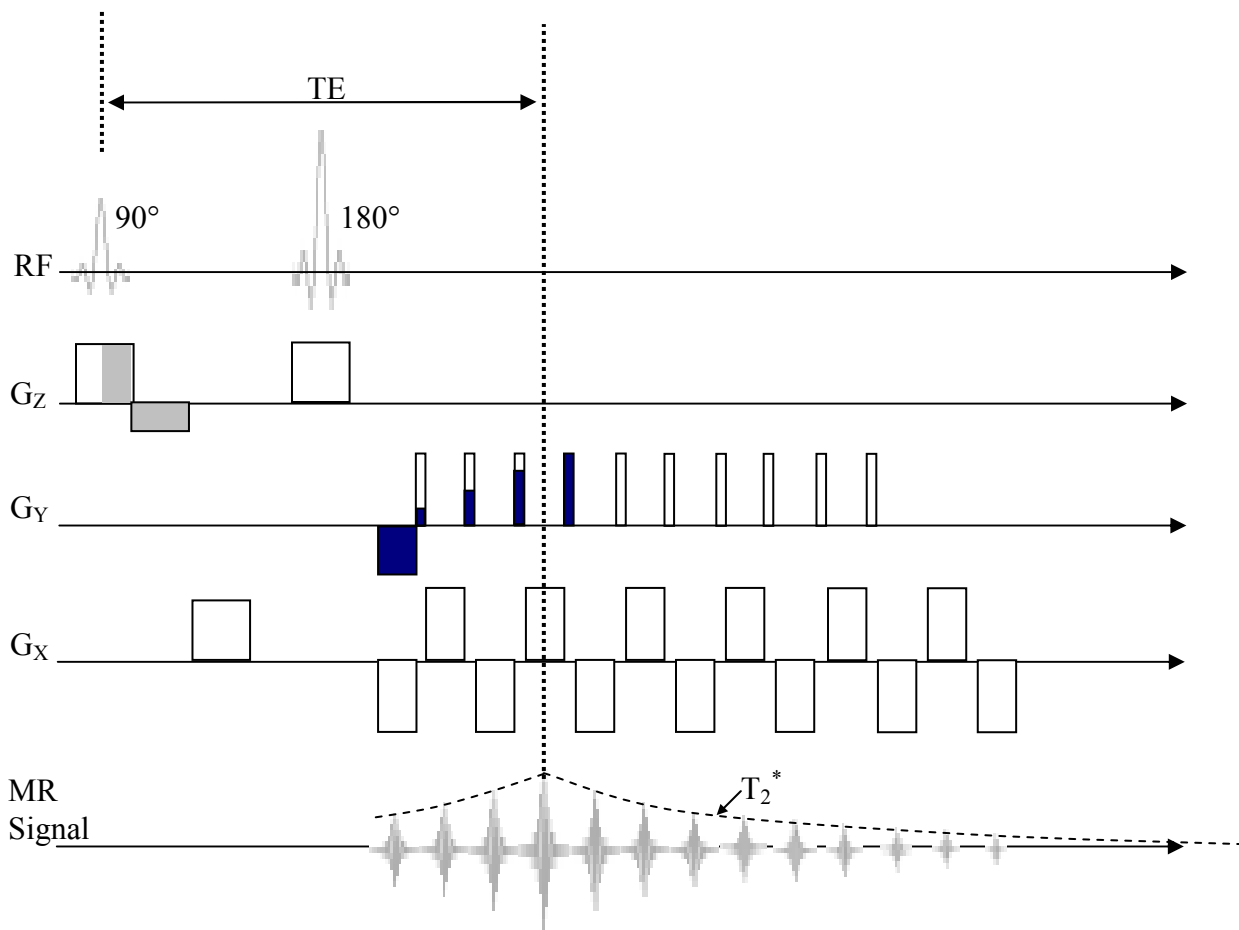


Figure 1-42: SE EPI MRI pulse sequence. As is the case for GRE EPI, the echo time (TE) for the gradient echoes formed in the sequence occurs at a time when the duration-time product of the positive-going “blipped” phase-encoding-gradient pulses ( $G_y$ ) is equal to the duration-time product of the initial  $G_y$  de-phasing gradient pulse. For SE EPI, the RF spin-echo produced by refocused magnetization (at time TE/2 after the  $180^\circ$  refocusing pulse) occurs at the same TE time as for the gradient echos. The successive accumulation of gradient duration-time product by positive-going  $G_y$  pulses is represented by the first four positive-going  $G_y$  pulses. All of k-space is filled before complete signal dephasing due to  $T_2/T_2^*$  effects ( $\sim 30$ - $100$ ms). The blipped phase-encoding scheme results in the k-space trajectory shown in Figure 1-40b.

## 2.8 Diffusion-Weighted Imaging

Diffusion-weighted imaging (DWI) is used extensively in clinical and animal studies. For brain imaging, DWI is sensitive to changes in brain water content and mobility. DWI finds clinical application in imaging tissue pathologies such as inflammation, edema, cell swelling, cell necrosis,

membrane damage, demyelination, axonal loss, and gliosis (16). A brief explanation of water diffusion theory is provided before discussing DWI in detail.

### 2.8.1 Diffusion of Water

All fluids have an associated diffusion constant  $D$  which provides a quantitative description of how the molecules within the fluid move among themselves. The movement of molecules within a fluid is governed by random thermal agitation and is generally referred to as Brownian motion (after Robert Brown of Scotland, 1827). The movement of fluid molecules within heterogeneous media, such as cells with the brain is less random due to the presence of physical boundaries that interfere with the translation of the molecules. For molecules in the bulk phase, the average displacement of the molecules as a function of time can be represented by a Gaussian probability distribution:

$$P(X, t) = \frac{1}{\sqrt{D4\pi t}} e^{-\frac{X^2}{4Dt}} \quad (1.34)$$

For the case of diffusion with no preferential direction, diffusion is said to be *isotropic*. For molecular diffusion in media with restricting boundaries, diffusion can be *anisotropic*. In anisotropic diffusion, a diffusion tensor is used to represent the degree of diffusion of molecules in nine different directions as follows:

$$D = \begin{bmatrix} D_{xx} & D_{xy} & D_{xz} \\ D_{yx} & D_{yy} & D_{yz} \\ D_{zx} & D_{zy} & D_{zz} \end{bmatrix}$$

where  $D_{xx}$ ,  $D_{yy}$ , and  $D_{zz}$  represent the diffusion constants along the reference frame axes. The diffusion tensor is symmetric since  $D_{ij} = D_{ji}$  and, therefore, the tensor can be accurately represented by the six elements:  $D_{xx}$ ,  $D_{yy}$ ,  $D_{zz}$ ,  $D_{xy}$ ,  $D_{xz}$ ,  $D_{yz}$ . In MR the net displacement of diffusing molecules is a variable of interest. Equation 1.34 only tells us the probability of finding a molecule at position  $X$  after a time  $t$ . Another means to characterize the net displacement of diffusing molecules is via the Einstein equation:

$$\langle (r - r')^2 \rangle = 2nDt \Rightarrow D = \frac{\langle (r - r')^2 \rangle}{2nt} \quad (1.35)$$

where  $n = \#$  dimensions,  $t =$  time allowed for diffusion to occur and  $\langle (r - r')^2 \rangle$  is defined as the square of the net distance traveled by a molecule undergoing random diffusion as shown in Figure 1-43:

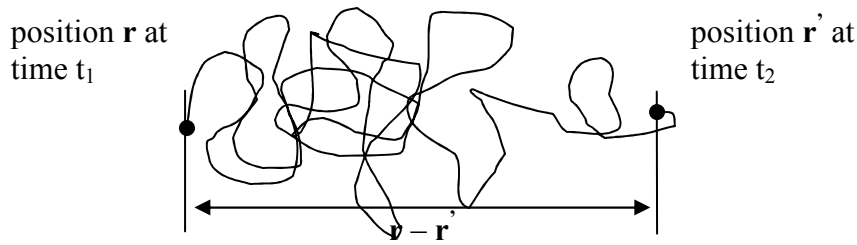


Figure 1-43: Random walk of a molecule undergoing random diffusion. The molecule accumulates a net displacement,  $r-r'$ , over time.

### 2.8.2 Stejskal-Tanner Diffusion-Weighted Pulse Sequence

MR can be used to measure the displacement of diffusing water molecules by application of a pair of magnetic field gradients surrounding the  $180^\circ$  RF refocusing pulse of a spin-echo imaging pulse sequence. This technique developed by Stejskal and Tanner in 1965 (17) is referred to as the ‘pulsed magnetic field gradient’ (PMF) technique. A typical Stejskal-Tanner PMF diffusion-weighted spin-echo MRI pulse sequence is shown in Figure 1-44.

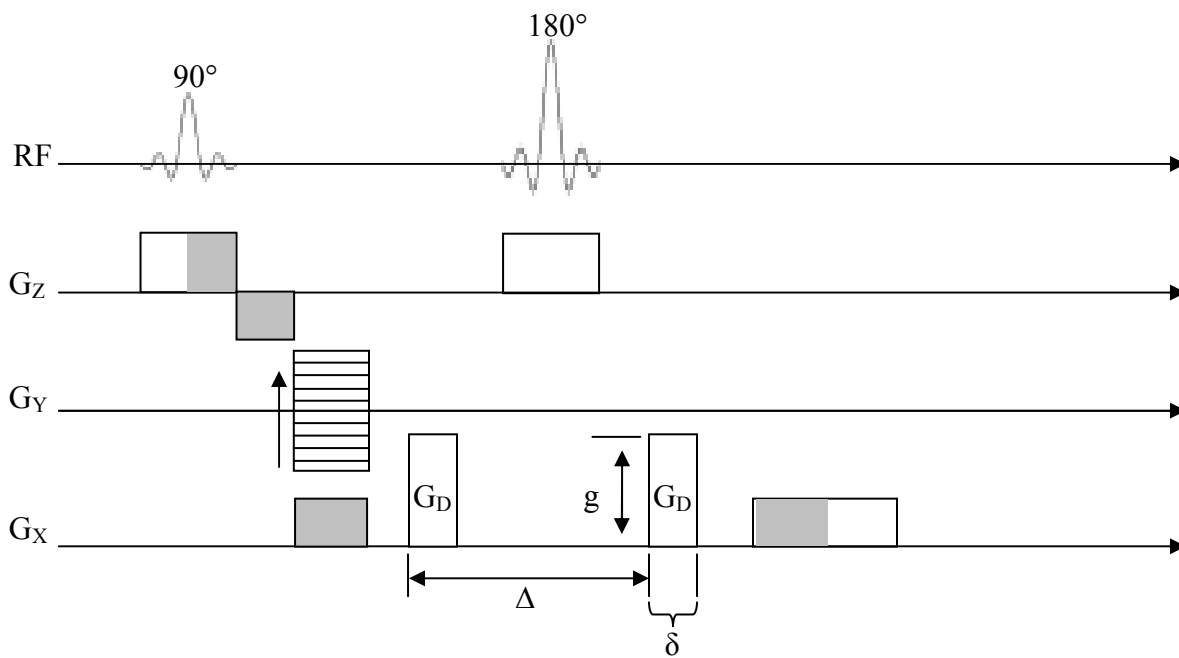


Figure 1-44: Stejskal-Tanner PFG diffusion-weighted spin-echo MRI pulse sequence. The amplitude of the spin-echo is determined by the separation ( $\Delta$ ), duration ( $\delta$ ), and amplitude ( $g$ ) of the diffusion-sensitive gradient pulses ( $G_D$ ). The diffusion time  $t_D$  is determined by  $\Delta$  and  $\delta$  as  $t_D = \Delta - \delta/3$  (16).

The first of the diffusion-sensitive-gradient pulses ( $G_D$ ) in the Stejskal-Tanner pulse sequence is designed to de-phase nuclear magnetization prior to the  $180^\circ$  refocusing pulse (which in turn inverts the phase of the nuclei). For molecules that are not moving (i.e., not diffusing), the second diffusion-sensitive-gradient pulse (which has an area identical to the first) completely removes the phase shifts imparted by the first diffusion-sensitive gradient pulses. Consequently, there is no loss of phase coherence for static molecules and the associated MR signal intensity is unaffected. For moving (i.e., diffusing) molecules, however, the second diffusion-sensitive-gradient pulse does not completely remove the phase shifts encoded by the first diffusion-sensitive-gradient pulse. This is because of the spatial displacement of the diffusing molecules to a different location along the direction of the applied magnetic field gradient. Consequently, the transverse magnetization from the nuclei in diffusing molecules will experience a loss of phase coherence and a concomitant reduction in the MR signal intensity. The magnitude of the MR signal reduction will be directly proportional to the area of the diffusion-sensitive-gradient pulses, the diffusion time, and the magnitude of the diffusion coefficient. For molecules in regions of restricted diffusion (e.g., brain white and gray matter), the signal intensity in a diffusion-weighted MRI (DWI) will be higher than for molecules in regions with relatively free diffusion (e.g., CSF). Using the Stejskal-Tanner pulse sequence, the degree to which the DWI signal intensity is attenuated (i.e., the degree of diffusion-weighting) depends on the factors  $\Delta$ ,  $\delta$ ,  $g$ , and  $D$  as follows:

$$S(TE, b) = M_0 e^{-bD} e^{-\frac{TE}{T_2}} \quad (1.36)$$

$$\text{where } b = \gamma^2 \delta^2 g^2 \left( \Delta - \frac{\delta}{3} \right).$$

The ‘b-value’ shown in Eq. 1.36 is the parameter that determines the amount of diffusion weighting applied to a DWI. The  $b$  value has units of seconds/mm<sup>2</sup> and typically range from 20 s/mm<sup>2</sup> (low diffusion weighting) to 1500 s/mm<sup>2</sup> (high diffusion weighting).

### 2.8.3 Quantification of Diffusion-Weighted Images: The ADC Map

To quantify diffusion *in vivo* using DWI requires the acquisition of at least two images; one with little or no diffusion-weighting (i.e.,  $b = 0$  or close to 0) and one with relatively high diffusion-weighting (e.g.,  $b$  on order of  $1400 \text{ s/mm}^2$ ). The Stejskal-Tanner formula can then be used to solve for the diffusion coefficient based on the two images as follows (16):

$$\ln \left[ \frac{S(TE, b)}{S(TE, 0)} \right] = -bD. \quad (1.37)$$

For molecular diffusion in biological systems that contain restricting barriers (e.g., cell membranes), the value for  $D$ , as shown in Eq. 1.37, is often referred to as the *apparent diffusion coefficient* (ADC). In this case, the ADC value is reduced compared to that of molecular diffusion in the bulk phase and its value often depends on the amount of time that the molecules are allowed to diffuse (i.e., the diffusion time). The ADC can be calculated using Eq. 1.37 by plotting the left hand of the equation as a function of  $b$ -value (as shown in Figure 1-45).

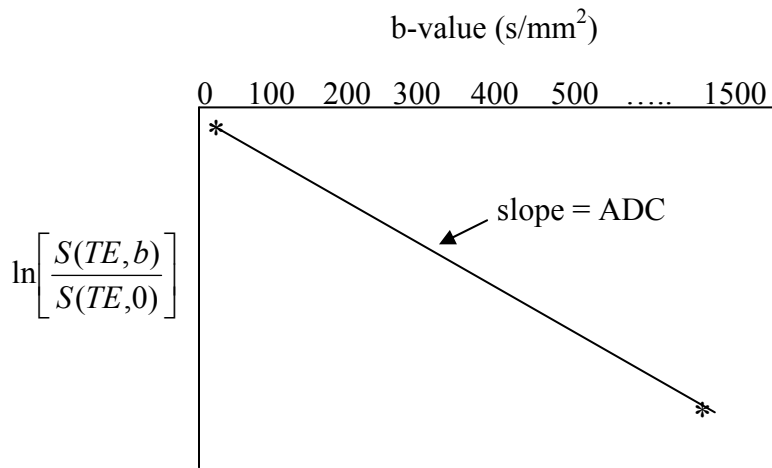


Figure 1-45: Calculation of the ADC by linear fitting of the natural log of the signal intensities from two (or more) DWIs (asterisks) as a function of  $b$  value. The ADC value is calculated from the slope of the line.

## REFERENCES

1. Haliday D., Resnick R. Fundamentals of Physics: John Wiley and Sons; 1989.
2. Bloch F., Hansen W.W., Packard M. Nuclear Induction. Phys Rev 1946;69:127
3. Bloembergen N., Purcell E.M., Pound R.V. Relaxation effects in nuclear magnetic resonance absorption. Phys Rev 1948;73:679-712
4. Hahn E.L. Spin Echos. Phys Rev 1950;80:580-594

5. Carr H.Y., Purcell E.M. Effects of diffusion on free precession in nuclear magnetic resonance absorption. *Phys Rev* 1954;94:630.
6. Meiboom S., Gill D. Modified Spin-Echo Method for Measuring Nuclear Relaxation Times. *Sci Instrum* 1958;29:688.
7. Oppenheim A.V., Schafer R.W. *Discrete-Time Signal Processing*. Oppenheim A.V., editor. Englewood Cliffs, NJ: Prentice Hall; 1989.
8. Paschal C.B., Morris H.D. K-Space in the Clinic. *JMRI* 2004;19:145-159
9. Elster A.D., Burdette J.H. *Questions and Answers in Magnetic Resonance Imaging*. Mosby, editor. St. Louis: Mosby; 2001.
10. Stark D.D., Bradley W.G. Jr. *Magnetic Resonance Imaging*. St. Louis: Mosby; 1999.
11. NessAiver M. *All you really need to know About MRI Physics*. Maryland: University of Maryland Medical Center; 1997.
12. Rooney W.D., Johnson G., Li X., Cohen E.R., Kim S-G., Ugurbil K., Springer C.S. Magnetic Field and Tissue Dependencies of Human Brain Longitudinal  $^1\text{H}_2\text{O}$  Relaxation *in vivo*. *Magn Reson Med* 2007;57:308-318.
13. Mansfield P. Multi-planar image formation using NMR spin echoes. *J Phys C* 1977;10:L55-L58.
14. Stehling M.K., Turner R., Mansfield P. Echo-Planar Imaging: Magnetic Resonance Imaging in a Fraction of a Second. *Science* 1991;254:43-50.
15. Edelman R.R., Wielopolski P., Schmitt F. Echo-planar imaging. *Radiology* 1994;192:600-612.
16. Tofts P. *Quantitative MRI of the Brain*. Chichester: John Wiley & Sons Ltd; 2003.
17. Stejskal E.O., Tanner J.E. Spin diffusion measurements: SEs in the presence of a time-dependent field gradient. *J Chem Phys* 1965;42:288.

# CHAPTER 2

## Characteristics and Manipulation of the Blood-Brain Barrier (BBB)

Blood-Brain Barrier (BBB) Background

Anatomy of the BBB  
Brain Capillary Epithelium

Techniques to Determine BBB Permeability  
Quantification of BBB Permeability using the Brain-Perfusion Technique  
A Semi-Quantitative Measure of BBB Permeability Using Evans Blue (EB) Dye

Hyperosmotic Disruption of the BBB  
Characteristics of Reversible Osmotic BBB Disruption  
Mannitol and Arabinose as Hyperosmolar Infusates for BBB Disruption

The BBB and Cerebral Edema

MRI Detection of BBB Disruption  
Gd-DTPA Used to Detect Regions of Pathological BBB Disruption



## 2.1 Blood-Brain Barrier (BBB) Background

The concept of a blood-brain barrier (BBB) was conceived in the early 1900s with experiments performed by Lewandowsky, Ehrlich, and Goldmann. Lewandowsky noticed during his experiments that the stain Prussian blue did not pass from the brain blood vessels into the brain (1). Ehrlich performed similar experiments using the stain Trypan Blue and found that while the whole body became stained with the dye, the brain was always an exception. Goldmann's experiments with Trypan Blue infusion into the cerebral spinal fluid allowed him to conclude that there was some form of barrier separating nervous tissue from brain tissue (1). Early investigators were therefore focused on determining the structure and function of the barriers separating blood, brain tissue and cerebrospinal fluid (CSF).

The modern concept of the BBB was not conceived until 1965 by Crone *et al.* (2). The BBB was found to be capable of regulating the active transport of substances into the brain at a time when it was generally accepted that substances crossed the BBB only by passive diffusion. Then, in 1967, in an attempt to better understand the anatomy of the BBB, Reese and Karnovsky (3) determined that the BBB consisted of endothelial cells that lined the cerebral vasculature. By 1976, it was apparent that the function of the BBB was to regulate the interfaces between blood and the nervous system (4). Methods to quantify the permeability of the BBB were established in 1963 by Crone (5) and in 1978 by Ohno *et al.*(6).

Experimental osmotic disruption of the BBB was first performed in the 1940s (7) and was quantified using Evans Blue dye by Rapoport in 1972 (8). Damage to the BBB can result from various insults such as trauma, oxygen deprivation, autoimmune disorders, brain tumor, hypertension, and excessive osmotic infusions (meant to transiently open the BBB). Osmotic BBB disruption in particular has also been shown to result in significant brain edema and long-term brain damage in animals. Magnetic resonance imaging (MRI) technology, aided by advances in MR contrast-agent design, has advanced our understanding of the function of the BBB and the effects of pathologies on the BBB.

## 2.2 Anatomy of the BBB

The role of the BBB is to separate the brain from the systemic blood circulation. The BBB selectively excludes certain blood constituents from being transported into the brain and maintains

the homeostasis of the central nervous system. Brain capillaries, therefore, must have the means to allow certain substances into the brain while excluding others. In the early days of BBB research, the capillaries of the brain were not thought to be different in structure to the capillaries of the musculoskeletal system. Scientists, therefore, were curious as to why Trypan Blue dye failed to stain the animal brain once injected intra-arterial. Arguments were made leading to a hypothesis that the Trypan Blue dye simply had nowhere to go into the brain due to an extremely small extracellular brain space (9). Ironically, this idea had already been disproved by Goldmann (10). Goldmann's second experiment included an injection of Trypan Blue into the CSF – which resulted in complete staining of the brain – suggesting that there was indeed sufficient extracellular volume to accommodate the diffusing Trypan Blue dye stain to diffuse into. Unfortunately, it was not until 1967 that researchers identified the true anatomical basis of the BBB as being the ultrastructure of the brain-capillary endothelium (3). In addition to brain-capillary endothelial cells, the BBB is comprised of astroglia, perivascular macrophages, pericytes, and a basal lamina (11). An artist's view of the capillary is provided in Figure 2-1.

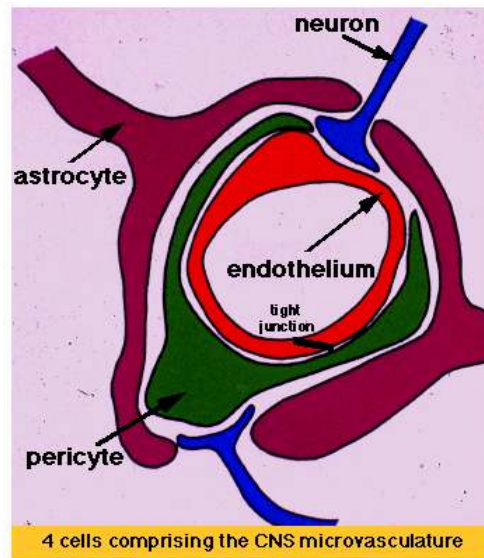


Figure 2-1: Artist's representation of a brain blood vessel and the surrounding endothelium, astrocyte, pericyte and neuron. A tight junction is also shown (black bar). From <http://bloodbrainbarrier.med.ucla.edu>.

## 2.2.1 Brain Capillary Epithelium

### *Tight Junctions*

Capillaries of the brain vasculature are lined with endothelial cells that are closely packed together and are apparently linked by 'tight junctions.' With the use of electron microscopy, the tight

junctions of endothelial cells came to be classified as *zonula occludens* (1). Other types of contact or junctions between cells exist such as *macula adherens*, and *zonula adherens*. In the adherens-type junction, cells remain separated by approximately 200 Å and are held together by electron-dense material (1). From Figure 2-2, the function of the tight junctions becomes clear; prevention of certain solutes from entry into the brain. A close-up view of a tight junction is provided in Figure 2-3. The permeability or 'leakiness' of the BBB to ions is believed to be a function of the number of 'tight-junction elements' that exist within an endothelial-cell tight junction (1). The electrical resistance across a tight junction (in Ohm/cm<sup>2</sup>) is a function of the number of tight-junction elements (12) and reflects the strength of the barrier to passage of ions from blood to brain.

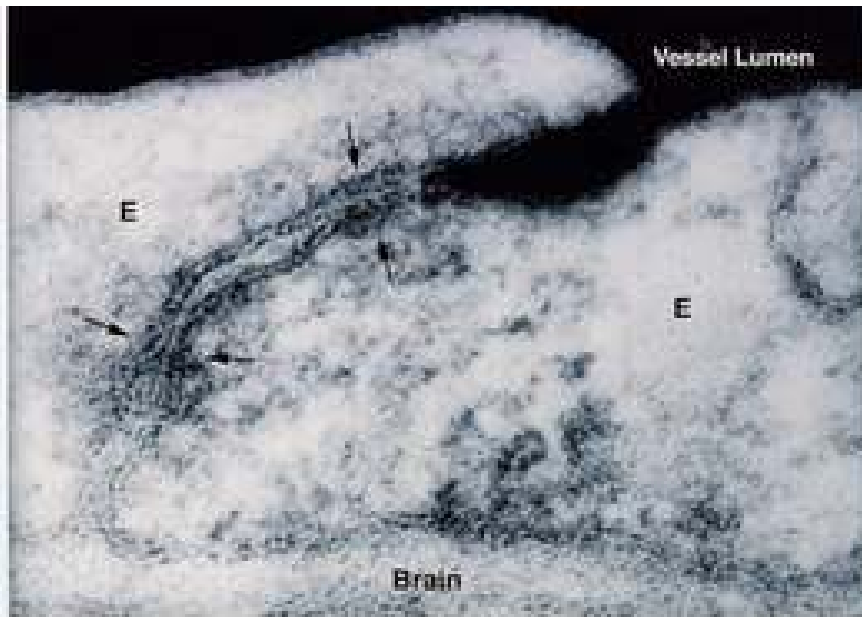


Figure 2-2: Tight junction (arrows) between two endothelial cells (E) prevent electron-dense lanthanum (dark areas in vessel lumen) from penetrating into brain ([http://www.ohsu.edu/bbb/forprof\\_program.html](http://www.ohsu.edu/bbb/forprof_program.html)).

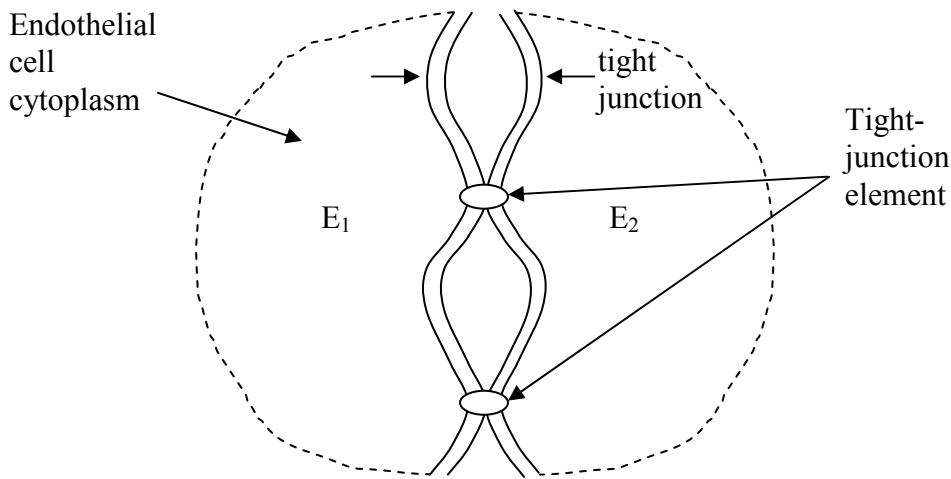


Figure 2-3: Close-up view of the tight junction between two endothelial cells. The number of tight-junction elements within the tight junction determines the electrical resistance of the tight junction to ions.

### *Pits and Vesicles*

Small semi-circular-shaped invaginations (vesicles), with a diameter of approximately 50-100 nm, line the inner (or luminal) membrane (opposite to the basement membrane); with muscle-capillary-endothelial cells containing fewer vesicles than cerebral-capillary-endothelial cells. The vesicles can move further into the endothelial membrane to become pits (9) and a chain of pits can form a *tubule*. It is believed that within tubules, solutes can be transferred from vesicle to vesicle, thus allowing certain solutes from the blood to be ‘carried through’ the endothelial cell membrane as summarized in Figure 2-4.

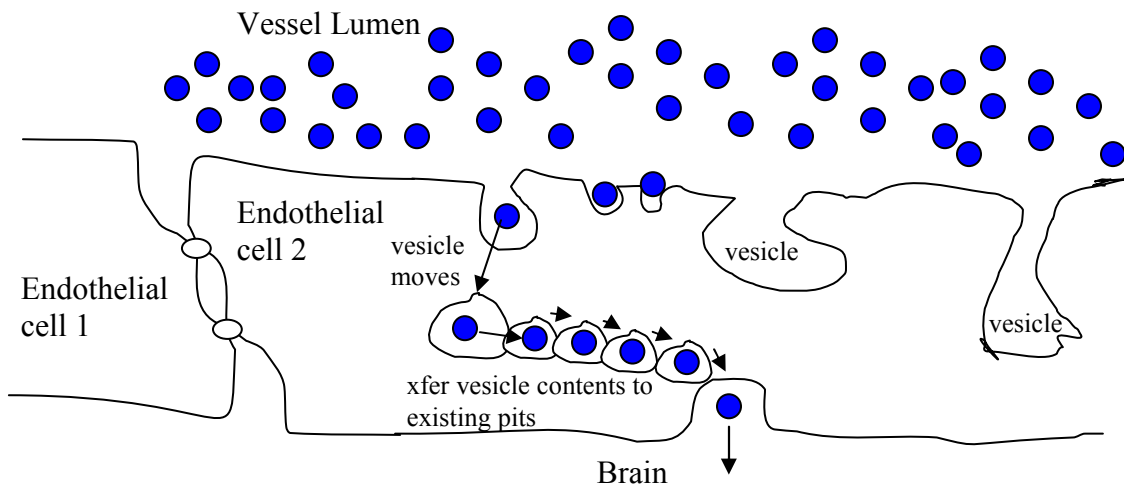


Figure 2-4: Solute transport across the BBB. Vesicles move from the lumen membrane into the endothelial cell to form pits; which combine with existing pits to form a chain or tubule. Part or all of the vesicle contents are shared (or transferred) between pits in the tubule until the solute reaches the brain (13).

## 2.3 Techniques to Determine BBB Permeability

By its nature, the BBB has limited permeability to substances in the blood. As previously discussed, the endothelial cells that line the cerebral capillaries are responsible for BBB function and integrity. Since the discovery of the anatomical nature of the BBB, researchers have been improving upon methods for quantifying the permeability of the BBB. The commonly available techniques for measuring the permeability of the brain include (but are not limited to) the IV administration technique, *the brain-perfusion technique*, the indicator-diffusion technique, the *brain-uptake-index (BUI) technique*, or the *single-injection external-registration technique* (9). For purposes of this dissertation, discussion will be limited to the *brain-perfusion technique*.

### 2.3.1 Quantification of BBB Permeability Using the Brain-Perfusion Technique

With the brain-perfusion technique of Takasato *et al.* (14), one brain hemisphere of an anesthetized animal is perfused by retrograde infusion of a particular fluid into the common (or external) carotid artery. The uptake into the brain of the perfusate can then be observed after sacrificing the animal and removing the brain. A diagram for the brain-perfusion technique is shown in Figure 2-5. The perfusion rate is such that blood flow to the right hemisphere is minimized and perfusion pressure does not rise significantly above normal blood pressure of the animal. The brain-

perfusion technique allows close scrutiny of the composition of fluid entering the brain. Osmolality, pH, protein concentrations and ionic content of the perfusate can be varied over a wider range versus perfusate administered systemically. Disadvantages of the brain-perfusion technique include perfusion of one hemisphere only and possible brain hypoxia due to low blood flow to the perfused hemisphere for the typical 30-120 second infusion.

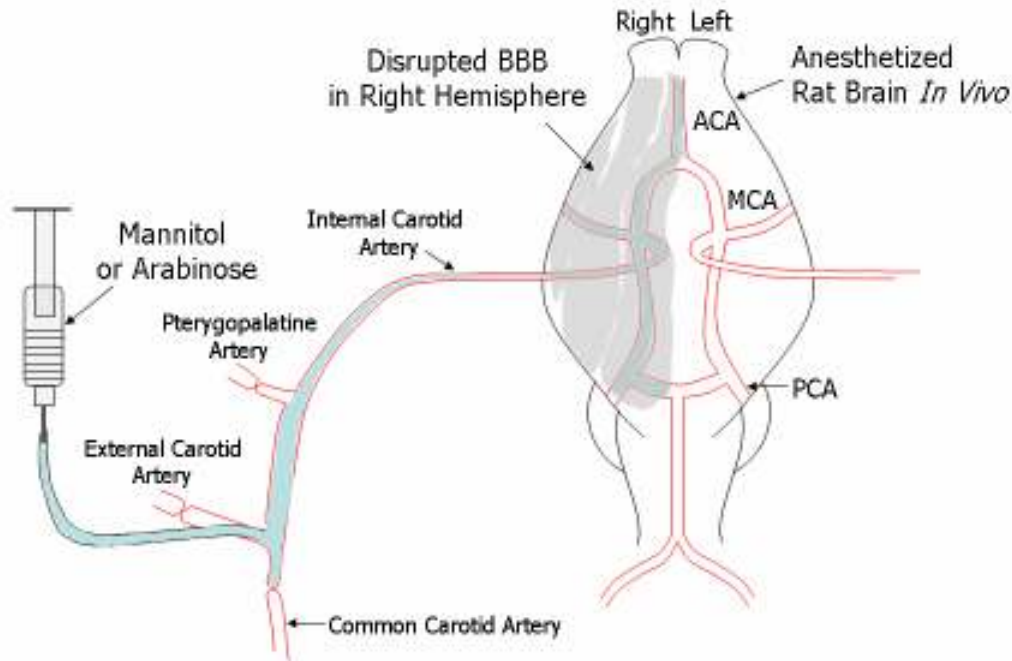


Figure 2-5: Brain-Perfusion Technique of Takasato *et al.* (14). For this technique, the external carotid artery is typically severed leaving a small ‘stump’ for insertion of tubing that will deliver fluid to the brain. The stump of the external carotid artery is then permanently ligated. The tubing is inserted into the internal carotid artery to ensure flow of fluid directly to the brain. The pterygopalatine artery is permanently ligated to prevent leakage of fluid through this route. The common carotid artery is left open until immediately before the infusion. A temporary clamp can be placed appropriately on the carotid artery to ensure delivery of perfusion fluid to the brain and not towards the heart. Also, temporary clamping of the carotid – instead of permanent ligation – helps to maintain the physiological state of the animal. ACA, anterior cerebral artery; MCA, middle cerebral artery; PCA, posterior cerebral artery. Reproduced from Ref. (14).

### 2.3.2 A Semi-Quantitative Measure of BBB Permeability Using Evans Blue (EB) Dye

Evans Blue (EB) dye has been used extensively in animals as a marker for BBB integrity (15-21). The dye in pure form [MW = 960.82 Daltons (Da)] is known to remain within the cerebral vasculature; unable to penetrate the healthy BBB. Evans Blue dye binds to serum albumin in blood after approximately five minutes. Wolman *et al.* (22) used electrophoretic-pattern analysis of free EB, cat plasma, and EB in a sample of cat plasma to determine the temporal dynamics of EB binding to serum albumin. After binding to serum albumin, the EB-albumin complex has a molecular weight of ~68 KDa. The chemical formula, name, and structure for EB dye are provided in Figure 2-6.

A)  $C_{34}H_{24}N_6O_{14}S_4Na_4$   
tetrasodium 6,6'-((3,3'-dimethyl-(1,1'-biphenyl-4,4'-diyl)bis(azo)bis(4-amino-5-hydroxy-1,3-naphthalenedisulphonate)

B)

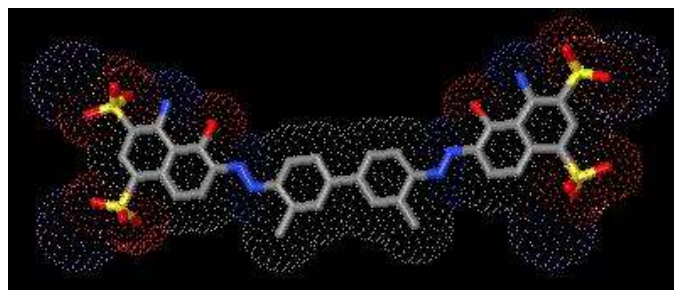


Figure 2-6: A) The empirical chemical formula and name for Evans Blue dye. B) Chemical Structure for Evans Blue dye.

Quantifying the permeability of the BBB using EB staining can be complicated by the fact that EB binds to serum albumin after five minutes within blood. If EB is infused into an animal with an experimentally or pathologically disrupted BBB, the degree of BBB disruption depends on when the animal was sacrificed relative to the time of EB infusion. For example, an animal that is sacrificed less than five minutes after i.v. infusion of EB will show EB staining in the brain that is indicative of BBB permeability to molecules of size 970 Da or less. Consequently, experimental use of EB as a marker for BBB permeability requires careful timing of EB infusion relative to animal sacrifice.

*Evans Blue Solution Preparation*

Evans Blue typically comes in powdered form (and is a known carcinogen). Most animal studies using EB as a marker for BBB integrity use a dose of 2ml/kg of 2% (2 g EB in 100 ml saline) EB. The powder dissolves readily in saline and the solution is tolerated well by the animal.

*EB Staining Histology*

Prior to removing the brain for histological examination, many studies suggest perfusing the animal by removing the blood via a controlled infusion of physiologically buffered saline into the heart until a colorless liquid prevails. This procedure prevents the vascular EB from staining the brain during the removal process. If perfusion of the animal is not possible, an infusion of EB into one hemisphere (using other hemisphere as control) may suffice to control for EB staining in brain by vascularized EB at time of sacrifice. Evans Blue staining of the brain is typically graded on a scale of 0-3 or 4 where 0 is no staining visible to the naked eye, and 3 or 4 is a deep blue staining.

2.4 Hyperosmotic Disruption of the BBB

Transport of certain molecules across the BBB is accomplished by transcellular diffusion (of lipophilic substances) and several transport mechanisms are shown in Figure 2-7.

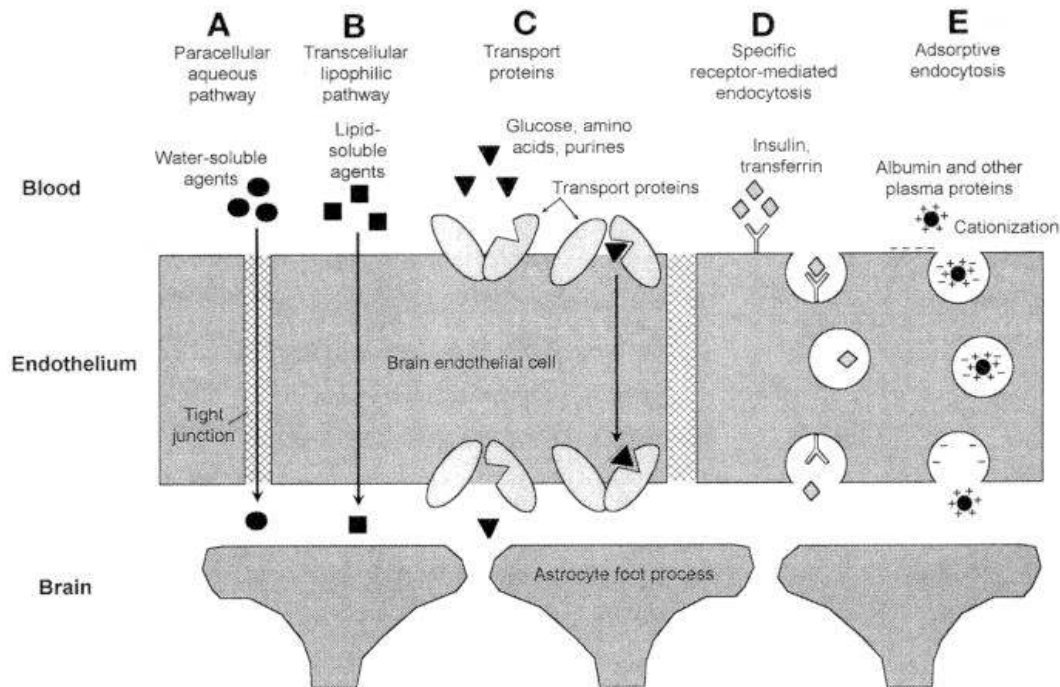


Figure 2-7: Various transport routes across the BBB. Taken from Ref. (23).



The most important factors that determine delivery of a substance from the blood into the brain are lipid solubility (expressed as the octanol/water partition coefficient), molecular mass, and charge (23). Certain substances – such as chemotherapeutic drugs – do not have the necessary characteristics for transport across the BBB. Therefore, another means of transport across the BBB is needed for efficacious delivery of drugs from the blood into the brain (and into brain tumors). As early as 1945, it was recognized that high osmolar solutions destroyed the cerebrovascular membranes (7). In 1961, Dodge *et al.* (24) reported an increase in staining of the brain by Trypan Blue after hyperosmotic infusions of NaCl, sucrose and urea into rat brain. In the early 1970s, Thompson and Rapoport suggested that the infusion of hyperosmotic solutions into brain resulted in dehydration of cerebral endothelial cells with resultant widening of tight junctions. Solutes not normally able to cross an intact BBB, such as the Evans Blue-albumin complex, were shown to penetrate the BBB for a limited time after hyperosmotic infusions into cerebral vasculature (8,25). For delivery of clinically useful drugs across the BBB, the disruption of the BBB by osmotic means must be a controlled transient event. Infusion of hyperosmolar solutions into the intracarotid artery is the most studied and proven method for a transient (or reversible) opening of the BBB (23). Hyperosmolar solutions available for use as a BBB disruption agent are mannitol, arabinose, urea, sucrose, and lactamide to name a few. For purposes of this dissertation, only the sugars mannitol and arabinose will be discussed further.

#### 2.4.1 Characteristics of Reversible Osmotic BBB Disruption

The action of shrinking endothelial cells using hyperosmotic solutions is consistent with what is known about osmotic shrinkage in cells in general. Consider first the definition of osmolality and solution osmotic pressure. The molality ( $m$ ) of a solution is moles of solute per kg of solvent. Osmolality is defined by:

$$\text{osmolality} = \sum_{k=1}^v \Phi_k m_k = \sum_{k=1}^v m'_k \quad 2.1$$

where  $k$  corresponds to a solute species (ion or non-electrolyte) and  $\Phi_k$  is the molal osmotic coefficient of that species (8). If  $k$  is an electrolyte,  $k = 1$  to  $v$  where  $v$  is the number of moles of ions formed from 1 mole of an electrolyte. If  $k$  is not an electrolyte, then  $v = 1$ . Solution osmotic pressure,  $\Pi$ , is defined as:

$$\Pi = RT \sum_m m'_k \quad 2.2$$

where R is the gas constant and T is absolute temperature (in Kelvins) (8).  $\Phi$  can be calculated from molal freezing-point depressions using the following equation:

$$\Phi = \frac{\text{molal freezing point depression, } ^\circ\text{C}}{1.858 ^\circ\text{C}} \quad 2.3$$

The final volume of a cell after osmotic shrinkage can be quantified as:

$$V_{final} = V_{initial} \left( \frac{(\sigma\Pi)_{initial}}{(\sigma\Pi)_{final}} \right) \quad 2.4$$

where  $\sigma$  is defined as:

$$\sigma = \frac{RT \sum_k \sigma_k m'_k}{\Pi} \quad 2.5$$

If the BBB is indeed opened by cell shrinkage, then certain conditions are expected to apply:

1) *Opening of the BBB should be a reversible event.* Indeed, as shown by Cosolo *et al.* (20), the BBB is permeable to Evans Blue tracer only up to ten minutes after BBB disruption by hyperosmolar mannitol. After ten minutes, it is likely that the endothelial cells begin to return to their normal size after shrinkage (thus reestablishing the tight junction contacts). This is in agreement with Eq. 2.4, which suggests that cell volume should return to normal if the cell environment returns to its original tonicity.

2) *The osmotic agent should not act on the endothelial cells as a drug.* As Eq. 2.4 indicates, osmotic pressure and cell shrinkage depend only on the concentration of solute and not on any drug action of the solute.

3) *With increasing molality BBB opening should increase.* Experiments by Rapoport *et al.* (16) (see also Table 2-1) showed that BBB opening occurred only when the sugar infusate (arabinose or mannitol) was made at a specific concentration (threshold concentrations for BBB opening used in Rapoport's experiments were reported in terms of molarity (M)).

4) *The osmotic threshold for BBB opening should be inversely related to endothelial cell membrane permeability.* The endothelial-cell membrane permeability increases with increasing lipid solubility of the solute. Therefore, for highly lipid-soluble solutes, the osmotic threshold for BBB disruption is low. Figure 2-8 shows the correlation between lipid solubility (expressed as the octanol/water partition coefficient) and BBB permeability.

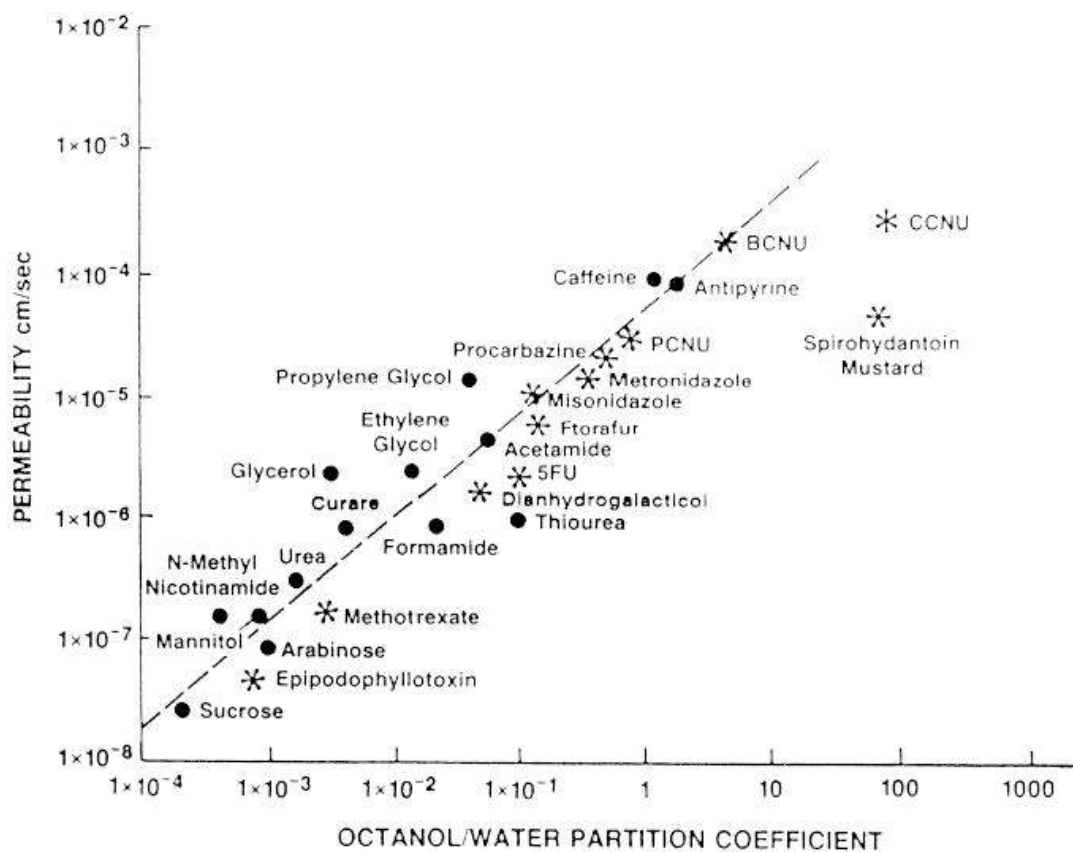


Figure 2-8: Correlation between lipid solubility and BBB permeability. From Ref. (23).

## 2.4.2 Mannitol and Arabinose as Hyperosmolar Infusates for BBB Disruption

### *Mannitol*

Mannitol is a sugar whose chemical name and empirical chemical formula are hexan-1,2,3,4,5,6-hexol and  $C_6H_8(OH)_6$ , respectively. The chemical structure of mannitol is shown in Figure 2-9. The solubility of mannitol in water is 1g mannitol to 5.5 ml water (1g/5.5ml).

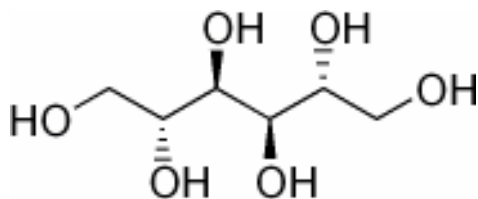


Figure 2-9: Chemical structure of the sugar mannitol.

### *Arabinose*

Arabinose is a monosaccharide. In nature, L-arabinose is found more commonly than D-arabinose. The empirical chemical formula for L-arabinose is  $C_5H_{10}O_5$ . The chemical structure of arabinose is shown in Figure 2-10. The solubility of arabinose in water is 1g arabinose to 1ml water (1g/1ml) and is 5.5 times more soluble than mannitol.

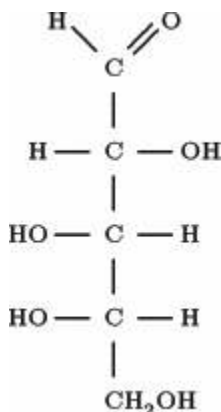


Figure 2-10: Chemical structure of L-arabinose.

### *Arabinose vs. Mannitol for Successful BBB Disruption*

Arabinose and mannitol have a rich history in experimental disruption of the BBB. Arabinose is not approved for clinical use, therefore, only mannitol is used in clinical BBB disruption protocols. In 1980, Rapoport *et al.* performed experiments to quantify the reversible opening of the BBB by infusing concentrated solutions of arabinose and mannitol into the carotid artery of rats (16). The dose and rate of infusion for each sugar was held constant at 0.12 ml/second while the concentration for each sugar was varied from 1.0 to 1.8 molal. No difference in BBB disruption (as verified by the Evans Blue staining technique) grade was noted between the two sugars.

Results from Rapoport's experiments have been reproduced and shown in Figure 2-11. For additional experiments to determine optimal concentration and infusion duration for the hyperosmotic solution, arabinose was used due to its lower solubility. Rapoport *et al.* reported that a concentration of 1.6 molal arabinose results in significant BBB disruption as compared to control (saline infusion) when infused at 0.12ml/sec for at least 30 seconds. A 20-second infusion resulted in less distinct BBB disruption and a 10-second infusion resulted in little or no BBB disruption as compared to control. Based on studies of Rapoport *et al.* in animal models, there is clearly an optimal concentration and infusion time required for effective BBB disruption.

Grade of Staining				Grade of Staining			
1+Solution		2+		1+Solution		2+	
# Of Animals				# Of Animals			
30s infusion of 0.9% Saline		15		30s infusion of 0.9% Saline		15	
Arabinose, molal				Arabinose, molal			
0	1	0	0	0	1	0	0
0	1	2	0	0	1	2	0
9	1	4	0	9	1	4	0
20	1	6	40	20	1	6	40
4	1	8	18(1)	4	1	8	18(1)
Mannitol, molal				Mannitol, molal			
0	1	0	0	0	1	0	0
1	1	2	0	1	1	2	0
5	1	4	1	5	1	4	1
13	1	6	23	13	1	6	23
4	1	8	13	4	1	8	13

Figure 2-11: Results from BBB disruption experiments by Rapoport *et al.* (16) Solutions of saline, arabinose, or mannitol were infused for 30 seconds into the right external carotid artery. Staining of the brain was determined 15 min to 2 h after infusion. Grade of staining is as follows: 0 = no staining, 3+ = deep blue stain. For the experimental protocol of Rapoport *et al.*, a 1.6 molal solution of either arabinose or mannitol was needed for reliable disruption of the BBB. Numbers in parentheses indicate the number of animals in which the infusate was not seen to pass into the internal carotid artery (i.e., infusate was likely infused towards the heart). NOTE: At 1.8 molal, mannitol is supersaturated and precipitates out at 37° C, possibly resulting in microinfarcts in brain after infusion.

In a separate study using only mannitol as the hyperosmolar solute, Cosolo *et al.* (20) determined the best dose and rate of infusion of 1.4 molar (mol/liter) mannitol to be 0.25 ml s<sup>-1</sup> kg<sup>-1</sup>. Furthermore, in the study of Cosolo *et al.*, EB did not stain the brain when infused 10 minutes after mannitol infusion. The degree of Evans Blue staining in the brain was maximal only when EB was

infused up to five minutes after mannitol infusion. Figure 2-12 represents data of Cosolo *et al.* which clearly suggests a transient opening of the BBB after mannitol infusion.

Taken together, the results of Rapoport *et al.* and Cosolo *et al.* suggest that optimal disruption of the BBB requires careful control over the concentrations, dose, and rate of infusion of the osmotic solutions. Furthermore, cerebral infusion of hyperosmotic solutions requires that the infusate is filtered with high-quality syringe filters in order to avoid the injection of microemboli. Additionally, if 1.4 M (25%) mannitol is used, the solution must be warmed to 37° C before infusion to prevent precipitation of infusate within the tubing prior to entry into the animal's blood stream.



Figure 2-12: Results from BBB disruption experiments by Cosolo *et al.* (20). Mannitol was infused at  $0.25 \text{ ml s}^{-1} \text{ kg}^{-1}$  for 30s. Evans Blue staining (measured on scale 0-4) of ipsilateral hemisphere occurred only when the dye was injected before mannitol or < 10min after mannitol administration.

#### *Other Factors Influencing Osmotic BBB Disruption*

In addition to the above requirements for the osmotic agents, the anesthetic type partial pressure of carbon dioxide ( $\text{PaCO}_2$ ) during animal experiments have been shown to be factors in the degree of BBB disruption achieved using hyperosmolar infusions (26). Figure 2-13 shows results from Remsen *et al.* indicating a clear dependence of anesthesia and  $\text{PaCO}_2$  on the degree of BBB disruption. These studies noted a significant difference in blood pressure between animal groups anesthetized with propofol and those anesthetized with isoflurane. These results were consistent with those of Gumerlock *et al.* (21); who, in earlier studies, had linked cardiovascular parameters to the degree of BBB disruption. Gumerlock *et al.* showed that the use of a volatile anesthetic

(methoxyflurane) resulted in poor BBB disruption using 1.4 M mannitol administered at 0.12 ml/s for 35 seconds. However, after the blood pressure was normalized (to levels achieved using pentobarbital) by pharmacological manipulation, good BBB opening was achieved with the methoxyflurane anesthetic. The investigators concluded that “Osmotic BBB [disruption] is maximized within specific cardiovascular parameters and probably correlates best with a normal cardiac output/index” (21).

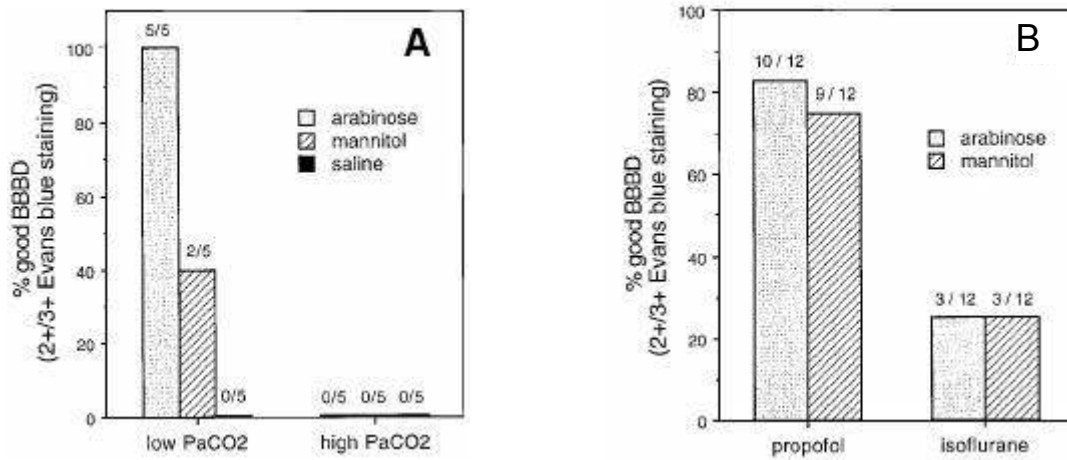


Figure 2-13: From Remsen *et al.* (26). (A) Percent good BBB disruptions by Evans Blue staining (2-3+) after infusion of arabinose, mannitol or saline at 0.12 ml/s for 30 seconds in low (25-30 mm Hg) and high (45-50 mm Hg) PaCO<sub>2</sub> animals. (B) Percent good BBB disruptions by Evans Blue staining in animals infused with arabinose or mannitol at 0.09 ml/s under propofol and 0.12 ml/s under isoflurane anesthesia.

While these findings may be true, there was no examination of the possible effects on the endothelial membrane by the anesthetics. For example, isoflurane (a volatile anesthetic similar to methoxyflurane) is a lipophilic agent and decreases cerebral metabolism. Therefore, the lipophilicity of the anesthetic may change the characteristics of endothelial cells in the cerebral vessel; the surface area of perfused capillaries in the brain, or both. Chi *et al.* (27) investigated these claims and found a decrease in the transport of small hydrophilic molecules across the BBB during isoflurane anesthesia. Chi *et al.* suggested that the apparently limited BBB permeability due to the presence of

hydrophilic molecules was related to the effect of isoflurane on the perfused-capillary-surface-area product; but, may also be due to the effect of isoflurane on the lipid bilayers of endothelial cells. In any case, the literature suggests that isoflurane protects the BBB from disruption to some degree.

#### *Brain Changes Associated with Osmotic BBB Disruption*

Osmotic disruption of the BBB is not without consequence. Several groups have investigated the aftermath of osmotic BBB disruption in animals and have found changes in the brain. These include ischemic neuronal death (28), collapsed, acidophilic neurons with macrophage response (29), and pronounced watery swelling of astrocytic processes and expansion of dendrites and axons (30). Additionally, several labs have show changes in brain structure after osmotic disruption, including results from the WPI NMR laboratory (to be presented later). Therefore, for experiments relying on delivery of substances across the BBB for later use by brain cells, osmotic BBB disruption, if used, must be accompanied by evidence of the brain-cell health/status at some appropriate time point following infusion of hyperosmotic perfusate.

## 2.5 The BBB and Cerebral Edema

Edema in the brain is defined formally as *abnormal accumulation of fluid within the brain parenchyma, producing a volumetric enlargement of tissue* (31). This is not to be confused with brain swelling which can occur as a result of increased cerebral blood volume (CBV), cerebral spinal fluid (CSF) volume, or a combination of increased water content, CBV and CSF volume (32). Several different types of cerebral edema are known to exist: vasogenic, ischemic, osmotic, interstitial, and cytotoxic. Cerebral edema and the BBB are linked because in some cases; the former causing the latter and vice versa. Figure 2-14 shows characteristics of various brain edema types (from (33)). Of particular interest for the current dissertation is vasogenic edema.

#### *Vasogenic Edema*

Vasogenic edema is swelling that results from damage to cerebral vessels, regardless of the origin of insult. Trauma, cerebrovascular insults, and brain disorders which result in increased BBB permeability, and associated entry of serum proteins into brain parenchyma, are essential elements of vasogenic brain edema (31). Therefore, damaged endothelial-cell membranes of the BBB are one obvious mechanism for extravasation of extraneous fluid from blood into brain, but may be only part



of a larger process. Permeability of the BBB can be affected by several other mechanisms, such as enhanced vesicular transport, creation of transcellular channels, opening of the tight junctions, and hypertension; each of which can lead to vasogenic edema. In addition, certain chemicals such as bradykinin, serotonin, histamine, arachnidonic acid, leukotrienes, and free radicals can affect BBB permeability, resulting in vasogenic edema formation (34). The clinical implications of vasogenic brain edema are coma, cerebral herniation, and death.

	Vasogenic BE	Cytotoxic BE	Osmotic BE
Development	Increased permeability of capillary endothelial cells caused by tissue necrosis (BBB disruption)	1. Increased cell membrane Na <sup>+</sup> /K <sup>+</sup> permeability 2. Na <sup>+</sup> /K <sup>+</sup> -ATPase failure 3. Uptake of osmotically active solutes	Osmotic gradient (plasma → tissue)
Permeability	Increased	Unchanged	Unchanged
Edema fluid	Rich in protein	No proteins Rich in electrolytes	No proteins Rich in electrolytes (tissue hyper-osmolality) Low in electrolytes (serum hyposmolality)
Morphology	No cell swelling Increased interstitial space	Cell swelling Decreased interstitial space	Cell swelling

Figure 2-14: Characteristics of different traumatic brain edema types. From Ref. (33)

*Retention of Brain Water Essential for Vasogenic Edema*

Damage to cerebral endothelial cells may allow for the entry of proteins and water into brain, but this is not the primary cause of edema because water is known to move in and out of brain fairly easily. A study by Vorbrodt *et al.* (35) showed that proteins that have traversed the BBB can be taken up in pinocytotic vesicles of endothelial cell membranes and digested or transported back into the blood vessel lumen. However, excess volumes of water left behind are *retained*, resulting in the formation and persistence of vasogenic brain edema (31).

### *Brain Defense Against Vasogenic Edema*

The brain has mechanisms which can protect against excessive edema; first and foremost is the BBB, which serves to maintain brain homeostasis. The inter-endothelial tight junctions of cerebral capillaries have a high resistance to fluid flow (hydraulic conductivity) (36), as compared to peripheral capillaries, and thus do not support vesicular transport of proteins or fluid. Since the brain does not have a lymphatic system, the continuous capillary endothelium is essential in preventing fluid entry into brain. Any plasma protein that does enter brain, and is not metabolized by astrocytes, must make its way through brain parenchyma slowly until it reaches the CSF, which is recycled every 8 hours (36). The structure of the brain also provides protection from edema. Gray matter is a dense tangle of cellular structures and offers significant resistance to edema fluid flow. White matter, however, has a more orderly arrangement of cells and therefore is less resistant to the flow of edema fluids. In addition, the brain is resistant to distortion by increased hydrostatic pressure and to fluid flow under a hydrostatic pressure gradient (36).

### *Spread of Edema*

Although the structure of the gray matter (and to a lesser extent white matter) in the brain may prevent the flow of edema fluid, the resistance of tissue elements may eventually be overcome. The force at which edema spreads is characterized by the Starling equation applied to fluid flow from blood into tissue:

$$J_v(\text{flow}) = L_p [(P^{\text{plasma}} - P^{\text{tissue}}) - \sigma (\Pi^{\text{plasma}} - \Pi^{\text{tissue}})] \quad 2.6$$

where  $J_v$  is the flow of fluid across the cerebral vessel wall,  $L_p$  is the hydraulic conductivity of the endothelial membrane,  $P^{\text{plasma}}$  is the intravascular hydrostatic pressure influenced by the systemic blood pressure,  $P^{\text{tissue}}$  is the brain tissue hydrostatic pressure,  $\sigma$  is the osmotic reflection coefficient (where a value of 0 indicates high or total permeability of the BBB to the solute, and 1 indicates low or no permeability of the BBB to the solute),  $\Pi^{\text{plasma}}$  is the osmotic pressure in plasma, and  $\Pi^{\text{tissue}}$  is the osmotic pressure in the brain tissue. Substances of different molecular weights have been shown to flow at the same rate from the site of BBB injury, suggesting a bulk flow of edema fluid (37). The speed and extent of distribution of edema fluid throughout brain is determined by the size of the BBB injury, arterial blood pressure and pressure gradients between edematous tissue and the CSF (31,32). The spread of edema stops when the fluid flow across BBB-injured sites is matched by the

clearance of edema fluid; which is again dependent on the size of the BBB injury and the arterial blood pressure.

#### *Brain Response to Vasogenic Edema After Hyperosmotic BBB Disruption*

Edema formation is not common during the acute stage of hyperosmolar infusion, when brain shrinkage is most likely to occur. Studies have shown that during acute hypernatremia (hyperosmolarity), the loss of brain water was less than expected because the brain is capable of accumulating solute to stabilize its volume (38). However, disruption of the BBB by hyperosmotic means is always associated with some degree of brain edema (23). Therefore, it should be expected that some cellular response to acute decreases in brain water volume is present within endothelial cells, astrocytes, glia, microglia, neurons or all brain cells during and after hyperosmotic insults to cerebrovasculature. It is well known that cells exposed to hypertonic extracellular fluid shrink, reflecting the osmometer characteristics of the cell, but the cell tends to return to its original volume by so-called regulatory cell-volume increase (RVI) (39). Due to volume-regulatory ion transport, RVI is accomplished within minutes of a cells exposure to hypertonic solute (39). During vasogenic edema, glia are known to influence extracellular K and Cl composition as well as metabolize serum albumin that may have crossed an injured BBB (36). In addition, astrocytes (macroglia) initiate calcium ( $\text{Ca}^{2+}$ ) signaling in response to many stimuli, including extracellular hypoosmolarity. Therefore, if the BBB is to be disrupted using hyperosmolar infusions, careful attention to the type and dynamics of the brain response is required.

## 2.6 MRI Detection of BBB Disruption

With the use of an extracellular MR contrast agent, such as gadopentate dimeglumine (gadolinium diethylenetriaminepentaacetic acid or Gd-DTPA), that does not cross a normally intact BBB, pathologies of the BBB are more easily detectable in human or animal subjects. After i.v. infusion, pathological alteration of the BBB allows passage of Gd-DTPA into the brain extravascular extracellular space (EES (40)), where it collects and results in positive localized enhancement in a MR image. Gd-DTPA remains in the extracellular space for many minutes or hours; after which it diffuses back into the vasculature and is excreted by the kidneys (40). Use of i.v.-administered Gd-DTPA to enhance the contrast of MR images is sometimes referred to as dynamic contrast-enhanced magnetic resonance imaging or DCE-MRI. Gd-DTPA can also be used to detect areas of BBB

detection as a binary event, i.e., to detect if enhancement is seen or not. When the degree of BBB disruption is of interest, methods such as DCE-MRI can be used to provide additional information regarding the response of tissue pathologies (as they relate to BBB disruption) to therapy (41).

### 2.6.1 Gd-DTPA Used to Detect Regions of Pathological BBB Disruption

Gd-DTPA-enhanced MRI allows detection of BBB disrupted regions in the brain. Therefore, MRI can detect BBB disruption resulting for a number of different pathologies such as multiple sclerosis (MS), brain tumor, and stroke.

#### *Multiple Sclerosis*

MS is recognized by inflammatory demyelinated lesions in brain white matter. Demyelinated, but less inflammatory lesions, are also observed in the cortex and normal appearing white matter (NAWM) of the brain (40). Figure 2-15 shows a MS lesion in the brain using two different MR techniques; Gd-DTPA enhancement and  $T_2$ -weighting. Note the difference in the shape of the lesion between the two images. The Gd-DTPA image indicates BBB damage in the area shown. Gd-DTPA-enhancing MS lesions microscopically show perivascular inflammation with demyelination and some myelin breakdown, while non-enhancing MS lesions show little inflammation and near complete loss of myelin (42).

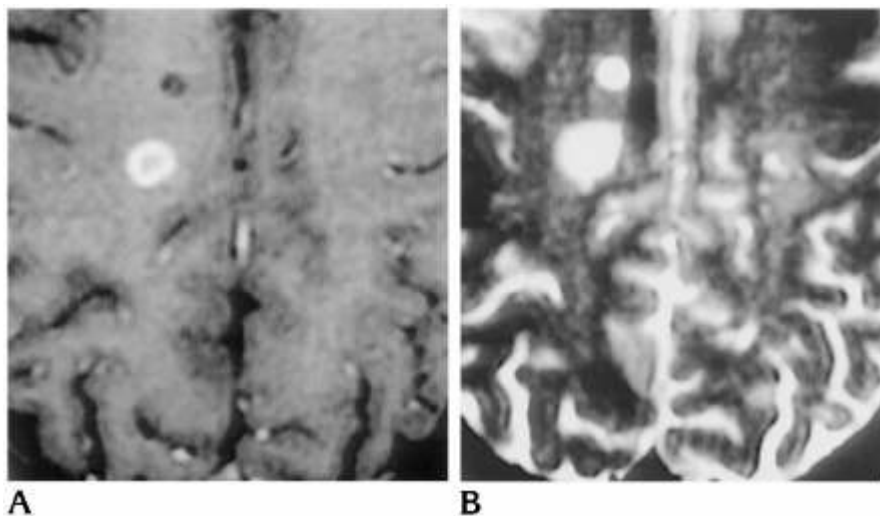


Figure 2-15: A) Example of a ring-enhancing lesion on a contrast-enhanced  $T_1$ -weighted MR image. B) The same lesion as seen on a  $T_2$ -weighted image. From Ref. (43).

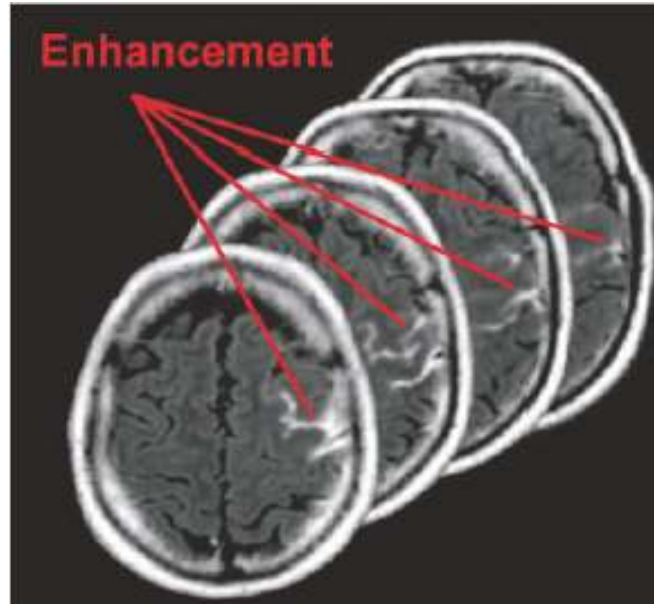


Figure 2-16: Magnetic resonance images exhibiting evidence of early BBB disruption. Hyperintense signal in the patient's left central and precentral sulci is caused by extravasation of Gd-DTPA contrast agent into the cerebral spinal fluid. Note that enhancement resides primarily in the sulci; the adjacent parenchyma is unexceptional. From Ref. (44).

### *Stroke*

The integrity of the BBB is compromised as a result of a reduction or loss of blood flow to brain. In clinical situations, reperusing occluded arteries is the most effective treatment for acute stroke (44,45). Reperfusion injury is possible, however, and may lead to exacerbated BBB and neuronal damage. Latour *et al.* showed that early detection of BBB damage by Gd-DTPA-enhanced MRI may be a useful target for adjunctive therapy to reduce the negative side-effects of occluded artery reperfusion, thus improving the clinical outcome of stroke. Results from Latour *et al.* are shown in Figure 2-16.

## REFERENCES

1. Davson H., Welch K., Segal M. *The Physiology and Pathophysiology of the Cerebrospinal Fluid*: Churchill Livingstone; 1987.
2. Crone C. Facilitated transfer of glucose from blood to brain tissue. *J Physiology (Lond)* 1965;181:103-113.

3. Reese T.S., Karnovsky M.J. Fine structural localization of a blood-brain barrier to exogenous peroxidase. *J Cell Biol* 1967;34:207-217.
4. Rapoport Stanley I. Blood-Brain Barrier in Physiology and Medicine. Press Raven, editor. New York: Raven Press; 1976.
5. Crone C. The permeability of capillaries in various organs as determined by use of the indicator diffusion method. *Acta Physiol Scand* 1963;58:292-305.
6. Ohno K., Pettigrew K.D., Rapoport S.I. Lower limits of cerebrovascular permeability to nonelectrolytes in the conscious rat. *Am J Physiol* 1978;235:H299-H307.
7. Broman T., Lindberg-Broman A.M. An experimental study of disorders in the permeability of the cerebral vessels ("the blood-brain barrier") produced by chemical and physico-chemical agents. *Acta Physiol Scand* 1945;10:102-125.
8. Rapoport S.I., Hori M., Klatzo I. Testing of a hypothesis for osmotic opening of the blood-brain barrier. *Am J Physiol* 1972;223:323-331.
9. Neuwelt E.A. Implications of the Blood-Brain Barrier and Its Manipulation. New York: Plenum Publishing; 1989. 633 p.
10. Goldmann E.E. Vitalfärbung am Zentralnervensystem. *Abh Preuss Akad Wiss Phys-Math* 1913;1:1-60.
11. Bradbury M.W. The blood-brain barrier: transport across the cerebral endothelium. *Circ Res* 1985;57:213-222.
12. Claude P., Goodenough D.A. Fractured faces of zonulae occludentes from "tight" and "leaky" epithelia. *J Cell Biol* 1973;58:390-400.
13. Clough G., Michel C.C. The role of vesicles in the transport of ferritin through frog endothelium. *J Physiology (Lond)* 1981;315:127-142.
14. Takasato Y., Rapoport S.I., Smith Q.R. An in situ brain perfusion technique to study cerebrovascular port in the rat. *Am J Physiol* 1984;247:H484-H493.
15. Ohno K., Fredericks W.R., Rapoport S.I. Osmotic Opening of the Blood-Brain Barrier to Methotrexate in the Rat. *Surg Neurol* 1979;12:323-328.
16. Rapoport S.I., Fredericks W.R., Ohno K., Pettigrew K.D. Quantitative aspects of reversible osmotic opening of the blood-brain barrier. *Am J Physiol* 1980;238:R421-R431.
17. Ziylan Y.Z., Robinson P.J., Rapoport S.I. Differential Blood-Brain Barrier Permeabilities to [<sup>14</sup>C]Sucrose and [<sup>3</sup>H]Inulin after Osmotic Opening in the Rat. *Experimental Neurology* 1983;79:845-857.
18. Ziylan Y.Z., Robinson P.J., Rapoport S.I. Blood-brain barrier permeability to sucrose and dextran after osmotic opening. *Am J Physiol* 1984;R634-R638.
19. Farrell C.L., Shivers R.R. Capillary Junctions of the Rat Are Not Affected by Osmotic Opening of the Blood-Brain Barrier. *Acta Neuropathol (Berl)* 1984;63:179-189.
20. Cosolo W.C., Martinello P., Louis W.J., N. Christophidis. Blood-brain barrier disruption using mannitol: time course and electron microscopy studies. *Am J Physiol* 1989;R443-R448.
21. Gumerlock M.K., Neuwelt E.A. The Effects of Anesthesia on Osmotic Blood-Brain Barrier Disruption. *Neurosurgery* 1990;26:268-277.
22. Wolman M., Klatzo I., Chui E., Wilmes F., Nishimoto K., Fujiwara K., Spatz M. Evaluation of the Dye-Protein Tracers in Pathophysiology of the Blood-Brain Barrier. *Acta Neuropathol (Berl)* 1981;54:55-61.
23. Kroll R.N., Neuwelt E.A. Outwitting the Blood-Brain Barrier for Therapeutic Purposes: Osmotic Opening and Other Means. *Neurosurgery* 1998;42:1083-1100.

24. Dodge P., Sotas J.F., Karlsson B. Influence of hypertonicity of the body fluids on the BBB. *Trans Amer neurol Ass* 1961;86:12-16.
25. Thompson A.M. Hyperosmotic effects on brain uptake of non-electrolytes. Lassen C.C Crone and N., editor. Munksgaard, Copenhagen; 1970. 459-467 p.
26. Remsen L.G., Pagel M.A., McCormick C.I., Fiamengo S.A., Sexton G., Neuwelt E.A. The Influence of Anesthetic Choice,  $P_aCO_2$ , and Other Factors on Osmotic Blood-Brain Barrier Disruption in Rats with Brain Tumor Xenografts. *Anesth Analg* 1999;88:559-567.
27. Chi O.Z. Effects of Isoflurane on Transport across the Blood-Brain Barrier. *Anesthesiology* 1992;76:426-431.
28. Suzuki M., Iwasaki Y., Yamamoto T., Konno H., Kudo H. Sequelae of the osmotic blood-brain barrier opening in rats. *J Neurosurg* 1988;69:421-428.
29. Salahuddin T.S., Johansson B.B., Kalimo H., Olsson Y. Structural Changes in the Rat Brain After Carotid Infusions of Hyperosmolar Solutions: A Light Microscopic and Immunohistochemical Study. *Neuropathol Appl Neurobiol* 1988;14:467-482.
30. Salahuddin T.S., Johansson B.B., Kalimo H., Olsson Y. Structural changes in the rat brain after carotid infusions of hyperosmolar solutions. *Acta Neuropathol* 1988;77:5-13.
31. Klatzo I. Pathophysiological aspects of brain edema. *Acta Neuropathol (Berl)* 1987;72:236-239.
32. Neuwelt E.A. Implications of the Blood-Brain Barrier and Its Manipulation. New York: Plenum Publishing; 1989.
33. Unterberg A.W., Stover J., Kress B., Kiening K.L. Edema and Brain Trauma. *Neurosci* 2004;129:1021-1029.
34. Wahl M., Unterberg A., Baethmann A., Schilling L. Mediators of Blood-Brain Barrier Dysfunction and Formation of Vasogenic Brain Edema. *JCBFM* 1988;8:621-634.
35. Vorbrodtt A.V., Lossinsky A.S., Wisniewski H.M., Suzuki R., Yamaguchi T., Masaoka H., Klatzo I. Ultrastructural observations on the transvascular route of protein removal in vasogenic brain edema. *Acta Neuropathol (Berl)* 1985;66:265-273.
36. Rapoport S.I. Brain edema and the blood-brain barrier. In: KMA Welch LR Caplan, DJ Reis, BK Siesjo, B Weir, editor. *Primer on cerebrovascular diseases*. London: Academic Press; 1997.
37. Reulen H.J., Graham R., Spatz M. et al. Role of pressure gradients and bulk flow in dynamics of vasogenic edema. *J Neurosurg* 1977;46:24-35.
38. Gullans S.R. Control of Brain Volume During Hyperosmolar and Hypoosmolar Conditions. *Annu Rev Med* 1993;44:289-301.
39. Lang F., Busch G.L., Ritter M., Volki H., Waldegger S., Gulbins E. Functional Significance of Cell Volume Regulatory Mechanisms. *Phys Rev* 1998;78:247-306.
40. Tofts P. *Quantitative MRI of the Brain*. Chichester: John Wiley and Sons Ltd; 2004.
41. Tofts P.S., Kermode A.G. Measurement of the Blood-Brain Barrier Permeability and Leakage Space Using Dynamic MR Imaging. 1. Fundamental Concepts. *Magn Reson Med* 1991;17:357-367.
42. Katz D. , Taubenberger J.K., Cannella B., McFarlin D.E., Raine C.S., McFarland H.F. Correlation between magnetic resonance imaging findings and lesion development in chronic, active multiple sclerosis. *Ann Neurol* 1993;34:661-669.
43. Petrella J.R., Grossman R.I., McGowan J.C., Campbell G., Cohen J.A. Multiple Sclerosis Lesions: Relationship between MR Enhancement Pattern and Magnetization Transfer Effect. *Am J Neuroradiol* 1996;17:1041-1049.

44. Latour L.L., Kang D-W., Ezzeddine M.A., Chalela J.A., Warach S. Early Blood-Brain Barrier Disruption in Human Focal Brain Ischemia. *Ann Neurol* 2004;56:468-477.
45. Brott T., Bogousslavsky J. Treatment of acute ischemic stroke. *New Engl J Med* 2000;343:710-722.



# CHAPTER 3

## Theory and Application of Manganese-Enhanced Magnetic Resonance Imaging (MEMRI)

Introduction to MEMRI

Magnetic Resonance Contrast Agent Physics

Effect of Contrast Agents MR Parameters

Relaxation Effects of Paramagnetic Ion Metal Complexes

Manganese ( $Mn^{2+}$ ) as Calcium Analog

Neurotransmission in Brain: The Role of Calcium Channels

M Passage into Cells via Voltage-Gated Calcium Channels

Manganese Toxicity and Cellular Effects of Manganese

$Mn^{2+}$  *In Vivo* After Intravenous (I.V.) Infusion

$Mn^{2+}$  Transport Across the Blood-Brain Barrier (BBB)

$Mn^{2+}$  as MR Contrast Agent –  $Mn^{2+}$ -Enhanced Magnetic Resonance  
Imaging (MEMRI)

MEMRI with Mn-DPDP

MEMRI with  $MnCl_2$

A Review of Experiments in Brain Imaging with  $MnCl_2$

## Introduction

Manganese-enhanced magnetic resonance imaging (MEMRI) is a relatively new MR technique for functional and anatomical MR imaging based on unique physiological response mechanisms to divalent manganese ( $Mn^{2+}$ ). Lin and Koretsky first used MEMRI for functional brain imaging. Following infusion of  $MnCl_2$  into the brain extracellular space, regions of the rat brain that responded to electrical forepaw stimulation could be visualized using MEMRI (1). Following Lin and Koretsky's work, a number of MEMRI studies of functional brain imaging were published. For example, MEMRI was used to trace odor-induced activation in the olfactory bulb of mice (2); for *in vivo* trans-synaptic tract tracing in murine striatum (3); for *in vivo* characterization of neuroarchitecture in rat brain (4); and for visualization of cortical spreading depression (CSD) in rat brain (5).

One of the characteristics that makes  $Mn^{2+}$  a unique MR contrast agent for visualizing brain function is its ability to enter cells through voltage-gated calcium channels (6). Manganese competes with calcium for cellular entry, is retained in cells for substantially longer time periods than calcium, and supports exocytosis (6,7). Once inside the cell, the paramagnetic properties of  $Mn^{2+}$  change the MR relaxation times of water protons in the cell; resulting in localized signal increases in  $T_1$ -weighted MR images in regions of  $Mn^{2+}$  uptake (1). The ability of MEMRI to image brain function is limited by  $MnCl_2$  toxicity *in vivo*, heterogeneous distribution of  $Mn^{2+}$  in the brain extracellular space, and non-specific brain activation by environmental stimuli. This chapter reviews some of the concepts needed to understand the use of MEMRI for the applications presented in this dissertation. These include MR-contrast-agent physics,  $Mn^{2+}$  in biological systems, and  $Mn^{2+}$  as a MR contrast agent.

### 3.1 Magnetic Resonance Contrast Agent Physics

The selection of an appropriate MR contrast agent depends on several important factors such as the tissue of interest, the type of contrast desired (i.e., positive or negative enhancement), and the experimental setting (i.e., clinical or animal research). In the design of MR contrast agents, several characteristics must be considered to effectively enhance the MR signal *in vivo* and to prevent

adverse side effects to the animal or patient receiving the MR contrast-agent injection. An extensive list (although not exhaustive) is provided here (8):

1) Effects of the contrast agent on the MR signal should depend on the concentration of the agent and should be reproducible from experiment to experiment.

2) The contrast agent should be a strong MR relaxation agent so low doses can be administered with efficacy.

3) In vivo reactivity of the contrast agent is low or non-existent and the contrast agent is non-toxic.

4) The contrast agent should have a reasonably long shelf-life.

5) The contrast agent is quickly (i.e., within hours) excreted and/or deactivated. In the case of animal studies, such as those performed in this dissertation, a number of non-clinical MR contrast agents (e.g., manganese chloride or  $\text{MnCl}_2$ ) are also available. Although the toxicity of  $\text{MnCl}_2$  precludes its use in humans, the compound has been used extensively at sub-lethal doses in animal models. This review will focus on  $\text{Mn}^{2+}$  (usually administered as  $\text{MnCl}_2$ ) as an MR contrast agent but will also discuss the use of gadolinium-based MR contrast agents in both experimental and clinical practice. Differences in contrast mechanisms between the two MR contrast agents will be noted where appropriate throughout the text.

### 3.1.1 Effect of Contrast Agents on MR Parameters

As discussed in Chapter 1, the  $T_1$  and  $T_2$  relaxation times are main MR parameters used to control MR image contrast (although proton density is also important, it is unaffected by MR contrast agents). For positive enhancement in an MR image (i.e., high signal-intensity regions in an image as compared to background tissue), the  $T_1$  relaxation time of a particular tissue must be shortened (while leaving  $T_2$  relatively unaffected). Negative contrast enhancement in an MR image (i.e., dark regions as compared to the surrounding tissue) is generally accomplished by shortening the  $T_2$  or  $T_2^*$  relaxation times of the tissue of interest (while leaving  $T_1$  unaltered). The  $T_2^*$ , or magnetic susceptibility agents, are also sensitive to molecular translation and can result in significant MR signal loss (again negative contrast) for molecules diffusing in the vicinity of the agents. The discussion in this chapter will focus on manganese ( $\text{Mn}^{2+}$ ) as a paramagnetic MR contrast agent that primarily affects  $T_1$ -weighted MRI contrast.

### 3.1.2 Relaxation Effects of Paramagnetic Ion Metal Complexes

Divalent manganese ( $\text{Mn}^{2+}$ ) ions possess five unpaired electrons and are therefore paramagnetic by nature. Each unpaired electron in the  $\text{Mn}^{2+}$  ion possesses an electron MDM (just as in the case of nuclei, electron spin pairing results in a net cancellation of the respective electron MDMs). The five unpaired electron MDMs then sum to form a net electron MDM for  $\text{Mn}^{2+}$ , which in turn co-adds with any external magnetic field that may be present (9). The presence of unpaired electrons in a paramagnetic ion is mandatory for the ability of the ion to affect the  $T_1$  and  $T_2$  relaxation times of nearby water protons (10). The relaxation rate of the paramagnetic ion is proportional to the spin quantum number  $S$  by  $S*(S+1)$  (10). Consequently, ions with the largest values of  $S$  have been exploited most often as MR contrast agents. For example,  $S=7/2$  for  $\text{Gd}^{3+}$  and  $S=5/2$  for  $\text{Fe}^{3+}$ ,  $\text{Dy}^{3+}$ , and  $\text{Mn}^{2+}$ . When a paramagnetic ion is introduced into a solvent (such as water), the longitudinal and transverse relaxation rates of the solvent nuclei,  $R_1$  ( $1/T_1$ ) and  $R_2$  ( $1/T_2$ ), respectively, increase. The magnetic fields associated with the paramagnetic center of the MR contrast agent then add to the observed relaxation rate of the solvent. This relationship is represented in Eq. 3.1:

$$\left(\frac{1}{T_{1,2}}\right)_{\text{observed}} = \left(\frac{1}{T_{1,2}}\right)_{\text{diamagnetic}} + \left(\frac{1}{T_{1,2}}\right)_{\text{paramagnetic}}, \quad 3.1$$

where the diamagnetic component of relaxation is that of the solvent in the absence of the paramagnetic metal ion. The paramagnetic component of  $(1/T_{1,2})_{\text{observed}}$  is dependent upon the random diffusional translation of the solvent and the paramagnetic complex as well as the chemical interactions that occur between the solvent and the metal ion. Since the strength of the local magnetic field associated with the paramagnetic center diminishes rapidly as a function of distance, the paramagnetic contribution to the solvent  $T_1$  relaxation time is not significant unless the solvent is in close proximity to the paramagnetic center. This generally requires a direct chemical interaction between the solvent and the paramagnetic complex. If this is not the case, then the paramagnetic effect will only be transmitted by diffusional interactions between the solvent and metal-ion complex; resulting in a much weaker effect. The chemical interactions that occur between solvent nuclei and the paramagnetic complex can be summarized by three distinct types: *primary*

*coordination sphere* interaction, *second coordination sphere* interaction, and *outer sphere relaxation* (9). These chemical interactions can be represented schematically as shown in Figure 3-1.

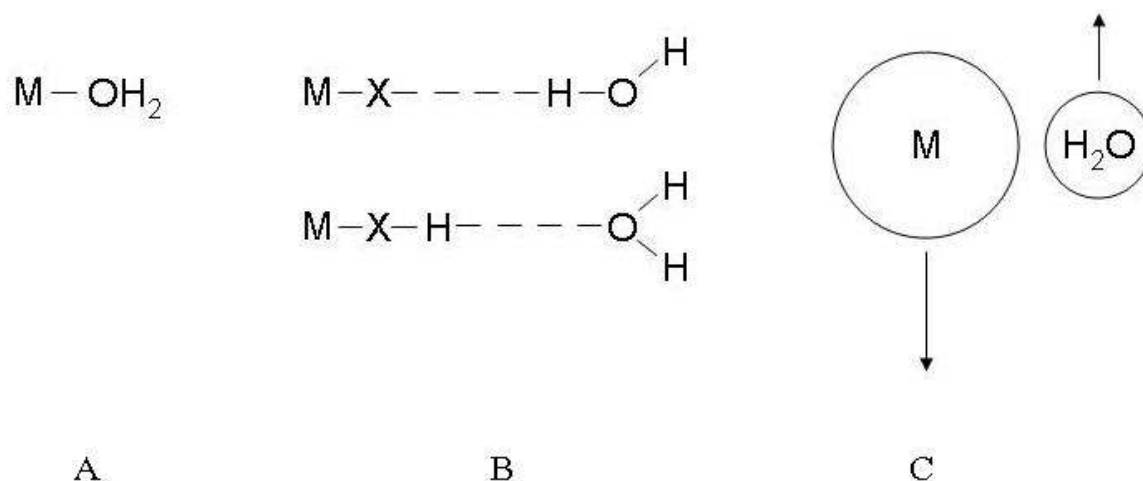


Figure 3-1: Chemical and non-chemical interactions between solvent molecules (in this case water) and a paramagnetic metal complex (M) that enhance the relaxation time of the solvent molecules. A) Solvent molecule primary coordination sphere; B) Solvent molecules binding indirectly (e.g., by hydrogen bonding) to the paramagnetic complex in its second coordination sphere; and C) translational diffusion of the solvent molecule in the *outer sphere* of the paramagnetic metal (or metal complex) with no direct or indirect chemical binding interaction between the two species. Reconstructed from Ref. (9).

Relaxation mechanisms by water-molecule binding to the primary and second coordination sphere of the metal ion are typically lumped into one relaxation effect referred to as “inner-sphere relaxation” (A and B of Figure 3-1). Relaxation mechanisms by translational diffusion of the water molecule past the metal ion is commonly referred to as “outer sphere relaxation” (10).

### *Inner-Sphere Relaxation*

In contrast agent design, it is important to consider the formation of a ‘coordinate covalent’ molecular bond between a water molecule and the primary coordination sphere of the paramagnetic ion. As the number of water molecules that are able to bind or interact with the paramagnetic ion increase, the relaxation effect also increases. Since water molecules are in rapid chemical exchange between the outer and inner spheres of the paramagnetic complex, the residence time – or the time each water molecule spends bound to the metal complex – is important. If the residence time is short, many water molecules in the vicinity of the paramagnetic complex have an opportunity to bind on the time scale of the MR experiment. A rapid exchange rate – on the order of one microsecond or

less – is desirable for a significant relaxation effect (10). The effect of inner-sphere relaxation on the longitudinal relaxation rate,  $R_1$  ( $1/T_1$ ) is given by Eq. 3.2 (9).

$$\left[ \frac{1}{T_1} \right] (\text{inner sphere}) = \frac{P_M q}{T_{1M} + \tau_M}, \quad 3.2$$

where  $P_M$  is the mole fraction of metal ion,  $q$  is the number of water molecules bound per metal ion,  $T_{1M}$  is the  $T_1$  relaxation time of the water protons bound to the metal, and  $\tau_M$  is the residence time of the bound water. Clearly, as the residence time of the bound water decreases, the relaxation rate ( $1/T_1$ ) increases. As the number of bound water molecules ( $q$ ) increases, the relaxation rate increases. Finally, as might be expected in the design of an MR contrast agent, an increase in the concentration of the MR contrast agent ( $P_M$ ) also increases the relaxation rate.

#### *Outer-Sphere Relaxation*

No direct bonding of chemical exchange is involved with outer-sphere relaxation effects of paramagnetic ions. The primary determinant of the outer-sphere relaxation properties of the paramagnetic ion is the rotational and translational diffusion properties of the ion. The faster a contrast agent can diffuse throughout solvent the greater the relaxation effect of the contrast agent because more water molecules are encountered and affected along its diffusional path. This is an important aspect of MR contrast-agent design because paramagnetic ions are typically chelated with a ligand, such as diethylenetriamenepentaaceticacid (DTPA), to minimize toxicity. In so doing, the rotational and translational diffusion rate of the chelated paramagnetic complex is reduced, resulting in a less efficient relaxation effect.

The outer-sphere relaxation effect is also dependent on how close water molecules can get to the magnetic dipole field at the center of the paramagnetic complex. If the attached chelates are too large, water molecules may only experience little or no effect from the paramagnetic ion dipole, resulting in low relaxation efficiency of the contrast agent (10). Indeed, the paramagnetic effect depends strongly on the distance between the metal ion and water proton, as shown in Eq. 3.3,

$$\text{paramagnetic effect} \propto \frac{1}{r^6}, \quad 3.3$$

where  $r$  is the mean distance between the paramagnetic center and the resonating water protons (11). The effect of outer-sphere relaxation on longitudinal relaxation is represented in general form by Eq. 3.4 and incorporates the effects of translational diffusion and electronic relaxation (9).

$$\left[ \frac{1}{T_1} \right]_{outer\ sphere} = \frac{C_\pi N_S \gamma_I^2 \gamma_S^2 \eta^2 S(S+1)}{d^3 \tau_D} [7I(\omega_S \tau_D T_{1e}) + 3I(\omega_I \tau_D T_{1e})] \quad 3.4$$

In Eq. 3.4,  $C$  is a numerical constant,  $N_S$  is the number of metal ions per cubic centimeter,  $d$  is the closest distance achieved between the metal complex and solvent molecule, and  $\tau_D$  is the translational diffusion time.  $\tau_D$  depends on the diffusion coefficients of the metal complex and water,  $D_S$  and  $D_I$ , respectively, as given by Eq. 3.5

$$\tau_D = \frac{d^2}{3(D_S + D_I)}. \quad 3.5$$

During the process of designing MR contrast agents, organic ligands are chemically bonded to the metal ion to form a metal chelate. Complexation ensures *in vivo* stability (minimizing the toxicity of the free metal) but also reduces the chemical exchange capability (and the inner-sphere relaxation effect) of the MR contrast agent. Therefore, enhancing the effects of outer-sphere relaxation is also an important consideration in the design of MR contrast agents.

### 3.2 Manganese as a Calcium (Ca) Analog

Divalent manganese ( $Mn^{2+}$ ) has an ionic radius similar to calcium ( $Ca^{2+}$ ) ( $0.92\text{\AA}$  for  $Mn^{2+}$  vs.  $1.14\text{\AA}$  for  $Ca^{2+}$ ) and is handled similarly to Ca by biological systems (6). The uptake of  $Mn^{2+}$  by active brain cells results in localized contrast enhancement in  $T_1$ -weighted MR images. This makes  $Mn^{2+}$  a useful brain anatomical and functional contrast agent. The mechanism of  $Mn^{2+}$  uptake by brain cells and the consequence regarding MR imaging and *in vivo* toxicity are discussed here.

### 3.2.1 Neurotransmission in Brain: The Role of Calcium Channels

The topic of neurotransmission in brain is vast and is not covered in detail in this section. However, a review of neuronal structure and function will serve as an appropriate foundation upon which the role of calcium channels in neurotransmission can be based.

#### *Brain Neuron Structure and Neurotransmission*

The neuron is unique in structure among mammalian cells. Three unique elements make up the neuron: the *axon*, specialized for intracellular information transfer; the *dendrite*, very often the site at which information is received from other neurons; and the *synapse*, which is the point of information transfer between neurons (12). Figure 3-5 is an artist's depiction of two adjacent neurons and one synapse between them. Communication between neurons is made possible by electrical impulses or action potentials along the axon and by chemical transmission of information – via neurotransmitters – across the synapse. Arrival of an action potential at the presynaptic terminal (signal-emitting neuron in Figure 3-2) initiates a sequence of events that leads to the release of neurotransmitters to the postsynaptic neuron (signal-receiving neuron in Figure 3-2). As part of this sequence, the opening of Ca channels causes a rapid influx of Ca into the presynaptic cleft, due to the steep concentration gradient of Ca across the cell membrane (external [Ca] ~ 1mM, internal [Ca] ~ 0.1 $\mu$ M) (13). In response to a transient rise in cytoplasmic calcium concentration, neurotransmitters are released from the presynaptic terminal to the postsynaptic terminal.



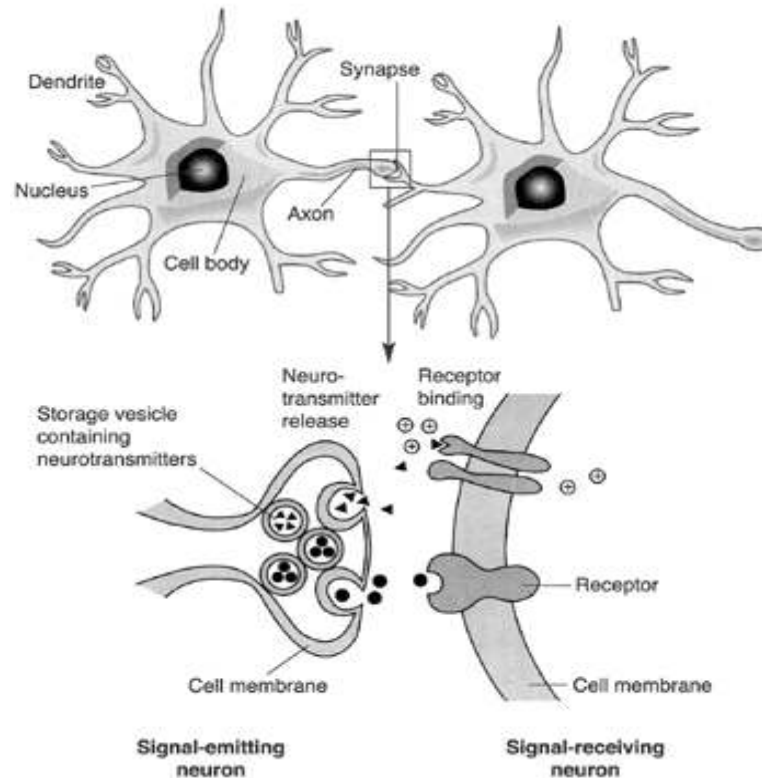


Figure 3-2: Two neurons separated by a synapse. From [www.niaaa.nih.gov/Resources/GraphicsGallery/Neuroscience/synapse.htm](http://www.niaaa.nih.gov/Resources/GraphicsGallery/Neuroscience/synapse.htm)

### 3.2.2 $Mn^{2+}$ Passage into Cells via Voltage-Gated Calcium Channels

Due to its similar ionic radius and charge,  $Mn^{2+}$  enters cells via voltage-gated calcium channels (VGCCs). Methods to show  $Mn^{2+}$  accumulation in cells through VGCCs have been performed by several groups using *in vitro* techniques. Drapeau *et al.* (6) used pinched-off presynaptic nerve endings (synaptosomes) isolated from rat brain to compare uptake of  $Ca^{2+}$  and  $Mn^{2+}$  after nerve stimulation. The time course of  $Mn^{2+}$  uptake was similar to that of  $Ca^{2+}$ , suggesting one mechanism for mediating cellular uptake of  $Ca^{2+}$  and  $Mn^{2+}$ . Figure 3-3 shows the  $Ca^{2+}$  and  $Mn^{2+}$  uptake time course from Drapeau *et al.* (6). To further support the hypothesis that  $Mn^{2+}$  enters cells through VGCCs, Drapeau *et al.* tested an organic calcium-channel antagonist (blocker), verapamil, for its effectiveness in preventing cellular uptake of  $Mn^{2+}$ . Results from these experiments are shown in Figure 3-4. Verapamil has also been used to inhibit uptake of  $Ca^{2+}$  and  $Mn^{2+}$  in frog motor nerve terminals. Narita *et al.* (14) showed a decline in the frequency of miniature end-plate

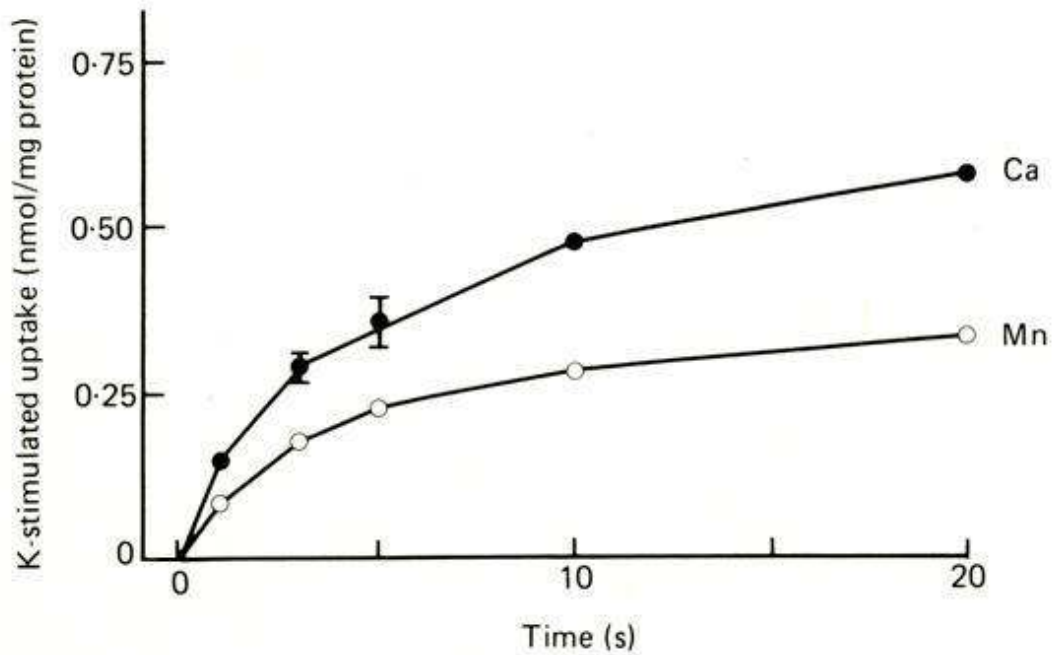


Figure 3-3: The time course of K-stimulated Ca<sup>2+</sup> or Mn<sup>2+</sup> uptake in striatal synaptosomes. The solutions with radiotracer Ca<sup>2+</sup> (filled circles) or Mn<sup>2+</sup> (open circles) contained 0.02mM of both these divalent cations. Reproduced from Ref. (6).

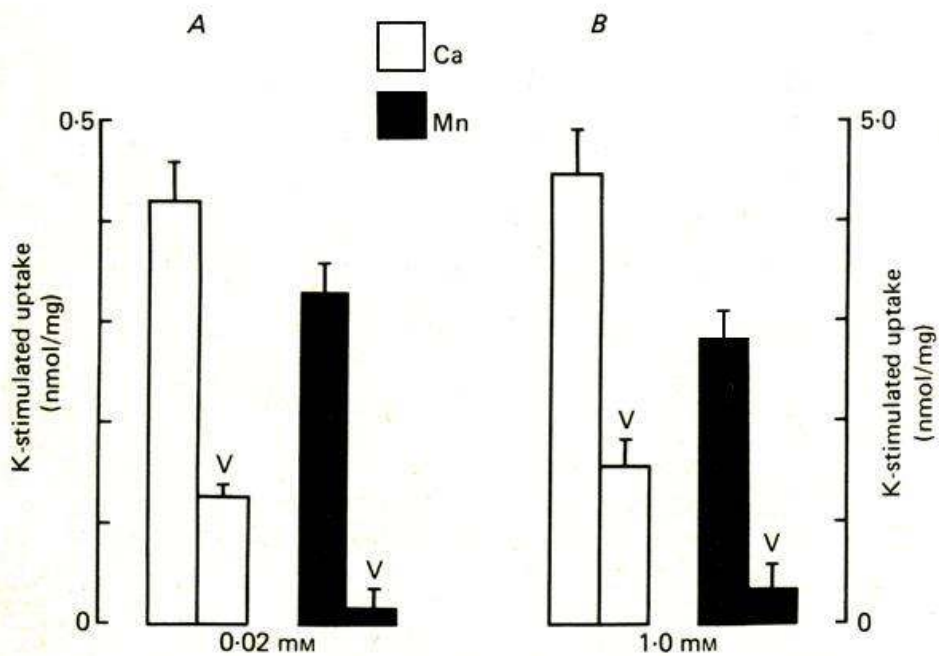


Figure 3-4: The effect of verapamil (80µM) on the K-stimulated uptake of Ca<sup>2+</sup> and Mn<sup>2+</sup>. The first bar of each pair shows the uptake in the absence of verapamil. The second bar shows the uptake in the presence of verapamil (V). Reproduced from Ref. (6)

potentials (MEPPs; generated by tetanic stimulation of the motor nerve) when verapamil was added to the  $Mn^{2+}$ -containing solution in which the nerve was bathed. Figure 3-5 shows the effect of verapamil on the frequency of MEPPs generated while in  $Mn^{2+}$  solution. The results of Narita *et al.* suggest that  $Mn^{2+}$  does indeed enter active nerve cells via VGCCs.

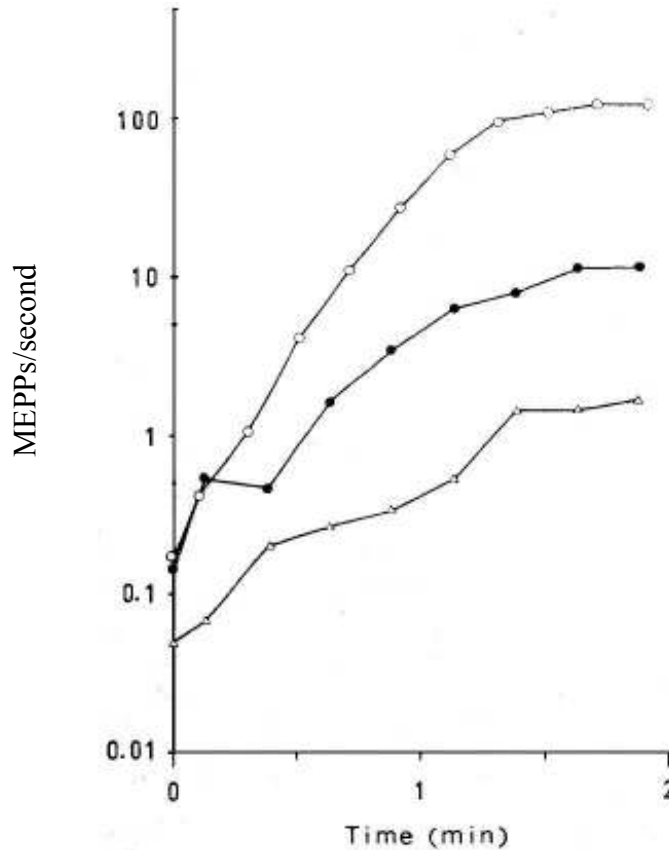


Figure 3-5: Effect of verapamil on the increase of MEPP frequency during tetanic stimulation of the [frog] motor nerve in  $Mn^{2+}$  solution. The preparation had been soaked for 4h in a low  $Ca^{2+}$  solution at 5 °C before the measurements were begun. The MEPP frequencies shown at 0 min are the average frequency during 10 min just before the tetanus in the respective solutions. The nerve was stimulated tetanically for 2 min. MEPPs before, during, and after tetanus were first recorded in the low  $Ca^{2+}$  solution ( $\Delta$ ), then in the  $Mn^{2+}$  solution (O), and finally in the same solution with 40  $\mu M$  verapamil ( $\bullet$ ). Reproduced from Ref. (14).

In addition to *in vitro* preparations of nerve cells used in experiments to monitor  $Mn^{2+}$  uptake by cells, whole rat hearts have been used to test whether  $Mn^{2+}$  could be used as a probe for the slow inward  $Ca^{2+}$  channel of the myocardial cell. Hunter *et al.* excised hearts from Sprague-Dawley rats and perfused them to maintain a semblance of *in vivo* conditions (see *Circ Res.* 47:721-727 (1980) for a description of this perfusion technique). To the working heart (~220 beats/min) was added radiolabeled  $Ca^{2+}$  and  $Mn^{2+}$  ( $^{45}Ca$  and  $^{54}Mn$ , respectively). The washout dynamics of  $^{45}Ca$  and  $^{54}Mn$

were monitored and showed that the cellular retention of  $Mn^{2+}$  was longer than that of  $Ca^{2+}$ , as shown in Figure 3-6 (15).

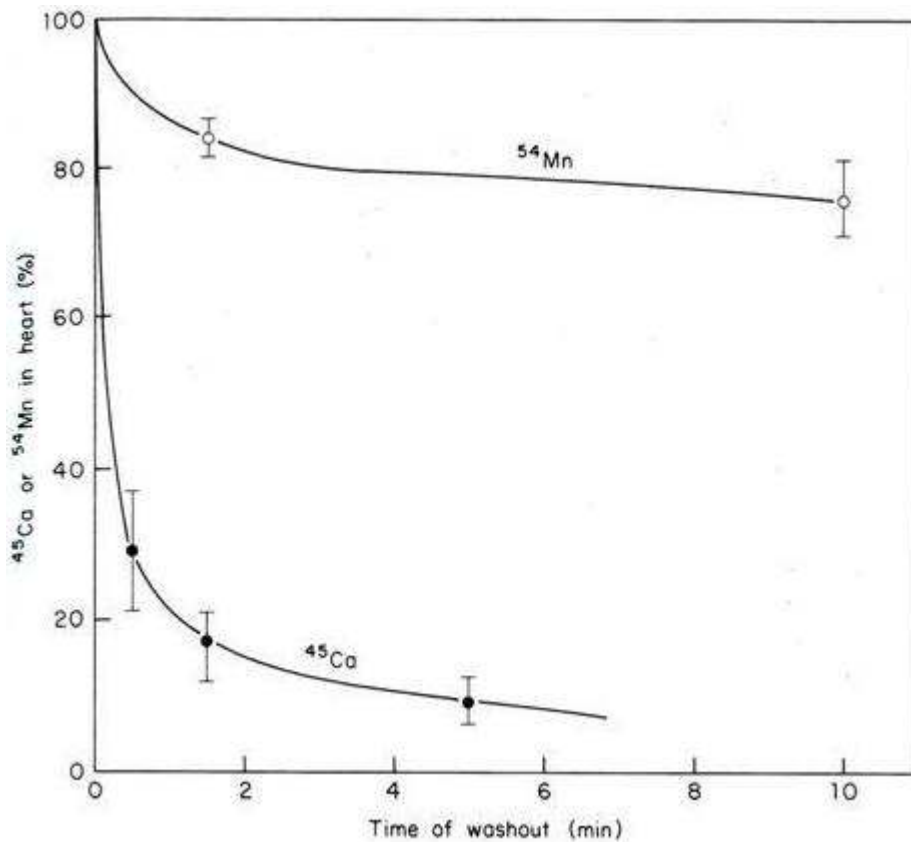


Figure 3-6: Comparison of  $^{45}Ca$  and  $^{54}Mn$  washout from rat heart. Hearts were perfused in the working mode for 10 min with the basal perfusate containing either  $^{45}Ca$  (●) or  $^{54}Mn$  (○). Reproduced from Ref. (15).

Data from Figure 3-6 were used to determine that the selective accumulation of  $Mn^{2+}$  by the heart 'compartment' is 8 times greater than that for  $Ca^{2+}$ . This compartment was suggested to be the heart cell and the method of entry was tested by using the  $Ca^{2+}$  channel blocking agent verapamil. Table 3-1 shows data from the Hunter *et al.* study, indicating that an inhibition of cellular  $Mn^{2+}$  accumulation was observed for hearts that were perfused with verapamil following perfusion with  $Mn^{2+}$ .

TABLE 1. Modulation of cellular Mn uptake by inhibitors and Ca

Condition	Total cellular Mn	Mitochondrial Mn	Number of hearts
Control	6.25 ± 1.21	2.48 ± 0.48	5
+ Verapamil (2 μM)	1.71 ± 0.10*	0.42 ± 0.06*	4
+ Oligomycin (2 μM)	2.83 ± 0.53*	1.12 ± 0.28*	4
Low perfusate Ca (0.2 mM)	14.81 ± 2.20*	2.54 ± 0.54	4

Table 3-1: Hearts were perfused with basal perfusate for 5-min in the working mode before turning on the perfusion pump which added verapamil, oligomycin or ethanol (control) to the perfusate. Reproduced from Ref. (15).

In addition to evidence showing the accumulation of  $Mn^{2+}$  within the cell via passage through VGCCs, Hunter *et al.* show that of the  $Mn^{2+}$  that enters cells, 30% is taken up by mitochondria. The accumulation of  $Mn^{2+}$  in mitochondria is suggested to occur via a mechanism of  $Ca^{2+}$ - $Mn^{2+}$  co-transport (15,16). The very slow rate of  $Mn^{2+}$  efflux from brain mitochondria is believed to contribute to brain mitochondria accumulation and uptake of  $Mn^{2+}$  in brain tissue in general. Apparently, brain mitochondria possess a mechanism for  $Mn^{2+}$  influx – but no method for  $Mn^{2+}$  clearance – other than by the slow  $Na^{+}$ -dependent mechanism (17). Ample evidence suggests that  $Mn^{2+}$  can enter cells through VGCCs.

Additional experiments show that  $Ca^{2+}$  and  $Mn^{2+}$  compete for the same entry routes into the cell. This suggests that  $Mn^{2+}$  could affect the function of the cell with possible adverse physiological effects to the cell *in vitro* or *in vivo*. Indeed,  $Mn^{2+}$  is known to be toxic in humans and animals at certain doses and MEMRI studies must confront this matter, especially for experiments *in vivo*. For infusions of low doses of  $Mn^{2+}$  that are not toxic, it is still important to consider the effects that  $Mn^{2+}$  may have on the cell after transport via VGCC's. These effects may alter the outcome of MEMRI experiments in brain; for example, those that rely on normal brain response to external stimuli, or the outcome of MEMRI experiments in other organs, such as the liver.

### 3.3 Manganese Toxicity and Cellular Effects of Manganese

#### *Manganese Toxicity*

Several heavy metals, such as lead (Pb), mercury (Hg), nickel (Ni), zinc (Zn), barium (Ba), and manganese ( $Mn^{2+}$ ), are known to be toxic in animals and humans. Most heavy metals interfere

with the voltage-gated entry of  $\text{Ca}^{2+}$  into the nerve terminal and interfere with normal rapidly-acting  $\text{Ca}^{2+}$ -buffering processes and ATP-dependent processes for maintenance of internal  $\text{Ca}^{2+}$  balance (18). Figure 3-7 shows the sites of action in the neuromuscular junction which may be affected by heavy metals.

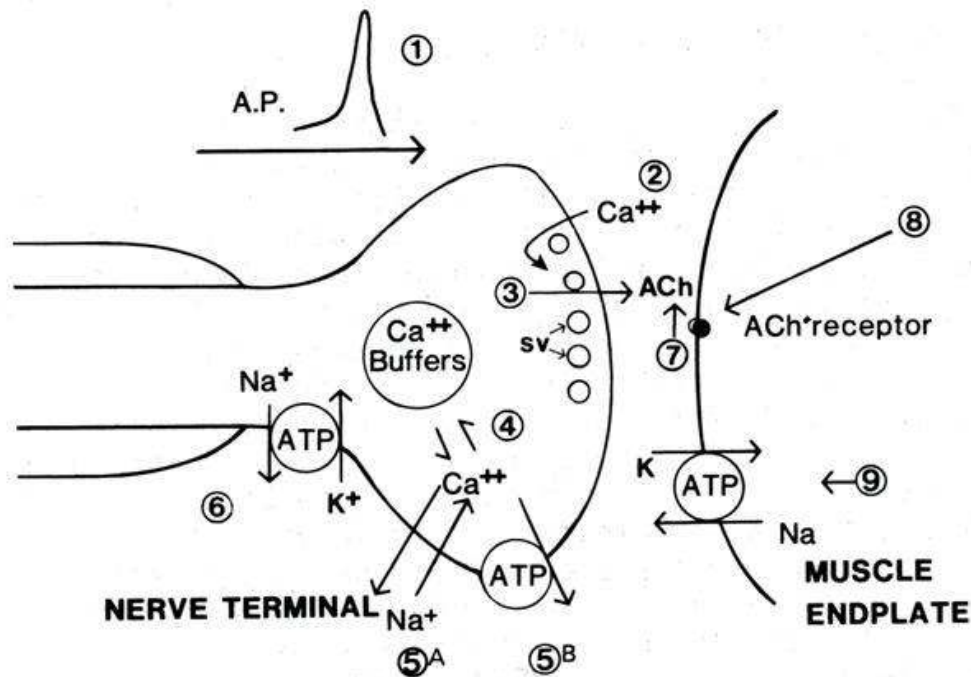


Figure 3-7: Simplified representation of the neuromuscular junction showing sites of action and processes which may be affected by heavy metals: (1) action potential propagation; (2) voltage-gated entry of  $\text{Ca}^{2+}$  into the nerve terminal; (3) interaction of  $\text{Ca}^{2+}$  with vesicles and plasmalemma at "active zones" to affect exocytosis; (4) buffering of  $\text{Ca}^{2+}$  by  $\text{Na}^{+}$ - $\text{Ca}^{2+}$  exchange and ATP-driven  $\text{Ca}^{2+}$  pumps; (5) maintenance of membrane potential by ATP-dependent  $\text{Na}^{+}$ - $\text{K}^{+}$  pumps; (6) diffusion of acetylcholine (ACh) (neurotransmitter) within the synaptic cleft and hydrolysis of ACh by acetylcholinesterase; (7,8) interaction of ACh with endplate receptors; and (9) maintenance of endplate potential and other membrane properties. Reproduced from Ref. (18).

Some heavy metals are clearly more toxic than others. Our main concern is the toxicity of  $\text{Mn}^{2+}$ . First, however, it is important to consider that  $\text{Mn}^{2+}$  is an essential trace element and is present within all mammalian cells. In humans, the normal body content of  $\text{Mn}^{2+}$  is 12 to 20 mg (218 to 364  $\mu\text{mol}$ ) (19). Normal dietary levels of  $\text{Mn}^{2+}$  are not likely toxic due to the regulation of gastrointestinal absorption.  $\text{Mn}^{2+}$  has important metabolic functions for the cell as a coenzyme in protein synthesis (19) and appears to be important for the proper function of the pancreas according to experimental evidence which showed that  $\text{Mn}^{2+}$  stimulates enzyme secretion from the rat pancreas (20). The toxicity of  $\text{Mn}^{2+}$  in man is typically a result of exposure to high levels of  $\text{Mn}^{2+}$  in dust

form (most notably in mine workers and employees of  $Mn^{2+}$ -processing industries).  $Mn^{2+}$  is known to be focused in three organs; the brain, lung and liver (7,19), but its specific mechanism of action is not known. Chronic  $Mn^{2+}$  toxicity manifests itself in humans by symptoms similar to those associated with Parkinson's disease and dystonia (bradykinesia, cephalalgia, hypersomnia, gait disturbances, speech disturbances, tremors, mask-like face, irregular handwriting, fatigability, anorexia, asthenia, apathy, and inability to concentrate) (19,21). Several theories to explain the neurotoxicity of  $Mn^{2+}$  have been proposed and are summarized in Table 3-2.

Direct toxicity of high-valence species of $Mn^{2+}$ (such as the trivalent cation ( $Mn^{3+}$ ) for the dopaminergic cells)
Ability of $Mn^{2+}$ to enhance the formation of reactive species (e.g., spheroid, hydroxyl radical, $H_2O_2$ )
Toxicity resulting from diminution of catalase and GSH peroxidase levels of the substantia nigra
$Mn^{2+}$ -induced production of 6-hydroxydopamine or other toxic catecholamines and quinines
Reduces glutathione (GSH) levels
Auto-oxidation of dopamine (eliminate dopamine and produce cytotoxic quinines)

Table 3-2: Hypotheses to explain  $Mn^{2+}$  neurotoxicity. Reproduced from Ref. (19)

In one case report of  $Mn^{2+}$  poisoning in man, Nelson *et al.* (1993) describe the effects of 15 years of  $Mn^{2+}$  dust inhalation in a 44-year old man who had been an arc-welder for 25 years. Eight months after leaving his job, the arc-welder “showed decreased hand grips, impaired vigilance, recall, rate of learning, amnesic processing, dysarthric speech, dyscalculia, and graphic construction dysfunction” (22). As part of the arc-welder's diagnosis, MRI showed hyperintensities in the basal ganglia and midbrain as shown in Figure 3-8. Experimental studies also have shown accumulation of  $Mn^{2+}$  in the brain after inhalation or intravenous  $MnCl_2$  injection. Regions of brain affected were detected by a shortening of the spin-lattice relaxation time ( $T_1$ ) in the caudate and lenticular nuclei, substantia nigra, subthalamic area, ventromedial hypothalamus, and the pituitary (23).

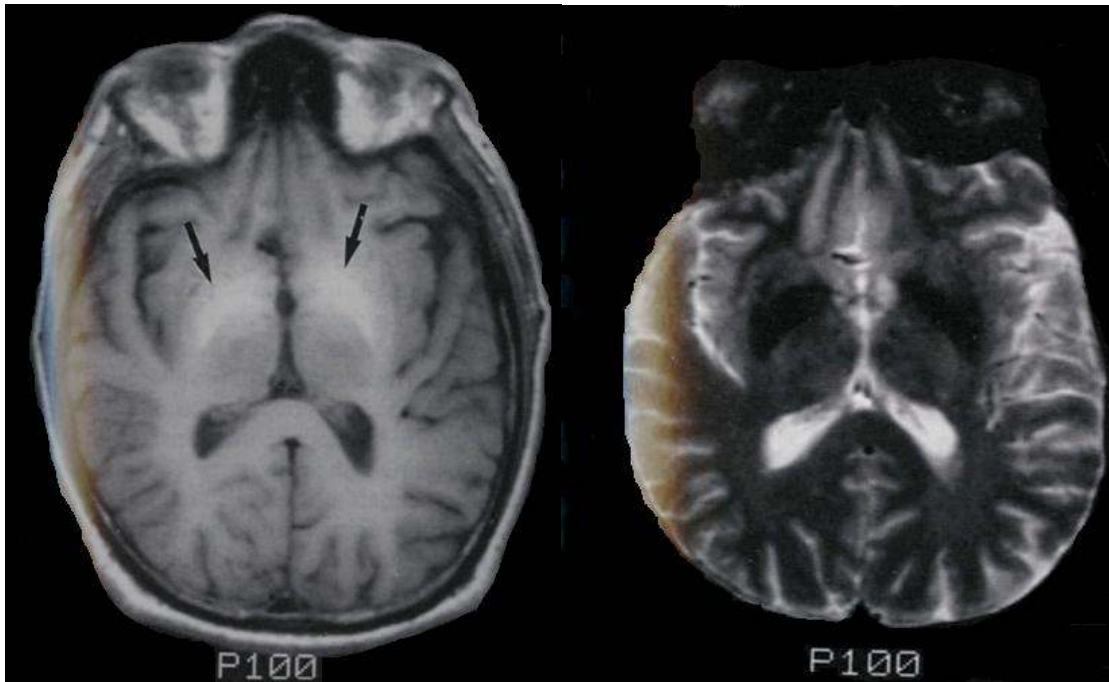


Figure 3-8: Left: Axial  $T_1$ -weighted image (TR/TE, 500/15ms) at the level of the basal ganglia. Increased signal intensity in the globus pallidus (arrows) that is bilateral and symmetrical reflects shortened  $T_1$  relaxation due to the paramagnetic effect of  $Mn^{2+}$ . Right:  $T_2$ -weighted image (TR/TE, 2500/70ms) is unremarkable. Some decreased signal intensity in the basal ganglia is normally expected for this age of patient. Reproduced from Ref. (22). Note: Although the author suggests here that the  $T_2$  image is 'unremarkable', this is not clear since the regional  $T_2$  hypointensities correspond very closely to the regions of  $T_1$  hyperintensity shown in the  $T_1$  image. Therefore, the  $T_2$  hypointensities may also be due to high local concentrations of paramagnetic  $Mn^{2+}$ . Discoloration in left side of image is due to artifacts from scanning images from reference material.

#### *Adverse Effects of Intracellular $Mn^{2+}$*

$Mn^{2+}$  is required for the basic metabolic regulation of the cell. For example,  $Mn^{2+}$  is complexed to the astrocytic enzyme, glutamine synthetase, involved in the synthesis of the excitatory and neurotoxic amino acid glutamate. Also,  $Mn^{2+}$  is an important cofactor for the outer-mitochondrial form of superoxide dismutase which is a major enzyme protecting cells from oxidative stress (24,25).  $Mn^{2+}$  homeostasis necessary to maintain normal cell function can be disrupted by overexposure of  $Mn^{2+}$ . In cases of  $Mn^{2+}$  overexposure, cell death can be provoked by apoptosis and necrosis. Apoptosis, however, is not the only means of cytotoxic actions of  $Mn^{2+}$ . Roth and colleagues showed that inhibitors of apoptotic markers, including the caspase family of proteases and p38 kinase, failed to prevent  $Mn^{2+}$ -induced cytotoxicity (26). Therefore,  $Mn^{2+}$  must provoke other methods of cytotoxic events in the cell. Indeed, it has been shown that  $Mn^{2+}$  disrupts



mitochondrial function by inhibiting the sodium-dependent and sodium-independent exporter of mitochondrial calcium (17,27).  $Mn^{2+}$  also interferes with oxidative phosphorylation resulting in depletion of ATP (28). Taken together, inhibition of mitochondria function and depletion of ATP may be the prevalent mechanism behind  $Mn^{2+}$ -induced cell death, even in the presence of apoptotic signaling (25). Figure 3-9 shows the mechanisms that are known to regulate cellular transport and toxicity of  $Mn^{2+}$ .

### 3.3.1 $Mn^{2+}$ *In Vivo* After Intravenous (I.V.) Infusion

#### *Regions of $Mn^{2+}$ Accumulation After I.V. Infusion*

In the arc-welder case study, the primary route of entry of  $Mn^{2+}$  was through inhalation with clear neurotoxic effects. After oral administration or ingestion, the gastrointestinal tract metabolizes  $Mn^{2+}$ . Manganese is then transported to the central nervous system (in  $Mn^{3+}$  form) by a path which includes the portal venous circulation, binding to transferrin in blood and then transported across the blood-brain barrier (BBB) via transferrin receptors (7). The rate at which  $Mn^{2+}$  is absorbed by the gastrointestinal tract depends on the amount ingested or administered and the plasma levels of  $Mn^{2+}$ .

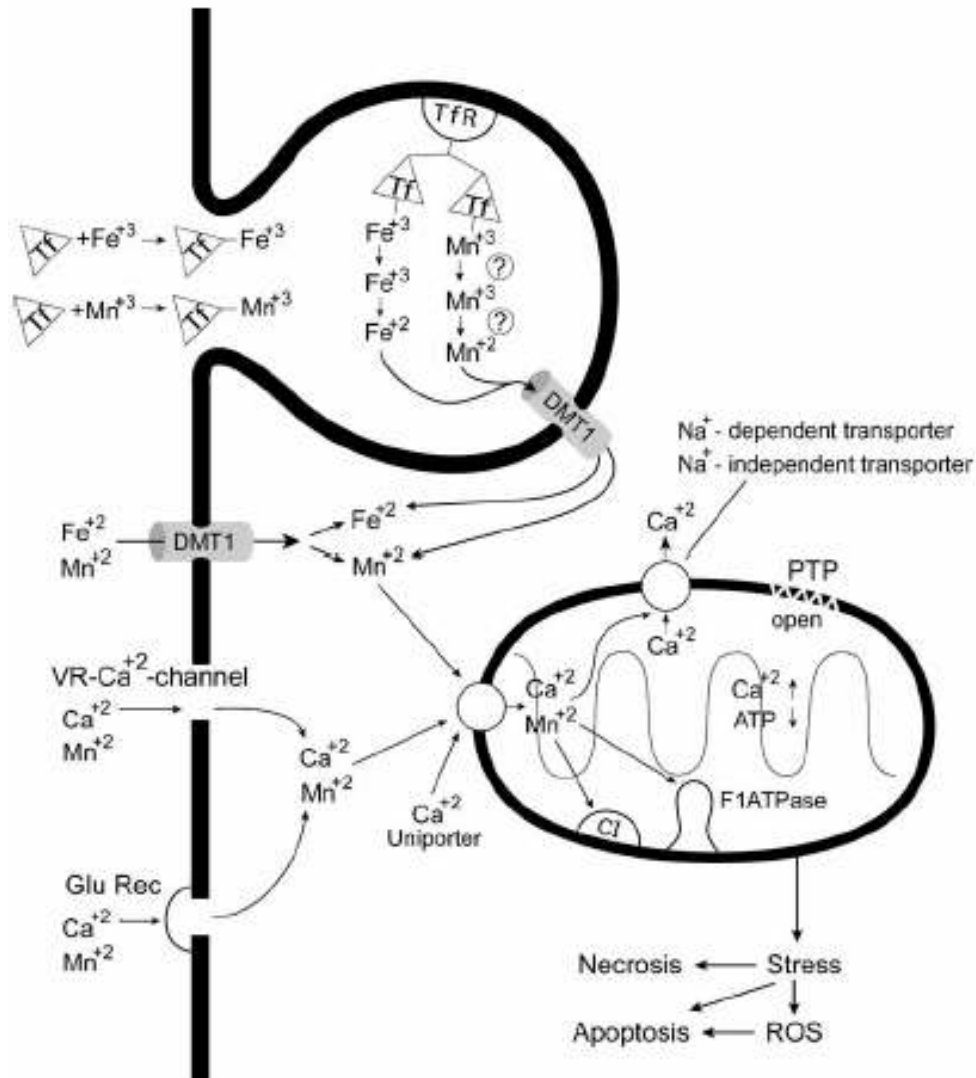


Figure 3-9: Mechanisms regulating  $\text{Mn}^{2+}$  cellular transport and toxicity.  $\text{Mn}^{2+}$  and iron are taken up into cells via transferrin-dependent and independent pathways requiring the divalent metal transporter 1 (DMT 1).  $\text{Mn}^{2+}$  is also transported into cells via the voltage-regulated  $\text{Ca}^{2+}$  channel (VR- $\text{Ca}^{2+}$ ) and glutamate receptor  $\text{Ca}^{2+}$  channel (Glu Rec). Once inside the cell,  $\text{Mn}^{2+}$  is transported into the mitochondria via the  $\text{Ca}^{2+}$  uniporter.  $\text{Mn}^{2+}$  interferes with mitochondrial F1-ATPase and complex I (CI) causing a decrease in ATP production.  $\text{Mn}^{2+}$  inhibits  $\text{Na}^{+}$ -dependent and -independent export of  $\text{Ca}^{2+}$  out of the mitochondria causing activation of the permeability transition pore (PTP), which eventually leads to disruption of mitochondrial function. Disruption of mitochondria leads to stress and possible reactive oxygen species (ROS) promoting both apoptotic and necrotic cell death. Reproduced from Ref. (25).

The amount of  $\text{Mn}^{2+}$  absorbed in rats is anywhere between 1% and 4% (7,29). Intravenous (i.v.) administration of  $\text{Mn}^{2+}$  is common and usually includes an infusion of solutions of  $\text{MnCl}_2$

experimentally or Mn-DPDP clinically. Intravenous infusion bypasses some of the body's safeguards or 'Mn<sup>2+</sup> filters', an idea supported by the fact that the median lethal dose of orally administered MnCl<sub>2</sub> in rats (7.5 mmol/kg) is 25 times higher than that after intravenous infusion (0.3 mmol/kg) in mice (30). After i.v. infusion, Mn<sup>2+</sup> accumulates in liver, kidney, pancreas, heart and brain. Of particular interest here is the accumulation of Mn<sup>2+</sup> in brain after an i.v. infusion (and without experimental blood-brain barrier disruption). Uptake of Mn<sup>2+</sup> into brain after i.v. infusion is a time-dependent phenomenon. Takeda *et al.* showed that 1h after i.v. infusion of <sup>54</sup>MnCl<sub>2</sub>, <sup>54</sup>Mn was largely concentrated in the lateral and third ventricles including the choroid plexus. At 6 days after injection, high levels of <sup>54</sup>Mn were found in the thalamus, hypothalamus, hippocampus and other subcortical brain regions (31). One day after i.v. infusion, Aoki *et al.* showed brain accumulation of Mn<sup>2+</sup> in ventricles, circumventricular organs without a blood-brain barrier such as Pit and subfornical organ (32-34), olfactory bulb, hippocampus, basal ganglia, ventral striatum, brain stem and spinal cord (4).

#### *Mn<sup>2+</sup> in Blood*

After a bolus i.v. infusion of Mn<sup>2+</sup> in rats, Mn<sup>2+</sup> concentration in plasma decays according to a bi-exponential equation. As indicated by the results of a study performed by Zheng *et al.*, a bolus i.v. injection of MnCl<sub>2</sub> into male Sprague-Dawley rats results in the blood plasma concentration-time profile shown in Figure 3-11. Concentration of Mn<sup>2+</sup> in blood as a function of time was also given as:

$$C(t) = 41.94e^{-4.24t} + 2.08e^{-0.44t}$$

After i.v. bolus injection, therefore, Mn<sup>2+</sup> appears to undergo two phases of elimination from the body; an initial fast phase and a slower terminal phase. Zheng *et al.* found the initial fast clearance phase to last for 1.8 hours while the slower terminal phase of Mn<sup>2+</sup> clearance lasted 12 hours; at which time the concentration of Mn<sup>2+</sup> in plasma returned to normal values in all animals (35).

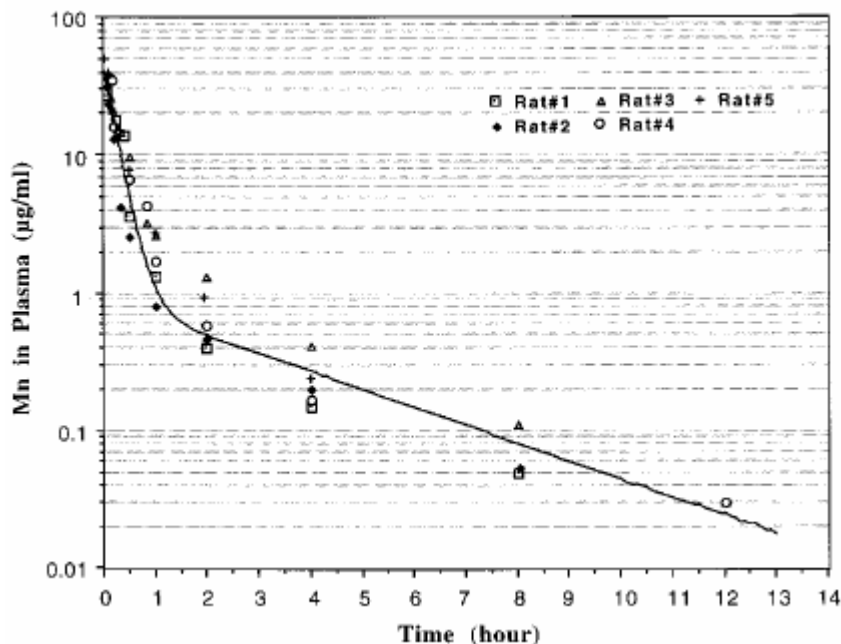


Figure 3-10: Plasma concentration-time profiles of  $Mn^{2+}$  in male Sprague-Dawley rats following an i.v. administration of  $MnCl_2$  (6.0 mg  $Mn^{2+}$ /kg). Plasma concentration of  $Mn^{2+}$  was determined by atomic absorption spectrophotometry analysis. The line indicates the best fit of a two-compartment model with first-order elimination from the central compartment to the observed data. Reproduced from Ref. (35).

The reason for the bi-exponential nature of  $Mn^{2+}$  clearance from blood is likely due to the different rates of clearance of  $Mn^{2+}$  from liver and from brain.  $Mn^{2+}$  levels in liver after i.v. injection are quick to decrease (90% decrease in 5 days) as compared to clearance in brain (which showed an increase in  $Mn^{2+}$  concentration in same 5-day period) (36). When in blood,  $Mn^{2+}$  binds weakly to serum albumin, and strongly to transferrin (7,37,38). As a result of binding to transferrin,  $Mn^{2+}$  may be transported across the BBB where it accumulates in areas of brain that are efferent to areas of high transferrin receptor density, such as ventral-pallidum and globus pallidus, which receive input from caudate-putamen and substantia-nigra (two regions rich in transferrin receptors (39)).

#### *Elimination of $Mn^{2+}$*

Excretion of free and protein-bound  $Mn^{2+}$  from the body occurs predominantly through the bile across a concentration gradient suggesting an active transport mechanism (7).  $Mn^{2+}$  is also excreted by gastrointestinal mucosa and pancreatic secretions with practically no secretion via the

kidneys (19). In situations of chronic liver disease, elimination of  $Mn^{2+}$  is incomplete, resulting in long-term storage of  $Mn^{2+}$  in the basal ganglia region of the brain (40).

### 3.4 $Mn^{2+}$ Transport Across the Blood-Brain Barrier (BBB)

Mechanisms exist for the transport of  $Mn^{2+}$  across the BBB as evidenced by the fact that proper brain cell function is dependent upon  $Mn^{2+}$  and that  $Mn^{2+}$  must be introduced into blood through dietary ingestion.  $Mn^{2+}$  transport across the BBB, therefore, must be mediated by transport and/or diffusion mechanisms to limit amounts of  $Mn^{2+}$  in blood that may prove cytotoxic. Understanding the mechanisms of  $Mn^{2+}$  transport across the BBB can help to elucidate the cytotoxicity of  $Mn^{2+}$ . In addition, as will be described later, certain experiments using  $Mn^{2+}$  as a MR contrast agent rely on the transport of blood  $Mn^{2+}$  across the BBB for brain anatomical and functional imaging.

#### *$Mn^{2+}$ Transport Across the BBB*

In most experimental studies,  $Mn^{2+}$  is infused *in vivo* as a solution of  $MnCl_2$ . In this form,  $Mn^{2+}$  is in the 2+ oxidation state (divalent  $Mn^{2+}$ ). In blood,  $Mn^{2+}$  can be oxidized to the 3+ oxidation state (trivalent  $Mn^{2+}$ ) by ceruloplasmin. Trivalent manganese has been shown to access the brain via a transferrin receptor-mediated mechanism at the BBB (41); but, as suggested later by experiments in hypotransferrinemic mice, tissue distribution of divalent  $Mn^{2+}$  did not depend on transferrin in blood (42,43). Additional experiments have argued for and against a divalent metal transporter (DMT-1) at the BBB. Gunshin *et al.* argue that  $Mn^{2+}$  ion influx into brain is mediated by DMT-1 (44) while a study by Crossgrove *et al.* suggests the lack of DMT-1 in rats does not affect the transport of  $Mn^{2+}$  into brain (45). An additional study by Crossgrove and Yokel provide further evidence against DMT-1 as a transporter of  $Mn^{2+}$  into brain. According to their results,  $Mn^{2+}$  entry into brain depends on at least two pathways; one that does not have a high affinity for calcium and one that is a nickel-blocked, cyclopiazonic acid-induced calcium pathway consistent with store-operated calcium channels (45). A study of  $Mn^{2+}$  transport using an *in vitro* model of the BBB tested the role that temperature, energy, pH, iron (Fe) and sodium (Na) may play in the transport of  $Mn^{2+}$  across the

BBB. In their model, Fitsanakis *et al.* confirmed that  $Mn^{2+}$  transport is temperature dependent suggesting that the transport of  $Mn^{2+}$  across the BBB is not due to simple diffusion (46). Also, their data suggest that a proton gradient is related to  $Mn^{2+}$  transport across the *in vitro* BBB and that  $Mn^{2+}$  transport is  $Na^+$ -dependent – but may not be Fe-dependent – due to discrepancies with *in vivo* Fe data (47). As Fitsanakis *et al.* suggest,  $Mn^{2+}$  and  $Fe^{2+}$  either share a common BBB-transport mechanism or regulation of brain  $Fe^{2+}$  and  $Mn^{2+}$  concentrations is tightly linked. According to the literature reviewed here (and others not cited), no single transporter is responsible for  $Mn^{2+}$  influx into brain. Experiments *in vitro* and *in vivo* clearly show passage of  $Mn^{2+}$  across the BBB and brain neurotoxicity due to  $Mn^{2+}$  exposure is well known. New methods are gaining acceptance as non-invasive means of detecting  $Mn^{2+}$  in brain. MRI is one method that can be used to detect significant quantities of  $Mn^{2+}$  in brain after experimental i.v. infusion of  $Mn^{2+}$  solutions.

### 3.5 $Mn^{2+}$ as MR Contrast Agent – $Mn^{2+}$ -Enhanced Magnetic Resonance Imaging (MEMRI)

Early uses of  $Mn^{2+}$  as a MR contrast agent were primarily focused on liver imaging, owing to the ability of  $Mn^{2+}$  to selectively accumulate in hepatocytes. A chelated form of  $Mn^{2+}$ , FDA-approved Mn-DPDP, was used to reduce the toxic side effects of the free manganese ion,  $Mn^{2+}$ . In this section, a brief review of imaging with Mn-DPDP is given followed by a review of MR imaging of brain anatomy and function using  $Mn^{2+}$  administered as  $MnCl_2$ . MR imaging after injections of either Mn-DPDP or  $MnCl_2$  constitute  $Mn^{2+}$ -enhanced magnetic resonance imaging or MEMRI.

#### 3.5.1 MEMRI with Mn-DPDP

Use of  $Mn^{2+}$  as a clinical organ-specific contrast agent requires the metal complex to be designed such that it continues to affect MR relaxation rates *in vivo* but does not adversely affect the health of the patient (thus becoming a ‘chelated’ contrast agent). Complexation of divalent manganese ( $Mn^{2+}$ ) with an organic ligand fodipir (DPDP) results in a paramagnetic chelate useful as a clinical contrast agent. This type of clinical  $Mn^{2+}$  contrast agent is referred to as Mangafodipir (Mn dipyradoxyl diphosphate) trisodium or Mn-DPDP (48). The molecular structure of Mn-DPDP is shown in Figure 3-12.

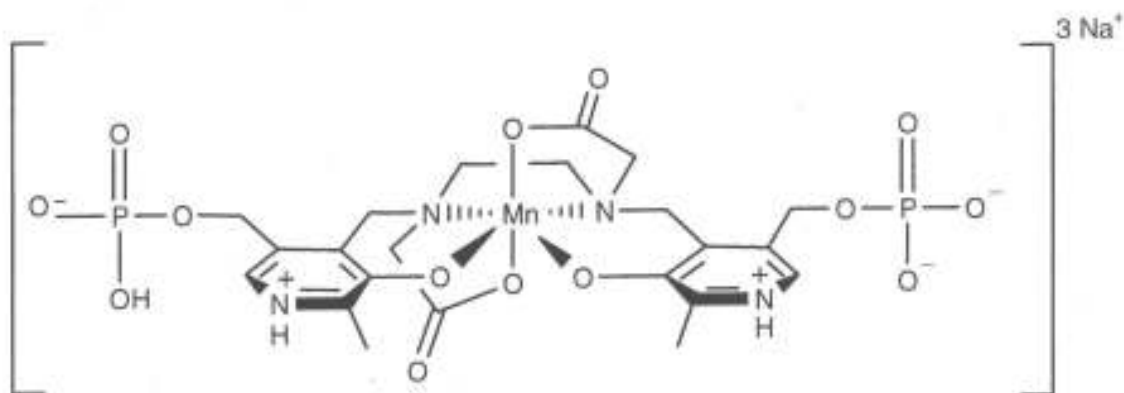


Figure 3-11: Molecular structure of Mn-DPDP trisodium. Reproduced from Ref. (48).

Mn-DPDP is metabolized by dephosphorylation to Mn dipyridoxyl monophosphate (Mn-DPMP) and  $\text{Mn}^{2+}$  dipyridoxyl ethylenediamine diacetate (Mn-PLED) and is simultaneously transmetallated with zinc to the corresponding zinc compounds (49). Transmetallation releases the  $\text{Mn}^{2+}$  from the ligand which is likely bound and transported to the liver by  $\alpha_2$ -macroglobulin and albumin (49). In normally functioning liver, hepatocytes take up the majority of  $\text{Mn}^{2+}$  (50), which is excreted in the feces via the bile (51). Liver metastases take up little or no  $\text{Mn}^{2+}$ , leading to a reliable method for increasing contrast between normal and diseased liver tissue on MR images. The first human liver MR imaging results using Mn-DPDP were reported by Lim *et al.* (52) in 1991. Images (acquired using a 1.5T clinical MR scanner) from their experiments are shown in Figure 3-12.



Figure 3-12: MR images of the liver obtained a) before and b) 10 minutes after injection of Mn-DPDP ( $10\mu\text{mol/kg}$ ,  $0.016\text{ml/sec}$ ). Reproduced from Ref. (52).

Mn-DPDP continues to be used as a liver MR contrast agent and is helpful in preparing for liver surgery. Joarder *et al.* used Mn-DPDP in preparation for MR-guided thermal ablation of liver tumor (53). Clinical images (using a 0.5T open MR scanner) from their work are shown in Figure 3-13.

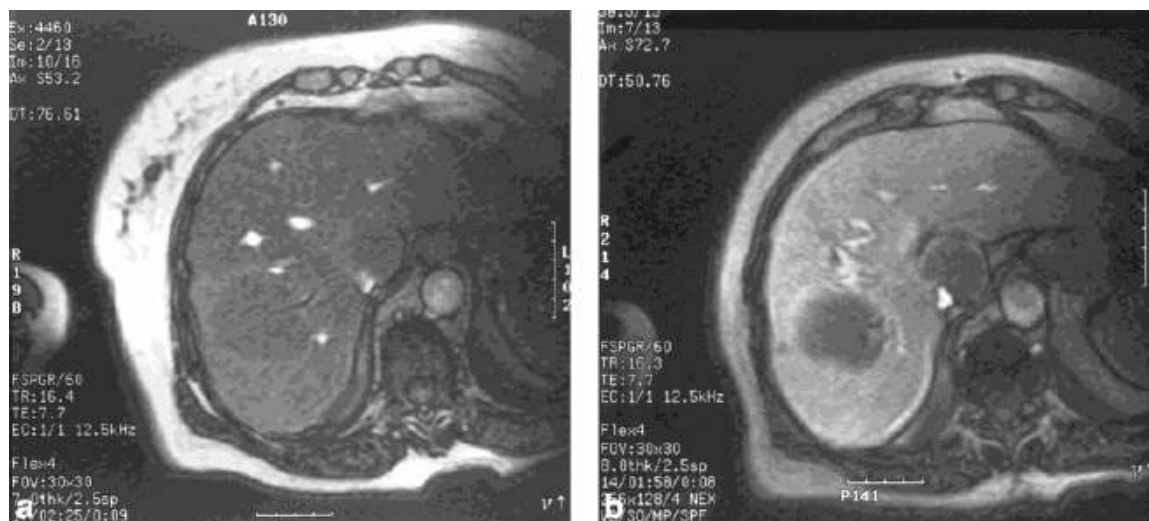


Figure 3-13: Axial FMSPPGR images showing two colorectal metastases before (a) and after (b) Mn-DPDP.

Note improved delineation of the metastases adjacent to the IVC and portal and hepatic veins on the post-Mn-DPDP scans.  $Mn^{2+}$  not only improves lesion conspicuity but also puncture planning, enabling the avoidance of structures such as the IVC and portal vein in this case. Reproduced from Ref. (53)

### 3.5.2 MEMRI with $MnCl_2$

#### *Working With Solutions of $MnCl_2$ – Dose, Concentration, pH, and Osmolarity*

Manganese chloride is a salt that is readily available from any major biochemical company and, in solution form, is the simplest way to deliver  $Mn^{2+}$  experimentally (i.e., in rats or mice). For experiments detailed in this thesis, the hydrated form of  $Mn^{2+}$  chloride,  $MnCl_2 \cdot 4H_2O$  (molecular weight 197.9 g/mol) was used. Solutions of  $MnCl_2$  must be compatible with the biological system of interest. Therefore, chemical properties of the solution such as osmolarity and pH should be considered to reduce potential toxic side effects of  $Mn^{2+}$ . Systemic infusions of  $MnCl_2$  solution should use a  $[MnCl_2]$  of 100mM to ensure the solution is neither hypertonic nor hypotonic (54). Hypertonicity or hypotonicity may be more important for targeted injections such as stereotaxic brain infusions. At 100mM,  $MnCl_2$  has a pH of 5.5-5.8 (54) significantly below the normal physiological level. Bicine dissolved to 100mM in deionized water and pH adjusted to 7.4 with



NaOH can be used to keep the pH of MnCl<sub>2</sub> solutions to within the physiological range (54). Dosing the MnCl<sub>2</sub> infusion requires careful attention to the route of administration of Mn<sup>2+</sup> and to the size of the animal. Doses used in past MEMRI studies are summarized in Table 3-3.

Species	Route	Dose	Reference
Rat	Intravenous	54 mg/kg	Lin and Koretsky (1)
	Intravenous	60 mg/kg	Duong <i>et al</i> (55)
	Intra-arterial	53 mg/kg	Aoki <i>et al</i> (56)
	Intravenous	175 mg/kg	Aoki <i>et al.</i> (57)
Mouse	Nasal	65 mg/kg	Pautler <i>et al.</i> (58)
	Intravenous	175 mg/kg	Lee <i>et al.</i> (59)
	Intravenous	6.6 mg/kg	Hu <i>et al.</i> (60)
	Intraperitoneal	20 mg/kg	Watanabe <i>et al.</i> (61)

Table 3-3: Systemic doses of MnCl<sub>2</sub> used in current MEMRI experiments. Reproduced from Ref. (54)

### 3.5.2.1 – A Review of Experiments in Brain Imaging with MnCl<sub>2</sub>

Experiments using MnCl<sub>2</sub> for experimental brain anatomical and functional imaging are numerous. Therefore, this section is divided into brain imaging using MnCl<sub>2</sub> with and without disruption of the blood-brain barrier. MEMRI of brain with an intact BBB is useful for brain anatomical imaging as well as general functional imaging (i.e., uptake of Mn<sup>2+</sup> in neuron-rich areas of hippocampus) while MEMRI of brain with a disrupted BBB is more appropriate for imaging of specific brain function such as the response to stroke, cortical spreading depression, or forepaw stimulation.

#### *MEMRI with MnCl<sub>2</sub> – Brain Imaging with Intact Blood-Brain Barrier (BBB)*

Early imaging studies utilizing MnCl<sub>2</sub> for Mn<sup>2+</sup>-induced contrast enhancement in MR images were focused on determining the distribution of Mn<sup>2+</sup> in the brain as part of Mn<sup>2+</sup> neurotoxicity studies. For example, London and colleagues (62) used i.p. injections of MnCl<sub>2</sub> in rats to show that brain uptake of MnCl<sub>2</sub> occurs relatively rapidly in the ventricles and pineal and pituitary glands (regions devoid of BBB), supporting further study of the toxicity of Mn<sup>2+</sup> after accumulation in these

brain regions. More recent MEMRI studies have used: (1) i.v. infusion (via the tail vein) of  $\text{MnCl}_2$  solutions for delineation of neuroarchitecture in rat (57); (2) direct CSF injection of  $\text{MnCl}_2$  to determine distribution of brain  $\text{Mn}^{2+}$  uptake via CSF (63); and (3) i.v. infusion of  $\text{MnCl}_2$  to determine the temporal evolution of  $T_1$  contrast in brain (59). Due to the fast initial clearance phase of  $\text{Mn}^{2+}$  in blood (~11 minutes) (35), studies using i.v. infusion of  $\text{Mn}^{2+}$  rely on fast uptake of  $\text{Mn}^{2+}$  by CSF and resulting homogeneous distribution of  $\text{Mn}^{2+}$  in brain by cardiac and respiratory pulsations that circulate CSF throughout both hemispheres. As shown in these studies, MEMRI is a powerful semi-noninvasive tool for imaging the neuroarchitecture of animals. Consider as examples, Figures 3-14 and 3-15, which show enhancement of brain neuroarchitecture in rat. MEMRI has the potential to become a useful tool to image changes in brain neuroarchitecture in response to pathologies.

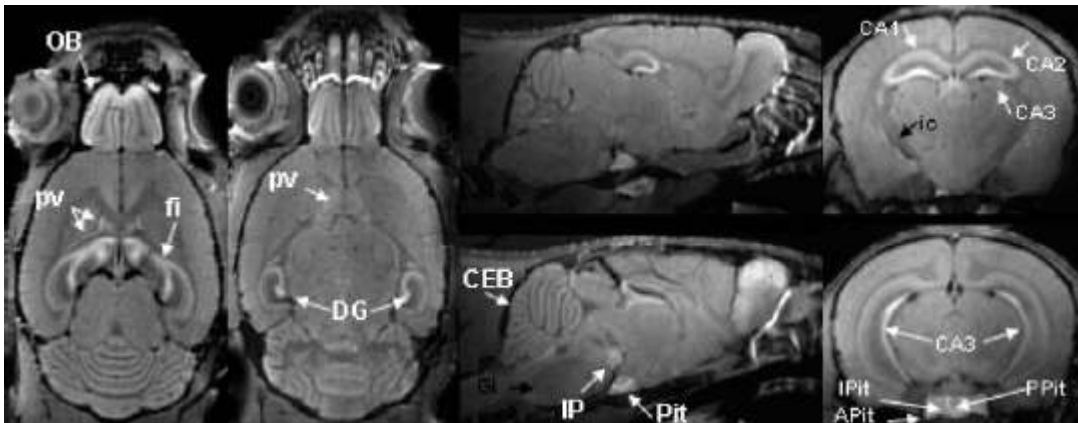


Figure 3-14: Typical horizontal (left), sagittal (center), and axial (right) cuts from a  $T_1$ -weighted spin-echo 3D-MEMRI of a mouse brain acquired 24 hr after a systemic injection of 88mg/kg of  $\text{MnCl}_2$ . Bright  $\text{Mn}^{2+}$ -enhanced structures are well visualized in all 3D orientations. CEB: cerebellum; CA1, CA2, CA3: CA formation of hippocampus; DG: dentate gyrus; fi: fimbria of hippocampus; IP: interpeduncular nucleus; OB: olfactory bulb; APit, IPit, PPit: anterior, intermediate, and posterior lobes of pituitary gland; pv: periventricular tissue zone. The increased contrast allows clear visualization of other anatomic details of the complex brain neuroarchitecture. For example, the internal capsule (ic) and the gigantocellular reticular nucleus (Gi, below 'CEB' in center view, black arrow), appear darker than surrounding tissue in the  $T_1$ -weighted MEMRI. Reproduced from Ref. (59).

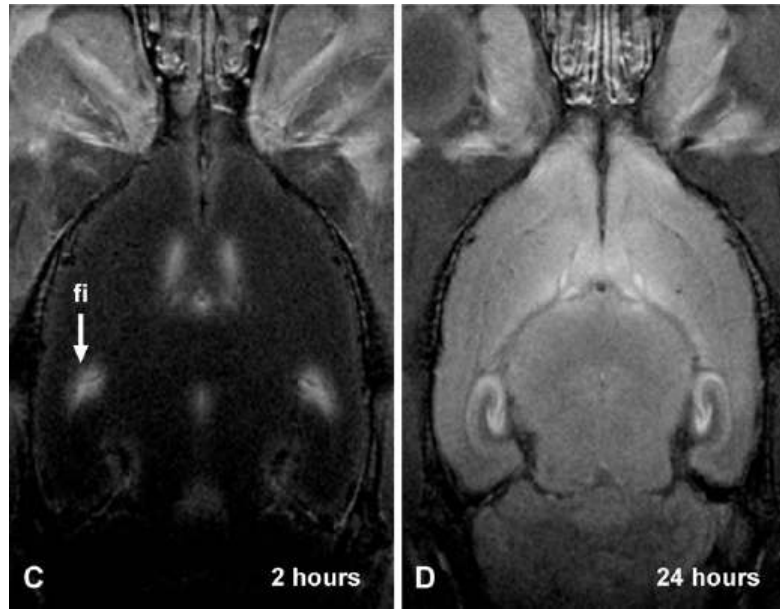


Figure 3-15:  $T_1$ -weighted MRI of the hippocampal formation in the rat after systemic  $MnCl_2$  infusion. Horizontal slices (Bregma: -6mm) of  $T_1$ -weighted MRI from the hippocampus of a rat after  $MnCl_2$  administration: (C) 2 h, and (D) 24 h after  $MnCl_2$  administration in the same rat. The characteristic arrowhead-shaped DG and hippocampal formation are readily detected. fi = fimbria of hippocampus. Reproduced from Ref. (4).

#### *MEMRI with $MnCl_2$ – Brain Imaging after Blood-Brain Barrier (BBB) Disruption*

$MnCl_2$  has recently been shown to be a MR contrast agent that is directly sensitive to brain activation (1). The implications of this approach is increased specificity over currently available functional brain MRI techniques such as blood oxygenation level dependent (BOLD) imaging (64). BOLD imaging tracks brain function by changes in hemoglobin oxygenation status and is, therefore, not able to detect brain function directly. Since  $Mn^{2+}$  has been shown to enter active cells through  $Ca^{2+}$  channels and  $Mn^{2+}$  is paramagnetic, active regions of brain can be imaged by MEMRI providing an approach for direct imaging of brain function.

An experimental limitation to using  $Mn^{2+}$  as a brain-activation-specific MR contrast agent is that the BBB must be disrupted to allow passage of  $Mn^{2+}$  into the brain interstitial space in a time-efficient manner. Historically, for MEMRI experiments, osmotic disruption of the BBB has been the method of choice for gaining  $Mn^{2+}$  access to the brain parenchyma. A summary of sugar solution concentration, dose, route and rate of infusion, as well as anesthetics used during experiments is given in Table 3-4. As is apparent in Table 3-4, a solution of concentrated mannitol is the substance

of choice for osmotic BBB disruption in most MEMRI experiments. The common usage of mannitol may be a historical trend based on the first MEMRI study used for brain activation. Also, mannitol is approved for clinical use, which may explain the typical use of this compound for MEMRI studies.

The use of mannitol as a BBB-opening agent has some disadvantages. Because of the limited solubility of 1.37 M (25%) mannitol at room temperature, the solution must be maintained at body temperature (37 °C) or warmer to prevent precipitation of the solute prior to *in vivo* administration. If 25% mannitol recrystallizes due to exposure to room temperature for an extended period of time, infusion of the solute may result in microinfarcts in the brain (65). For the studies described in this dissertation, solutions of arabinose were deemed to be a better choice for osmotic BBB disruption. At 1.4 M arabinose will not precipitate out at room temperature because arabinose is 5.5 times more soluble than mannitol (see Chapter 2 for more details on arabinose and mannitol). It is noteworthy that of the studies listed in Table 3-4 no evidence of BBB disruption is provided. Some experiments also fail to list the rate of mannitol infusions. It is well known that the rate of infusion of mannitol is an important factor that determines the success of BBB disruption (66).

Male Rat Species	Osmotic Agent (OA)	OA Dose (ml/kg) / [OA] (Molar)	OA Route of Infusion / Rate of Infusion (ml/min)	Anesthetic	Reference
Sprague-Dawley	Mannitol	5 / 1.37	Right ECA / ???	1.8-2.5% halothane, pancuronium bromide	Lin <i>et al.</i> (1)
Sprague-Dawley	Mannitol	5 / 1.37	Right ECA / 2.3 – 2.7	1-2% halothane, continuous $\alpha$ -chloralose	Duong <i>et al.</i> (55)
Wistar-Hamamatsu	Mannitol	5 / 1.37	Right ECA / ???	enflurane, urethane/ $\alpha$ -chloralose mixture	Morita <i>et al.</i> (67)
Wistar	Mannitol	5 / 1.37	Right ECA / ??? (“Bolus”)	diethyl ether, 2.0-2.3% halothane, urethane/ $\alpha$ -chloralose mixture, Pancuronium bromide	Aoki <i>et al.</i> (56)
Wistar	Mannitol	5 / 1.37	Right ECA / 0.83	diethyl ether, 1.2-1.5% halothane, pentobarbital	Aoki <i>et al.</i> (68)
Sprague-Dawley	Mannitol	5 / 1.37	Right ECA / ??? (“Bolus”)	chloral hydrate, 1.2% isoflurane	Henning <i>et al.</i> (5)

Table 3-4: Summary of osmotic agent, dose, concentration, route and rate of infusion, and anesthetics used during MEMRI experiments that employ osmotic disruption of the BBB for passage of  $Mn^{2+}$  into brain parenchyma.

Future MEMRI studies that depend on homogeneous delivery of  $Mn^{2+}$  to one hemisphere of brain should incorporate evidence of BBB disruption to circumvent this discrepancy. A diagram showing the arteries that need to be ligated to ensure flow of osmotic solution to one hemisphere of brain (with the other hemisphere acting as control) is shown in Figure 3-16.

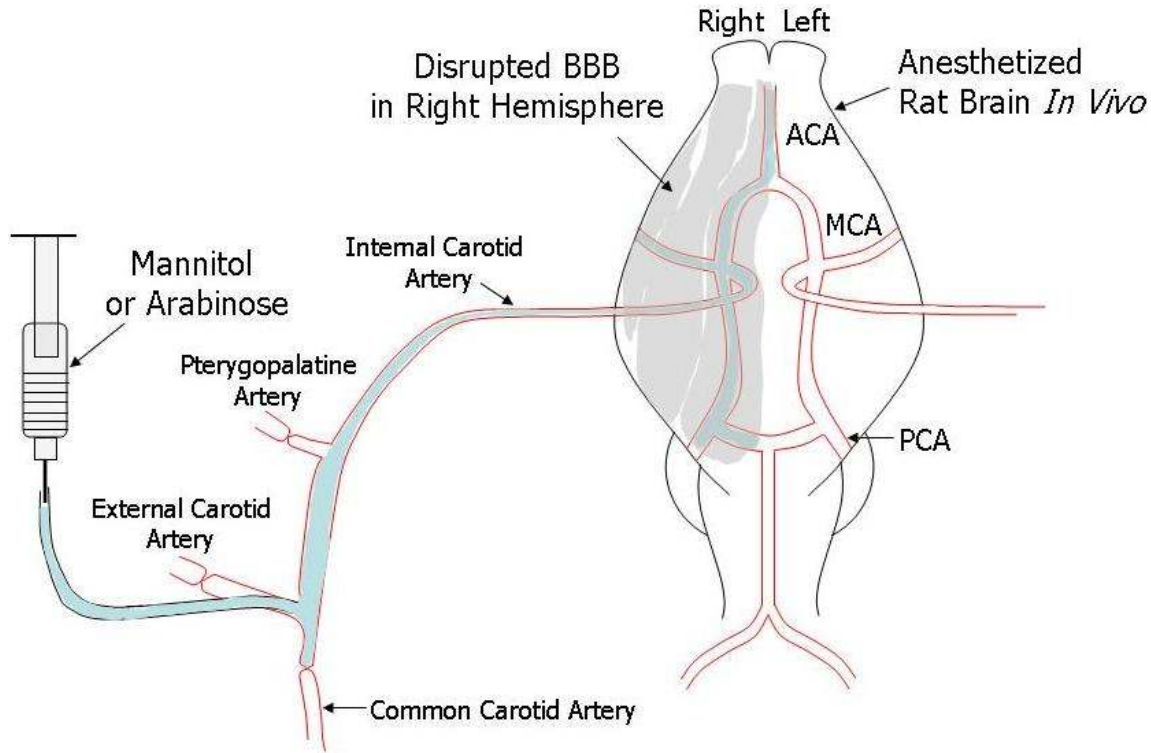


Figure 3-16: Arteries in the rat brain that must be ligated to ensure flow of mannitol or arabinose to one hemisphere of the brain for successful osmotic BBB disruption. The common carotid artery (CCA) can be permanently ligated without ischemic damage to the brain. However, clamping the CCA temporarily (only during the osmotic infusion) is recommended to ensure flow towards the brain during infusion while maintaining normal physiological state of the animal for as long as possible. ACA; anterior cerebral artery, MCA: middle cerebral artery, PCA: posterior cerebral artery. Recreated based on Ref. (31)

Although similar concentration, dose and route of infusion are used to deliver mannitol in the studies of Table 3-4, there were some differences in concentration and route of delivery of  $\text{MnCl}_2$ . This information is summarized in Table 3-5. Infusion of  $\text{MnCl}_2$  via the femoral vein has the advantage of fairly simple surgical preparation for catheter placement. However,  $\text{MnCl}_2$  infused into the femoral vein is directed towards the heart and can result in cardiac arrest at high concentrations of  $\text{MnCl}_2$  or at rapid infusion rates (unpublished results). Additionally, if  $\text{MnCl}_2$  infusion via the femoral vein is initiated prior to osmotic disruption of the BBB, further stress on the heart by the subsequent mannitol infusion (66) can lead to death. A safer route of  $\text{MnCl}_2$  infusion is via the external carotid artery. The same catheter employed for BBB disruption can also be used for delivery

of  $\text{MnCl}_2$ , as long as the catheter is warmed (to 37 °C if mannitol is used and remains within tubing) between infusions. An alternative is to flush the catheter with saline between infusions.

Male Rat Species	Dose of $\text{MnCl}_2$ [ $\text{MnCl}_2$ ]	$\text{MnCl}_2$ : Route of infusion / Rate of infusion	Reference
Sprague-Dawley	3.6 $\mu\text{mol}/\text{min}$ 120 mM	Femoral vein / 1.8 ml/h	Lin <i>et al.</i> (1)
Sprague-Dawley	4.0 $\mu\text{mol}/\text{min}$ (0.7 - 1.0 ml) 120 mM	Femoral vein / 2.0 ml/h	Duong <i>et al.</i> (55)
Wistar-Hamamatsu	2.1 – 3.0 $\mu\text{mol}/\text{min}$ (1.1 – 1.6 ml) 100 mM	Femoral vein / 1.25 – 1.8 ml/h	Morita <i>et al.</i> (67)
Wistar	3.97 $\mu\text{mol}/\text{min}$ (1.7 ml) 74.5 mM	Right Carotid Artery / 3.2 ml/h	Aoki <i>et al.</i> (56)
Wistar	1.0 $\mu\text{mol}/\text{min}$ (0.3ml) 10 mM	Right External Carotid Artery / 4.5 ml/h	Aoki <i>et al.</i> (68)
Sprague-Dawley	3.97 $\mu\text{mol}/\text{min}$ (1.7 ml) 74.5 mM	Femoral vein / 3.2 ml/h	Henning <i>et al.</i> (5)

Table 3-5:  $\text{MnCl}_2$  dose, concentration, route and rate of infusion in previous MEMRI experiments.

#### *MEMRI with $\text{MnCl}_2$ – $T_1$ -Enhancement Due to the BBB-Disruption Process*

Ideally, in MEMRI experiments that utilize osmotic BBB disruption, the BBB-opening process itself should not result in  $\text{Mn}^{2+}$ -induced  $T_1$ -enhancement. Such enhancement may obscure or confound any subsequent changes in  $T_1$  contrast that might arise from a specific neuronal stimulus. Based on the six references in Table 3-4 and 3-5, two show dynamic data that includes MR signal intensity before, during, and after mannitol infusion. This data is reproduced here as Figure 3-16 and 3-17.

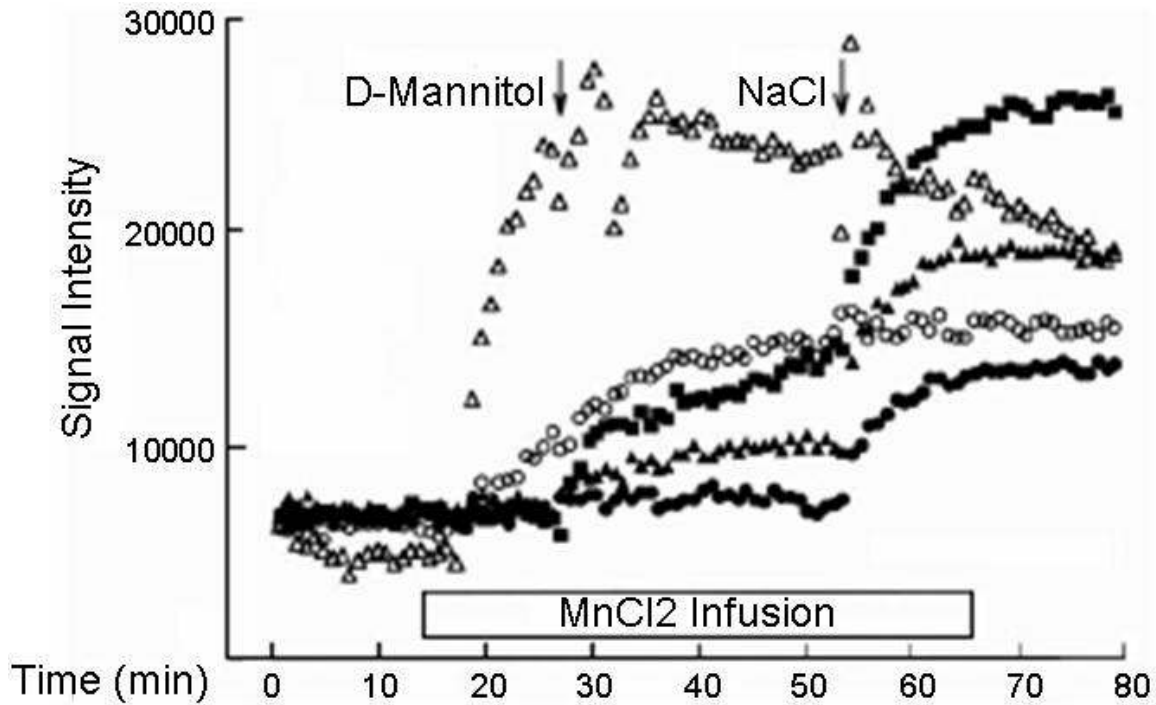


Figure 3-16: Time course of  $T_1$ -weighted MRI signal intensity changes in the cortex (■), paraventricular hypothalamic nucleus (●), lateral habenular nucleus (▲), lateral ventricle (○), and superior sagittal sinus (Δ) in rat brain. Time 0 is the start of MR imaging. The period of  $MnCl_2$  infusion is shown by the horizontal bar and the points at which the mannitol and NaCl injections were given are shown by the arrows. Reproduced from Ref. (67).

Data points shown in Figures 3-16 and 3-17 are MR signal intensity values in various regions of the brain as a function of time relative to the initiation of  $MnCl_2$ , mannitol, glutamate, and NaCl infusion. As shown in Figure 3-16, brain MR signal intensity changes due to  $MnCl_2$  infusion alone do not vary as a function of time except in the lateral ventricle and the superior sagittal sinus. Following mannitol infusion, however, significant signal changes are detected in the ventricle and the cortex. Following BBB disruption (and with concurrent  $MnCl_2$  infusion), the injection of glutamate – an excitatory neurotransmitter – initiates  $Mn^{2+}$  uptake into excitable cells. The resulting increase in  $T_1$ -weighted MR signal intensity allows visualization of the excited brain regions. From Figure 3-17, it is apparent that glutamate administration is associated with further MR signal-intensity increases; however, the relative change is somewhat obscured by the previous signal increase observed following BBB disruption by mannitol. Although the specifics of the two experiments depicted in Figure 3-16 and 3-17 are different, such as delivery route and concentration of  $MnCl_2$ , there is a clear need to monitor MR signal intensity after disrupting the BBB. Non-



specific changes in  $T_1$ -contrast, such as those shown in Figure 3-16 and 3-17, could be misinterpreted as brain activity resulting from a specific neuronal stimulus.

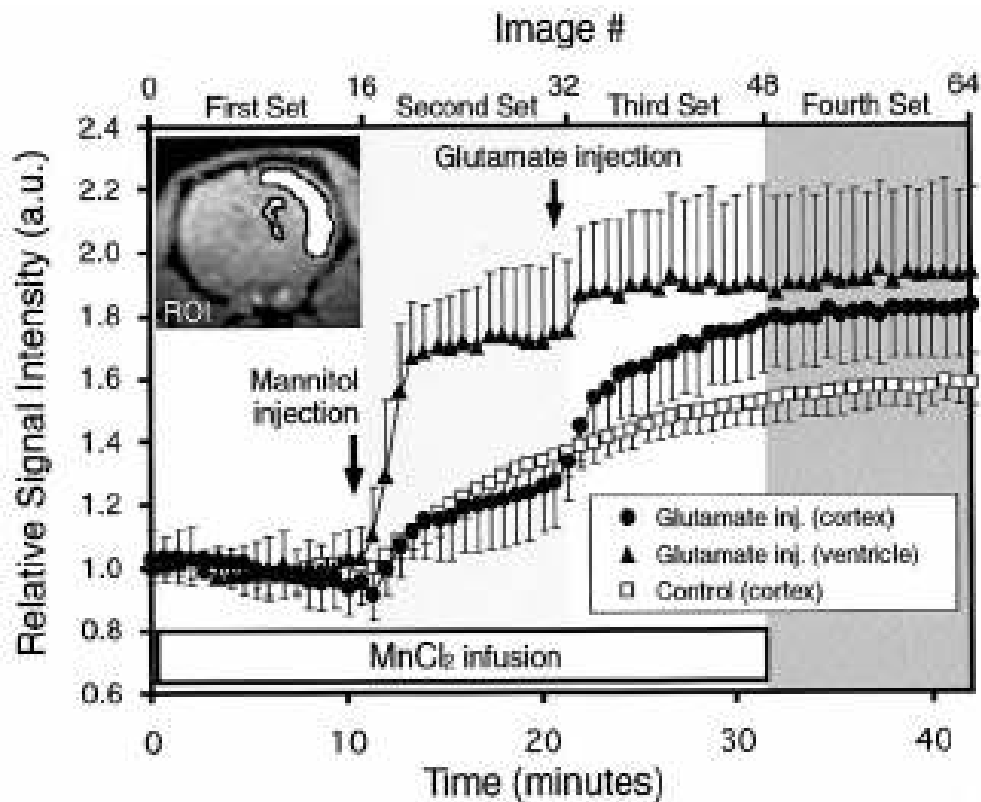


Figure 3-17: Typical dynamic activity-induced time-courses of relative signal intensities in the cortex and ventricle obtained from the glutamate administration (filled symbols) and control (open squares) groups. The inset indicates typical ROIs. The first set of images (#1-16) was obtained before D-mannitol administration, but after start of  $MnCl_2$  infusion. The second set (#17-32) was obtained before injection of glutamate, but after opening the BBB with mannitol. The signal increases significantly, in a non-specific manner, following opening of the BBB. The third set (#33-48) was obtained after glutamate injection. The signal intensity in the cortex of the glutamate-administration group (filled circles) increases substantially after glutamate injection, but not in the control group following saline administration (open squares). The fourth set (#49-64) was obtained during rest after cessation of the  $MnCl_2$  infusion. Reproduced from Ref. (56).

#### *MEMRI with $MnCl_2$ after BBB Disruption – The Importance of Anesthetic Depth*

In addition to non-specific  $T_1$ -contrast due to the BBB disruption process, insufficient levels of anesthetic have been shown to result in  $Mn^{2+}$ -induced  $T_1$ -contrast in MR images. Lin and Koretsky showed that when halothane anesthetic level was reduced from 1.3% to 0.3%, large non-specific signal intensity changes were seen in the  $Mn^{2+}$ -loaded brain after BBB disruption by

mannitol (1). Figure 3-18 is a reproduction of images acquired by this group under these circumstances. Clearly, the level of anesthesia is critical for suppression of non-specific  $T_1$ -enhancement in MEMRI experiments. Curiously, however, the subject of anesthesia and the electrical state of brain during MEMRI experiments has not been discussed in depth in the literature. A brief discussion of depth of anesthesia, as it relates to MEMRI, has been reported as a subsection in an article by Aoki *et al.* (57). An important conclusion by these investigators, with regard to anesthetics and MEMRI, is that “the optimal anesthetic level is the one that suppresses overall baseline activation without inhibiting activation of intentionally stimulated areas.” Much work is needed to determine the proper level of anesthesia for suppression of baseline brain activity in MEMRI experiments. Comparisons of different anesthetics and anesthetic mixtures are needed to optimize the results from MEMRI experiments that rely on specific neuronal stimuli.

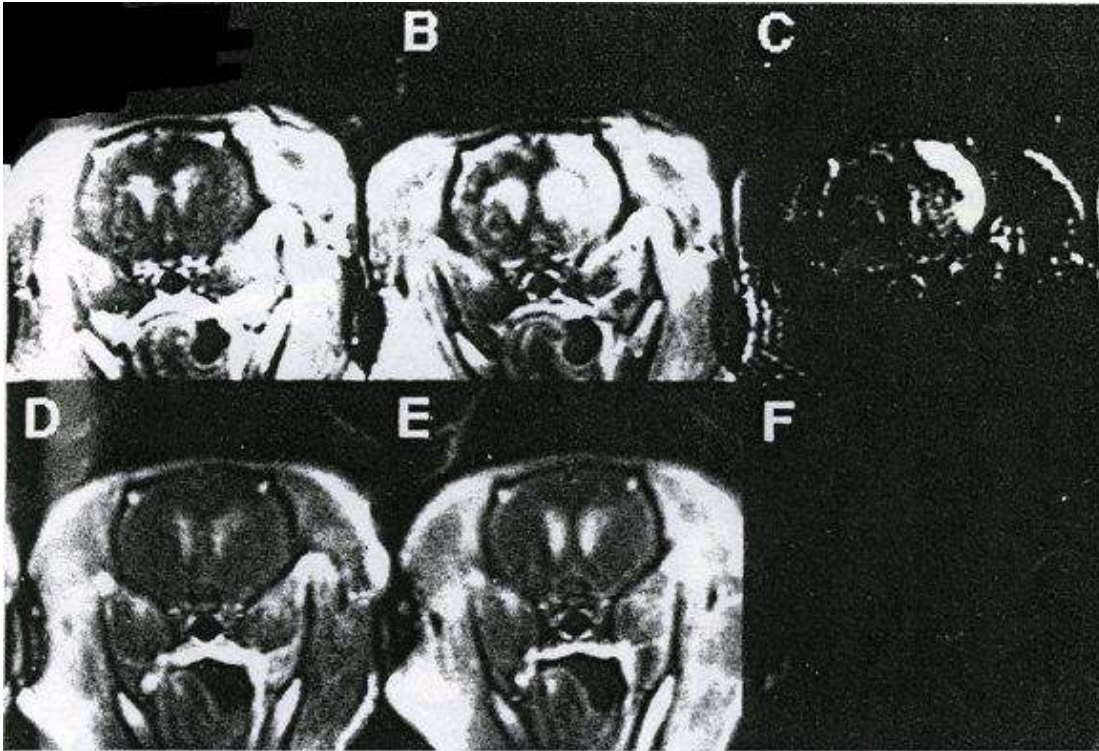


Figure 3-18:  $T_1$ -weighted MRI signal enhancement in the presence of  $MnCl_2$  due to light anesthesia (A, B, and C) and compared with normal anesthesia (D, E, and F). (A,B) Representative images obtained from a rat anesthetized with 0.3% halothane. The steady-state  $MnCl_2$  infusion ( $3.6 \mu\text{mol}/\text{min}$ ) was started 25 min after lowering the halothane dose. (A)  $T_1$ -weighted image obtained 47 min after initiating  $MnCl_2$  infusion with intact BBB. (B)  $T_1$ -weighted image taken 18 min after unilateral BBB opening and 70 min after the onset of  $MnCl_2$  infusion. (C) Difference image formed from (B) – (A). (D,E) Representative images obtained from a rat anesthetized with 1.3% halothane. (D)  $T_1$ -weighted image obtained 37 min after initiating  $MnCl_2$  infusion with an intact BBB. (E)  $T_1$ -weighted image taken 20 min after unilateral BBB opening and 60 min after the onset of  $MnCl_2$  infusion. (F) Difference image formed from (E) – (D). Reproduced from Ref. (1)

## REFERENCES

1. Lin Y.J., Koretsky A.P. Manganese Ion Enhances  $T_1$ -Weighted MRI during Brain Activation: An Approach to Direct Imaging of Brain Function. *Magn Reson Med* 1997;38:378-388.
2. Pautler R.G., Koretsky A.P. Tracing Odor-Induced Activation in the Olfactory Bulbs of Mice Using Manganese-Enhanced Magnetic Resonance Imaging. *Neuroimage* 2002;16:441-448.
3. Pautler R.G., Mongeau R., Jacobs R.E. In Vivo Trans-Synaptic Tract Tracing From the Murine Striatum and Amygdala Utilizing Manganese-Enhanced MRI (MEMRI). *Magn Reson Med* 2003;50:33-39.

4. Aoki I., Lin Wu Y.J., Silva A.C., Lynch R.M., Koretsky A.P. In vivo detection of neuroarchitecture in the rodent brain using manganese-enhanced MRI. *Neuroimage* 2004;22:1046-1059.
5. Henning E.C., Meng X., Fisher M., Sotak C. Visualization of Cortical Spreading Depression Using Manganese-Enhanced MRI. *Magn Reson Med* 2005;53:851-857.
6. Drapeau P., Nachshen D.A. Manganese Fluxes and Manganese-Dependent Neurotransmitter Release in Presynaptic Nerve Endings Isolated From Rat Brain. *J Physiol* 1984;348:493-510.
7. Aschner M., Aschner J.L. Manganese Neurotoxicity: Cellular Effects and Blood-Brain Barrier Transport. *Neurosci and Biobehav Rev* 1991;15:333-340.
8. Brasch R.C. Work in Progress: Methods of Contrast Enhancement for NMR Imaging and Potential Applications. *Radiology* 1983;147:781-788.
9. Lauffer R.B. Paramagnetic Metal Complexes as Water Proton Relaxation Agents for NMR Imaging: Theory and Design. *Chem Rev* 1987;87:901-927.
10. Runge V.M., Nelson K.L. Contrast Agents. In: Stark D., Bradley W.G. Jr., editors. *Magnetic Resonance Imaging*. 3 ed. Volume 1. St. Louis: Mosby, Inc.; 1998.
11. Runge V.M., Stewart R.G., Clanton J.A., Jones M.M., Lukehart C.M., Partain C.L., James A.E. Jr. Work in Progress: Potential Oral and Intravenous Paramagnetic NMR Contrast Agents. *Radiology* 1983;147:789-791.
12. Levitan I.B., Kaczmarek L.K. Signaling in the Brain. *The Neuron: Cell and Molecular Biology*. New York Oxford: Oxford University Press; 1997.
13. Augustine G.J. Synaptic Transmission. In: Purves Dale, editor. *Neuroscience*. 2 ed. Sunderland, MA: Sinauer Associates, Inc; 2001.
14. Narita K., Kawasaki F., Kita H. Mn and Mg influxes through Ca channels of motor nerve terminals are prevented by verapamil in frogs. *Brain Res* 1990;510:289-295.
15. Hunter D.R., Haworth R.A., Berkoff H.A. Cellular Manganese Uptake by the Isolated Perfused Rat Heart: a Probe for the Sarcolemma Calcium Channel. *J Mol Cell Cardiology* 1981;13:823-832.
16. Hunter D.R., Komai H., Haworth R.A., Jackson M.D., Berkoff H.A. Comparison of  $\text{Ca}^{2+}$ ,  $\text{Sr}^{2+}$ , and  $\text{Mn}^{2+}$  Fluxes in Mitochondria of the Perfused Rat Heart. *Circ Res* 1980;47:721-727.
17. Gavin C.E., Gunter K.K., Gunter T.E. Manganese and calcium transport in mitochondria: implications for manganese toxicity. *Neurotoxicology* 1999;20:445-454.
18. Cooper G.P., Suszkiw J.B., Manalis R.S. Presynaptic Effects of Heavy Metals. In: Narahashi Toshio, editor. *Cellular and Molecular Neurotoxicology*. New York: Raven Press; 1984.
19. Misselwitz B., Muhler A., Weinmann H.J. A Toxicologic Risk for Using Manganese Complexes? A Literature Survey of Existing Data Through Several Medical Specialties. *Invest Radiol* 1995;30:611-620.
20. Argent B.E., Case R.M., Hirst F.C. The effects of manganese, cobalt, and calcium on amylase secretion and calcium homeostasis in rat pancreas. *J Physiol* 1982;323:353-375.
21. Barbeau A. Manganese and extrapyramidal disorders. *Neurotoxicology* 1984;5:13-36.
22. Nelson K., Golnick J., Korn T., Angle C. Manganese encephalopathy: utility of early magnetic resonance imaging. *British J Ind Med* 1993;50:510-513.
23. Newland M.C., Cox C., Hamada R., Oberdoerster G., Weiss B. The clearance of manganese chloride in the primate. *Fundam Appl Toxicol* 1987;9:314-328.
24. Zhang P., Anglade P., Hirsch E.C., Javoy-Agid F., Agid Y. Distribution of manganese-dependent superoxide dismutase in the human brain. *Neuroscience* 1994;6:317-330.

25. Roth J., Garrick M. Iron interactions and other biological reactions mediating the physiological and toxic actions of manganese. *Biochem Pharma* 2003;66:1-13.
26. Roth J.A., Horbinski C., Higgins D., Lein P., Garrick M.D. Mechanisms of manganese-induced rat pheochromocytoma (PC12) cell death and cell differentiation. *Neurotoxicology* 2002;23:147-157.
27. Gavin C.E., Gunter K., Gunter T.E. Mn<sup>2+</sup> sequestration by mitochondria and inhibition of oxidative phosphorylation. *Toxicol Appl Pharmacol* 1992;115:1-5.
28. Chen C. J., Liao S. L. Oxidative stress involves in astrocytic alterations induced by manganese. *Exp Neurol* 2002;175:216-225.
29. Abrams E., Lassiter J. W., Miller W. J., Neathery M. W., Gentry R. P., Scarth R. D. Absorption as a factor in manganese homeostasis. *J Anim Sci* 1976;42:630-636.
30. Kreft B. P., Baba Y., Tanimoto A., Finn J. P., Stark D. D. Orally administered manganese chloride: enhanced detection of hepatic tumors in rats. *Radiology* 1993;186:543-548.
31. Takeda A., Akiyama T., Sawashita J., Okada S. Brain uptake of trace metals, zinc and manganese, in rats. *Brain Res* 1994;640:341-344.
32. Cottrell G. T., Ferguson A. V. Sensory circumventricular organs: central roles in integrated autonomic regulation. *Regul Pept* 2004;117:11-23.
33. Shibata O., Tanaka J., Nomura M. Non-NMDA glutamatergic receptors modulate acetylcholine release in the rat subfornical organ area. *Auton Neurosci* 2006;124:96-102.
34. McKinley M. J., McAllen R. M., Davern P., Giles M. E., Penschow J., Sunn N., Uschakov A., Oldfield B. J. The sensory circumventricular organs of the mammalian brain. *Adv Anat Embryol Cell Biol* 2003;172:III-XII, 1-122, back cover.
35. Zheng W., Kim H., Zhao Q. Comparative Toxicokinetics of Manganese Chloride and Methylcyclopentadienyl Manganese Tricarbonyl (MMT) in Sprague-Dawley Rats. *Toxicol Sci* 2000;54:295-301.
36. Klaassen C. D. Biliary excretion of manganese in rats, rabbits, and dogs. *Toxicol Appl Pharmacol* 1974;29:458-468.
37. Keefer R. C., Barak A. J., Boyett J. D. Binding of manganese and transferrin in rat serum. *Biochim Biophys Acta* 1970;221:390-393.
38. Davidsson L., Lonnerdal B., Sandstrom B., Kunz C., Keen C. Identification of Transferrin as the Major Plasma Carrier Protein for Manganese Introduced Orally or Intravenously or After In Vitro Addition in the Rat. *J Nutrition* 1989;119:1461-1464.
39. Nagy J.I., Carter D.A., Fibiger H.C. Evidence for a GABA-containing projection from the entopeduncular nucleus to the lateral habenula in the rat. *Brain Res* 1978;145:360-364.
40. Mosher T.J., Lacey P.G., Barron T.F., McNamara K.P., Devenyi A.G. Increased signal intensity in the basal ganglia on T<sub>1</sub>-weighted MRI correlates with elevated erythrocyte manganese in patients with chronic liver disease. 1994; San Francisco.
41. Aschner M., Gannon M. Manganese (Mn) Transport Across the Rat Blood-Brain Barrier: Saturable and Transferrin-dependent Transport Mechanisms. *Brain Res Bull* 1994;33:345-349.
42. Aschner M. The transport of manganese across the blood-brain barrier. *Neurotoxicology* 2006;27:311-314.
43. Dickinson T. K., Devenyi A. G., Connor J. R. Distribution of injected iron 59 and manganese 54 in hypotransferrinemic mice. *J Lab Clin Med* 1996;128:270-278.

44. Gunshin H., Mackenzie B., Berger U. V., Gunshin Y., Romero M. F., Boron W. F., Nussberger S., Gollan J. L., Hediger M. A. Cloning and characterization of a mammalian proton-coupled metal-ion transporter. *Nature* 1997;388:482-488.
45. Crossgrove J. S., Yokel R. A. Manganese distribution across the blood-brain barrier. IV. Evidence for brain influx through store-operated calcium channels. *Neurotoxicology* 2005;26:297-307.
46. Fitsanakis V.A., Piccola G., Aschner J.L., Aschner M. Characteristics of manganese (Mn) transport in rat brain endothelial (RBE4) cells, an *in vitro* model of the blood-brain barrier. *NeuroToxicology* 2006;27:60-70.
47. Malecki E., Devenyi A., Beard J., Connor J. Transferrin response in normal and iron-deficient mice heterozygotic for hypotransferrinemia; effects on iron and manganese accumulation. *Biometals* 1998;11:265-276.
48. Tirkkonen B., Aukrust A., Couture E., Grace D., Haile Y., Holm K.M., Hope H., Larsen A., Lunde H.S., Sjogren C.E. Physicochemical Characterisation of Manganofodipir Trisodium. *Acta Radiologica* 1997;38:780-789.
49. Toft K.G., Hustvedt S.O., Grant D., Martinsen I., Gordon P.B., Friisk G.A., Korsmo A.J., Skotland T. Metabolism and Pharmacokinetics of MnDPDP in Man. *Acta Radiologica* 1997;38:677-689.
50. Ni Y., Petre C., Bosmans H., Miao Y., Grant D., Baert A. L., Marchal G. Comparison of manganese biodistribution and MR contrast enhancement in rats after intravenous injection of MnDPDP and MnCl<sub>2</sub>. *Acta Radiol* 1997;38:700-707.
51. Grant D., Zech K., Holtz E. Biodistribution and *in vivo* stability of manganese dipyridoxyl diphosphate in relation to imaging efficacy. *Invest Radiol* 1994;29:S249.
52. Lim K.O., Stark D.D., Leese P.T., Pfefferbaum A., Rocklage S.M., Quay S.C. Hepatobiliary MR Imaging: First Human Experience with MnDPDP. *Radiology* 1991;178:79-82.
53. Joarder R., de Jode M., Lamb G. A., Gedroyc W. M. The value of MnDPDP enhancement during MR guided laser interstitial thermoablation of liver tumors. *J Magn Reson Imaging* 2001;13:37-41.
54. Silva A.C., Lee J.H., Aoki I., Koretsky A.P. Manganese-enhanced magnetic resonance imaging (MEMRI): methodological and practical considerations. *NMR In Biomed* 2004;17:532-543.
55. Duong T.Q., Silva A.C., Lee S.P., Kim S.G. Functional MRI of calcium-dependent synaptic activity: cross correlation with CBF and BOLD measurements. *Magn Reson Med* 2002;43:383-392.
56. Aoki I., Tanaka C., Takegami T., Ebisu T., Umeda M., Fukunaga M., Fukuda K., Silva A.C., Koretsky A.P., Naruse S. Dynamic activity-induced manganese-dependent contrast magnetic resonance imaging (DAIM MRI). *Magn Reson Med* 2002;48:927-933.
57. Aoki I., Naruse S., Tanaka C. Manganese-enhanced magnetic resonance imaging (MEMRI) of brain activity and applications to early detection of brain ischemia. *NMR In Biomed* 2004;17:569-580.
58. Pautler R.G., Silva A.C., Koretsky A.P. *In Vivo* neuronal tract tracing using manganese-enhanced magnetic resonance imaging. *Magn Reson Med* 1998;40:740-748.
59. Lee J.H., Silva A.C., Merkle H., Koretsky A.P. Manganese-Enhanced Magnetic Resonance Imaging of Mouse Brain after Systemic Administration of MnCl<sub>2</sub>: Dose-Dependent and Temporal Evolution of *T*<sub>1</sub> Contrast. *Magn Reson Med* 2004;53:640-648.

60. Hu T.C., Pautler R.G., MacGowan G.A., Koretsky A.P. Manganese-enhanced MRI of mouse heart during changes in inotropy. *Magn Reson Med* 2001;46:884-890.
61. Watanabe T., Natt O., Boretius S., Frahm J., Michaelis T. *In vivo* 3D MRI staining of mouse brain after subcutaneous application of MnCl<sub>2</sub>. *Magn Reson Med* 2002;48:852-859.
62. London R.E., Toney G., Gabel S.A., Funk A. Magnetic Resonance Imaging Studies of the Brains of Anesthetized Rats Treated With Manganese Chloride. *Brain Res Bull* 1989;23:229-235.
63. Lie C.H., D'Arceuil H.E., de Crespigny A.J. Direct CSF Injection of MnCl<sub>2</sub> for Dynamic Manganese-Enhanced MRI. *Magn Reson Med* 2004;51:978-987.
64. Ogawa S., Menon R. S., Tank D. W., Kim S. G., Merkle H., Ellermann J. M., Ugurbil K. Functional brain mapping by blood oxygenation level-dependent contrast magnetic resonance imaging. A comparison of signal characteristics with a biophysical model. *Biophys J* 1993;64:803-812.
65. Rapoport S. I. Microinfarction: osmotic BBB opening or microcrystals in infusate? *J Neurosurg* 1991;74:685.
66. Cosolo W.C., Martinello P., Louis W.J., N. Christophidis. Blood-brain barrier disruption using mannitol: time course and electron microscopy studies. *Am J Physiol* 1989R443-R448.
67. Morita H., Ogino T., Seo Y., Fujiki N., Tanaka K., Takamata A., Nakamura S., Murakami M. Detection of hypothalamic activation by manganese ion contrasted T<sub>1</sub>-weighted magnetic resonance imaging in rats. *Neurosci Lett* 2002;326:101-104.
68. Aoki I., Ebisu T., Tanaka C., Katsuta K., Fujikawa A., Umeda M., Fukunaga M., Takegami T., Shapiro E., Naruse S. Detection of the Anoxic Depolarization of Focal Ischemia Using Manganese-Enhanced MRI. *Magn Reson Med* 2003;50:7-12.

# CHAPTER 4

## Nonspecific $T_1$ -Weighted Manganese Enhancement in Rat Brain Correlates with Evans Blue Staining After Osmotic Blood-Brain Barrier Disruption

### Introduction

Challenges in MEMRI

Evans Blue as a Marker for Osmotic Blood-Brain Barrier (BBB) Disruption

Co-Infusion of  $MnCl_2$  and Evans Blue (EB) Dye as a Qualitative Method for Validating  $MnCl_2$

Distribution in Brain

Experimental Design to Test Mechanisms of Nonspecific MEMRI Signal-Enhancement

Relevance of Experiments to Future Work

### Methods

Animal Preparation

Osmotic BBB Disruption and  $MnCl_2$ +Evans Blue (EB) Administration

Timing of Drug Administration

Level of Anesthetic During  $MnCl_2$ +EB Infusion

EB Stain Histology

MRI Measurements

Data Analysis

Statistical Analysis

### Results

MEMRI Signal-Enhancement

Evans Blue (EB) Stain

Correlation Between Regions of MEMRI Signal-Enhancement and Evans Blue Staining

### Discussion

Isoflurane and Halothane Level and Nonspecific MEMRI Signal-Enhancement

Nonspecific  $T_1$ -Enhancement after Osmotic BBB Disruption

Cellular Uptake of  $MnCl_2$ +Evans Blue (EB) Dye after Osmotic BBB Disruption



# Nonspecific $T_1$ -Weighted Manganese Enhancement in Rat Brain Correlates with Evans Blue Staining After Osmotic Blood-Brain Barrier Disruption

David G. Bennett<sup>1</sup>, Nils Henninger<sup>3</sup>, Marc Fisher<sup>3,4</sup>, Christopher H. Sotak<sup>1,2,4</sup>

Departments of Biomedical Engineering<sup>1</sup> and Chemistry & Biochemistry<sup>2</sup>

Worcester Polytechnic Institute

Worcester, Massachusetts 01609

Department of Neurology<sup>3</sup>

University of Massachusetts Memorial Healthcare – Memorial Campus

Worcester, Massachusetts 01605

Department of Radiology<sup>4</sup>

University of Massachusetts Medical School

Worcester, Massachusetts 01605

Part of this work was presented at the 13<sup>th</sup> annual meeting of the International Society of Magnetic Resonance in Medicine, Miami Beach, FL, USA, 2005.

*Manuscript in Progress*

## Abstract

Blood-Brain Barrier (BBB) opening was visualized using manganese-enhanced MRI (MEMRI) following hyperosmotic disruption of the endothelial cells in the cerebral vasculature of the rat brain. BBB disruption was verified histologically using Evans Blue (EB) staining. Evans Blue dye was mixed with  $\text{MnCl}_2$  to provide a means of tracing the distribution of i.v. administered  $\text{Mn}^{2+}$  in brain following osmotic BBB disruption. Nonspecific MEMRI signal increase (MEMRI signal-enhancement) was observed following infusion of 5ml/kg 1.6M arabinose into the internal carotid artery. Relative to the contralateral control region, MEMRI signal-enhancement was: (1)  $81\% \pm 23\%$  in animals anesthetized with 2% isoflurane ( $\text{MnCl}_2$ +EB infused two minutes after osmotic BBB disruption); (2)  $77\% \pm 22\%$  in animals anesthetized with 3% isoflurane ( $\text{MnCl}_2$ +EB infused two minutes after osmotic BBB disruption); (3)  $76\% \pm 33\%$  in animals infused with  $\text{MnCl}_2$ +EB ten minutes following osmotic BBB disruption (2% isoflurane anesthesia); and (4) 42% in one animal infused with  $\text{MnCl}_2$  only. A significant difference ( $P < 0.05$ ) in MEMRI signal-enhancement was found between the animal infused with  $\text{MnCl}_2$  only (ten minutes after osmotic BBB disruption, 2% isoflurane) and animals infused with  $\text{MnCl}_2$ +EB (two minutes after BBB disruption, 2% isoflurane). MEMRI signal-enhancement was seen in the hippocampus (CA1-CA3), cortex, caudate putamen, hypothalamus and geniculate nucleus. A quantitative comparison of brain regions with MEMRI signal-enhancement and those stained on Evans Blue histological sections showed good correlation and correspondence between the two methods. It is not likely that MEMRI signal-enhancement, as reported here, is due to the uptake of manganese into active brain cells as a result of low anesthetic depth. We hypothesize that nonspecific MEMRI signal-enhancement is due to diffuse uptake of  $\text{Mn}^{2+}$  by brain cells adjacent to endothelial-cell tight junctions undergoing osmotic transitions or by irreversibly damaged neurons. The results from this study suggest that the osmotic BBB-opening process itself gives rise to non-specific MEMRI signal-enhancement following  $\text{MnCl}_2$  administration. This source of MEMRI signal-enhancement confounds the interpretation of data from experiments that attempt to visualize a specific neuronal stimulus in the brain using the same method. Alternatively, MEMRI may prove to be a useful method for imaging experimental BBB disruption as a result of disease.

**Key words:** manganese-enhanced MRI, blood-brain barrier, osmotic shock, rat brain

## 4.1 Introduction

Manganese has recently been reported as a cell membrane depolarization-dependent magnetic resonance (MR) contrast agent useful for functional imaging (1), neuronal fiber tracking (2,3), and ischemia detection in the brain (4,5). The manganese ion,  $Mn^{2+}$ , has an ionic radius and charge similar to calcium and is treated similarly to calcium in biological systems (6). With five unpaired electrons,  $Mn^{2+}$  is a strong paramagnetic cation and thus useful as a MR contrast agent. The  $T_1$  and  $T_2$  relaxation times of cellular water can be significantly reduced when  $Mn^{2+}$  enters glia and/or neurons through voltage-gated calcium channels during nerve action potentials (1,6). This mode of  $Mn^{2+}$  entry is supported by observations that the calcium-channel blocker verapamil can inhibit the influx of  $Mn^{2+}$  into cells (7). The manganese-induced changes in  $T_1$  result in localized increases in signal intensity on  $T_1$ -weighted MR images (i.e., MEMRI signal-enhancement). Experiments using MEMRI to image brain function rely on delivery of divalent manganese ion ( $Mn^{2+}$ ) to the brain parenchyma via an osmotically-disrupted blood-brain barrier (BBB). Subsequent brain activation results in cellular uptake of  $Mn^{2+}$  through voltage-gated calcium channels. Ideally, the action of osmotic BBB disruption does not itself induce cellular uptake of  $Mn^{2+}$  that would give rise to MEMRI signal-enhancement. However, if this is not the case, any change in  $T_1$  contrast by the action of osmotic BBB disruption could potentially obscure subsequent MEMRI signal-enhancement related to a specific neuronal stimulus.

### 4.1.1 Challenges in MEMRI

#### *Non-Specific MEMRI Signal-Enhancement in MEMRI Experiments*

Monitoring specific brain activity using MEMRI requires minimal activity in brain due to baseline neuronal activity, environmental stimuli and/or physiological state of the animal. These factors can be controlled by deep anesthesia, pain relief, immobilizing drugs, and physiological monitoring during the experiment. Lin and Koretsky showed the importance of anesthetic depth in preventing unintended (i.e., non-specific) brain activity during an MEMRI experiment (1). During their experiment, halothane anesthetic was reduced from 1.3% to 0.3% resulting in non-specific MEMRI signal-enhancement. Aoki *et al.* (4) also detected non-specific brain activity on MEMRI

when animals were anesthetized with 2.5% isoflurane; experienced brain swelling (after mannitol injection); and responded to MR scanner acoustic noise. A summary of images acquired by Aoki *et al.* is given in Figure 4-1.

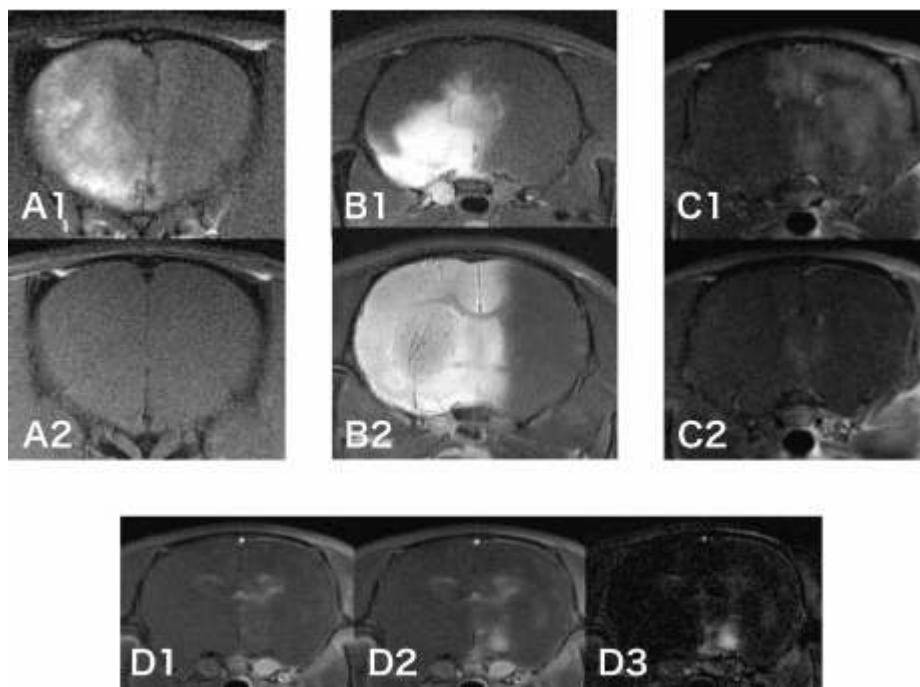


Figure 4-1: Brain swelling after mannitol injection (A), inhomogeneous BBB disruption and MEMRI signal-enhancement after infusions of glutamate (B), MEMRI signal-enhancement due to acoustic noise from gradient coil (C), and MEMRI signal-enhancement in lateral hypothalamus without stimulation 15 min after  $\text{MnCl}_2$  administration (D). (A) Images obtained from a rat on 2.0% halothane without control of intracranial pressure (A1) and with pre-infusion of 15% mannitol (A2, 0.25 ml/min) before BBB disruption. (B) MEMRI signal-enhancement obtained after 25mM  $\text{MnCl}_2$  and glutamate mixture injection with BBB disruption. Inhomogeneous BBB disruption was observed after Anti-EBA injection in this case (B1). MEMRI signal-enhancement was homogeneous after  $\text{MnCl}_2$  and glutamate injection in the case (B2). (C) Moderate MEMRI signal-enhancement was observed over the entire cortex and caudate-putamen without (C1) and with (C2) earplug for blocking noise from the magnetic-field-gradient coils used for MRI. (D)  $T_1$ -weighted images obtained immediately (D1) and 15 min (D2) after 25 mM  $\text{MnCl}_2$  injection from carotid artery without any stimulation under 2.5% isoflurane. MEMRI signal-enhancement in the lateral hypothalamus was observed on the difference image (D3) formed from (D2) – (D1). Reproduced from Ref. (4).

Non-specific MEMRI signal changes following osmotic BBB disruption in presence of intravascular  $\text{Mn}^{2+}$  were also observed in rats anesthetized with urethane/ $\alpha$ -chloralose mixture (8) and chloral hydrate (9). Therefore, although low levels of anesthetic are detrimental for certain

MEMRI experiments, the timing of osmotic BBB disruption relative to  $Mn^{2+}$  infusion may also contribute significantly to unwanted non-specific MEMRI signal-enhancement.

#### *Delivery of Mn into Brain - Challenges at the Blood-Brain Barrier (BBB)*

A technical challenge accompanying certain MEMRI experiments is the introduction of  $Mn^{2+}$  into the brain extracellular space prior to a specific neuronal stimulus.  $Mn^{2+}$  in blood plasma crosses from blood into brain via carrier-mediated processes at the blood-brain barrier (BBB) but this process is relatively slow. For MEMRI experiments investigating brain response to specific neuronal stimuli, the  $Mn^{2+}$  must be present in the brain parenchyma at the time of neuronal stimulus to ensure that different levels and/or regions of MEMRI signal-enhancement accurately reflect different levels and/or regions of brain activity, respectively. The  $Mn^{2+}$  is generally delivered to the interstitial space by disrupting the blood-brain barrier (BBB) by infusion of hyperosmolar sugar (mannitol or arabinose) solution (osmotic BBB disruption). Recent MEMRI experiments report no MEMRI signal-enhancement as a result of osmotic BBB disruption (1,9); however, these and other recent MEMRI experiments have not reported evidence of the degree of BBB disruption (1,5,8-11). Without evidence of BBB disruption, the distribution of  $Mn^{2+}$  in the brain prior to neuronal stimulus is assumed to be spatially homogeneous. This assumption may prove false leading to inaccurate interpretation of images during MEMRI experiments. Additionally, BBB disruption may be spatially heterogeneous resulting in higher concentrations of  $Mn^{2+}$  being delivered to certain regions. Heterogeneous MEMRI signal-enhancement in this situation can be difficult to interpret with respect to the regional response to brain activation.

#### **4.1.2 Evans Blue as a Marker for Osmotic BBB Disruption**

The BBB – located at the cerebrovascular endothelium – prevents passage of proteins, electrolytes, and water-soluble non-electrolytes from blood into the brain. To open the BBB to non-permeable substances – such as chemotherapeutic drugs – the BBB can be disrupted by infusion of hyperosmolar mannitol (12) or arabinose (13) solutions. Evans Blue (EB) dye (a tetrasodium diazo organic salt with MW = 960.8 (14)) has been used for several decades as a means to measure the integrity of the BBB in animals after hyperosmotic insult (13,15,16). The pure dye, or the dye bound to serum albumin, is excluded from the brain by a healthy intact BBB.

### 4.1.3 Co-Infusion of $\text{MnCl}_2$ and Evans Blue (EB) Dye as a Qualitative Method for Validating $\text{MnCl}_2$ Distribution in Brain

After infusion into the bloodstream, Evans Blue (EB) dye binds quickly ( $\leq 5$  min (17)) and strongly (14) to albumin resulting in a molecule with molecular weight of approximately 68,500 Da. Manganese can also bind to albumin in the blood plasma; however, depending on the residence time,  $\text{Mn}^{2+}$  is oxidized to  $\text{Mn}^{3+}$  and then binds preferentially to transferrin at iron (Fe) binding sites (18,19). Critchfield *et al.* (20) showed *in vitro* that  $^{54}\text{Mn}$  binds to several proteins and after 1 minute and 1 hour approximately 15% and 40%, respectively, of the  $^{54}\text{Mn}$  in blood binds to transferrin. During the early stages ( $< 30$  min), most plasma  $\text{Mn}^{2+}$  is bound to a very low molecular weight (VLMW) ligand ( $< 1$  kDa) which may be responsible for regulating the oxidation of  $\text{Mn}^{2+}$  to  $\text{Mn}^{3+}$  (20). The VLMW ligand is not albumin since the protein is known to have a molecular weight of 66.3 kDa (21). Additionally, there is almost no tendency for  $\text{Mn}^{2+}$  to bind to  $-\text{SH}$  groups or to amines and  $\text{Mn}^{2+}$  has very low affinity for endogenous complexing ligands ( $\log_{10}k = 3, 4, 5, \text{ and } 3$ , for glycine, cysteine, riboflavin, and guanosine, respectively, where  $k$  is the affinity constant) (22,23). Although Mn and EB bind to different serum proteins in blood – resulting in different size molecules – in a solution containing Mn and EB, both protein complexes are expected to have similar access to the brain parenchyma following osmotic disruption of the BBB.

Indeed, Ziylan and coworkers suggest that convective bulk flow contributes to molecular size-independent BBB transfer following osmotic BBB disruption (24). The physiological evidence to support bulk flow following osmotic BBB disruption is a transient increase of 1-1.5% in brain water content 10 minutes after hyperosmolar arabinose infusion into rat brain (13). Consequently, for blood infused with a solution of both  $\text{Mn}^{2+}$  and EB, the evidence suggests that since the two substances will not compete for binding to the same serum protein, the protein complexes of both compounds will be transported across the osmotically-disrupted BBB to a similar extent. One aim of this study is to use EB dye to provide evidence of BBB opening in MEMRI experiments by co-infusing EB dye with  $\text{Mn}^{2+}$  following disruption with hyperosmotic arabinose. Since EB dye is a known marker for BBB integrity (12), co-infusing EB with  $\text{Mn}^{2+}$  should provide a qualitative and quantitative marker for the degree of osmotic BBB disruption as well as the distribution of  $\text{Mn}^{2+}$  in rat brain that could potentially contribute to MEMRI signal-enhancement.

Although  $T_1$  enhancement associated with the  $\text{Mn}^{2+}$  delivery process itself is undesirable, the ability to visualize the spatial extent and degree of BBB disruption could be important. For example, the lack of MEMRI signal-enhancement following a stimulus could result from ineffective delivery

of  $Mn^{2+}$  to the parenchyma of brain regions that are expected to exhibit a neuronal response; potentially confounding the interpretation of the experimental results. Alternatively, MEMRI may be useful for visualizing pathology whose etiology involves BBB disruption.

#### 4.1.4 Experimental Design to Test Mechanisms of Nonspecific MEMRI Signal-Enhancement

In this paper we evaluate the experimental conditions that may give rise to nonspecific MEMRI signal-enhancement following  $Mn^{2+}$  delivery to the brain parenchyma via osmotic BBB disruption. Quantitative characterization of the mechanistic and spatio-temporal aspects of these changes would be helpful in separating MEMRI signal changes associated with  $Mn^{2+}$  delivery from those associated with a particular response to a neuronal stimulus. Specifically, we have designed experiments to test the dependency of non-specific MEMRI signal-enhancement on; 1) anesthetic (isoflurane) level and 2) the timing of  $MnCl_2+EB$  infusion relative to osmotic BBB disruption.

As noted by Aoki *et al.* (4) and Lin *et al.* (1) the anesthetic condition of the animal is important for prevention of non-specific MEMRI signal change. However, in these past studies, data from only one animal is provided. In the current study, therefore, we propose a controlled study of anesthetic level and its effect on non-specific MEMRI signal-enhancement following osmotic BBB disruption. In addition, because mannitol causes blood pressure fluctuations in rats that stabilize approximately 2 min following bolus injection (25) we propose to test the dependency of non-specific MEMRI signal- enhancement on the timing of  $MnCl_2$  infusion in relation to osmotic challenge by infusing  $MnCl_2+EB$  2 and 10 minutes after osmotic BBB disruption. We restrict the later  $MnCl_2+EB$  infusion time to 10 minutes in order to correspond to the time window during which the BBB is open to molecules of size large enough to allow entry of  $MnCl_2$  (MW=198), EB (MW=961), and EB bound to serum albumin (MW=68,500) (24). We hypothesize that increasing the level of anesthesia from 2% isoflurane to 3% isoflurane and delaying the infusion time of  $MnCl_2+EB$  from 2 to 10 minutes following osmotic BBB disruption will significantly reduce non-specific MEMRI signal-enhancement.

#### 4.1.5 Relevance of Experiments to Future Work

Ideally, following osmotic BBB disruption, no MEMRI signal-enhancement will be observed allowing for subsequent neuronal stimulus to generate localized  $T_1$ -weighted signal changes in brain.

Specifically, in our pursuit of imaging experimental anoxic depolarization in brain in real-time (in-bore), experimental methods that decrease or eliminate non-specific MEMRI signal changes would be very helpful if not absolutely essential. Therefore, in this chapter we investigate methods to reduce or eliminate unwanted MEMRI signal changes in brain. As a continuation of this work in Chapter 5, we investigate other unwanted side effects of osmotic BBB disruption that can obscure desired MEMRI signal-enhancement and changes in brain that would normally be related specifically to anoxic depolarization and/or stroke. Indeed, Aoki *et al.* have suggested that anoxic depolarization is detectable by MEMRI methods (5), but their work does not include histological evidence of BBB disruption or of tissue damage by anoxic depolarization making their results difficult to interpret.

## 4.2 Methods

### 4.2.1 Animal Preparation

This study was approved by the Institute Animal Care and Use Committee (IACUC) of the University of Massachusetts Medical School (IACUC Protocol A-1756). Male Sprague-Dawley rats (250-360g; Charles River Laboratories, Worcester, MA) were divided into five groups: infusion with  $MnCl_2+EB$  2 minutes following BBB disruption while breathing 2% isoflurane (2% iso/2-min group, N=3), infusion with  $MnCl_2+EB$  2 minutes following BBB disruption while breathing 3% isoflurane (3% iso/2-min group, N=6), infusion with  $MnCl_2+EB$  10 minutes following BBB disruption while breathing 2% isoflurane (2% iso/10-min group, N=4), infusion with EB only while breathing 2% isoflurane (EB control group, N=2), and infusion with  $MnCl_2$  only while breathing 2% isoflurane ( $MnCl_2$ -only group, N=1). Data from the 2% iso/2-min group were compared to the 3% iso/2-min group and the 2% iso/10-min group to monitor potential changes in MEMRI signal-enhancement due to; 1) infusion of  $MnCl_2+EB$  at 2 and 10 minutes following osmotic BBB disruption and 2) an increase in anesthetic level. Three rats in the 3% iso/2-min group died due to severe cardiac depression and were not used for data analysis. Rats were initially anesthetized with 5% isoflurane and maintained at 2% isoflurane during surgery. PE-50 and PE-10 polyethylene catheters were placed in the left femoral vein (i.v.) for blood pressure and gas monitoring and right external carotid artery (ECA) for drug administration, respectively.

For catheterization of the right ECA, a ventral midline incision was made in the neck. The omohyoid muscle was separated longitudinally and retracted laterally to isolate and expose the right



common carotid artery (CCA), ECA, internal carotid artery (ICA) and pterygopalatine artery (PPA). The PPA was permanently ligated. Following temporary clamping of the CCA, the ECA was ligated and a small incision was made into it for placement of the PE-10 catheter. The PE-10 catheter tip was inserted such that the tip would not disturb blood flow in the CCA towards the ICA. After properly securing the PE-10 catheter, the CCA clamp was removed allowing normal blood flow to the right ICA (the CCA was clamped for 10 minutes on average). Cannulation of the right ECA limited drug delivery to the right side of the brain allowing the left side to serve as control. During the surgical procedures, body temperature was continuously monitored with a rectal probe and maintained at 37.0 °C using a thermostatically-controlled heat lamp (Model 73ATD, YSI Inc., Yellow Spring, OH).

#### **4.2.2 Osmotic BBB Disruption and MnCl<sub>2</sub>+Evans Blue Administration**

To disrupt the BBB, 1.6 M L-arabinose or 1.4 M D-mannitol solution (5 ml/kg, Sigma, St. Louis) was infused into the right ECA over a period of 55 seconds using an infusion pump (Model PHD 2000; Harvard Apparatus, Holliston, MA). Two minutes prior to the 55-second infusion of L-arabinose, a slow (6 ml/hr) infusion of L-arabinose – at the same concentration – was initiated and continued for 1 minute in an effort to reduce vasogenic edema induced by the osmotic BBB disruption (4). Physiologically buffered saline (PBS), containing 10mM manganese chloride (MnCl<sub>2</sub>·H<sub>2</sub>O; Sigma, St. Louis) and 2% Evans Blue (EB) (Sigma, St. Louis), was infused into the right ECA at a rate of 4.5 ml/hr using an infusion pump (Model 11; Harvard Apparatus, Holliston, MA) until a volume equivalent to 2 ml/kg was infused. MnCl<sub>2</sub>+EB mixture solution was infused at 2 or 10 minutes following osmotic BBB disruption. Infusion of the MnCl<sub>2</sub>+EB solution in certain animals commenced 2 minutes after arabinose injection to coincide with the optimal time window during which the BBB is maximally open after osmotic disruption (5-10 minutes (12)). Infusion of the MnCl<sub>2</sub>+EB solution in other animals at 10 minutes after arabinose was scheduled to coincide with the optimal time window during which the physiological state of the animal begins to stabilize following intraarterial infusion of hyperosmolar agents (25). To minimize the likelihood of recrystallization in the catheter tubing during infusion, arabinose was chosen as the osmotic agent because of its higher solubility relative to mannitol (a commonly used agent for osmotic BBB disruption). To avoid introduction of any micro-emboli, all solutions were filtered with 0.22 µm syringe filters (Nygene) prior to administration.

### 4.2.3 Timing of Drug Administration

In order to evaluate the effects of administration of  $MnCl_2+EB$  infusion time (relative to BBB disruption) on non-specific MEMRI signal-enhancement, a group of animals received  $MnCl_2+EB$  infusion at 10 minutes after BBB disruption (N=4). Timing of infusions are summarized in Figure 4-2.

### 4.2.4 Level of Anesthetic During $MnCl_2+EB$ Infusion

To determine the effect of different levels of anesthesia on non-specific MEMRI signal-enhancement, animals were subdivided into two groups: infusion of  $MnCl_2+EB$  with animals spontaneously breathing 2% isoflurane in breathing-quality air (N=3) and infusion of  $MnCl_2+EB$  with animals spontaneously breathing 3% isoflurane in breathing-quality air (N=6).

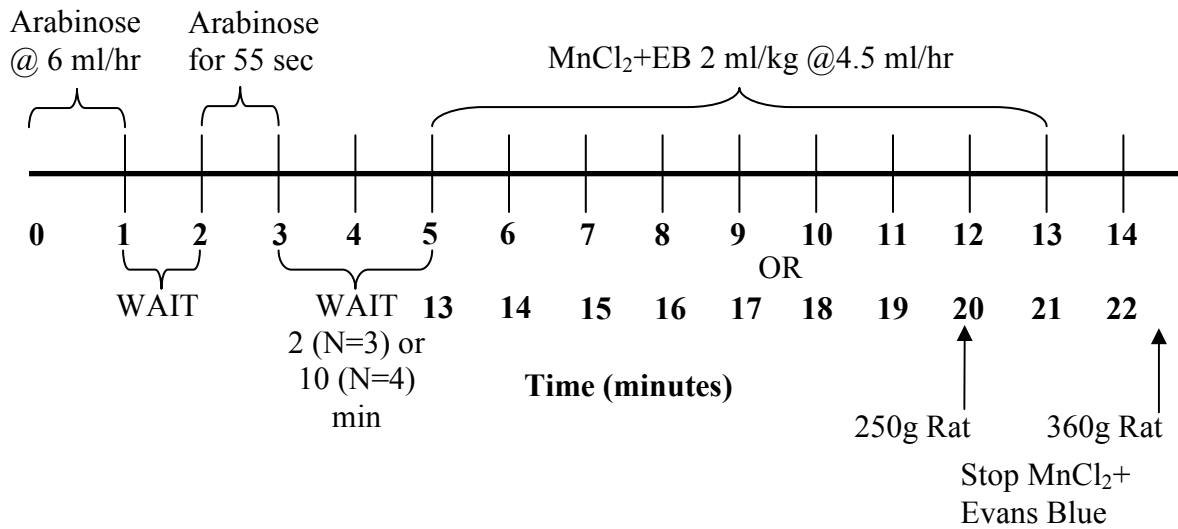


Figure 4-2: Timing of  $MnCl_2+EB$  infusion relative to arabinose infusion.

### 4.2.5 EB Stain Histology

Immediately following imaging, isoflurane anesthetic was increased to 5% and shortly thereafter animals were decapitated. The brain was quickly removed, placed on a section of parafilm and subsequently cooled for thirty minutes to facilitate handling. Brains were then dissected into six 2-mm slices that corresponded spatially to MR slices (first slice at 1mm ventral to the rhinal fissure of olfactory bulb). After dissection, brain slices were placed in zinc formalin for fixation overnight.

The next day brain slices were scanned using a Hewlett-Packard Scanner (Model #3970) at a resolution of 1200 dpi. For the EB control group, animals were perfused with 4% paraformaldehyde via the aorta prior to sacrifice to remove EB from the brain capillary system prior to removal of the brain. The EB group was used to test whether or not EB staining artifacts were present as a result of trapped EB in the brain capillary system.

#### 4.2.6 MRI Measurements

MR experiments were performed using a Bruker Biospin 2.0T/45 cm imaging spectrometer equipped with  $\pm 20$  G/cm self-shielded gradients.  $T_1$ -weighted imaging was performed with the following acquisition parameters: TR/TE = 500.0/10.8 ms, FOV = 3 cm x 3 cm, matrix size = 128x128, six slices with 2-mm thickness, NEX = 8. The imaging plane was referenced to the rhinal fissure at the boundary of the olfactory bulb. Acquisition time for one set of images was 8.5 minutes. Animals were imaged continuously for approximately 2 hours to monitor changes in MEMRI signal-enhancement. During imaging, animals were placed prone within a home-built animal holder. The head of the animal was fixed within an 8-element, 4.3-cm diameter, birdcage  $^1\text{H}$  volume coil. Animals were anesthetized with 2% or 3% isoflurane delivered at 1.5 L/min in breathing-quality air. Body temperature was maintained at  $37.0 \pm 1^\circ\text{C}$  in the magnet by circulated warm air using a T-type thermocouple and a double-point feedback control system.

#### 4.2.7 Data Analysis

##### *MEMRI Signal-Enhancement*

MR image reconstruction was performed using Paravision's Image Processing and Display Software (Xtip). Region of interest definitions and calculations were made using ImageJ (NIH) software (Rasband, W.S., ImageJ, U. S. National Institutes of Health, Bethesda, Maryland, USA, <http://rsb.info.nih.gov/ij/>, 1997-2006.). Regions of MEMRI signal-enhancement were determined by correlation to a standard rat brain atlas (26), based on the slice location relative to the distance from bregma. ROIs were user defined using ImageJ to distinguish between MEMRI signal-enhanced regions and normal brain tissue. The percent-signal increase in  $T_1$ -weighted images was calculated by comparing MEMRI signal-enhanced regions in the ipsilateral hemisphere to the homologous contralateral control regions on a slice-by-slice basis:

$$MEMRI - Signal\ Enhancement\ Increase(\%) = \frac{SI_{IC} - SI_{CC}}{SI_{CC}} \times 100 \quad 4.1$$

where  $SI_{IC}$  is the signal intensity for an ROI in the ipsilateral hemisphere and  $SI_{CC}$  is the signal intensity in the homologous contralateral ROI. Ipsilateral ROIs, drawn for percent signal increase calculations, and ROIs drawn around the brain were used to determine the spatial extent (area) of MEMRI signal-enhancement in  $mm^2$  as shown by Eq. 4.2. Data are presented as mean  $\pm$  standard deviation (SD), with a separate term for the inter-slice signal variability (IS-SD).

$$\% MEMRI - Signal - Enhanced\ Area = \frac{Ipsilateral\ MEMRI\ Enhancement\ Area\ (mm^2)}{Total\ Brain\ Area\ (mm^2)} \times 100 \quad 4.2$$

#### *Evans Blue (EB) Histological Image Analysis*

EB stain images (RGB) were transformed into Hue, Saturation, and Intensity using ImageJ software. Hue refers to the dominant wavelength in the color image; Saturation represents the degree to which white is mixed with the dominant wavelength; and Intensity represents the intrinsic reflectivity of the object viewed (27). EB-Saturation images were compared to MR images for correlation of EB-stained regions with MEMRI signal-enhanced regions. Percent-saturation increase in EB-stained images was calculated by comparing EB-stained regions in the ipsilateral hemisphere with the homologous contralateral control regions on a slice-by-slice basis:

$$EB\ Saturation\ Increase(\%) = \frac{SatInt_{IC} - SatInt_{CC}}{SatInt_{CC}} \times 100 \quad 4.3$$

where  $SatInt_{IC}$  is the saturation intensity for an ROI in the ipsilateral hemisphere and  $SatInt_{CC}$  is the saturation intensity in the homologous contralateral ROI. Ipsilateral ROIs, drawn for saturation increase calculations, and ROIs drawn around the brain (using RGB EB stain images) were used to determine the spatial extent of EB saturation in  $mm^2$  as shown by Eq. 4.4. Data are presented as mean  $\pm$  standard deviation (SD), with a separate term for the inter-slice saturation variability (IS-SD).

$$\% EB \text{ Saturation Area} = \frac{\text{Ipsilateral EB Saturation Area (mm}^2\text{)}}{\text{Total Brain Area (mm}^2\text{)}} \times 100 \quad 4.4$$

#### 4.2.8 Statistical Analysis

Comparison between 2% iso/2-min, 3% iso/2-min, 2% iso/10-min, and MnCl<sub>2</sub>-only groups was performed using analysis of variance (ANOVA) with the Tukey multiple comparison method. For EB saturation-increase-specific data, Kruskal-Wallis one-way ANOVA was used. Correlation between EB-staining data and MEMRI signal-enhancement data was performed using the Pearson product moment correlation coefficient. A *P* value of less than 0.05 was considered significant for all statistical tests. All statistical analyses were performed using SigmaStat (v3.5, Dundas Software, Ltd. Germany).

### 4.3 Results

#### 4.3.1 MEMRI Signal-Enhancement

##### *Regional Coverage and Enhancement Level*

Figure 4-3 shows multi-slice *T*<sub>1</sub>-weighted MRI for animals in the EB control group (2% isoflurane), MnCl<sub>2</sub>-only group (2% isoflurane), 2% iso/2-min group, 3% iso/2-min group, and the 2% iso/10-min group. The MEMRI signal-enhancement is non-specific in each of the groups, since no neuronal stimulus was applied to any subjects in the groups. The average percentage increase in signal intensity in MEMRI signal-enhanced regions was 42% ± 29% in the MnCl<sub>2</sub>-only group, 81% ± 23% in the 2% iso/2-min group, 77% ± 22% in the 3% iso/2-min group, and 76% ± 33% in the 2% iso/10-min group. In almost every animal from every group, MEMRI signal-enhancement was visible across all six MR slices (exceptions were slice #4 & #5 in 1 animal in the 3% iso/2-min group and slice #6 in 1 animal in the 2% iso/10-min group). Brain regions with MEMRI signal-enhancement included cortex, hippocampus (CA1-CA3), geniculate nucleus, deep mesencephalic nucleus, thalamic nucleus, hippocampal commissure, and caudate putamen. Patterns of MEMRI signal-enhancement within or across groups were not observed.

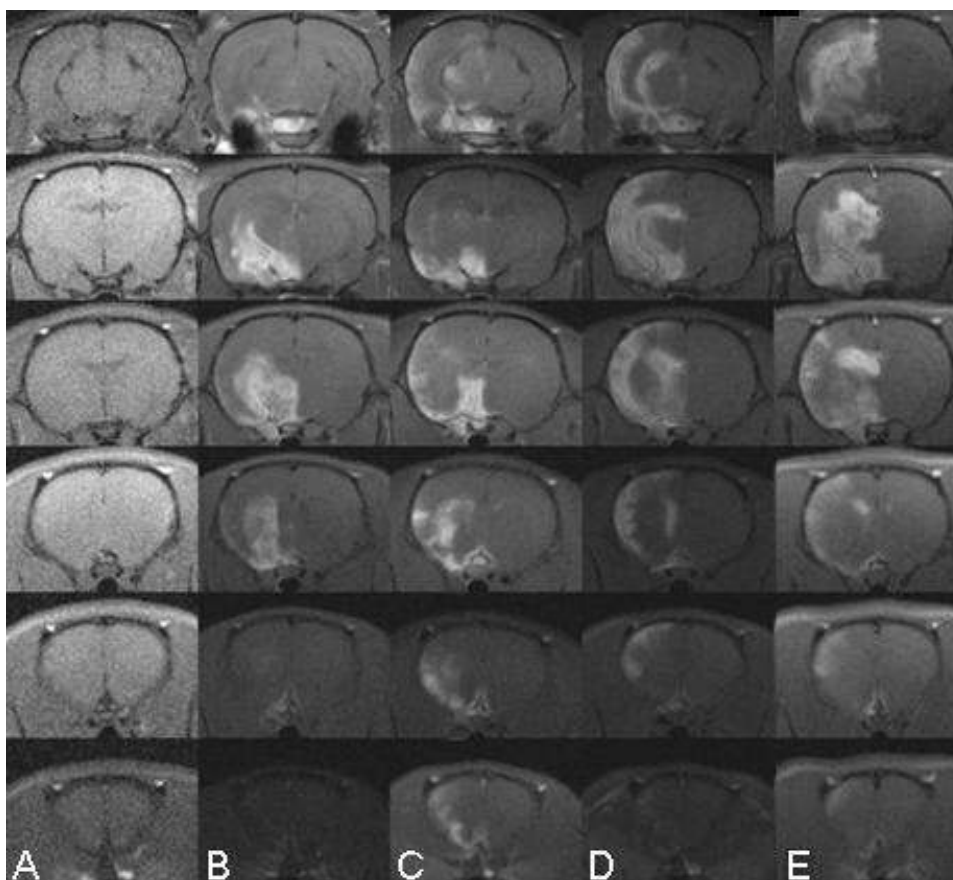


Figure 4-3.  $T_1$ -weighted MRI (i.e., MEMRI) following Evans Blue administration only (2% isoflurane),  $MnCl_2$  only (2% isoflurane), and administration of a solution of  $MnCl_2+EB$  at different anesthetic levels and at a different time relative to osmotic BBB disruption. (A)  $T_1$ -weighted imaging in rat with infusion of EB (2%, 2ml/kg) only 2 minutes following osmotic BBB disruption. No contrast enhancement is present. (B) MEMRI signal-enhancement in a rat infused with  $MnCl_2$  (10 mM, 2 ml/kg, 4.5 ml/hr) 10 minutes after osmotic BBB disruption ( $MnCl_2$ -only group). (C) MEMRI signal-enhancement in a rat infused with a solution of  $MnCl_2+EB$  2 minutes after BBB disruption while breathing 2% isoflurane anesthetic (2% iso/2-min group). (D) MEMRI signal-enhancement in rat infused with a solution of  $MnCl_2+EB$  2 minutes after BBB disruption while breathing 3% isoflurane anesthetic (3% iso/2-min group). In this case, there is more contrast enhancement compared to (C). (E) MEMRI signal-enhancement in rat infused with a solution of  $MnCl_2+EB$  10 minutes following osmotic BBB disruption while breathing 2% isoflurane (2% iso/10-min group).

#### *Quantitative Summary of MEMRI Signal-Enhancement*

Table 4-1 shows the average percentage signal intensity increase and average MEMRI signal-enhancement area for different brain regions for the  $MnCl_2$ -only group, 2% iso/2-min group, 3% iso/2-min group, and the 2% iso/10-min group. A significant difference in signal intensity was detected only between the 2% iso/2-min and  $MnCl_2$ -only groups ( $P < 0.05$ , one-way ANOVA, Tukey

multiple comparison method). Increasing isoflurane anesthetic level from 2% to 3% did not result in a significant reduction of non-specific MEMRI signal-enhancement.

Table 4-1: Average MEMRI percentage (%) signal intensity increase (relative to the homologous contralateral region), and average MEMRI signal-enhancement area [as a percentage (%) of the total slice volume], for the various treatment groups.

Treatment Group	Average MEMRI Percentage (%) Signal Intensity Increase in All Brain Regions (using Eq. 4.1)		Average MEMRI Signal-Enhancement Area (as a percentage (%) of the total slice volume) in All Brain Regions (using Eq. 4.2)	
	Mean $\pm$ SD	ISSD <sup>a</sup>	Mean $\pm$ SD	ISSD <sup>a</sup>
MnCl <sub>2</sub> -only	42 $\pm$ 29	29	15 $\pm$ 13	13
2% iso/2-min	81 $\pm$ 23	15	24 $\pm$ 12	9
3% iso/2-min	77 $\pm$ 22	11	24 $\pm$ 14	10
2% iso/10-min	76 $\pm$ 33	16	32 $\pm$ 13	13

<sup>a</sup>To account for intra-animal variability, the inter-slice standard deviation (ISSD) was calculated from values for the average percentage (%) signal intensity increase (relative to the homologous contralateral region) across slices with MEMRI signal-enhancement.

#### *Stability of MEMRI Signal-Enhancement*

MEMRI signal-enhancement in all animals was found to change over time. MEMRI signal-enhancement had a tendency to spread to surrounding pixels over the 90-100 minutes of scanning. In an animal from the 2% iso/2-min group, signal intensity in the caudate putamen was found to increase 36% over the 100-minute imaging time (the homologous contralateral control region showed a *decrease* in signal intensity of 9% in the same time period). The ROIs used to determine the signal intensity increase over time are shown in Figure 4-6. The signal intensity dynamic curve for these ROIs is shown in Figure 4-7.

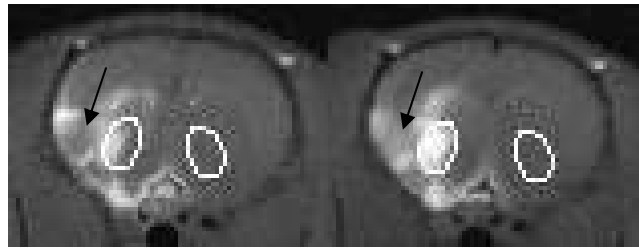


Figure 4-6: ROI definitions for determination of MEMRI signal-enhancement over time. Left: first  $T_1$ -weighted image (slice #5). Right: Last  $T_1$ -weighted image acquired ~100 minutes following the first image. Notice the spread of the MEMRI signal-enhancement over time as well as the increase in signal intensity within the ipsilateral ROI. Note also the diffuse MEMRI signal intensity changes over time in some regions (black arrows).

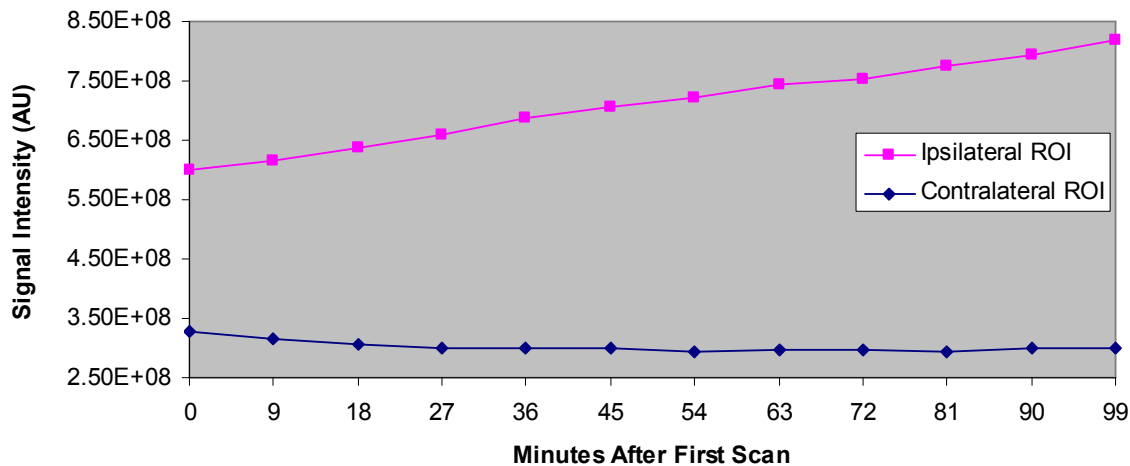


Figure 4-7: Dynamic MEMRI signal intensity changes from the respective ROIs shown in Figure 4-6. As the ipsilateral ROI is ‘filled in’ with MEMRI signal-enhancement, the mean signal intensity in this region increases. The maximum signal intensity value in the ipsilateral ROI increased from  $9.1 \times 10^8$  to  $10.2 \times 10^8$  (AU); however, the average values plotted above are lower due to the inclusion of unenhanced pixels within the ROI.

### 4.3.2 Evans Blue (EB) Stain

#### *Regional Coverage and Saturation Enhancement Level*

Figure 4-8 shows multi-slice EB-stained images for animals in the EB control group, 2% iso/2-min group, 3% iso/2-min group, and the 2% iso/10-min group. To quantify the degree of EB staining, the EB-stained images were transformed into Hue, Saturation, and Intensity images. An example of this transformation is provided in Figure 4-9 using one animal from the 2% iso/2-min group. The EB-Saturation image provided the best contrast for quantifying the EB-staining level as compared to the EB-Hue and EB-Brightness images. The average percentage increase in saturation intensity in the EB-stained regions was  $273\% \pm 80\%$  in the 2% iso/2-min group,  $332\% \pm 170\%$  in the 3% iso/2-min group,  $157\% \pm 80\%$  in the 2% iso/10-min group, and  $28\% \pm 30\%$  (0% in one out



of two animals) in the EB control group. Brain regions with EB staining included cortex, hippocampus (CA1-CA3), geniculate nucleus, deep mesencephalic nucleus, thalamic

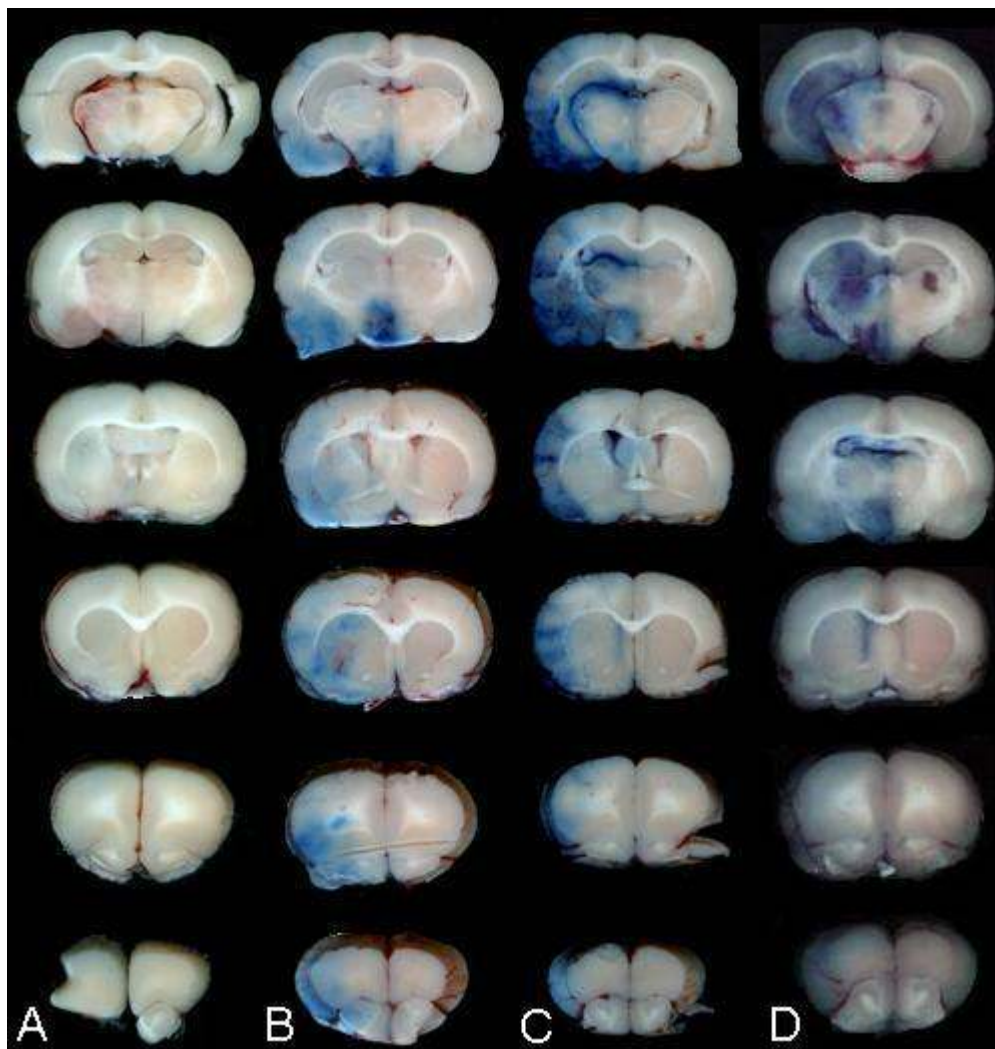


Figure 4-8: Evans Blue (EB) staining following EB administration only, and administration of a solution of  $MnCl_2+EB$  at different anesthetic levels and at different times relative to osmotic BBB disruption. (A) EB staining in rat with infusion of EB (2%, 2ml/kg) following osmotic BBB disruption (EB control group). This rat was perfused with saline prior to removal of the brain which may account for the lack of gross EB stain in these slices. (B) EB stain in rat infused with a solution of  $MnCl_2+EB$  2-min after osmotic BBB disruption while breathing 2% isoflurane (2% iso/2-min group) (C) EB staining in rat infused with a solution of  $MnCl_2+EB$  2-min after osmotic BBB disruption while breathing 3% isoflurane anesthetic (3% iso/2-min group). (D) EB staining in rat infused with a solution of  $MnCl_2+EB$  10-min after osmotic BBB disruption while breathing 2% isoflurane anesthetic (2% iso/10-min group).

nucleus, and caudate putamen. Patterns of EB staining within or across groups were not observed but were always confined to the right hemisphere as expected.

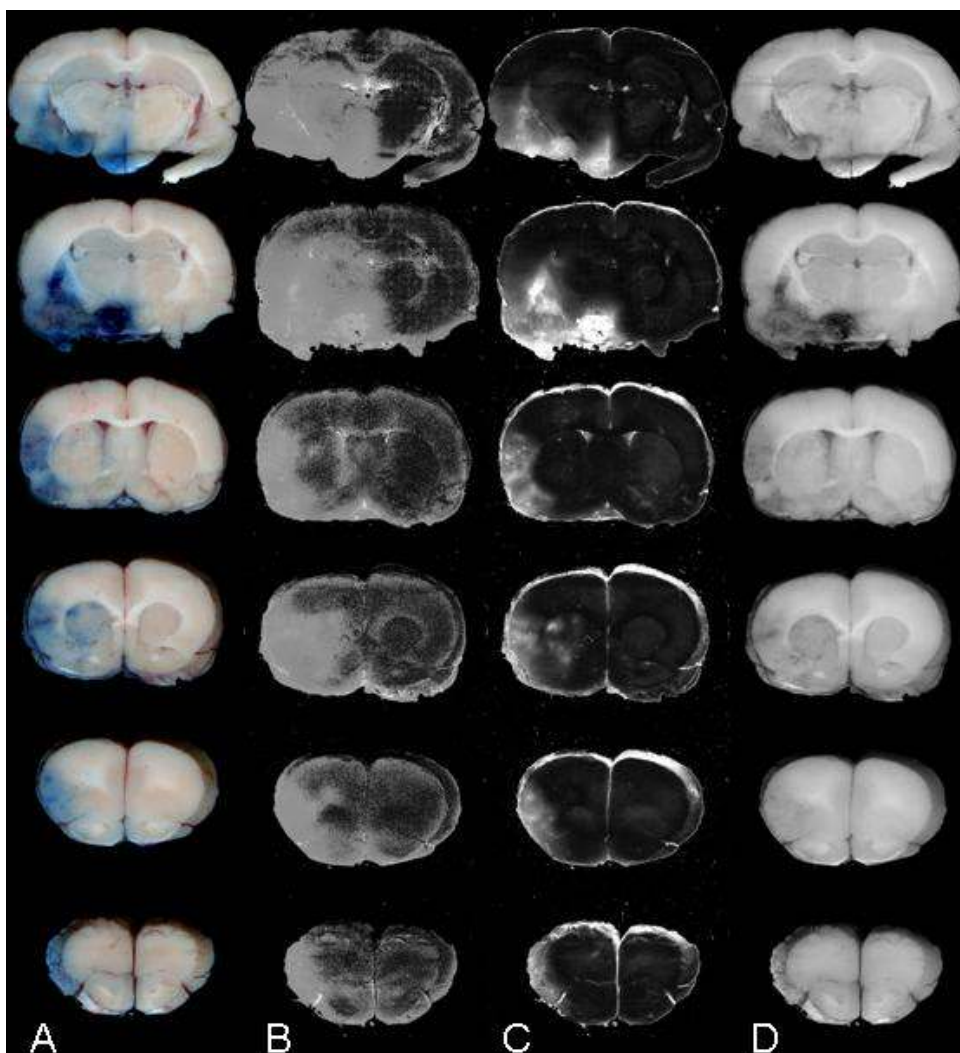


Figure 4-9: Evans Blue (EB)-stained image (A, RGB image) transformed into Hue (B), Saturation (C), and Brightness (D) images (8-bit grayscale). The EB-Saturation image provides the best contrast for determining the degree of EB staining and the spatial extent of EB-stained regions. The EB-Hue images in this case (and all other animals aside from the EB control group) show gross saturation in EB-stained regions and thus are not useful for determining the level of EB staining; however, the EB-Hue images may be useful for determining the spatial extent of EB staining.

#### *Quantitative Summary of Evans Blue (EB)-Staining Intensity*

Table 4-2 shows the average percentage increase in EB-Saturation intensity for different brain regions for the EB control group, 2% iso/2-min group, 3% iso/2-min group, and the 2% iso/10-min group. Significant differences in EB-Saturation intensity were detected between the EB control group and all other groups ( $P < 0.05$  for all comparisons) and between the 3% iso/2-min group and

the 2% iso/10-min group ( $P < 0.05$ ). For the EB control group, one animal (out of 2) showed no increase in EB-Saturation intensity in the ipsilateral hemisphere compared to the homologous contralateral region. However, when the EB-Hue image was considered, a difference in EB-Hue intensity was observed between ipsilateral and contralateral hemispheres. The EB-Hue image may be a more sensitive way to detect EB staining when staining is not grossly visible to the naked eye. EB-Hue intensity data for both animals in the EB control group are provided in Table 4-3.

Table 4-2: Average percentage (%) increase in EB-Saturation signal intensity (relative to the homologous contralateral region), and average EB-Saturation signal-enhancement area [as a percentage (%) of the total slice volume], for the various treatment groups. The EB control group was perfused with paraformaldehyde, which may account for the significant difference in EB staining and EB-Saturation signal intensity shown here.

Treatment Group	Average Percentage (%) Increase in EB-Saturation Signal Intensity in All Brain Regions (using Eq. 4.3)		Average EB-Saturation Signal-Enhancement Area [as a percentage (%) of the total slice volume] in All Brain Slices (using Eq. 4.4)	
	Mean $\pm$ SD	ISSD <sup>a</sup>	Mean $\pm$ SD	ISSD <sup>a</sup>
EB control	28% $\pm$ 30%***	6%	17 $\pm$ 18	4
2% iso/2-min	273% $\pm$ 80%	38%	24 $\pm$ 10	5
3% iso/2-min	332% $\pm$ 170%**	71%	21 $\pm$ 12	11
2% iso/10-min	157% $\pm$ 80%**	77%	32 $\pm$ 10	10

<sup>a</sup>To account for intra-animal variability, the inter-slice standard deviation (ISSD) was calculated from values for the average EB-Saturation signal-intensity increase across slices with EB staining. \*\*\*Significant difference between this and all other groups,  $P < 0.05$ . \*\*Significant difference between these groups,  $P < 0.05$ .

Table 4-3: Average percentage (%) increase in EB-Hue signal intensity (relative to the homologous contralateral region), and average EB-Hue signal-enhancement area [as a percentage (%) of the total slice volume], for the EB control group following Infusion of EB solution. The EB control group was perfused with formaldehyde prior to sacrifice.

Treatment Group	Average Percentage (%) Increase in EB-Hue Signal Intensity in All Brain Regions (using Eq. 4.3)		Average EB-Hue Signal-Enhancement Area [as a percentage (%) of the total slice volume] in All Brain Slices (using Eq. 4.4)	
	Mean ± SD	ISSD	Mean ± SD	ISSD
EB control	72 ± 23	14	34 ± 13	7

### 4.3.3 Correlation Between Regions of MEMRI Signal-Enhancement and Evans Blue (EB) Staining

#### *Regional Coverage, Signal and Saturation Enhancement Level*

Figure 4-10 shows multi-slice EB-stained histological sections and corresponding  $T_1$ -weighted MRI slices, for animals in the 2% iso/2-min, 3% iso/2-min, and 2% iso/10-min groups. Although EB-stained sections and MR images are not exactly co-registered, it is apparent that there is good spatial correspondence between regions of EB staining and MEMRI signal-enhancement. When EB staining is not grossly visible on the histological section, the MEMRI signal-enhancement in the corresponding regions is low or undetectable.

Figure 4-11 shows multi-slice EB-stained histological sections (RGB format), EB-Saturation images, and the corresponding  $T_1$ -weighted MEMR images for an animal in the 3% iso/2-min group (left) and 2% iso/2-min group (right). In this case, EB-Saturation images provide another means to quantitatively and/or qualitatively correlate EB-stained regions with those showing MEMRI signal-enhancement in the brain. Quantitative correlation of MEMRI signal-enhancement level and EB-saturation signal level – on a slice by slice basis – resulted in a correlation coefficient,  $r$ , of 0.57 ( $P < 0.05$ ) in the 2% iso/2-min group, 0.58 ( $P < 0.05$ ) in the 3% iso/2-min group, and 0.41 ( $P = 0.09$ ) in the 2% iso/10-min group. A stronger correlation was shown between the average percentage MEMRI signal-enhancement area and the average percentage EB-saturation signal-enhancement area – on a slice-by-slice basis – with  $r = 0.80$  ( $P < 0.0001$ ) in the 2% iso/2-min group,  $r = 0.80$  ( $P < 0.0001$ ) in the 3% iso/2-min group, and  $r = 0.82$  ( $P < 0.0001$ ) in the 2% iso/10-min group.

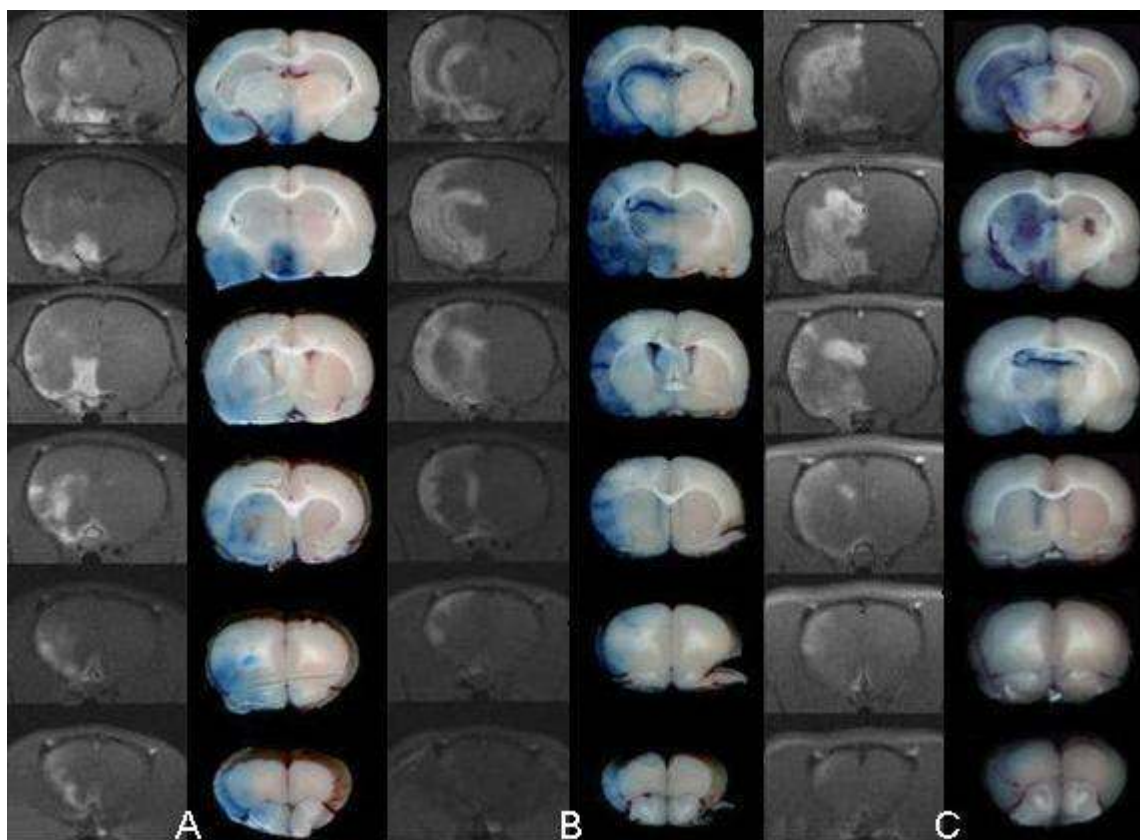


Figure 4-10: MEMRI and corresponding EB-stained histological images (RGB format). MEMRI slices and EB-stained sections for one animal each from the 2% iso/2-min group (A), 3% iso/2-min group (B), and 2% iso/10-min group (C). Only one side of the EB-stained histological section shown and does not account for variations in EB staining through the 2-mm thickness of the slice (in contrast to the MEMRI image, which volume averages the MRI signal intensity through the 2-mm thickness of the slice). Slight differences in spatial registration between the two methods arise from inherent difficulties in reproducing the slice thickness and slice positions of the histological sections relative to those acquired using MEMRI. However, in spite of this issue, the spatial correlation between regions of MEMRI signal-enhancement and the corresponding EB-stained regions on the histological sections is readily apparent.

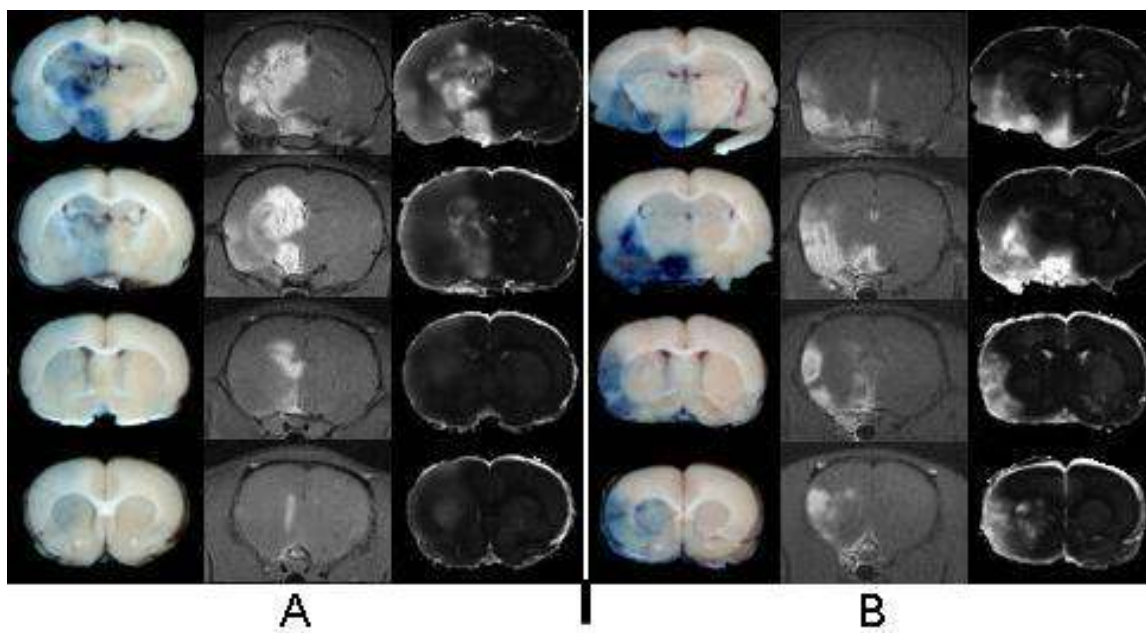


Figure 4-11: Evans Blue (EB)-stained histological (left), MEMRI (middle), and EB-Hue images (right) in an animal from (A) the 3% iso/2-min group and (B) the 2% iso/2-min group. The EB-Hue transformation provides useful contrast for quantifying gross (i.e., by eye) correlations of regions of EB-staining and MEMRI signal-enhancement in brain.

*Quantitative Summary of Correlation between MEMRI Signal-Enhancement and Evans Blue (EB) Staining*

Table 4-4 summarizes the correlation between MEMRI signal-enhancement level and Evans Blue (EB)-Saturation signal-enhancement level and the correlation between MEMRI signal-enhancement area and EB-Saturation signal-enhancement area. A weak trend was detected in the average percentage change in MEMRI and EB-Saturation signal-enhancement levels in all of the animal groups. A stronger trend was detected in the correlation between the areas of MEMRI and EB-Saturation enhancement in the brain.

Table 4-4: Summary of the correlation between MEMRI signal-enhancement level and Evans Blue (EB)-Saturation signal-enhancement level; and the correlation between MEMRI signal-enhancement area and EB-Saturation signal-enhancement area for all treatment groups.

Treatment Group	Average Percentage (%) MEMRI and EB-Saturation Signal Intensity Increase in All Brain Slices (using Eqs. 4.1 & 4.3)			Average MEMRI and EB-Saturation Signal-Enhancement Area [as a percentage (%) of the total slice volume] in All Brain Regions (using Eqs. 4.2 & 4.4)		
	MEMRI Signal-Enhancement Mean $\pm$ SD	EB Saturation Mean $\pm$ SD	Corr. Coeff. (r) <sup>a</sup>	MEMRI Signal-Enhancement Mean $\pm$ SD	EB Saturation Mean $\pm$ SD	Corr. Coeff. (r) <sup>a</sup>
MnCl <sub>2</sub> -only	42 $\pm$ 29	NA	NA	15 $\pm$ 13	NA	NA
EB Control	NA	28 $\pm$ 30	NA	NA	17 $\pm$ 18	NA
2% iso/2-min	81 $\pm$ 23	273 $\pm$ 80	0.57 (P<0.05)	24 $\pm$ 12	24 $\pm$ 10	0.80 (P<0.0001)
3% iso/2-min	77 $\pm$ 22	332 $\pm$ 170	.58 (P<0.05)	24 $\pm$ 14	21 $\pm$ 12	0.80 (P<0.0001)
2% iso/10-min	76 $\pm$ 33	157 $\pm$ 80	0.41 (P = .09)	32 $\pm$ 13	32 $\pm$ 10	0.82 (P<0.0001)

<sup>a</sup>Pearson product moment correlation coefficient.

#### 4.4 Discussion

Mn<sup>2+</sup> is a paramagnetic ion and has been used as a brain activation-specific contrast agent in rats after osmotic disruption of the BBB (1). Mn<sup>2+</sup> enters cells via ligand- or voltage-gated calcium channels during nerve action potentials (6) and binds to magnesium and iron-binding sites and accumulates within the mitochondria (19). Retention of paramagnetic Mn<sup>2+</sup> by cells makes Mn<sup>2+</sup> an attractive means to ‘record’ brain function by MR imaging. Previous experiments have shown that unintended (non-specific) brain activation in the presence of extracellular Mn<sup>2+</sup> may be due to a low anesthetic state in animals (1) or to the process of osmotic BBB disruption (11). Unintended brain activation in MEMRI experiments can obscure subsequent changes in MEMRI signal-enhancement

due to specific neuronal stimulus. No previous MEMRI study has shown histological evidence of osmotic BBB disruption prior to or following brain activation. Knowledge of the extent of BBB disruption prior to i.v. administration of  $Mn^{2+}$  can aid in the interpretation of MEMRI signal-enhancement in the presence of specific or non-specific neuronal stimuli.

In this study we evaluated several groups of animals in an effort to eliminate nonspecific MEMRI signal-enhancement and to test the efficacy of co-infused  $MnCl_2+EB$  for elucidating the extent of BBB disruption and  $Mn^{2+}$  distribution in the brain. Experiments were performed at different anesthetic levels and using different  $MnCl_2+EB$  infusion times relative to BBB disruption. The two major findings of this study were: 1) using the infusion protocols described in this study, nonspecific MEMRI signal-enhancement is a reproducible occurrence when animals are anesthetized using either 2% and 3% isoflurane; and 2) the spatial extent of nonspecific MEMRI signal-enhancement is strongly correlated with the spatial extent of osmotic BBB disruption as verified by histological staining.

#### **4.4.1 Isoflurane and Halothane Level and Nonspecific MEMRI Signal-Enhancement**

The anesthetic condition of the animal is important in MEMRI experiments for prevention of nonspecific MEMRI signal-enhancement. Lin and Koretsky suggested that nonspecific MEMRI signal-enhancement was present when animals were anesthetized with 0.3% halothane and non-existent when animals were anesthetized with 1.3% halothane (1). Aoki *et al.* failed to elicit specific MEMRI signal-enhancement in animals that were heavily anesthetized (2.5% halothane), suggesting an optimal anesthetic condition that suppresses baseline activity but does not inhibit activation of intentionally stimulated areas (4). The results of this study are comparable to those of Lin and Koretsky since similar levels of volatile anesthetics were used (1.3% halothane versus 2% and 3% isoflurane, respectively). At 1.3% concentration, halothane has a similar minimum alveolar concentration (MAC – level of anesthesia required to just prevent response to painful stimulus, usually a tail clamp) as compared to 2% isoflurane (~1.7 MAC for halothane and isoflurane (28)) so at these levels we would expect similar anesthetic conditions. Indeed, Hudetz (28) showed that the differences in inter-hemispheric electroencephalogram (EEG) readings in rats anesthetized with halothane or isoflurane disappear when both anesthetics reach a concentration of 1.5%. Below 1.5%, the potency of isoflurane to depress EEG signals (i.e., brain activity) was greater than that of halothane at similar concentrations (29). In a study of electrophysiological recordings from CA1



neurons in rat hippocampal brain slices, MacIver and coworkers showed that depression of electrophysiological signals (glutamate-mediated excitatory synaptic transmissions) was equivalently achieved with 1.0% isoflurane and 1.3% halothane (30). Experimental evidence based on general (EEG) and localized (electrophysiological) brain activity using isoflurane and halothane anesthetics suggest that isoflurane is at least as potent if not more so than halothane at similar concentrations. Therefore, when comparing the results from this study to those of others for which a similar concentration of anesthetic was used (and considering that no significant difference in MEMRI signal-enhancement between the 2% isoflurane and 3% isoflurane groups was found in this study), other aspects of our experimental protocol were considered for their potential contribution to the nonspecific MEMRI signal-enhancement. Indeed, Lin and Koretsky used 1.4 molar mannitol to disrupt the BBB but did not report the rate of mannitol infusion (1). In their case, the BBB-disruption process may have been just severe enough to allow  $\text{MnCl}_2$  to permeate the barrier while not damaging cerebral capillary endothelial cells, brain astrocytes, or glia.

#### 4.4.2 Nonspecific $T_1$ -Enhancement after Osmotic BBB Disruption

For many MEMRI experiments investigating brain function, it is necessary to disrupt the BBB using an i.v. infusion of a hyperosmolar agent prior to or shortly after i.v. infusion of  $\text{MnCl}_2$ . However, the osmotic BBB-disruption process itself should ideally not induce cellular influx of  $\text{Mn}^{2+}$  since this could lead to nonspecific MEMRI signal-enhancement. Data from several studies indicates that osmotic BBB disruption does result in varying degrees of nonspecific MEMRI signal-enhancement. Aoki and colleagues used a dynamic imaging approach to show MEMRI signal-enhancement during  $\text{MnCl}_2$  infusion and prior to, during, and after osmotic BBB disruption by mannitol injection (11). This imaging approach showed a clear increase in nonspecific MEMRI signal-enhancement immediately following mannitol injection. Results from the study of Aoki *et al.* are shown in Figure 4-12. Morita and coworkers (11) also showed a nonspecific increase in MEMRI signal-enhancement in a dynamic imaging experiment. Mannitol infusion in the studies of both Aoki *et al.* and Morita *et al.* result in large increases in nonspecific MEMRI signal-enhancement in the BBB-disrupted cortex of rat brain (~50% increase compared to baseline signal). Results from the study of Morita *et al.* are shown in Figure 4-13 (8).

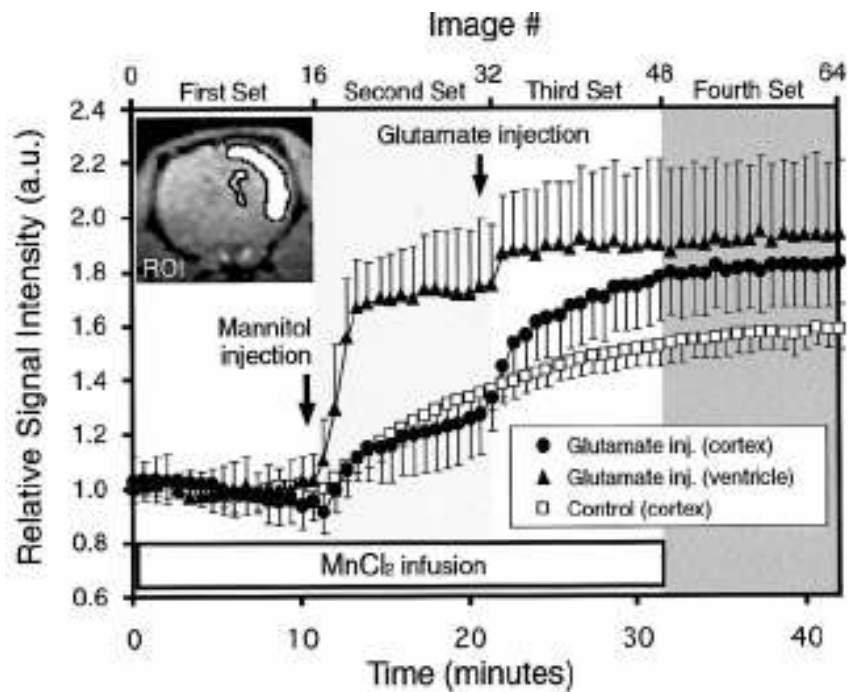


Figure 4-12. Typical time-courses of relative signal intensities in the cortex and ventricle obtained from the glutamate administration (filled symbols) and control (open squares) groups. The inset indicates typical ROIs. The rise in signal intensity (MEMRI signal-enhancement) following mannitol injection (arrow at 10 minutes) is clear. Reproduced from Ref. (11).

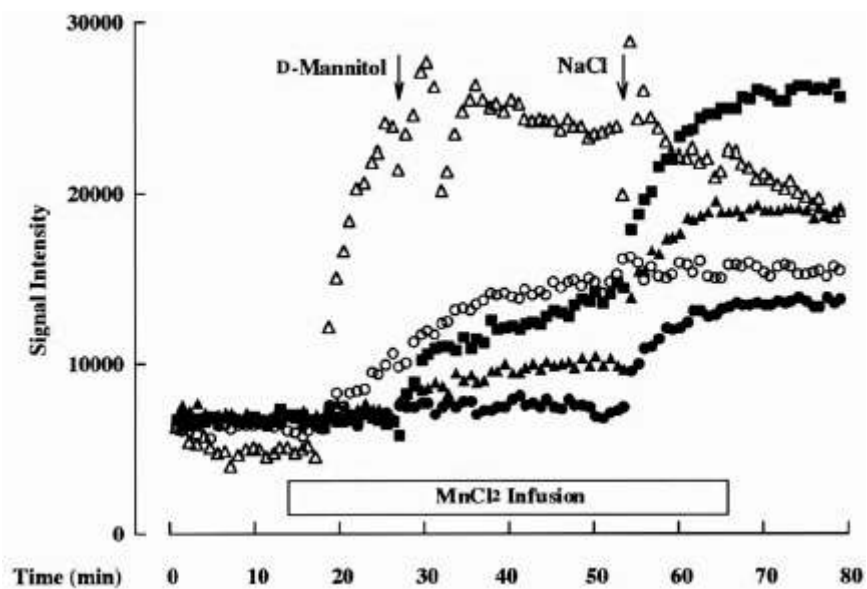


Figure 4-13. Time course of  $T_1$ -weighted MRI signal intensity (MEMRI signal-enhancement) changes in the cortex (filled squares), lateral habenular nucleus (filled triangles), and other brain regions. Notice the abrupt change in MEMRI signal-enhancement immediately following mannitol infusion (to break the BBB) in the cortex and lateral habenular nucleus.

Although Aoki *et al.* and Morita *et al.* used different concentrations of  $\text{MnCl}_2$  (74.5 mM and 100mM respectively) and different routes of administration of  $\text{MnCl}_2$  (Aoki *et al.*, right carotid artery; Morita *et al.*, left femoral vein), it is possible that the nonspecific MEMRI signal-enhancement observed in this study is also related to the osmotic disruption of the BBB. When  $\text{MnCl}_2$ +EB is co-infused immediately after osmotic BBB disruption (2% iso/2-min and 3% iso/2-min groups), the results suggest that cellular uptake of  $\text{Mn}^{2+}$  may be indicative of parenchymal cells undergoing osmotic transitions. Introduction of a waiting period after osmotic BBB disruption, that does not exceed the time window that the BBB remains open (~15 minutes after osmotic BBB disruption), may circumvent the osmotic transitions of the parenchymal cells and allow passage of  $\text{MnCl}_2$  only into the extracellular space of the brain. To test this hypothesis, an experiment was designed to investigate the effect of delaying co-infusion of  $\text{MnCl}_2$ +EB from two to ten minutes following osmotic BBB disruption. The results suggest, however, that there is no significant difference between infusion of  $\text{MnCl}_2$ +EB at two minutes (2% iso/2-min and 3% iso/2-min groups) or ten minutes (2% iso/10-min group) following osmotic BBB disruption with respect to levels of nonspecific MEMRI signal-enhancement or the area of MEMRI signal-enhancement. Therefore, other effects of osmotic BBB disruption that may contribute to nonspecific MEMRI signal-enhancement – such as influx of  $\text{Mn}^{2+}$  into damaged neurons, influx of  $\text{Mn}^{2+}$  into disturbed endothelial cells, or a combination of these – should be considered.

#### 4.4.3 Cellular Uptake of $\text{MnCl}_2$ +Evans Blue (EB) Dye after Osmotic BBB Disruption

Several studies report damage to brain cells and uptake of Evans Blue (EB) dye into cells following osmotic BBB disruption. Salahuddin and coworkers (30) used electron microscopy to observe brain cells in the brain hemisphere that received an infusion of 1.4 molar mannitol 90 minutes after an i.v. infusion of EB solution. Their experiments revealed darkly EB-stained, shrunken, and irreversibly injured neurons in the ipsilateral hemisphere. Kozler *et al.* (31) infused EB dye two minutes following osmotic BBB disruption by 1.1 M mannitol and used fluorescence microscopy to determine the ratio of intracellular to extracellular EB dye. The results of Kozler *et al.* show that of the EB dye in the brain following osmotic BBB disruption, most is found intracellularly (>60% of the dye was found intracellularly in cortex, and CA1, CA3 of hippocampus) (31).

The notion that EB dye can enter cells via i.v. infusion after osmotic BBB disruption has ramifications for the results of the present study. The experimental protocol of Salahuddin *et al.* (30)

(EB dye was injected 90 min before osmotic BBB disruption with 1.4 M mannitol @0.12 ml/sec) differs significantly from that in this study (where EB dye was injected 2 min after BBB disruption with 1.6 M arabinose @~0.03ml/sec), but the effect on the cells may be similar to those in this study. The experimental protocol of Kozler *et al.* (31) was very similar to that used in this study (same EB infusion protocol) with the only difference being the rate of infusion of the hyperosmolar agent (5 ml/kg @0.12 ml/sec for Kozler *et al.* vs. 5 ml/kg @55 seconds in this study). Therefore, by analogy, the MnCl<sub>2</sub>+EB and arabinose infusion protocol used in this study may result in diffuse cellular uptake of EB *and* MnCl<sub>2</sub> into cells. Indeed, in another study by Salahuddin *et al.* (32), pinocytotic and diffuse uptake of fibronectin and fibrinogen into brain cells was reported following osmotic BBB disruption with 1.4 M mannitol (1.5 ml in 30 seconds via carotid artery). If Mn<sup>2+</sup> enters neurons by a diffuse process following damage by hyperosmolar agents, Mn<sup>2+</sup> would be expected to reduce the intracellular water proton  $T_1$  and  $T_2$  relaxation times in a manner similar to the situation when Mn<sup>2+</sup> enters the cell via voltage-gated Ca<sup>2+</sup> channels after membrane depolarization.

#### 4.4.4 Limitations

##### *MR Image and Histological Image Correlation*

Correlation of regions of MEMRI signal-enhancement with those observed on EB-stained histological sections were performed without careful spatial co-registration of the respective images. The signal intensity in MR images are inherently volume averaged (i.e., in these studies, the signal intensity at each pixel location represents the integral of the entire signal through the 2-mm thick brain slice). By comparison, the EB-stained region on the histological section only represents the stained area on the surface of the slice and does not take into account variations in EB staining through the thickness of the slice). Consequently, these differences can give rise to systematic errors when comparing the relative areas determined by the two methods. Ideally, the histological slice is dissected into very thin slices (on order of  $\mu\text{m}$ ) and several of these thin slices can be used to estimate the EB-stained area on the histological section. In a future study, in place of many micrometer thick histological slides, 2-mm-thick histological sections could be imaged on both sides and then averaged to give a more accurate representation of the EB staining through the slice thickness. In addition, dissecting the brain 'by hand' produced errors by slightly varying the thickness of the histological sections as well as slight misregistration between the histological slice positions and those of the MRI slices (which were positioned relative to the rhinal fissure of the

olfactory bulb). In light of these potential errors, the already strong correlation between the spatial extent of the MEMRI signal-enhancement and the spatial extent of the EB-stained regions may in fact be better than that reported in this study.

#### *Evans Blue (EB) Staining After Perfusion*

The data from the EB control group of our study is perplexing and suggests that the source of EB staining, and indeed MEMRI signal-enhancement, may not be within brain but within brain capillaries. This group showed very little or no EB staining (no MEMRI signal-enhancement because no  $\text{MnCl}_2$  was infused) at the same time point of histological staining of all other animals. Future studies should include perfusion of all animals prior to brain removal to eliminate any staining artifact that may occur as a result of the decapitation and brain removal process.

#### **4.4.5 Conclusions**

In summary, we have shown that co-infusion of  $\text{MnCl}_2$ +Evan Blue (EB) dye following osmotic BBB disruption allows for the quantification of BBB permeability changes and an inference as to the extent of  $\text{Mn}^{2+}$  distribution in the brain. In addition, we have shown that a particular infusion protocol of  $\text{MnCl}_2$ +EB and 1.6 M arabinose consistently results in nonspecific MEMRI signal-enhancement, the extent of which strongly correlates with the extent of BBB disruption. Although our protocol results in nonspecific MEMRI signal-enhancement that may obscure subsequent changes in MEMRI signal-enhancement by a specific neuronal stimulus, this method may be a useful alternative to imaging BBB disruption in rats.

#### **Acknowledgements**

The authors thank Dr. Karl Helmer (Massachusetts General Hospital, Cambridge, MA) and James Bouley (University of Massachusetts Medical School, Worcester, MA) for helpful advice with MR imaging and surgical protocols.

## REFERENCES

1. Lin Y.J., Koretsky A.P. Manganese ion enhances T<sub>1</sub>-weighted MRI during brain activation: an approach to direct imaging of brain function. *Magn Reson Med* 1997;38:378-388.
2. Pautler R.G., Mongear R., Jacobs R.E. In vivo trans-synaptic tract tracing from the murine striatum and amygdala utilizing manganese-enhanced MRI (MEMRI). *Magn Reson Med* 2003;50:33-39.
3. Aoki I., Wu Y.J., Silva A.C., Lynch R.M., Koretsky A.P. In vivo detection of neuroarchitecture in the rodent brain using manganese-enhanced MRI. *Neuroimage* 2004;22:1046-1059.
4. Aoki I., Naruse S., Tanaka C. Manganese-enhanced magnetic resonance imaging (MEMRI) of brain activity and applications to early detection of brain ischemia. *NMR Biomed* 2004;17:569-580.
5. Aoki I., Ebisu T., Tanaka C., Katsuta K., Fujikawa A., Umeda M., Fukunaga M., Takegami T., Shapiro E.M., Naruse S. Detection of the anoxic depolarization of focal ischemia using manganese-enhanced MRI. *Magn Reson Med* 2003;50:7-12.
6. Drapeau P., Nachshen D.A. Manganese Fluxes and Manganese-Dependent Neurotransmitter Release in Presynaptic Nerve Endings Isolated From Rat Brain. *J Physiol* 1984;348:493-510.
7. Narita K., Kawasaki F., Kita H. Mn and Mg influxes through Ca channels of motor nerve terminals are prevented by verapamil in frogs. *Brain Res* 1990;510:289-295.
8. Morita H., Ogino T., Seo Y., Fujiki N., Tanaka K., Takamata A., Nakamura S., Murakami M. Detection of hypothalamic activation by manganese ion contrasted T(1)-weighted magnetic resonance imaging in rats. *Neurosci Lett* 2002;326:101-104.
9. Henning E.C. , Meng X. , Fisher M. , Sotak C. Visualization of Cortical Spreading Depression Using Manganese-Enhanced MRI. *Magn Reson Med* 2005;53:851-857.
10. Duong T.Q., Silva A.C., Lee S.P., Kim S.G. Functional MRI of calcium-dependent synaptic activity: cross-correlation with CBF and BOLD measurements. *Magn Reson Med* 2000;43:383-392.
11. Aoki I., Tanaka C., Takegami T., Ebisu T., Umeda M., Fukunaga M., Fukuda K., Silva A.C., Koretsky A.P., Naruse S. Dynamic activity-induced manganese-dependent contrast magnetic resonance imaging (DAIM MRI). *Magn Reson Med* 2002;48:927-933.
12. Cosolo W.C., Martinello P., Louis W.J., N. Christophidis. Blood-brain barrier disruption using mannitol: time course and electron microscopy studies. *Am J Physiol* 1989;R443-R448.
13. Rapoport S.I., Fredericks W.R., Ohno K., Pettigrew K.D. Quantitative aspects of reversible osmotic opening of the blood-brain barrier. *Am J Physiol* 1980;238:R421-R431.
14. Freedman F.B., Johnson J.A. Equilibrium and kinetic properties of the Evans blue-albumin system. *Am J Physiol* 1969;216:675-681.
15. Ohno K., Fredericks W.R., Rapoport S.I. Osmotic Opening of the Blood-Brain Barrier to Methotrexate in the Rat. *Surg Neurol* 1979;12:323-328.
16. Remsen L.G., Pagel M.A., McCormick C.I., Fiamengo S.A., Sexton G., Neuwelt E.A. The Influence of Anesthetic Choice, P<sub>a</sub>CO<sub>2</sub>, and Other Factors on Osmotic Blood-Brain Barrier Disruption in Rats with Brain Tumor Xenografts. *Anesth Analg* 1999;88:559-567.
17. Wolman M., Klatzo I., Chui E., Wilmes F., Nishimoto K., Fujiwara K., Spatz M. Evaluation of the Dye-Protein Tracers in Pathophysiology of the Blood-Brain Barrier. *Acta Neuropathol (Berl)* 1981;54:55-61.
18. Scheuhammer A.M., Cherian M.G. Binding of manganese in human and rat plasma. *Biochim Biophys Acta* 1985;840:163-169.

19. Aschner M., Aschner J.L. Manganese Neurotoxicity: Cellular Effects and Blood-Brain Barrier Transport. *Neurosci and Biobehav Rev* 1991;15:333-340.
20. Critchfield J.W., Keen C.L. Manganese<sup>+2</sup> Exhibits Dynamic Binding to Multiple Ligands in Human Plasma. *Metabolism* 1992;41:1087-1092.
21. Davidsson L., Lonnerdal B., Sandstrom B., Kunz C., Keen C. Identification of Transferrin as the Major Plasma Carrier Protein for Manganese Introduced Orally or Intravenously or After In Vitro Addition in the Rat. *J Nutrition* 1989;119:1461-1464.
22. Aschner M., Aschner J. Manganese Transport Across the Blood-Brain Barrier: Relationship to Iron Homeostasis. *Brain Res Bull* 1990;24:857-860.
23. Martin B. The chemistry of aluminum as related to biology and medicine. *Clin Chem* 1986;32:1797-1806.
24. Ziylan Y.Z., Robinson P.J., Rapoport S.I. Blood-brain barrier permeability to sucrose and dextran after osmotic opening. *Am J Physiol* 1984R634-R638.
25. Cosolo W. C., Martinello P., Louis W. J., Christophidis N. Blood-brain barrier disruption using mannitol: time course and electron microscopy studies. *Am J Physiol* 1989;256:R443-447.
26. Paxinos G., Watson C. *The Rat Brain in Stereotaxic Coordinates*. Orlando: Academic Press; 1986.
27. Fermin C.D., Degraw S. Colour thresholding in video imaging. *J Anat* 1995;186:469-481
28. Miller K.W. General Anesthetics. In: Feldman S.A., Scurr C.F., Paton W., editors. *Drugs in Anaesthesia: mechanisms of action*. London: Edward Arnold, Ltd; 1987.
29. Hudetz A.G. Effect of volatile anesthetics on interhemispheric EEG cross-approximate entropy in the rat. *Brain Research* 2002;954:123-131.
30. MacIver M.B., Mikulec A.A., Amagasu S.M., Monroe F.A. Volatile Anesthetics Depress Glutamate Transmission Via Presynaptic Actions. *Anesthesiology* 1996;85:823-834.
31. Kozler P., Pokorny J. Altered Blood-Brain Barrier Permeability and Its Effect on the Distribution of Evans Blue and Sodium Fluorescein in the Rat Brain Applied by Intracarotid Injection. *Physiol Res* 2003;52:607-614.

# CHAPTER 5

## Brain Damage and Mismatch Between Manganese-Enhanced MRI (MEMRI) and Diffusion-Weighted MRI in the Absence of Specific Neuronal Stimuli; Potential Pitfalls in MEMRI After Osmotic Blood-Brain Barrier (BBB) Disruption

### Introduction

MEMRI Background  
Side Effects of Osmotic BBB Disruption

### Methods

Animal Preparation  
Osmotic BBB Disruption and MnCl<sub>2</sub>+Evans Blue (EB) Administration  
MRI Measurements  
EB and 2,3,4 Triphenyltetrazolium Chloride (TTC) Histology  
Data Analysis  
Statistical Analysis

### Results

Animal Physiology  
Brain Edema  
MEMRI Signal-Enhancement  
ADC Deficit  
TTC Lesion Area  
MEMRI-DWI Mismatch  
Correlation of MEMRI-DWI Mismatch to TTC Lesion Area

### Discussion

Nonspecific MEMRI Signal-Enhancement: Relation to Anesthesia and Blood Gases  
Brain Edema After Osmotic BBB Disruption  
Is MEMRI Signal-Enhancement Indicative of Tissue Damage?  
Brain Damage Verified by TTC Lesion  
MEMRI-DWI Mismatch



# Brain Damage and Mismatch Between Manganese-Enhanced MRI (MEMRI) and Diffusion-Weighted MRI in the Absence of Specific Neuronal Stimuli; Potential Pitfalls in MEMRI After Osmotic BBB Disruption

David G. Bennett<sup>1</sup>, Nils Henninger<sup>3</sup>, Marc Fisher<sup>3,4</sup>, Christopher H. Sotak<sup>1,2,4</sup>

Departments of Biomedical Engineering<sup>1</sup> and Chemistry & Biochemistry<sup>2</sup>

Worcester Polytechnic Institute

Worcester, Massachusetts 01609

Department of Neurology<sup>3</sup>

University of Massachusetts Memorial Healthcare – Memorial Campus

Worcester, Massachusetts 01605

Department of Radiology<sup>4</sup>

University of Massachusetts Medical School

Worcester, Massachusetts 01605

Part of this work was presented at the 15<sup>th</sup> annual meeting of the International Society of Magnetic Resonance in Medicine, Berlin, Germany, May 2007.

*Manuscript in Progress*

## Abstract

The goal of this study was to determine the effects of two osmotic blood-brain barrier (BBB) disruption protocols on brain tissue, apparent diffusion coefficient (ADC), manganese-enhanced magnetic resonance imaging signal changes (MEMRI signal-enhancement), and differences in area of ADC deficit and nonspecific MEMRI signal-enhancement (MEMRI-DWI mismatch) in the rat brain following infusion of manganese chloride ( $\text{MnCl}_2$ ) and Evans Blue (EB). Significant brain edema, tissue damage, ADC deficit, and nonspecific MEMRI signal-enhancement was detected in the rat following osmotic BBB disruption by arabinose (arabinose group) or mannitol (mannitol group) and  $\text{MnCl}_2$ +EB infusion in rat. Histology by 2,3,5 triphenyltetrazolium chloride (TTC) and EB stain verified brain damage and BBB-permeability changes respectively. The mean value of ipsilateral hemisphere brain area, TTC lesion area, ADC deficit and deficit area, and MEMRI signal-enhancement and enhancement area were all increased (or decreased in the case of ADC deficit) compared to homologous regions in the contralateral hemisphere by 12%, 7%, 23%, 28%, and 76% in the arabinose group and 15%, 9%, 22%, 21%, and 69% in the mannitol group, respectively.

Nonspecific MEMRI signal-enhancement was seen in the hippocampus (CA1-CA3), cortex, caudate putamen, hypothalamus and geniculate nucleus. The percentage of the ipsilateral hemisphere with a MEMRI-DWI mismatch was 9% and 8% in the arabinose and mannitol groups, respectively. The MEMRI-DWI mismatch in these experiments is noteworthy because the ADC deficit was not elicited by stroke and MEMRI signal-enhancement was not specific to a predefined neuronal stimulus. The results of this study suggest that ADC deficit and nonspecific MEMRI signal-enhancement is related to cytotoxic brain edema following osmotic BBB disruption. In addition, brain regions with MEMRI-DWI mismatch were found to correlate to regions of brain tissue damage as verified by TTC stain in several animals. The results of these experiments stress the need for careful assessment of baseline MEMRI-DWI mismatch prior to any subsequent neuronal stimulus or ischemic intervention; in order to ensure that the osmotic disruption of the BBB itself does not contribute significantly to any non-specific brain  $T_1$  or ADC changes.

**Key words:** manganese-enhanced MRI, blood-brain barrier, osmotic shock, rat brain

## 5.1 Introduction

### 5.1.1 MEMRI Background

Manganese-enhanced magnetic resonance imaging (MEMRI) is a useful imaging method for functional brain imaging (1,2) and neuronal tract tracing (3). In response to cell membrane depolarization, paramagnetic manganese ion ( $Mn^{2+}$ ) enters voltage-gated calcium ( $Ca^{2+}$ ) channels. Once in the cell,  $Mn^{2+}$  alters cell water-proton relaxation times resulting in a localized increase in  $T_1$ -weighted ( $T_1W$ ) signal intensity (MEMRI signal-enhancement) (1). This characteristic of  $Mn^{2+}$  has been used to advantage for imaging experimental neuropathologies such as cortical spreading depression (CSD) (4) and stroke (5,6). These experiments rely on the delivery of  $Mn^{2+}$  in a homogeneous fashion to the brain extracellular space prior to neuronal stimulus (i.e., experimental CSD or anoxic depolarization in stroke) via osmotic disruption of the BBB.

### 5.1.2 Side Effects of Osmotic BBB Disruption

Unfortunately, osmotic BBB disruption can have severe side effects such as vasogenic edema (7) and tissue damage (8). Therefore, the adverse effects of osmotic BBB disruption may interfere with normal brain response to neuronal stimulus in certain MEMRI experiments.

#### *MEMRI Experiments That Rely on Osmotic BBB Disruption*

Henning *et al.* used osmotic BBB disruption to introduce  $Mn^{2+}$  into brain prior to initiating experimental CSD via the cortical application of 4 M KCl (4). In their report, no evidence of the extent of BBB disruption or the possible side effects of osmotic agent infusion is provided. Nonspecific MEMRI signal-enhancement in their case, although possibly due to the intrinsic neuronal connectivity between specifically-stimulated and non-stimulated brain regions as discussed, may also be due to cellular response to osmotic BBB disruption. In addition, 3M KCl has been shown to induce areas of tissue necrosis local to the site of application on the exposed cortex (9,10) as shown in Figure 5-1. Without evidence of BBB disruption, and considering potential tissue injury by high concentrations of KCl applied to exposed cortex, interpretation of MEMRI signal-enhancement is speculative in MEMRI experiments designed to detect experimental CSD.

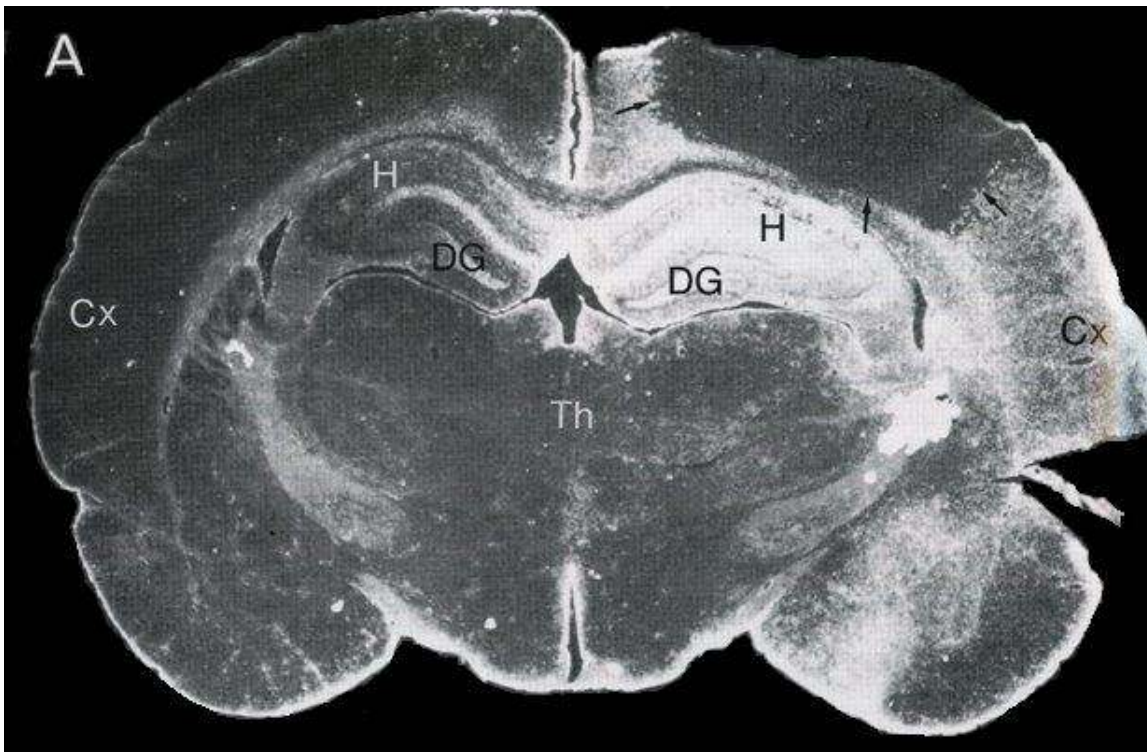


Figure 5-1. Time-dependent and region-specific pattern of labeling of tissue from KCl-exposed animals following in situ hybridization with  $^{35}\text{S}$ -labelled cRNA probes complimentary to glial fibrillary acidic protein mRNA. At 24 hours post application of 3M KCl (ten minute exposure) to the exposed parietal cortex, a focal area of tissue necrosis is evident (arrows). Reproduced from Ref. (10).

Of additional interest is the study by Aoki *et al.*, for which MEMRI was used to detect anoxic depolarization following experimental focal ischemia in rats (5). In their study, Aoki *et al.* used osmotic BBB disruption to introduce  $\text{Mn}^{2+}$  into the brain parenchyma prior to initiating experimental focal ischemia by permanent occlusion of the middle cerebral artery. In their study, Aoki *et al.* used diffusion-weighted (DW) and  $T_1\text{W}$  MRI to monitor the degree of tissue damage after stroke and qualitatively compared the spatial extent of apparent diffusion coefficient (ADC) deficit (in calculated ADC maps) to the spatial extent of MEMRI signal-enhancement. In so doing, the term ‘MEMRI-DWI mismatch’ was coined and was suggested to represent an area of salvageable tissue not readily detectable by DWI alone. Missing from the study of Aoki *et al.* was evidence of BBB disruption, distribution of  $\text{Mn}^{2+}$  in brain, and baseline MR images to indicate the presence or absence of a MEMRI-DWI mismatch prior to experimental stroke (i.e., by osmotic BBB disruption and infusion of  $\text{MnCl}_2$  into brain parenchyma). Also lacking was histological evidence showing the effects, if any, of osmotic BBB disruption on brain tissue. Demonstration of healthy

brain tissue following osmotic BBB disruption is important because osmotic disruption of the BBB has been shown to result in pronounced neuronal changes and astrocytic swelling (11). Therefore, without knowledge of the degree and extent of BBB disruption, and the state of brain tissue following osmotic BBB disruption, interpretation of MEMRI signal-enhancement and ADC changes detected after stroke intervention is potentially ambiguous.

### *Osmotic BBB Disruption Leads to Changes in MRI Contrast and to Tissue Damage*

In the present study, the goal was to investigate the effects of an infusion of manganese chloride following osmotic BBB disruption on DW images and the corresponding ADC maps, T<sub>1</sub>W images, and brain tissue based on the use of two different BBB disruption protocols; one using arabinose and one using mannitol as the hyperosmotic agent. The mannitol protocol in our study is based on a protocol reported by Aoki *et al.* (5). The results of our work show significant changes in DW image contrast, nonspecific MEMRI signal-enhancement that correlates with Evans Blue-stained regions, and brain tissue damage by 2,3,5 triphenyltetrazolium chloride (TTC) staining in animals with osmotically-disrupted BBB; but without experimental stroke. These findings are important considerations for future MEMRI experiments that may utilize similar experimental protocols as described here and that rely on normal tissue response to specific neuronal stimuli following osmotic BBB disruption.

## 5.2 Methods

### 5.2.1 Animal Preparation

This study was approved by the Institute Animal Care and Use Committee (IACUC) of the University of Massachusetts Medical School (IACUC Protocol A-1756 and A-875). Male Sprague-Dawley rats (250-385g; Charles River Laboratories, Worcester, MA) were divided into two groups: 1) infusion of 5 ml/kg of 1.6M arabinose over 55 seconds and 2 ml/kg of MnCl<sub>2</sub>+Evans Blue (EB) solution while under 2-3% isoflurane anesthesia (arabinose group, N=10); and 2) infusion of 5 ml/kg of 1.4M mannitol at 50 ml/hr (5) and 0.3 ml of MnCl<sub>2</sub>+EB mixture solution while under 0.5% isoflurane and chloral hydrate (400 mg/kg i.p.) anesthesia (mannitol group, N=4). Arabinose was chosen as an alternate osmotic agent based on the higher solubility of compound as compared to mannitol. Rats in the arabinose group were initially anesthetized with 5% isoflurane and maintained at 2-3% isoflurane during surgery. Rats in the mannitol group were initially anesthetized with 5%

isoflurane followed by an i.p. injection of 400 mg/kg chloral hydrate. Isoflurane was reduced to 0.5% while the rats were under chloral hydrate anesthesia. PE-50 and PE-10 polyethylene catheters were placed in the left femoral vein (i.v.) for blood pressure and gas monitoring and right external carotid artery (ECA) for drug administration, respectively.

For catheterization of the right ECA, a ventral midline incision was made in the neck. The omohyoid muscle was separated longitudinally and retracted laterally to isolate and expose the right common carotid artery (CCA), ECA, internal carotid artery (ICA) and pterygopalatine artery (PPA). The PPA was permanently ligated. Following temporary clamping of the CCA, the ECA was ligated and a small incision was made into the vessel for placement of the PE-10 catheter. The PE-10 catheter tip was inserted such that the tip would not disturb blood flow in the CCA towards the ICA. After properly securing the PE-10 catheter, the CCA clamp was removed allowing normal blood flow to the right ICA (the right CCA was clamped for approximately 10 minutes in each animal). Cannulation of the right ECA limited drug delivery to the right side of the brain allowing the left side to serve as control. Rectal temperature was continuously monitored with a rectal probe and maintained at 37 °C using a thermostatically-controlled heat lamp (Model 73ATD, YSI Inc., Yellow Spring, OH) during preparation.

Five minutes prior to osmotic BBB disruption, animals were switched from air/isoflurane to 100% O<sub>2</sub>/isoflurane in preparation for apnea during arabinose and mannitol infusion. Animals were switched back to air/isoflurane thirty seconds following the end of the arabinose or mannitol infusion. Arterial blood gases were recorded (i-STAT Portable Clinical Analyzer, Heska Corp. Waukesha, WI) while breathing air/2-3% isoflurane (N=4 arabinose and mannitol groups) and while breathing 100% O<sub>2</sub>/0.5% isoflurane (N=4, arabinose group) before osmotic BBB disruption. Blood pressure (World Precision Instruments Pressure Monitor, Model BP-1) was sampled twice per second using Labview-based data acquisition software (N=3, arabinose and mannitol group).

### **5.2.2 Osmotic BBB Disruption and MnCl<sub>2</sub>+EB Administration**

To disrupt the BBB, 1.6M L-arabinose or 1.4M D-mannitol solution (5 ml/kg, Sigma, St. Louis) was infused into the right ECA over a period of 55 seconds or 50 ml/hr, respectively, using a syringe pump (Model PHD 2000; Harvard Apparatus, Holliston, MA). Two minutes prior to the infusion of L-arabinose or D-mannitol, a slow (6 ml/hr) infusion of (the same) L-arabinose or D-mannitol was started and continued for 1 minute in an effort to compensate for vasogenic edema

induced by the bolus L-arabinose or D-mannitol infusion (12). Physiologically-buffered saline (PBS) containing 10 mM manganese chloride ( $\text{MnCl}_2 \cdot 4\text{H}_2\text{O}$ ; Sigma, St. Louis) and 2% EB (Sigma, St. Louis) was infused into the right ECA at a rate of 4.5 ml/hr using a syringe pump (Model 11; Harvard Apparatus, Holliston, MA) until a volume of 2 ml/kg or 0.3 ml was infused in the arabinose and mannitol groups, respectively. The  $\text{MnCl}_2$ +EB solution was infused 10 minutes following osmotic BBB disruption in both groups. Infusion of the  $\text{MnCl}_2$ +EB solution was initiated 10 minutes after arabinose injection to approximate the time of  $\text{MnCl}_2$  infusion relative to osmotic BBB disruption used by Aoki *et al.* (5). All solutions were warmed to 37 °C and filtered with 0.45  $\mu\text{m}$  syringe filters (Nalgene). Immediately after concluding the  $\text{MnCl}_2$ +EB infusion, rats in the mannitol group were switched from 0.5% isoflurane to 1.5% isoflurane in order to maintain anesthetic depth without additional chloral hydrate injections. Timing of infusions is summarized in Figure 5-2.

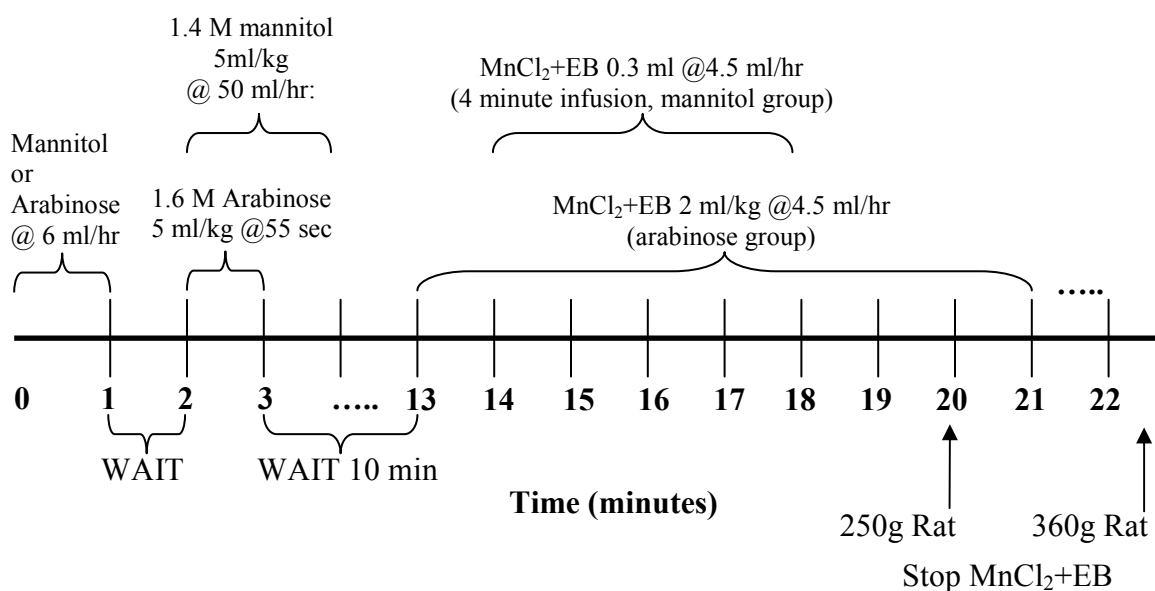


Figure 5-2: Timing of  $\text{MnCl}_2$ +EB infusion relative to arabinose or mannitol infusion.

### 5.2.3 MRI Measurements

MR experiments were performed using a Bruker Biospin 2.0T/45 cm imaging spectrometer equipped with  $\pm 20\text{G/cm}$  self-shielded gradients.  $T_1\text{W}$  MRI was performed using the following acquisition parameters: TR/TE = 500.0/10.8 ms, FOV = 3 cm x 3 cm, matrix size = 128x128, six slices with 2-mm thickness, NEX = 8. DWI was performed using a DW spin-echo, echo-planar MRI pulse sequence with TR/TE = 2000/51 ms, FOV = 3 cm x 3 cm, matrix size = 64x64 zero-filled to

128x128 before Fourier transformation, six slices with 2-mm thickness, NEX = 8, six b-values (23, 92, 207, 828, 1126, and 1471 s/mm<sup>2</sup>),  $\Delta = 6.0$  ms, and  $\delta = 24.31$  ms. The slice profiles of DW and T<sub>1</sub>W images were matched. The imaging plane was referenced to the rhinal fissure at the boundary of the olfactory bulb. Acquisition time for one set of images was 8.5 minutes for T<sub>1</sub>W and 4.8 minutes for DW imaging. During imaging, animals were placed prone within a home-built animal holder. The head of the animal was fixed within an 8-leg, 4.3 cm diameter <sup>1</sup>H volume coil. Animals were anesthetized with 2-3% (arabinose group) or 1.5% (mannitol group) isoflurane delivered at 1.5 L/min in breathing-quality air. Body temperature was maintained at 37.0 ± 1°C by circulated warm air using a T-type thermocouple and a double-point feedback control system. T<sub>1</sub>W and DW MRI continued sequentially for 3 hours to check for consistency in MEMRI signal-enhancement and DW image contrast over time.

#### **5.2.4 EB and 2,3,5 TriphenylTetrazolium Chloride (TTC) Histology**

Immediately following imaging, isoflurane anesthetic was increased to 5% and shortly thereafter animals were decapitated. The brain was quickly removed, placed on a section of parafilm and subsequently cooled for thirty minutes to facilitate handling. Brains were then dissected into six 2-mm slices that corresponded spatially to MR slices (first slice at 1mm ventral to the rhinal fissure of olfactory bulb). After dissection, brain slices were placed in saline and scanned using a Hewlett-Packard Scanner (Model #3970) at a resolution of 1200 dpi. After scanning, brain slices were placed in a 2% solution of TTC (a water and ethanol soluble tetrazolium salt; C<sub>19</sub>H<sub>15</sub>ClN<sub>4</sub>; FW = 335 (13)) and warmed to 37 °C in a lab oven (Fisher Isotemp 500 Series). The time from osmotic BBB disruption to brain slice placement in TTC solution was approximately 4 hours in each animal. After ten minutes in the lab oven, all slices were placed in zinc formalin for fixation overnight. The next day, brain slices were scanned using a Hewlett-Packard Scanner (Model #3970) at a resolution of 1200 dpi. TTC ‘stains’ the brain tissue differently as compared to Evans Blue dye. TTC is reduced by enzymes in normal tissue to a red, fat soluble, light-sensitive compound (formazan) that turns normal tissue red thereby delineating normal from damaged tissue (14). Specifically, after histological staining of brain by TTC, regions that do not appear red are likely to have irreversible mitochondrial damage, such as may be caused by stroke or severe hypoxia. Evans Blue, in contrast, is a dye that stains brain tissue (and most other tissues) blue upon contact.



### 5.2.5 Data Analysis

Region of interest (ROI) definitions and calculations in T<sub>1</sub>W images and ADC maps were made using ImageJ (NIH) software (Rasband, W.S., ImageJ, U. S. National Institutes of Health, Bethesda, Maryland, USA, <http://rsb.info.nih.gov/ij/>, 1997-2006). ROIs were drawn freehand to distinguish between MEMRI signal-enhanced regions, ADC-deficit regions, and normal brain tissue. MEMRI signal-enhancement increase, MEMRI signal-enhancement area, ADC deficit, and ADC-deficit area (DA) were all calculated using ROIs drawn freehand by 1) observer visualization; and 2) intensity-thresholding on T<sub>1</sub>W images and calculated ADC maps, respectively. For intensity-thresholding on T<sub>1</sub>W images, MEMRI signal-enhancement in the ipsilateral hemisphere was determined by voxels whose signal intensity was 2 standard deviations above the mean of all voxels in the contralateral hemisphere. This method of analyzing MEMRI signal-enhancement was chosen to match the technique of Aoki *et al.* (5) thus allowing us to compare our MEMRI signal-enhancement results to theirs.

For thresholding ADC maps, ADC deficit in the ipsilateral hemisphere was determined by pixels whose values were 2 standard deviations below the mean of all pixels in the contralateral hemisphere. Results from the two ROI definition techniques were compared to determine if ROI thresholding significantly underestimates the degree and spatial extent of MEMRI signal-enhancement and ADC deficit. Data are presented as mean  $\pm$  standard error of the mean (SEM), with a separate term for the inter-slice standard deviation (ISSD). Regions of MEMRI signal-enhancement, ADC deficit, and MEMRI-DWI mismatch were determined by correlation to a standard rat brain atlas (15) based on the slice location in terms of distance from bregma. T<sub>1</sub>W and DW image reconstruction was performed using Paravision's Image Processing and Display Software (Xtip).

#### *Percent Edema*

Edema in the ipsilateral hemisphere was calculated by comparing the area of the ipsilateral hemisphere to the area of the contralateral hemisphere in both T<sub>1</sub>W and histological images on a slice-by-slice basis. Percent edema was calculated using Eq. 5.1.

$$\% \text{ Edema} = \frac{\text{Ipsi Hem Area} - \text{Contra Hem Area}}{\text{Contra Hem Area}} \times 100 \quad 5.1$$

where ‘Ipsi Hem Area’ is the area of the ipsilateral hemisphere in  $\text{mm}^2$ , and ‘Contra Hem Area’ is the area of the contralateral hemisphere in  $\text{mm}^2$ .

### *MEMRI Signal-Enhancement*

MEMRI signal-enhancement in  $T_1W$  images was calculated through comparison of  $T_1W$  MR signal intensity in MEMRI signal-enhanced regions in the ipsilateral hemisphere and  $T_1W$  MR signal intensity in the homologous contralateral control regions on a slice-by-slice basis:

$$\text{MEMRI Signal - Enhancement (\%)} = \frac{S_{IH} - SI_{CH}}{SI_{CH}} \times 100 \quad 5.2$$

where  $SI_{IH}$  is the mean signal intensity for an ROI in the ipsilateral hemisphere and  $SI_{CH}$  is the mean signal intensity for the equivalent ROI in the contralateral control hemisphere. Percent area of MEMRI signal-enhancement in  $T_1W$  images was calculated on a slice-by-slice basis by comparison of MEMRI signal-enhancement area to the area of the entire ipsilateral hemisphere.

$$\text{MEMRI Signal - Enhanced Area (\%)} = \frac{\text{MEMRI Signal - Enhanced Area}}{\text{Total Ipsi Hem Area}} \times 100 \quad 5.3$$

### *Apparent Diffusion Coefficient (ADC) Parameter Mapping*

ADC mapping was performed on DW images on a pixel-by-pixel basis using in-house Interactive Data Language (v5.3 Research Systems, Boulder, CO) software based on the relationship between the natural log of the signal intensity in DW images and b-value as shown by Eq. 5.4.

$$M(t) = M_0 e^{-bD} \quad 5.4$$

where  $M(t)/M_0$  is the signal intensity at a particular b-value and  $D$  is the apparent diffusion coefficient along a particular gradient direction (e.g., x, y, or z). Maps of the average ADC were generated by taking the mean of the ADC values acquired along each of the x, y, and z-gradient directions.

*Percent ADC Deficit and Percent-Deficit Area (DA)*

Percent ADC deficit in the average ADC maps was calculated through comparison of the mean ADC deficit in the ROI of the ipsilateral hemisphere and the mean ADC in the entire contralateral hemisphere on a slice-by-slice basis:

$$ADC\ Deficit\ (\%) = \frac{-(ADC_{IH} - ADC_{CH})}{ADC_{CH}} \times 100 \quad 5.5$$

where  $ADC_{IH}$  is the mean ADC in the ADC deficit region in the ipsilateral hemisphere and  $ADC_{CH}$  is the mean ADC in the entire contralateral hemisphere. Percent-ADC-deficit area in the average ADC maps was calculated on a slice-by-slice basis by comparison of ADC-deficit area to the area of the entire ipsilateral hemisphere.

$$ADC\ Deficit\ Area\ (\%) = \frac{Ipsilateral\ ADC\ Deficit\ Area}{Total\ Ipsi\ Hem\ Area} \times 100 \quad 5.6$$

*MEMRI-DWI Mismatch*

MEMRI-DWI mismatch area was calculated as the area of ADC deficit in the ipsilateral hemisphere that exceeded the boundaries of the MEMRI signal-enhancing regions in the ipsilateral hemisphere. In most instances, MEMRI signal-enhancement was confined to the region with ADC deficit. For the few cases where MEMRI signal-enhancement extended beyond the boundaries of the ADC deficit region, MEMRI-DWI mismatch remained consistently defined as the region of ADC deficit outside the border of MEMRI signal-enhancement. Using ImageJ, ADC-deficit ROIs were overlaid on the  $T_1W$  images with regions of MEMRI signal-enhancement. Regions of ADC deficit that exceeded the boundaries of the regions of MEMRI signal-enhancement were outlined and defined as MEMRI-DWI mismatch. Regions of MEMRI signal-enhancement that exceeded the boundaries of the ADC-deficit region were not considered in any calculation. DW and  $T_1W$  images were registered for each slice in every animal. Percent MEMRI-DWI mismatch in  $T_1W$  images was calculated on a slice-by-slice basis by comparison of MEMRI-DWI mismatch area to the area of the entire ipsilateral hemisphere.

$$\% MEMRI - DWI\ Mismatch\ Area = \frac{MEMRI - DWI\ Mismatch\ Area}{Total\ Ipsi\ Hem\ Area} \times 100 \quad 5.7$$

### *TTC Histology*

For technical reasons, TTC staining was performed in 4 of the 10 animals of the arabinose group, and 3 of the 4 animals of the mannitol group. TTC staining was performed with Evans Blue present in brain. Therefore, in regions with deep Evans Blue stain, it was not clear by visualization if the underlying brain was or was not stained by TTC. To address this problem, RGB image deconvolution was used to separate the two colors (red by TTC and blue by Evans Blue) in the histological images. Deconvolved images were subsequently transformed into Hue, Saturation, and Brightness images. Saturation images were used due to the superior contrast between stained and unstained tissue. Based on the work of Ruifrok and Johnston, histological images (in RGB format) can be deconvolved into images that represent the independent contributions of red (Fast Red) and blue (Alcian Blue) stains (16). This method, based on an orthonormal transformation of the optical density values found in RGB images of each stain separately (i.e., a RGB histological image of red stain only and a RGB image of blue stain only) is summarized in Figure 5-3. Since we were not able to experimentally determine the optical density (OD) values for TTC and Evans Blue, we used previously determined OD values for Fast Red and Alcian Blue stain. Fast Red and Alcian Blue absorb at wavelengths similar to those of Evans Blue and TTC, respectively. The optical deconvolution calculations were performed using ImageJ (based on an algorithm written by G. Landini; <http://www.dentistry.bham.ac.uk/landinig/software/software.html>). The TTC-stained lesion was defined as that region of the brain that did not stain red after exposure to TTC. Brain regions with a TTC lesion were outlined freehand in both anterior-posterior and posterior-anterior views of the TTC histological image. The area (in mm<sup>2</sup>) of TTC lesion in both views was averaged and compared to the entire brain area. Percent-TTC-lesion area in the TTC histological images (after deconvolution and saturation transformation) was calculated on a slice-by-slice basis by comparison of TTC lesion area to the area of the entire ipsilateral hemisphere as shown in Eq. 5.8.

$$\% \text{ TTC Lesion Area} = \frac{\text{TTC Lesion Area}}{\text{Total Ipsi Hem Area}} \times 100 \quad 5.8$$

### Deconvolution (Independent Separation) of Two Stain Colors from One RGB Image

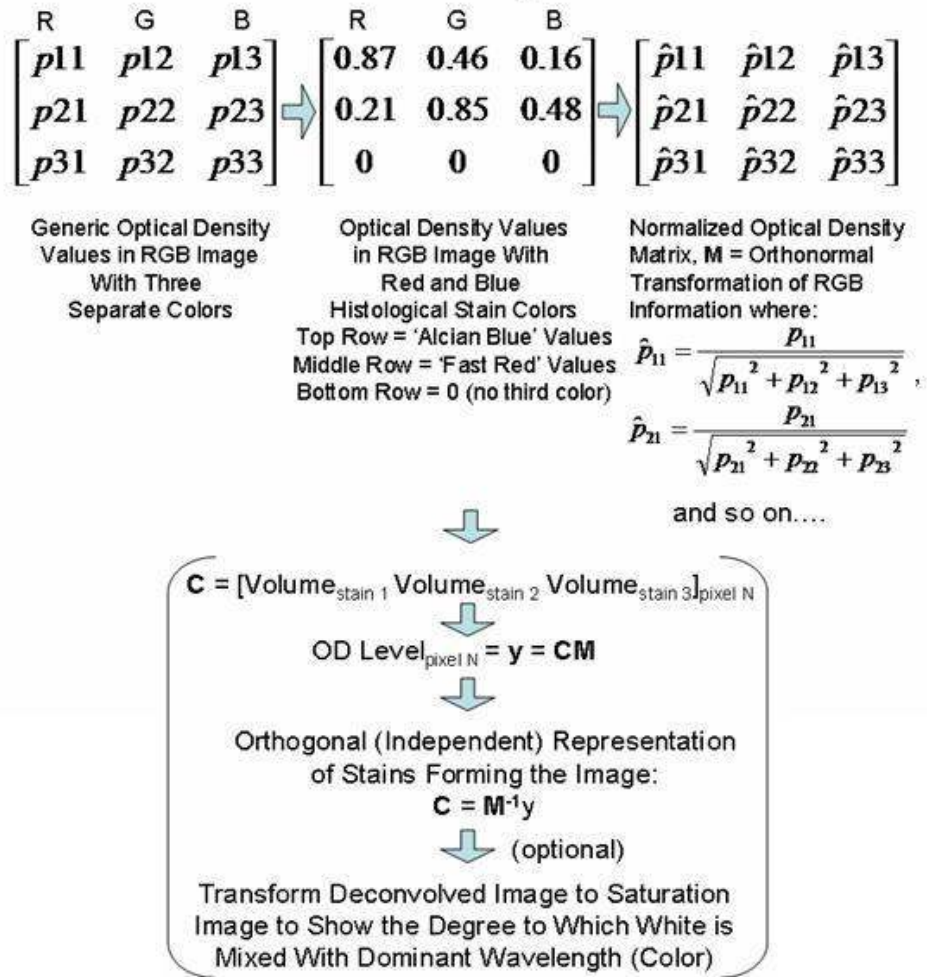


Figure 5-3: Flow chart for the color deconvolution algorithm from Ref. (16). The optical density (OD) values are experimentally determined for each stain alone. Since experimental determination of TTC and Evans Blue OD values was not possible in this study, the OD values of Fast Red and Alcian Blue (previously determined by G. Landini and provided within the ImageJ software) were used to approximate the OD values for TTC and Evans Blue, respectively. The OD values of Fast Red and Alcian Blue are comparable to those of TTC and Evans Blue, respectively ((e.g., Fast Red: 266 nm, TTC: 247 nm, Alcian Blue: 615 nm, Evans Blue: 611 nm; from Ref (13)). The orthonormal transformation of the OD matrix (normalized OD matrix) results in a matrix that describes the independent contribution of each stain color to the overall Red, Green, and Blue (RGB) values in a RGB image. If  $C$  is defined as a 3x1 vector of the stain intensity at a particular pixel N, the OD level at pixel N is defined by  $y = CM$ , where  $M$  is the normalized OD matrix and  $C$  is the orthogonal (independent) representation of the stains forming the RGB image. Finally, solving for  $C$  is done by  $C = M^{-1}y$ .

*Edema Correction*

All MEMRI signal-enhancement area, ADC-deficit area, and TTC-lesion area data were corrected for edema. T<sub>1</sub>W images and calculated average ADC maps were edema-corrected based on percent edema calculated from T<sub>1</sub>W images. TTC-lesion area was edema-corrected based on percent edema calculated from TTC-stain images. Percent MEMRI signal-enhancement, percent ADC deficit, and percent TTC-lesion area were all edema corrected according to Eq. 5.9.

$$EC = Original \times \left( 1 - \frac{(Ipsi\ Hem\ Area - Contra\ Hem\ Area)}{Contra\ Hem\ Area} \right) \quad 5.9$$

where ‘EC’ is the edema-corrected version of the original percent MEMRI signal-enhancement, percent ADC deficit, or percent TTC-lesion area and ‘Ipsi Hem Area’ and ‘Contra Hem Area’ are the areas of the ipsilateral hemisphere and contralateral hemisphere in the T<sub>1</sub>W or histological (TTC) images.

**5.2.6 Statistical Analysis**

Data are reported as mean ± s.e.m.. Data from the arabinose and mannitol groups were compared by paired and unpaired Student’s t-tests. Statistically significant differences were reported when P<0.05.

**5.3 Results****5.3.1 Animal Physiology***Blood Pressure*

The mean arterial blood pressures before osmotic BBB disruption were 89.8 ± 0.4 mmHg in the arabinose group and 72.0 ± 0.4 mmHg in the mannitol group. During infusion of arabinose and mannitol, the blood pressure fluctuated by approximately 10 mmHg. As shown in Figure 5-4, blood pressure reached a steady-state immediately following the end of arabinose and mannitol infusions, but followed a downward trend from 90 mmHg to 80 mmHg two minutes later in the arabinose group and an upward trend from 80 mmHg to 98 mmHg two minutes later in the mannitol group. Immediately following the start of MnCl<sub>2</sub>+EB infusion in the arabinose group, blood pressure dropped by approximately 5 mmHg and then fluctuated between ±10 mmHg until the end of the infusion. Blood pressure in the arabinose group reached a steady state after the end of MnCl<sub>2</sub>+EB infusion. Blood pressure in the mannitol group started to drop before the MnCl<sub>2</sub>+EB infusion and

continued to drop until a steady-state was reached. Blood pressure in the mannitol group dropped again in response to an increase in isoflurane anesthetic concentration.

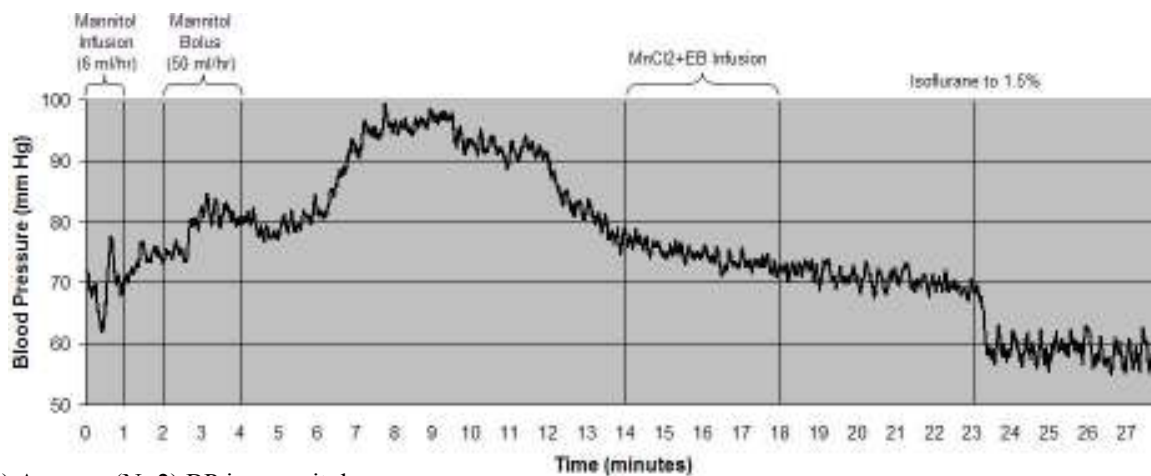
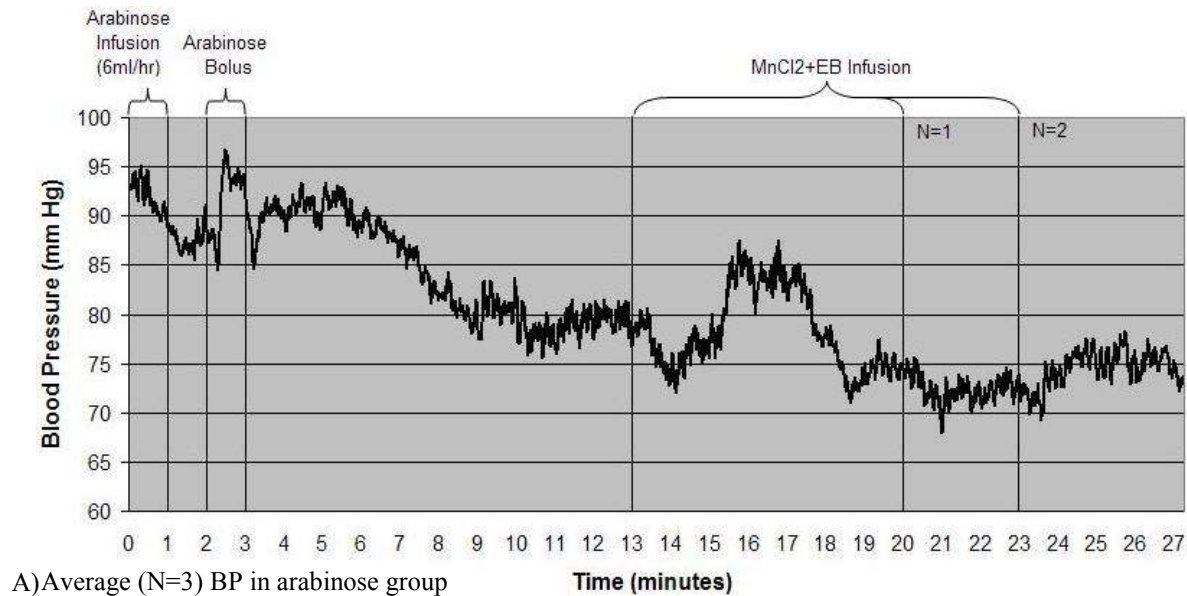


Figure 5-4: Blood pressure dynamic before, during, and after osmotic BBB disruption and  $MnCl_2+EB$  infusions. The curves represent a 10-point moving average of blood pressure readings from three animals in the arabinose group (A) and two animals in the mannitol group (B) for which blood pressure data was acquired. The difference in infusion times of  $MnCl_2+EB$  in the arabinose group was due to the different weights of the animals (250g, 375g, and 385g). Blood pressure decreased immediately after and during  $MnCl_2+EB$  infusion in the arabinose and mannitol group, respectively. A decrease in blood pressure during i.v.  $MnCl_2$  infusion is expected because  $Mn^{2+}$  competes for  $Ca^{2+}$  in the heart.

*Blood Gases*

Blood gases were recorded in certain animals (N=4 arabinose group, N=3 mannitol group) prior to osmotic BBB disruption and prior to switching from air/isoflurane to 100% O<sub>2</sub>/isoflurane. Blood-gas data is summarized in Table 5-1.

Table 5-1: Blood Gases Measured from Animals in the Arabinose and Mannitol Groups.

Blood Gas Variable	Arabinose Group (N=4) Average ± SEM	Mannitol Group (N=3) Average ± SEM
pH	7.4 ± 0.0	7.4 ± 0.0
PCO <sub>2</sub>	49.8 ± 2.0	48.0 ± 1.8
PO <sub>2</sub>	57.8 ± 2.0	74.0 ± 0.6
BE <sub>ECF</sub> (mmol/L)	2.3 ± 0.7	0.7 ± 0.3
HCO <sub>3</sub> (mmol/L)	27.8 ± 0.7	26.5 ± 0.5
TCO <sub>2</sub> (mmol/L)	29.5 ± 0.8	28.0 ± 0.6
SO <sub>2</sub> (%)	87.5 ± 1.0	93.7 ± 0.3
Na (mmol/L)	136.0 ± 0.7	135.3 ± 0.9
K (mmol/L)	4.5 ± 0.2	5.5 ± 0.1
iCa (mmol/L)	1.4 ± 0.0	1.2 ± 0.0
Glu (mg/dL)	261.5 ± 17.0	245.7 ± 10.3
Hct (%PCU)	37.3 ± 0.4	42.3 ± 1.5
Hb (g/dL)	12.7 ± 0.1	14.4 ± 0.5

**5.3.2 Brain Edema***Percent Edema in T<sub>1</sub>W and Histological Images*

Figure 5-5 shows histological images from one animal in which edema of the right hemisphere is apparent. Percent-edema in both animal groups was calculated separately using T<sub>1</sub>W and histological images. Percent-edema in the arabinose group was 4% ± 1% and 12% ± 2% using T<sub>1</sub>W and histological images for edema calculation, respectively. Percent-edema in the mannitol group was 9% ± 1% and 15% ± 2% using T<sub>1</sub>W and histological images for edema calculation, respectively. A significant difference between the use of T<sub>1</sub>W and histological images to calculate



edema was detected in the arabinose group ( $P < 0.01$  paired Student's t-test). A significant difference between percent-edema in the arabinose and mannitol groups was detected when edema was calculated using T<sub>1</sub>W images ( $P < 0.05$ , unpaired Student's t-test).



Figure 5-5. Histological images from one animal in the arabinose group shown with the outline of the contralateral (left) hemisphere superimposed on the ipsilateral (right) hemisphere of each image. The images correspond to dissected brain slices 6 mm posterior (leftmost image) to 4 mm anterior (rightmost image) of bregma. Starting with the image at 6 mm posterior of bregma, edema becomes grossly evident in the image at 0 bregma and becomes more severe as the slices progress anterior to bregma.

*Quantitative Summary of Edema*

Table 5-2 shows the average percent-edema across all dissected brain regions for the arabinose and mannitol groups.

Table 5-2: Average Percent-Edema Area (% ipsilateral hemisphere area increase over contralateral hemisphere area) from T<sub>1</sub>W MR and Histological Images Following Osmotic BBB Disruption and Infusion of MnCl<sub>2</sub>+EB Solution.

Group	Average Percent-Edema in Brain (using Eq. 5.1)			
	T <sub>1</sub> W Images		Histological Images	
	Mean ± SEM (%)	ISSD <sup>a</sup> (%)	Mean ± SEM (%)	ISSD <sup>a</sup> (%)
Arabinose	4 ± 1	2	12 ± 2 <sup>**</sup>	4
Mannitol	9 ± 1 <sup>*</sup>	1	15 ± 2	2

\*P < 0.05 between arabinose and mannitol groups by T<sub>1</sub>W images , \*\*P < 0.01 between T<sub>1</sub>W and histological images within arabinose group.

### 5.3.3 MEMRI Signal-Enhancement

#### *Enhancement Level, Enhancement Area, and Regional Coverage*

Figure 5-6 shows representative multi-slice T<sub>1</sub>W MRI for animals in the arabinose and mannitol groups. MEMRI signal-enhancement is nonspecific, i.e., no neuronal stimulus was applied to any animal in either group. The average percentage increase in signal intensity in MEMRI signal-enhanced regions was  $88\% \pm 6\%$  and  $77\% \pm 6\%$  in the arabinose group by T<sub>1</sub>W image visualization and intensity-thresholding, respectively. For the mannitol group, the comparable values were  $91\% \pm 8\%$  and  $69\% \pm 11\%$  by T<sub>1</sub>W-image visualization and intensity-thresholding, respectively. Calculation of MEMRI signal-enhancement by T<sub>1</sub>W-image visualization and intensity-thresholding methods within the arabinose and mannitol groups did not produce significantly different results. There was no significant difference in signal intensity in MEMRI signal-enhanced regions between the arabinose and mannitol groups (by either T<sub>1</sub>W-image visualization or intensity-thresholding methods).

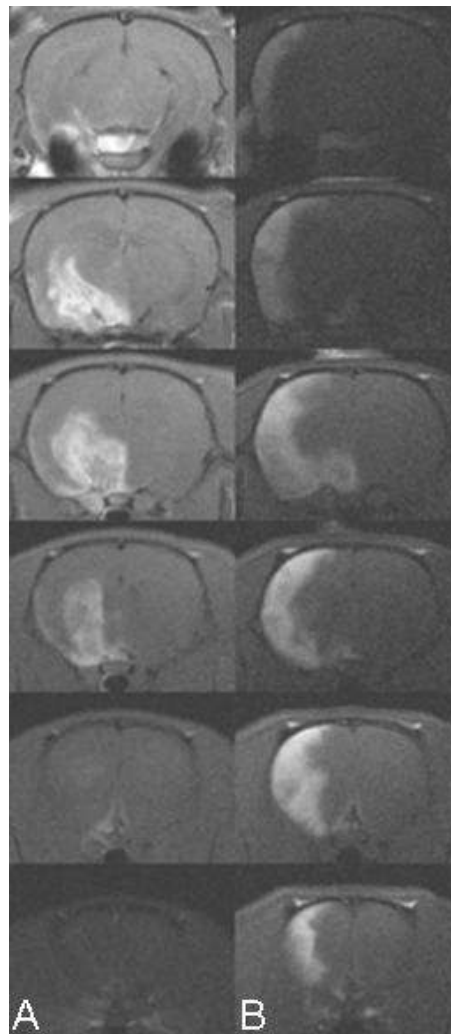


Figure 5-6: Multi-slice  $T_1W$  MRI for representative animals in the arabinose (A) and mannitol (B) groups (left side of image = right hemisphere). MEMRI signal-enhancement in the right (ipsilateral) hemisphere is apparent in both cases.  $T_1W$  images were acquired approximately 50 minutes after osmotic BBB disruption and 40 minutes after infusion of the  $MnCl_2+EB$  solution.

Percent-area of MEMRI signal-enhancement (before edema correction) in the arabinose group was  $26\% \pm 2\%$  and  $21\% \pm 2\%$  by the  $T_1W$ -image visualization and intensity-thresholding methods, respectively. For the mannitol group, the comparable values were  $25\% \pm 4\%$  and  $16\% \pm 5\%$ , by the  $T_1W$ -image visualization and intensity-thresholding methods, respectively. Calculation of percent-area of MEMRI signal-enhancement by the  $T_1W$ -image visualization and intensity-thresholding methods within the arabinose and mannitol groups did not produce significantly different results. There was no significant difference in percent area of MEMRI signal-enhanced regions between the arabinose and mannitol groups (by either  $T_1W$ -image visualization or intensity-

thresholding methods). Brain regions with MEMRI signal-enhancement included cortex, hippocampus (CA1-CA3), geniculate nucleus, deep mesencephalic nucleus, thalamic nucleus, deep mesencephalic nucleus, and caudate putamen. Patterns of MEMRI signal-enhancement within or across groups were not observed. MEMRI signal-enhancement was, however, always confined to the right (ipsilateral) hemisphere.

#### *Quantitative Summary of MEMRI Signal-Enhancement*

Tables 5-3 and 5-4 show the average percent MEMRI signal-enhancement and average percent area of MEMRI signal-enhancement, respectively, for different brain regions for the arabinose and mannitol groups.

Table 5-3: Average Percent MEMRI Signal-Enhancement (% , relative to a homologous region in the contralateral hemisphere) from T<sub>1</sub>W MRI for all MEMRI Signal-Enhanced Brain Regions Following Infusion of the MnCl<sub>2</sub>+EB solution.

Group	Average Percent MEMRI Signal-Enhancement Across All Brain Slices (using Eq. 5.2)			
	MEMRI Signal-Enhanced Regions Determined By Visualization		MEMRI Signal-Enhanced Regions Determined By Intensity-Thresholding	
	Mean ± SEM (%)	ISSD <sup>a</sup> (%)	Mean ± SEM (%)	ISSD <sup>a</sup> (%)
Arabinose	76 ± 6	12	88 ± 6	16
Mannitol	69 ± 11	19	91 ± 8	13

<sup>a</sup>To account for intra-animal variability, the inter-slice standard deviation (ISSD) was calculated from values for the average signal increase (%) across slices with MEMRI signal-enhancement.

Table 5-4: Average Percent Area of MEMRI Signal-Enhancement (relative to the total brain area) from T<sub>1</sub>W MRI for all MEMRI Signal-Enhanced Brain Regions Following Infusion of the MnCl<sub>2</sub>+EB solution.

Group	Average Percent-Area of MEMRI signal-enhancement Across All Brain Slices (using Eq. 5.6)							
	MEMRI Signal-Enhanced Regions Determined By Visualization				Intensity-Thresholding			
	Before Edema Correction		After Edema Correction		Before Edema Correction		After Edema Correction	
	Mean	ISSD <sup>a</sup>	Mean	ISSD <sup>a</sup>	Mean	ISSD <sup>a</sup>	Mean	ISSD <sup>a</sup>
	± SEM (%)	(%)	± SEM (%)	(%)	± SEM (%)	(%)	± SEM (%)	(%)
Arabinose	26 ± 2	10	24 ± 2	9	21 ± 2	7	20 ± 2	7
Mannitol	25 ± 4	4	22 ± 4	4	16 ± 5	4	15 ± 4	4

<sup>a</sup>To account for intra-animal variability, the inter-slice standard deviation (ISSD) was calculated from values for the average signal-intensity increase (%) across slices with MEMRI signal-enhancement.

### 5.3.4 ADC Deficit

#### *ADC Deficit Level, ADC Deficit Area, and Regional Coverage*

Figure 5-7 shows representative multi-slice, calculated average ADC maps for representative animals in the arabinose and mannitol groups. The average percent decrease in ADC value in regions with ADC deficit was 23% ± 1% and 29% ± 1% in the arabinose group by the ADC-map visualization and intensity-thresholding methods, respectively. For the mannitol group, the corresponding values were 22% ± 3% and 34% ± 5% by the ADC-map visualization and intensity-thresholding methods, respectively. Calculation of percent-ADC deficit by ADC-map visualization and intensity-thresholding methods within the arabinose and mannitol groups was significantly different in both groups ( $P < 0.001$  arabinose group;  $P < 0.05$  mannitol group). There was no significant difference in ADC deficit between the arabinose and mannitol groups (by either ADC-map visualization or intensity-thresholding methods).

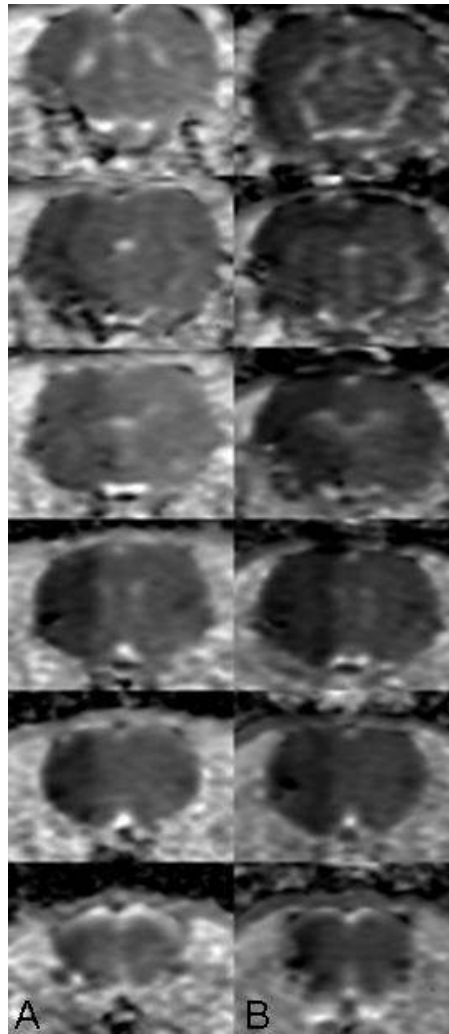


Figure 5-7: Multi-slice, calculated average ADC maps for animals in the arabinose (A) and mannitol (B) groups (left side of image = right hemisphere). ADC deficit in the right (ipsilateral) hemisphere is apparent in most of the slices in both cases. The DW images used to generate the ADC maps in (A) and (B) were acquired approximately 60 minutes after osmotic BBB disruption.

Percent-area of ADC deficit (before edema correction) was  $30\% \pm 2\%$  and  $19\% \pm 1\%$  in the arabinose group by the ADC-map visualization and intensity-thresholding methods, respectively. For the mannitol group, the corresponding values were  $24\% \pm 7\%$  and  $8\% \pm 4\%$  by the ADC-map visualization and intensity-thresholding methods, respectively. Calculation of percent-area of ADC deficit by the ADC-map visualization and intensity-thresholding methods was significantly different in the arabinose group only ( $P < 0.001$  arabinose group;  $P = 0.06$  mannitol group). Calculated percent-area of ADC deficit was significantly different between the arabinose and mannitol groups (by ADC-map intensity-thresholding method only,  $P < 0.05$ ; by ADC-map visualization,  $P = 0.45$ ).

Brain regions with ADC deficit included cortex, hippocampus (CA1-CA3), geniculate nucleus, deep mesencephalic nucleus, thalamic nucleus, and caudate putamen. ADC deficit was confined to the right (ipsilateral) hemisphere and may reflect changes in brain volume due to osmotic BBB disruption or moderate hypoxia. Patterns of ADC deficit within or across groups were not observed.

### *Quantitative Summary of ADC Deficit*

Tables 5-5 and 5-6 show the average percent-ADC deficit and average percent-area of ADC deficit, respectively, for different brain regions for the arabinose and mannitol groups.

Table 5-5: Average Percent-ADC Deficit (% relative to a homologous region in the contralateral hemisphere) from ADC Maps for all Brain Regions with ADC Deficit Following Osmotic BBB Disruption and Infusion of the  $MnCl_2+EB$  Solution.

Group	Average Percent-ADC Deficit Across All Brain Slices (using Eq. 5.5)			
	ADC Deficit Region Determined By Visualization		ADC Deficit Region Determined By Intensity-Thresholding	
	Mean $\pm$ SEM (%)	ISSD <sup>a</sup> (%)	Mean $\pm$ SEM (%)	ISSD <sup>a</sup> (%)
Arabinose	23 $\pm$ 1	4	29 $\pm$ 1 <sup>***</sup>	6
Mannitol	22 $\pm$ 3	4	34 $\pm$ 5 <sup>*</sup>	10

<sup>a</sup>To account for intra-animal variability, the inter-slice standard deviation (ISSD) was calculated from values for the average ADC deficit (%) across slices with MEMRI signal-enhancement. <sup>\*\*\*</sup>P<0.001 compared to ADC-map visualization method, <sup>\*</sup>P<0.05 compared to ADC-map visualization method.

Table 5-6: Average Percent-Area of ADC Deficit (% relative to a homologous region in the contralateral hemisphere) from ADC Maps for all Brain Regions with ADC Deficit Following Osmotic BBB Disruption and Infusion of the MnCl<sub>2</sub>+ EB Solution.

Group	Average Percent-Area of ADC Deficit Across All Brain Regions (using Eq. 5.3)							
	ADC Deficit Region Determined By ADC Map:				Intensity-Thresholding			
	Visualization		After		Before		After	
	Before		Edema		Edema		Edema	
	Correction		Correction		Correction		Correction	
	Mean	ISSD <sup>a</sup>	Mean	ISSD <sup>a</sup>	Mean	ISSD <sup>a</sup>	Mean	ISSD <sup>a</sup>
±	(%)	±	(%)	±	(%)	±	(%)	
SEM		SEM		SEM		SEM		
(%)		(%)		(%)		(%)		
Arabinose	30 ± 2	9	28 ± 2	8	19 ± 1 <sup>***</sup>	10	18 ± 1 <sup>***</sup>	10
Mannitol	24 ± 7	7	21 ± 6	7	8 ± 4 <sup>*</sup>	6	8 ± 3 <sup>*</sup>	6

<sup>a</sup>To account for intra-animal variability, the inter-slice standard deviation (ISSD) was calculated from values for the average area of ADC deficit across slices with ADC deficit. <sup>\*\*\*</sup>P<0.001 compared to the ADC map visualization method. <sup>\*</sup>P<0.05 compared to the arabinose group.

### 5.3.5 TTC Lesion Area

#### *TTC- Stain Deconvolution and Saturation Transform*

Figure 5-10 shows representative multi-slice histological images after TTC staining for one animal in the arabinose group and one animal in the mannitol group. Figure 5-10 also shows the same TTC stain images after deconvolution (using the algorithm summarized in Figure 5-3) into independent representative EB and TTC images and after transformation into Saturation images. As shown in Figure 5-10, deconvolution is useful for separating multicolor histological images (in RGB format) into images that represent the contribution of each stain color to the RGB image. The Saturation transform is useful for enhancing the contrast between stained and unstained regions in the deconvolved images.



*Percent-TTC-Lesion Area and Regional Coverage*

Percent-TTC-lesion area was  $8\% \pm 1\%$  and  $7\% \pm 1\%$  in the arabinose group before and after edema correction, respectively. For the mannitol group, the corresponding values were  $11\% \pm 6\%$  and  $9\% \pm 5\%$  before and after edema correction, respectively. Percent-TTC-lesion area was not significantly different between the arabinose and mannitol groups. Regional coverage of TTC lesion included regions in which MEMRI signal-enhancement, EB stain, and ADC deficit were detected such as cortex (primary somatosensory cortex, secondary somatosensory cortex, primary motor cortex, secondary motor cortex), hippocampus (CA1-CA3), geniculate nucleus, deep mesencephalic nucleus, thalamic nucleus, and caudate putamen.

*TTC-Lesion Area and ADC Deficit*

When the TTC-lesion area was analyzed on an animal-by-animal basis, there were instances when the TTC lesion was outside of the region of MEMRI signal-enhancement and EB stain, but not outside of the region of ADC deficit. An animal (from the arabinose group) with TTC lesion outside the region of MEMRI signal-enhancement is shown in Figure 5-11. The spatial extent of the TTC lesion in this animal does not correlate with areas of MEMRI signal-enhancement or EB staining, but does correlate well with a homologous region of ADC deficit and average DW hyperintensity. Another slice from the same animal is shown in Figure 5-12 and shows a distinct TTC lesion in the cortex on both sides of the histological slice. Brain regions which suffered injury are shown in adjacent rat-atlas images and are summarized in Table 5-9. Without the TTC histological staining, the absence of MEMRI signal-enhancement in  $T_1W$  images and/or EB staining in this region may be misinterpreted as a region that did not respond to specific neuronal stimulus and/or a region which did not experience BBB disruption. As shown here, ipsilateral regions devoid of MEMRI signal-enhancement may be, in fact, regions with permanent brain damage not capable of responding to specific neuronal stimulus. TTC staining, in this case, clearly provides helpful additional information. No significant difference in TTC lesion area was detected between the arabinose group (N=4) and mannitol (N=3) group.

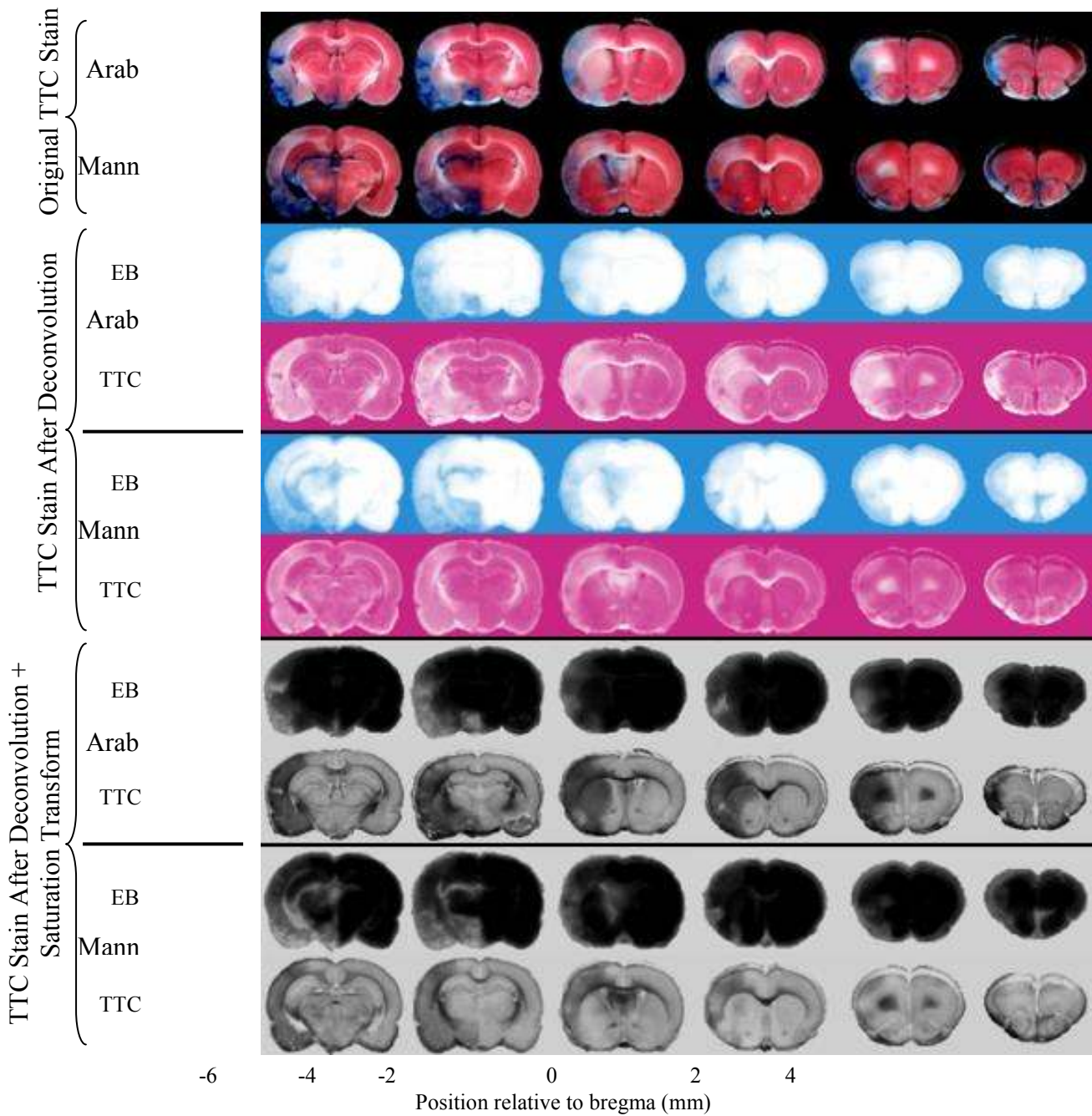


Figure 5-10: Multi-slice, histological images after TTC and EB staining in two animals, one each from the arabinose and mannitol groups. The TTC/EB-stained images were deconvolved into images representative of the independent contributions of EB and TTC staining in the ipsilateral hemisphere. Deconvolved images were then transformed into Saturation images to enhance contrast differences between stained and unstained tissue. In TTC Saturation images, healthy tissue appears bright (relative to surrounding tissue) and dark regions (outside of white matter) correspond to regions with tissue injury. Bright regions in the EB Saturation images correspond to EB-stained regions.

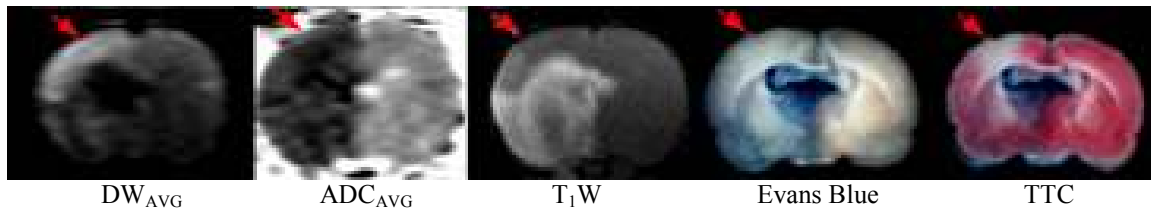


Figure 5-11: Averaged signal intensity of DW images acquired separately with diffusion-sensitization in the x, y, and z directions ( $b=1126 \text{ s/mm}^2$ ), average calculated ADC map, T<sub>1</sub>W, EB, and TTC images from one animal in the arabinose group. Red arrows point to a region with TTC lesion in which no MEMRI signal-enhancement or EB staining is present. The TTC lesion in this case is suggestive of blood-flow levels below the threshold necessary to support cellular viability. Low blood flow in this region may be the result of severe edema following osmotic disruption of the BBB. The ‘black hole’ in the middle of the slice in the DW<sub>AVG</sub> image is due to the large paramagnetic reduction of  $T_2$  (relative to TE) at a high concentration of  $\text{Mn}^{2+}$  as verified by dark EB staining and MEMRI signal-enhancement in the same region.

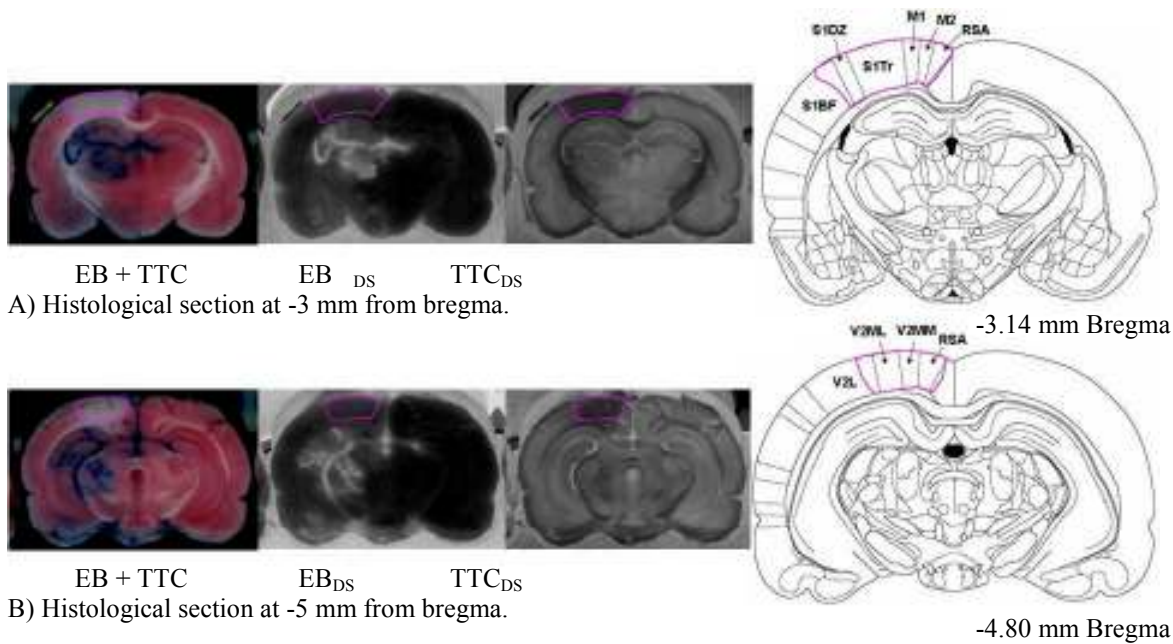


Figure 5-12: TTC lesion area from an animal in the arabinose group viewed from both sides of a histological slice. EB<sub>DS</sub> and TTC<sub>DS</sub> are the deconvolved and saturation-transformed representations of EB and TTC staining in the histological image. The purple-outlined region defines the TTC lesion. A) Histological slice at -3 mm from bregma. The TTC lesion in this slice is confined to the cortex. B) Opposite side of histological slice in A) at -5 mm from bregma (histological slices are 2-mm thick). The TTC lesion in this part of the slice is also confined to the cortex. Specific cortical regions within the TTC lesion are shown in the corresponding rat-brain-atlas slices (reproduced from Ref. (15)). White areas in the EB<sub>DS</sub> images correspond to sites of EB staining and dark regions in TTC<sub>DS</sub> images correspond to sites of no TTC staining (tissue injury). The region of brain damage indicated by the TTC lesion was likely due to severe edema and subsequent lack of blood flow in this region prior to the administration of the  $\text{MnCl}_2$ +EB solution. The lack of EB staining in this region supports this assertion. Table 5-9 provides definitions for the abbreviations of brain-region names included within TTC-lesion area.

Table 5-9: Brain-Region Abbreviations and Corresponding Names from Rat Brain Atlas in Figure 5-12.

-3.14 mm Bregma		-4.80 mm Bregma	
Abbreviation	Name	Abbreviation	Name
RSA	Retrosplenial agranular cortex	RSA	Retrosplenial agranular cortex
M2	Secondary motor cortex	V2MM	Secondary visual cortex, mediomedial area
M1	Primary motor cortex	V2ML	Secondary visual cortex, mediolateral area
S1Tr	Primary somatosensory cortex, trunk region	V2L	Secondary visual cortex, lateral area
S1DZ	Primary somatosensory cortex, dysgranular region		
S1BF	Primary somatosensory cortex, barrel field		

*Quantitative Summary of TTC-Lesion Area*

Table 5-10 summarizes the average percent-TTC-lesion area for different brain regions before and after edema correction in the arabinose and mannitol groups.

Table 5-10: Average Percent Area of TTC Lesion Area (% relative to total brain area) from TTC Histological Images for all Brain Regions with TTC Lesion Following Osmotic BBB Disruption and Infusion of the MnCl<sub>2</sub>+ EB Solution.

Group	Average Percent-Area of TTC Lesion in All Brain Regions (using Eq. 5.3)			
	TTC Lesion Region Determined By Visualization Before Edema Correction		After Edema Correction	
	Mean ± SEM	ISSD <sup>a</sup>	Mean ± SEM	ISSD <sup>a</sup>
	(%)	(%)	(%)	(%)
Arabinose	8 ± 1	3	7 ± 1	3
Mannitol	11 ± 6	3	9 ± 5	2

<sup>a</sup>To account for intra-animal variability, the inter-slice standard deviation (ISSD) was calculated from values for the average lesion area (%) across slices with TTC lesion.

### 5.3.6 MEMRI-DWI Mismatch

#### *Percent Area of MEMRI-DWI Mismatch and Regional Coverage*

Figure 5-8 shows representative multi-slice,  $T_1W$  images and a calculated average ADC map for an animal in the arabinose group. Images in Figure 5-8 are spatially co-registered and were reconstructed with the same matrix size (128x128) by Bruker Paravision software (Xtip). Percent-area of MEMRI-DWI mismatch (before edema correction) was  $10\% \pm 3\%$  and  $10\% \pm 2\%$  in the arabinose group by the visualization and intensity-thresholding methods (using both  $T_1W$  images and ADC maps), respectively. For the mannitol group, the corresponding values were  $9\% \pm 4\%$  and  $4\% \pm 3\%$  by the visualization and intensity-thresholding methods (using both  $T_1W$  images and ADC maps), respectively. Calculation of percent-area of MEMRI-DWI mismatch by visualization and intensity-thresholding methods within the arabinose and mannitol groups did not produce significantly different results. Calculated percent-area of MEMRI-DWI mismatch was not significantly different between the arabinose and mannitol groups (by either visualization or intensity-thresholding methods). Brain regions with MEMRI-DWI mismatch included cortex (primary somatosensory cortex, secondary somatosensory cortex, primary motor cortex, secondary motor cortex), hippocampus (CA1-CA3), geniculate nucleus, deep mesencephalic nucleus, thalamic nucleus, and caudate putamen. Regions of MEMRI-DWI mismatch were determined by correlation to a standard rat brain atlas (15) based on the slice location in terms of distance from bregma as shown in Figure 5-9 and summarized by Table 5-7. Patterns of MEMRI-DWI mismatch within or across groups were not observed. MEMRI-DWI mismatch was always confined to the right (ipsilateral) hemisphere.

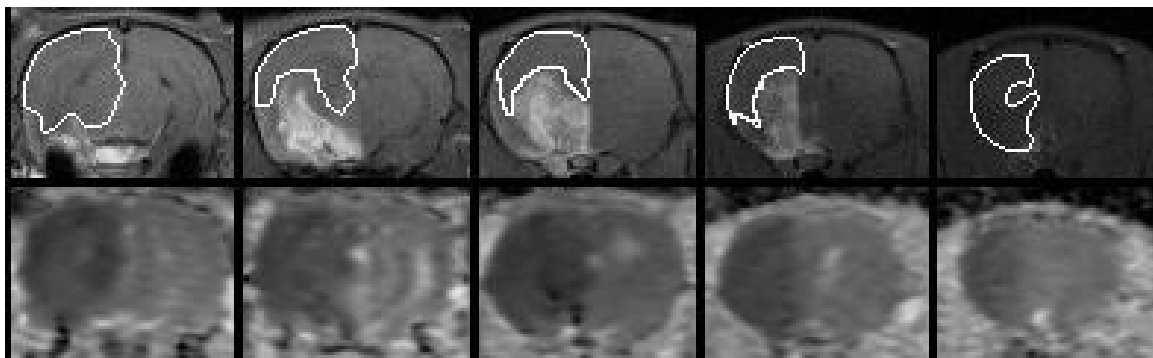
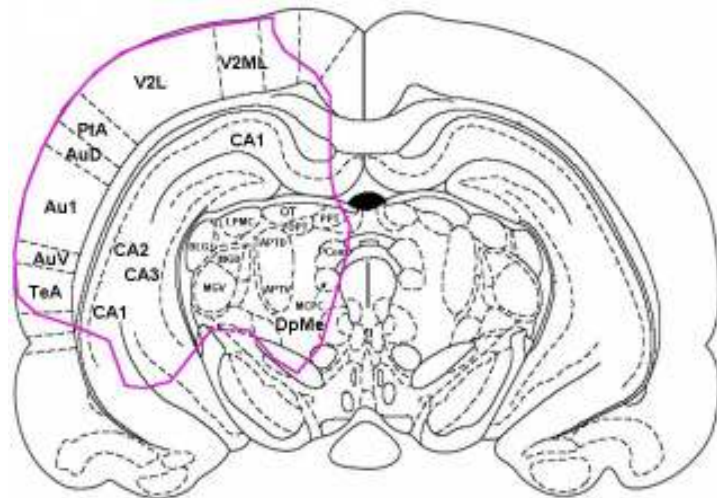


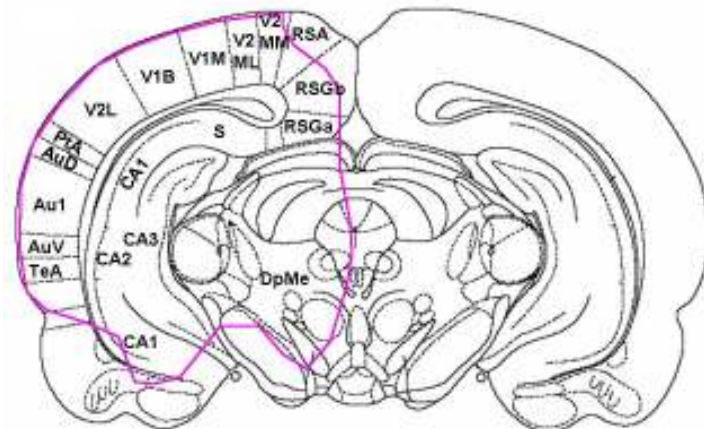
Figure 5-8:  $T_1W$  (top row) images and ADC maps (bottom row) from one animal in the arabinose group (left side of image = right hemisphere). The images and maps correspond to brain slices 6 mm posterior (leftmost image) to 2 mm anterior (rightmost image) of bregma. The white outline in  $T_1W$  images is the region of MEMRI-DWI mismatch. MEMRI-DWI mismatch for all animals is defined as the region of ADC deficit that is outside the region of MEMRI signal-enhancement. Area of MEMRI-DWI mismatch was greatest in this particular animal.



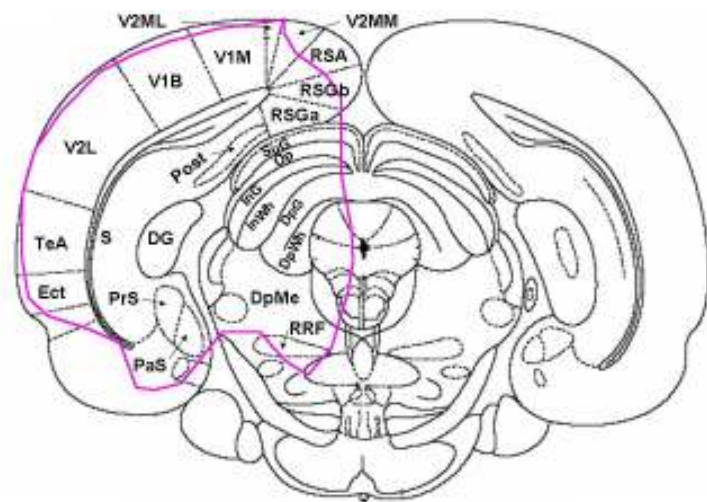
T<sub>1</sub>W MRI with MEMRI-DWI mismatch region (white outline). This T<sub>1</sub>W MR slice (2mm thick) includes MR signal from brain regions located -5 mm to -7 mm bregma.



-5.2 mm Bregma



-5.8 mm Bregma



-6.8 mm Bregma

Figure 5-9. Correlation of MEMRI-DWI mismatch region to a standard rat atlas (15). Abbreviations shown here are expanded in Table 5-7.

Table 5-7. Names for Brain-Region Abbreviations in Figure 5-9. From Ref. (15)

V2ML: Secondary visual cortex, mediolateral area
V2L: Secondary visual cortex, lateral area
PtA: Parietal association cortex
AuD: Secondary auditory cortex, dorsal area
Au1: Primary auditory cortex
AuV: Secondary auditory cortex, ventral area
TeA: Temporal association cortex
CA1: field CA1 of hippocampus
CA2: field CA2 of hippocampus
CA3: field CA3 of hippocampus
OT: Nucleus of the optic tract
PPT: Posterior pretectal nucleus
OPT: Olivary pretectal nucleus
LPMC: Lateral posterior thalamic nucleus, mediocaudal part
DLG: Dorsal lateral geniculate nucleus
MGD: Medial geniculate nucleus, dorsal part
MGV: Medial geniculate nucleus, ventral part
APTD: Anterior pretectal nucleus, dorsal part
APTV: Anterior pretectal nucleus, ventral part
DpMe: Deep mesencephalic nucleus
McPC: Magnocellular nucleus of the posterior commissure
PCom: Nucleus of the posterior commissure
RSA: Retrosplenial agranular cortex
RSGb: Retrosplenial granular b cortex
RSGa: Retrosplenial granular a cortex
V2MM: Secondary visual cortex, mediomedial area
V1M: Primary visual cortex, monocular area
V1B: Primary visual cortex, binocular area
S: Subiculum
PrS: Presubiculum
PaS: Parasubiculum
RRF: Retrorubral field
DpWh: Deep white layer of the superior colliculus
DpG: Deep gray layer of the superior colliculus
InWh: Intermediate white layer of the superior colliculus
InG: Intermediate gray layer of the superior colliculus
Op: Optic nerve layer of the superior colliculus
SuG: Superficial gray layer of the superior colliculus
Post: Postsubiculum

*Quantitative Summary of MEMRI-DWI Mismatch*

Table 5-8 summarizes the average percent-area of MEMRI-DWI mismatch for different brain regions before and after edema correction for the arabinose and mannitol groups.

Table 5-8: Average Percent-Area of MEMRI-DWI Mismatch (% relative to total brain area) from T<sub>1</sub>W Images and ADC Maps for all Brain Regions with ADC Deficit Regions Outside of MEMRI Signal-Enhanced Regions Following Osmotic BBB Disruption and Infusion of the MnCl<sub>2</sub>+ EB Solution.

Group	Average Percent-Area of MEMRI-DWI Mismatch in All Brain Regions (using Eq. 5.7)							
	MEMRI-DWI Mismatch Regions Determined By Visualization				Intensity-Thresholding			
	Before Edema Correction		After Edema Correction		Before Edema Correction		After Edema Correction	
	Mean	ISSD <sup>a</sup>	Mean	ISSD <sup>a</sup>	Mean	ISSD <sup>a</sup>	Mean	ISSD <sup>a</sup>
	± SEM (%)	(%)	± SEM (%)	(%)	± SEM (%)	(%)	± SEM (%)	(%)
Arabinose	10 ± 3	4	9 ± 3	4	10 ± 2	4	10 ± 2	4
Mannitol	9 ± 4	4	8 ± 4	4	4 ± 3	4	4 ± 3	3

**5.3.7 Correlation of MEMRI-DWI Mismatch to TTC Lesion Area**

For certain animals, the region of MEMRI-DWI mismatch appears to be spatially correlated with the corresponding region of infarction; as defined on the TTC histological sections. This correlation is intuitive at first because a region with reduced ADC deficit – but lacking MEMRI signal-enhancement and EB staining – may indeed be a brain region with severely impaired blood flow and tissue damage that occurs prior to the administration of the MnCl<sub>2</sub>+EB solution (which is not expected to reach areas with impaired blood flow). Regions of cellular swelling (cytotoxic edema) and reduced blood flow are likely to appear hyperintense on DW images and dark on the corresponding calculated ADC maps.

Most animals for which TTC staining was performed showed an observable spatial correlation between MEMRI-DWI mismatch area and TTC lesion area; two such animals are shown in Figure 5-13. It is clear, however, that there are slices that do not show a MEMRI-DWI mismatch



but do exhibit infarction on the TTC histological sections (e.g., in the arabinose group, the top two slices and the bottom slice; in the mannitol group, the two bottom slices). Conversely, there are also regions of MEMRI-DWI mismatch which do not exhibit infarction on the TTC histological sections. These particular observations should be interpreted carefully due to volume averaging effects in DW images.

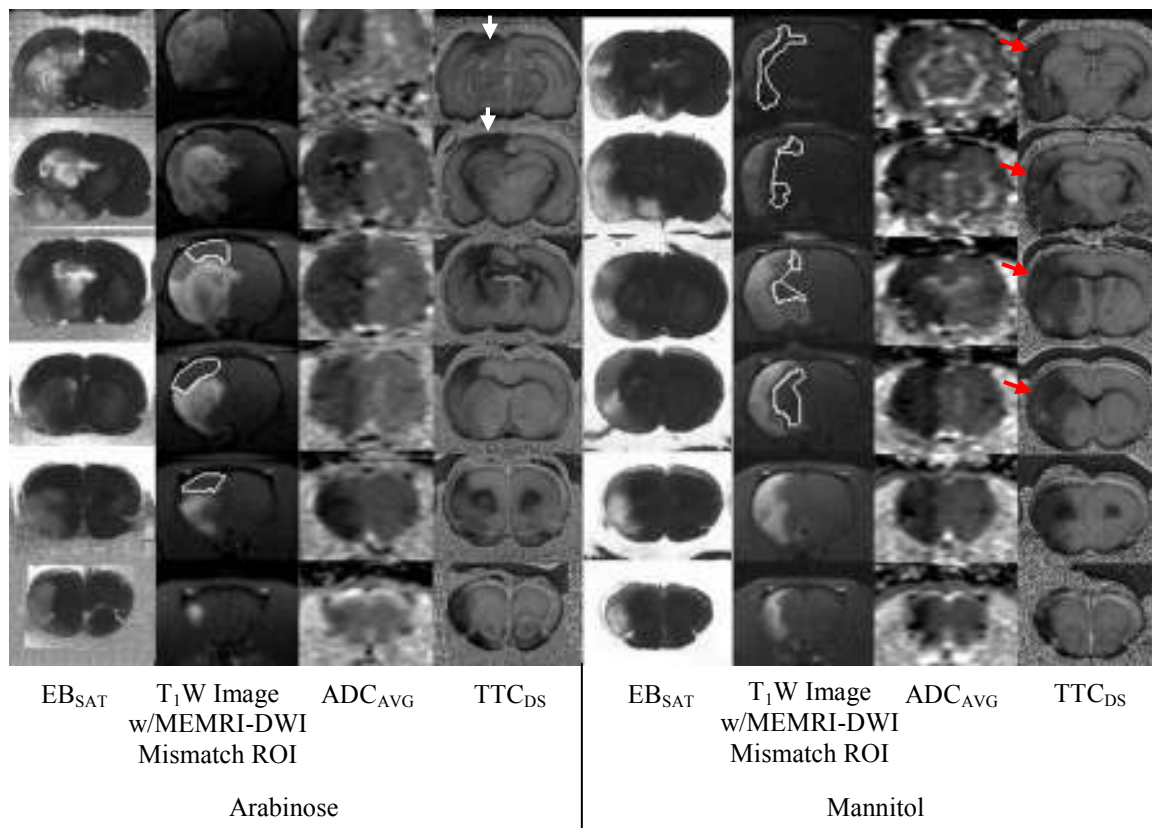


Figure 5-13: EB stain image after Saturation transform (EB<sub>SAT</sub>), T<sub>1</sub>W MRI (i.e., MEMRI), average ADC map (ADC<sub>AVG</sub>), and TTC stain image after deconvolution and Saturation transform (TTC<sub>DS</sub>) in two animals; one from the arabinose group (left) and the other from the mannitol group (right). Regions outlined in white on the T<sub>1</sub>W images indicate regions of MEMRI-DWI mismatch. Dark regions in TTC<sub>DS</sub> images (excluding white matter) correspond to regions of tissue injury (infarction). For both animals, the spatial correlation between regions of MEMRI-DWI mismatch and infarction of the TTC histological section is apparent. However, there are instances where there is no spatial correlation between TTC-lesion area and the MEMRI-DWI mismatch (white arrows in top two slices of arabinose group) and when TTC lesion area is adjacent to MEMRI-DWI mismatch (red arrows in top four slices in mannitol group).

## 5.4 Discussion

The results of this study have shown that infusions of hyperosmolar mannitol or arabinose – followed by i.v.  $\text{MnCl}_2$ +EB in a spontaneously breathing rat anesthetized with isoflurane – lead to brain edema, ADC deficit, nonspecific MEMRI signal-enhancement, and permanent brain damage in the ipsilateral hemisphere. Previous MEMRI experiments in rats have indicated little or no MEMRI signal-enhancement following osmotic BBB disruption and i.v.  $\text{MnCl}_2$  infusion (1,4,5). In these studies, however, DWI was either not performed (1,4) or DWIs were acquired only after stroke (5). In addition, there are no reports in the MEMRI literature that have examined brain-tissue status following osmotic BBB disruption using histology. Therefore, although there is experimental evidence showing that nonspecific MEMRI signal-enhancement is avoidable; it is not known if these methods can prevent brain edema, tissue damage, and/or changes in brain ADC. In an attempt to explain the results of this study, brain edema and its relationship to the water ADC, TTC staining, and tissue damage is discussed. Furthermore, the implications of the MEMRI-DWI mismatch, in absence of a specific neuronal stimulus or experimental stroke, is considered.

### 5.4.1 Nonspecific MEMRI Signal-Enhancement: Relation to Anesthesia and Blood Gases

One major difference between the experimental protocol used in this study and that of Aoki *et al.* is the anesthetic regimen and the  $\text{MnCl}_2$ +EB infusion protocol. Evans Blue is not biologically inert (17) and has been shown to cause electrical and behavioral seizures in rats (18), but is not expected to affect MEMRI signal-enhancement levels. In a previous study conducted by the authors (see Chapter 4), a MEMRI experimental protocol identical to the protocol used in the present study (arabinose group) was used with the exception that no EB was mixed with  $\text{MnCl}_2$ . MEMRI signal-enhancement was clearly present in the absence of EB, ruling out the dye as the primary factor in nonspecific MEMRI signal-enhancement. The study of Aoki *et al.* used a range of anesthetics that included diethyl ether, halothane and a 1:1 oxygen/nitrous oxide gas mixture, and pentobarbital; all with the animal under artificial ventilation. The use of artificial ventilation allowed for blood pressure, pH,  $\text{PCO}_2$ , and  $\text{PO}_2$  to be held within the physiological range. By contrast, animals in the present study were anesthetized with 2% isoflurane under spontaneously-breathing conditions. Even without ventilation, blood pressure,  $\text{PO}_2$ , and  $\text{PCO}_2$  was maintained within the optimal physiological range. Table 5-13 summarizes pH,  $\text{PO}_2$ , and  $\text{PCO}_2$  in animals from the Aoki *et al.* sham group and

the mannitol and arabinose groups in this study. Blood gases were taken prior to the infusion of mannitol or arabinose.

Table 5-13: Blood Pressure Immediately Before Osmotic BBB Disruption and Blood Gases Measured from Animals in the Aoki *et al.* Sham Group and the Arabinose (N=4) and Mannitol (N=3) Groups.

Blood Gas Variable	Aoki <i>et al.</i> Sham Group (N=5) Average $\pm$ SD	Arabinose Group (N=4) Average $\pm$ SD	Mannitol Group (N=3) Average $\pm$ SD
Blood pressure (mm Hg)	91.4 $\pm$ 9.9	88.0 $\pm$ ?	75.0 $\pm$ ?
pH	7.5 $\pm$ 0.1	7.4 $\pm$ 0.0	7.4 $\pm$ 0.0
PCO <sub>2</sub> (mm Hg)	37.2 $\pm$ 5.3	49.8 $\pm$ 2.0	48.0 $\pm$ 1.8
PO <sub>2</sub> (mm Hg)	129.6 $\pm$ 20.6	<b>57.8 <math>\pm</math> 2.0*</b>	<b>74.0 <math>\pm</math> 0.6*</b>

\*Moderately hypoxic

Although this study did not use a combined non-volatile and volatile anesthetic regimen as described by Aoki *et al.*, this approach may be helpful in reducing or eliminating any nonspecific MEMRI signal-enhancement under these conditions. Indeed, isoflurane, specifically, has been shown to increase blood plasma glutamate levels in humans (19,20) and exacerbate brain edema in brain-injured rats (20). It is possible that increased levels of glutamate in the brain during isoflurane anesthesia established a baseline neuronal activity high enough to induce nonspecific MEMRI signal-enhancement with the presence of extracellular Mn<sup>2+</sup>. In addition, moderate hypoxia (21) in our animals before mannitol or arabinose infusion, together with possible exacerbation of brain edema from isoflurane anesthesia, may have led to the significant reduction in brain ADC detected in our experiments.

#### 5.4.2 Brain Edema After Osmotic BBB Disruption

##### *Vasogenic Edema*

Brain edema has historically been categorized into two types; vasogenic and cytotoxic. Cytotoxic edema is cellular swelling that is caused by a loss of ionic pump function and osmoregulation due to reduction of oxygen and nutrients to the cell resulting from a blood-flow

deficit or cessation. Vasogenic edema is characterized by damage to the BBB resulting in bulk flow of water from the vasculature to brain. Endothelial cell shrinkage by hyperosmolar agents – such as mannitol and arabinose – increases the permeability of the BBB to molecules with higher molecular weights, such as [ $^{14}\text{C}$ ]Sucrose (MW = 340 daltons) and [ $^3\text{H}$ ]Inulin (MW = 5500); implying bulk flow of these molecules from blood to brain (22). Using an osmotic-BBB-disruption protocol similar to that used in this study, Rapoport *et al.* found the arabinose-infused cerebral hemisphere to be edematous within 10-minutes after BBB disruption (7). Other studies report consistent vasogenic edema in the side of the brain that received the infusion of hyperosmolar mannitol (23,24). Vasogenic edema, however, has been suggested to play only a minor role in brain tissue injury as compared to cytotoxic edema (25).

#### *Vasogenic Edema and DW Imaging*

Vasogenic edema has been shown to increase the calculated ADC values on DW images. In a study specifically designed to determine the effect of vasogenic edema on ADC values, Ito *et al.* showed that vasogenic edema (by infusion of mock CSF into rat brain) results in an increase in ADC value while cytotoxic edema (by middle cerebral artery occlusion in rat) results in a decrease in ADC value in the affected regions (25). Although vasogenic edema may have been present within animals prior to acquiring the initial DWIs in this study, the observed ADC *deficits* (up to 34%) and the absence of ADC increases in any of the study animals suggests that vasogenic edema does not have a significant effect on the acute ADC changes observed in either animal group. However, since gross brain edema was clearly present following acute osmotic BBB disruption (Fig. 5-5), the BBB-disruption process itself appears to initiate vasogenic brain edema similar to that observed following the loss of BBB integrity that would result, for example, from ischemic damage to the cerebrovascular endothelium (except on a much shorter time scale).

#### *Cytotoxic Edema and Percent ADC Deficit*

Using cortical tissue-impedance measurements, cytotoxic edema has been shown to accompany early (one minute after middle cerebral artery occlusion in the brain) ischemia-induced changes in the volume of the brain extracellular space (26). The water ADC values in regions with cytotoxic edema were previously shown to be reduced by ~37% as compared to contralateral hemisphere at 1 hour after the onset of focal cerebral ischemia (27). Interestingly, the percent-reductions in water ADC values measured in this study (22% to 34%) are similar to those that

accompany acute cerebral ischemia; suggesting that a process similar to cytotoxic edema may be responsible for the ADC reductions observed following osmotic BBB disruption in the brain.

#### **5.4.3 Is MEMRI Signal-Enhancement Indicative of Tissue Damage?**

Aoki *et al.* asserted that the irreversibly-damaged stroke core following MCAO could be visualized as the region of MEMRI signal-enhancement contained within the region of ADC deficit. However, the experimental protocol used in this study also demonstrates similar regions of MEMRI signal-enhancement within the region of reduced ADC; even though neither animal group was subjected to a cerebral ischemic insult. The water ADC changes observed in this study identify brain regions where cell-volume changes or other injury result in alterations of the intracellular/extracellular tissue-water content. Since the mannitol BBB-disruption protocol and MnCl<sub>2</sub> infusion protocol used in this study were similar to those of the sham group of Aoki *et al.*, the results of the two studies might be expected to be similar. Table 5-11 summarizes results of comparisons between the mannitol group in this study and the corresponding sham group of Aoki *et al.* As shown in Table 5-11, ADC deficit area in our mannitol group is comparable to that in Aoki's sham group. However, ADC deficit area in our arabinose group shows a large difference (that would likely be statistically significant) from the ADC deficit area in the sham group of Aoki *et al.* These differences may be the result of a different anesthetic regimen used in our study. Other conditions such as severity of BBB disruption and cytotoxic edema in our experiments may also have been responsible for the differences in ADC deficit and MEMRI signal-enhancement between our animal groups and Aoki's sham group.

Table 5-11: Comparison of Mannitol and Arabinose Group Data for Percent-Area of ADC Deficit and MEMRI Signal-Enhancement in Rat Brain After Osmotic BBB Disruption with the Results of Aoki *et al.* (5).

Percent-Area Measurement	Group		
	Aoki <i>et al.</i> Sham* (N=5)	Present Study: Mannitol* (intensity- thresholding before EC, N=4)	Present Study: Arabinose (intensity- thresholding before EC, N=10)
	Mean $\pm$ SD (%)	Mean $\pm$ SD (%)	Mean $\pm$ SD (%)
ADC Deficit	8 $\pm$ 4	8 $\pm$ 7	19 $\pm$ 4
MEMRI Signal- Enhancement	5 $\pm$ 3	16 $\pm$ 9	21 $\pm$ 6
TTC Lesion	?	11 $\pm$ 11	8 $\pm$ 2

\* Aoki *et al.* (5) sham and mannitol groups listed in the table received the same concentration (1.4M) and dose (5 ml/kg) of mannitol administered at the same rate (50 ml/hr) and via the same intravenous route (ICA). The region of ADC deficit in the sham group of Aoki *et al.* was determined by thresholding the ADC map pixels at  $5.0 \times 10^{-4}$  mm<sup>2</sup>/s (i.e., ADC pixel values less than this threshold were included in the calculation of the ischemic lesion area). The region of ADC deficit in the mannitol and arabinose groups was determined by thresholding the ADC map pixels at 2 SDs below the mean of all ADC pixel-values in the contralateral hemisphere.

#### 5.4.4 Brain Damage Verified by TTC Lesion

##### *TTC Lesion Indicates Damage to Brain Tissue*

The use of TTC staining for the detection of ischemic brain damage was first reported by Bederson *et al.* in 1986 (14). Bederson *et al.* compared the use of TTC to that of the conventional hematoxylin and eosin (H&E) staining technique for the evaluation of ischemic brain damage after 24 h in the rat. Although TTC staining clearly demarcates region of brain infarction at 24 h after ischemia, Bederson *et al.* notes difficulty in correlating ischemic regions defined by TTC staining to

those delineated by H&E staining at times less than 6 h after the onset of ischemia. However, because many animals from both groups displayed an absence of TTC staining that was spatially correlated to regions of severe ADC deficit in certain brain regions we believe that our TTC stain data (acquired 4 hours after osmotic BBB disruption) provides reliable evidence of brain damage.

#### 5.4.5 MEMRI-DWI Mismatch

##### *Comparison of ADC Deficit Calculation: Aoki et al. Study vs. Present Study*

In a study to determine the efficacy of MEMRI for the evaluation of experimental stroke in rats, Aoki *et al.* found that MEMRI signal-enhanced regions in the ischemic brain were smaller than regions of ADC deficit. As a result of this observation, Aoki *et al.* coined the term ‘MEMRI-DWI mismatch’ (5) and suggested that the region of MEMRI signal-enhancement was restricted to (and indicative of) the irreversibly-damaged, ischemic core of the lesion.

As indicated in Table 5-11, the percent-area of ADC deficit in the sham group of Aoki *et al.* is similar to that of the mannitol group in this study. However, this result must be interpreted with some caution since the methods for calculating percent-area of ADC deficit were different in each case. For the sham group in the study of Aoki *et al.*, the ADC deficit was determined by using a fixed threshold ( $5.0 \times 10^{-4} \text{ mm}^2/\text{s}$ ) to identify pixels in the calculated ADC map that should be included as part of the ischemic lesion in the ipsilateral cortex. For the mannitol group in the present study, the region of ADC deficit was determined as those pixels in the ipsilateral hemisphere of the calculated ADC map that were 2 SDs below the mean of all ADC pixel-values in the contralateral hemisphere.

##### *MEMRI-DWI Mismatch: TTC-Lesion Area, ADC-Deficit Area, and Area of MEMRI Signal-Enhancement*

In this study, the MEMRI-DWI-mismatch region was defined as the region of ADC deficit that resides outside the boundary of the region of MEMRI signal-enhancement. Brain regions with reduced ADC, but that do not demonstrate MEMRI signal-enhancement or EB staining, are likely regions that experienced cytotoxic edema as a result of a cerebral-blood-flow deficit following mannitol (or arabinose) infusion. Regional patterns of EB staining, TTC staining, and MEMRI signal-enhancement (Fig. 5-13, arabinose group) indicate that the  $\text{MnCl}_2$ +EB solution did not permeate the BBB within regions that progressed to infarction (as defined by TTC staining) in those particular cases.

In contrast to the example in the previous paragraph, there were many instances in this study where the region of MEMRI signal-enhancement and EB staining were contained within the infarcted region as defined by TTC staining and reduced ADC (e.g., Fig. 5-13, mannitol group). In this case, reduced water ADC within the regions of BBB disruption suggests a condition that mimics cytotoxic edema. For example, osmotic BBB disruption may induce cell-volume changes similar to those observed during cytotoxic edema (i.e., cell swelling due to acute membrane depolarization), but via a different mechanism. These osmotically-induced cell-volume changes may be related to the uptake of  $Mn^{2+}$  into cells; assuming that the extracellular  $Mn^{2+}$  is present during that process. In this case, extracellular  $Mn^{2+}$  could be transported into the cell along with water that is moving under the influence of an osmotic gradient. Once inside the cell,  $Mn^{2+}$  would reduce the  $T_1$  relaxation time of the intracellular water, in the same manner that  $Mn^{2+}$  would do so had it entered the cell via voltage-gated calcium channels (VGCCs) following a specific neuronal stimulus. However, in this case,  $Mn^{2+}$  enters the cell as a result of osmotic water shifts that accompany BBB disruption, rather than via water shifts that accompany cell-membrane depolarization. The idea of  $Mn^{2+}$  entry into cells via osmotically-induced cell-volume changes is supported by reports of cellular volume regulation during exposure to hypertonic solutions (28,29). In one such report, McManus *et al.* used laser light scattering to monitor Rat C6 glioma cells in culture during exposure to hypertonic mannitol (30). In their study, McManus *et al.* show rapid cell shrinkage upon abrupt exposure to mannitol (+70 mOsm and +40 mOsm in separate experiments). After a brief lag time, cell volume was observed to return to baseline and proceeded to increase to a swollen state for the duration of a 30-minute observation period. Data from McManus *et al.* is shown in Figure 5-14. Based on the data in Figure 5-14, cell shrinkage and swelling are apparent for at least 5 minutes following exposure to hypertonic mannitol. If these *in vitro* conditions are close indicators of potential *in vivo* cell response to hyperosmolar mannitol (or arabinose) during osmotic BBB disruption, changes in ADC (ADC decrease due to cell swelling and loss of extracellular space) and entry of  $Mn^{2+}$  into cells is expected.



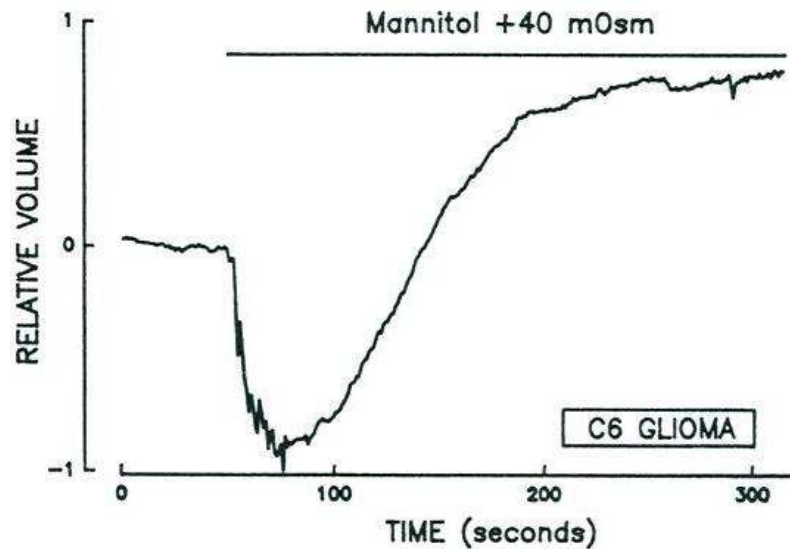


Figure 5-15: A representative recording of the volume behavior of C6 cells exposed to +40 mOsm hypertonic mannitol. Reproduced from Ref. (30)

It is not clear at this point how the BBB-disruption process might contribute to the irreversible tissue damage demonstrated on TTC (and indirectly on ADC). In this case, the mechanism of cell death may or may not be related to blood-flow deficits in brain.

#### *Mechanisms of MEMRI Signal-Enhancement; Nonspecific or Due to Anoxic Depolarizations?*

In the study of Aoki *et al.*, MEMRI signal-enhancement was suggested to result from anoxic depolarization of brain cells following experimental stroke in the presence of extracellular manganese. This suggestion was supported by data from sham animals, in which no stroke was induced and very little MEMRI signal-enhancement was observed as compared to animals in the experimental group.

The present study revealed significant MEMRI signal-enhancement without experimental stroke. As with the ADC deficit, the mannitol group in the present study was expected to exhibit a similar level of MEMRI signal-enhancement as compared to the sham group of Aoki *et al.*, due to the similarity of the experimental protocols between the two studies. Table 5-12 compares the MEMRI signal-enhancement in the sham group of Aoki *et al.* and the mannitol and arabinose groups in this study. Although it is clear the differences in MEMRI signal-enhancement between the two studies are statistically significant, the differences in the  $B_0$ -field strength (and other experimental details) between the two studies make it difficult to interpret the significance of this result.

Since experimental stroke was not induced in the present study, questions remain as to the underlying mechanism responsible for the MEMRI signal-enhancement observed in the mannitol and arabinose groups. It is important to consider that TTC lesion area was not always correlated to regions with MEMRI signal-enhancement. Therefore, MEMRI signal-enhancement, even when correlated to regions of ADC deficit, may not indicate regions of tissue damage. MEMRI signal-enhancement may indeed be due to low levels of anesthesia or to an undetermined mechanism following osmotic BBB disruption that results in sequestration of  $Mn^{2+}$  by brain cells (glia or astrocytes) and endothelial cells of the BBB (e.g., the scenario described in the previous section).

Table 5-12: Comparison of Aoki *et al.* Sham, and Mannitol and Arabinose Group Data for % MEMRI Signal-Enhancement in Rat Brain After Osmotic BBB Disruption.

	Group			
	Aoki Sham* (N=5)	Aoki Experimental (stroke group) (N=5)	Present Study Mannitol* (intensity-thresholding before EC, N=4)	Present Study Arabinose (intensity-thresholding before EC, N=10)
Average Percent:	Mean $\pm$ SD (%)	Mean $\pm$ SD (%)	Mean $\pm$ SD (%)	Mean $\pm$ SD (%)
MEMRI Signal-Enhancement	8.4 $\pm$ 1.32	71.0 $\pm$ 17.5	91 $\pm$ 13	88 $\pm$ 20

\* Aoki *et al.* sham and the mannitol group in the present study depicted in the table received the same concentration (1.4M) and dose (5 ml/kg) of mannitol at the same rate (50 ml/hr) and by the same intravenous route (ICA). The MEMRI signal-enhanced region in the Aoki *et al.* sham group and the mannitol and arabinose groups was defined as those pixels in the  $T_1W$  images with signal intensities that exceeded the mean +2SDs in the contralateral hemisphere. Clearly, the level of MEMRI signal-enhancement in our mannitol (and arabinose) group is significantly different from MEMRI signal-enhancement in Aoki's sham group (but not Aoki's stroke group).

It has been widely reported that  $Mn^{2+}$  is a calcium analog and acts similarly to  $Ca^{2+}$  in biological systems (1,31,32). Anoxic depolarizations open  $Ca^{2+}$  channels and is expected to enhance  $Mn^{2+}$  accumulation in cells with the presence of extracellular  $Mn^{2+}$  (5). However, since Aoki *et al.*

did not provide histological confirmation of tissue damage following anoxic depolarizations, or DC potential measurements during anoxic depolarizations, the notion that anoxic depolarization accounts for all of the observed MEMRI signal-enhancement in their study is somewhat speculative. Nonspecific MEMRI signal-enhancement has been reported due to a low level of anesthesia (1,33), local to regions with brain edema (33), and following osmotic BBB disruption with the presence of extracellular  $Mn^{2+}$  (34). Although the data of Aoki *et al.* is not supported by histology or DC potential measurements, they do report a relatively low level of MEMRI signal-enhancement in their sham animals (i.e., nonspecific MEMRI signal-enhancement). In this case, the low levels of nonspecific MEMRI signal-enhancement may be a result of the anesthetic regimen used.

### *Conclusions*

Tissue damage by focal edema (8), microvascular pathology (35), and pyknotic neurons (36) is, among others, of major concern when using hyperosmolar agents to disrupt the BBB to allow passage of  $Mn^{2+}$  (or other substances) from blood to brain. For MEMRI experiments that rely on specific neuronal stimulus to stimulate brain cells and sequester extracellular  $Mn^{2+}$  via voltage-gated calcium channels, tissue damage by osmotic BBB disruption must be minimized or prevented altogether. An optimal osmotic BBB disruption protocol has yet to be determined for MEMRI experiments that rely on a homogeneous distribution of  $Mn^{2+}$  to the brain parenchyma prior to specific neuronal stimulus. The results of these studies suggest careful study of brain structure and function following infusions of hyperosmolar agents for osmotic BBB disruption and delivery of  $Mn^{2+}$  to the brain parenchyma.

Additionally, in future studies that use a combined  $MnCl_2$ +EB solution, acquisition of the electroencephalogram (EEG) signal would be helpful to determine if EB dye has any potential side effects on brain function. Perhaps more importantly, the EEG could also provide a measure of the anesthetic state of the animal, which could then be correlated to any existing nonspecific MEMRI signal-enhancement, in an attempt to rule out anesthesia as a source of unwanted uptake of  $Mn^{2+}$  into active brain cells.

Based on ADC deficit area calculations, arabinose may inflict a larger region of edema when infused at 1.6M for 55 seconds as compared to an infusion of 1.4 M mannitol at 50 ml/hr. This point again stresses the need to find an optimal osmotic BBB disruption protocol for MEMRI studies. Because  $MnCl_2$ +EB solution does not always reach regions that have ADC deficit, as indicated by a correlation between regions without MEMRI signal-enhancement (or EB staining) and regions with

TTC lesion, the lack of MEMRI signal-enhancement in particular regions may be difficult to interpret unambiguously when histological confirmation of BBB disruption is not available.

### Acknowledgements

The authors thank James Bouley for helpful assistance with surgical procedures and TTC staining.

### REFERENCES

1. Lin Y.J., Koretsky A.P. Manganese ion enhances T<sub>1</sub>-weighted MRI during brain activation: an approach to direct imaging of brain function. *Magn Reson Med* 1997;38:378-388.
2. Duong T.Q., Silva A.C., Lee S.P., Kim S.G. Functional MRI of calcium-dependent synaptic activity: cross-correlation with CBF and BOLD measurements. *Magn Reson Med* 2000;43:383-392.
3. Aoki I., Wu Y.J., Silva A.C., Lynch R.M., Koretsky A.P. In vivo detection of neuroarchitecture in the rodent brain using manganese-enhanced MRI. *Neuroimage* 2004;22:1046-1059.
4. Henning E.C. , Meng X. , Fisher M. , Sotak C. Visualization of Cortical Spreading Depression Using Manganese-Enhanced MRI. *Magn Reson Med* 2005;53:851-857.
5. Aoki I., Ebisu T., Tanaka C., Katsuta K., Fujikawa A., Umeda M., Fukunaga M., Takegami T., Shapiro E.M., Naruse S. Detection of the anoxic depolarization of focal ischemia using manganese-enhanced MRI. *Magn Reson Med* 2003;50:7-12.
6. Ke F., Yingxia L., Hua L., Weijing L., Hao L. Tracing neuronal tracts in the olfactory pathway of rat and detecting ischemic core in a rat model of focal ischemia using manganese-enhanced magnetic resonance imaging. *Chinese Sci Bull* 2004;49:1834-1840.
7. Rapoport S.I., Fredericks W.R., Ohno K., Pettigrew K.D. Quantitative aspects of reversible osmotic opening of the blood-brain barrier. *Am J Physiol* 1980;238:R421-R431.
8. Suzuki M., Iwasaki Y., Yamamoto T., Konno H., Kudo H. Sequelae of the osmotic blood-brain barrier opening in rats. *J Neurosurg* 1988;69:421-428.
9. Nedergard M., Hansen A.J. Spreading depression is not associated with neuronal injury in the normal brain. *Brain Res* 1988;449:395-398.
10. Bonthius D.J., Steward O. Induction of cortical spreading depression with potassium chloride upregulates levels of messenger RNA for glial fibrillary acidic protein in cortex and hippocampus: inhibition by MK-801. *Brain Res* 1993;618:83-94.
11. Salahuddin T. S., Johansson B. B., Kalimo H., Olsson Y. Structural changes in the rat brain after carotid infusions of hyperosmolar solutions. An electron microscopic study. *Acta Neuropathol (Berl)* 1988;77:5-13.
12. Aoki I., Naruse S., Tanaka C. Manganese-enhanced magnetic resonance imaging (MEMRI) of brain activity and applications to early detection of brain ischemia. *NMR Biomed* 2004;17:569-580.
13. Horobin R.W., Kiernan J.A. *Conn's Biological Stains*. Oxford: BIOS Scientific Publishers Ltd; 2002.
14. Bederson J.B., Pitts L.H., Germano S.M., Nishimura M.C., Davis R.L., Bartkowski H.M. Evaluation of 2,3,5-Triphenyltetrazolium Chloride as a Stain for Detection and Quantification of Experimental Cerebral Infarction in Rats. *Stroke* 1986;17:1304-1308.

15. Paxinos G., Watson C. *The Rat Brain in Stereotaxic Coordinates*. Orlando: Academic Press; 1986.
16. Ruifrok A.C., Johnston D.A. Quantification of Histological Staining by Color Deconvolution. *Analyt Quant Cytol Histol* 2001;23:291-299.
17. LeBmann V., Gottmann K., Lux H.D. Evans blue reduces macroscopic desensitization of non-NMDA receptor mediated currents and prolongs excitatory postsynaptic currents in cultured rat thalamic neurons. *Neurosci Lett* 1992;146:13-16.
18. Durmuller N., Graham J.L., Sowinski P., Meldrum B.S. The vital dye Evans blue mimics limbic seizures induced by kainate or pilocarpine. *Brain Res* 1997;753:283-290.
19. Stover J.F., Kempfski O.S. Anesthesia increases circulating glutamate in neurosurgical patients. *Acta Neurochir (Wien)* 2005;147:847-853.
20. Stover J.F., Kroppenstedt S.N., Thomale U.W., Kempfski O.S., Unterberg A.W. Isoflurane double plasma glutamate and increases posttraumatic brain edema. *Acta Neurochir Suppl* 2000;76:375-378.
21. Meyer B., Schultheiss R., Schramm J. Capillary oxygen saturation and tissue oxygen pressure in the rat cortex at different stages of hypoxic hypoxia. *Neurol Res* 2000;22:721-726.
22. Ziylan Y.Z., Robinson P.J., Rapoport S.I. Differential Blood-Brain Permeabilities to [<sup>14</sup>C]Sucrose and [<sup>3</sup>H]Inulin after Osmotic Opening in the Rat. *Exp Neurol* 1983;79:845-857.
23. Cosolo W.C., Martinello P., Louis W.J., N. Christophidis. Blood-brain barrier disruption using mannitol: time course and electron microscopy studies. *Am J Physiol* 1989R443-R448.
24. Brown R.C., Egleton R.D., Davis T.P. Mannitol opening of the blood-brain barrier: regional variation in the permeability of sucrose, but not <sup>86</sup>Rb<sup>+</sup> or albumin. *Brain Res* 2004;1014:221-227.
25. Ito J., Marmarou A., Barzo P., Fatouros P., Corwin F. Characterization of edema by diffusion-weighted imaging in experimental traumatic brain injury. *J Neurosurg* 1996;84:97-103.
26. Schuier F.J., Hossmann K.-A. Experimental Brain Infarcts in Cats II. Ischemic Brain Edema. *Stroke* 1980;11:593-601.
27. Perez-Trepichio A.D., Xue M., Ng T.C., Majors A.W., Furlan A.J., Awad I.A., Jones S.C. Sensitivity of Magnetic Resonance Diffusion-Weighted Imaging and Regional Relationship Between the Apparent Diffusion Coefficient and Cerebral Blood Flow in Rat Focal Cerebral Ischemia. *Stroke* 1995;26:667-675.
28. Kempfski O., Chaussy L., Gross U., Zimmer M., Baethmann A. Volume regulation and metabolism of suspended C6 glioma cells: an in vitro model to study cytotoxic brain edema. *Brain Res* 1983;279:217-228.
29. McManus M. L., Strange K. Acute volume regulation of brain cells in response to hypertonic challenge. *Anesthesiology* 1993;78:1132-1137.
30. McManus M. L., Soriano S. G. Rebound swelling of astroglial cells exposed to hypertonic mannitol. *Anesthesiology* 1998;88:1586-1591.
31. Gavin CE Gunter KK, Gunter TE. Manganese and calcium efflux kinetics in brain mitochondria. *Biochem J* 1990;266:329-334.
32. Gavin CE Gunter KK, Gunter TE. Manganese and calcium transport in mitochondria: implications for manganese toxicity. *Neurotoxicology* 1999;20:445-454.
33. Aoki I., Naruse S., Tanaka C. Manganese-enhanced magnetic resonance imaging (MEMRI) of brain activity and applications to early detection of brain ischemia. *NMR In Biomed* 2004;17:569-580.

34. Morita H., Ogino T., Seo Y., Fujiki N., Tanaka K., Takamata A., Nakamura S., Murakami M. Detection of hypothalamic activation by manganese ion contrasted T<sub>1</sub>-weighted magnetic resonance imaging in rats. *Neurosci Lett* 2002;326:101-104.
35. Lossinsky A.S., Vorbrodt A.W., Wisniewski H.M. Scanning and transmission electron microscopic studies of microvascular pathology in the osmotically impaired blood-brain barrier. *J Neurocytol* 1995;24:795-806.
36. Salahuddin T.S., Johansson B.B., Kalimo H., Olsson Y. Structural changes in the rat brain after carotid infusions of hyperosmolar solutions. *Acta Neuropathol* 1988;77:5-13.

# CHAPTER 6

## Blood-Brain Barrier Disruption in Embolic Stroke Detected by Manganese-Enhanced Magnetic Resonance Imaging (MEMRI)

### Introduction

Stroke Background  
Stroke and the BBB  
The Embolic Stroke Model and Associated BBB Injury  
Intracellular Calcium Level Increase During Stroke – Implications for MEMRI

### Methods

Animal Preparation  
Embolic Middle Cerebral Artery Occlusion (eMCAO)  
MR Imaging  
MnCl<sub>2</sub> + Evans Blue Infusion Protocol  
EB and 2,3,5 TriphenylTetrazolium Chloride (TTC) Histology  
Data Analysis

### Results

MEMRI Enhancement  
ADC Deficit  
MEMRI-DWI Mismatch & Match  
MEMRI Signal-Enhancement and ADC Correlation With Evans Blue and TTC Histology

### Discussion

MEMRI Signal-Enhancement: Detection of Hemorrhagic Transformation During Acute Stages of Embolic Stroke?  
MEMRI Signal-Enhancement in Stroke: Mechanisms Related to Cell Calcium Uptake

# Blood-Brain Barrier Disruption in Embolic Stroke Detected by Manganese-Enhanced Magnetic Resonance Imaging (MEMRI)

David G. Bennett<sup>1</sup>, James Bouley<sup>3</sup>, Nils Henninger<sup>3</sup>, Marc Fisher<sup>3,4</sup>, Christopher H. Sotak<sup>1,2,4</sup>

Departments of Biomedical Engineering<sup>1</sup> and Chemistry & Biochemistry<sup>2</sup>

Worcester Polytechnic Institute

Worcester, Massachusetts 01609

Department of Neurology<sup>3</sup>

University of Massachusetts Memorial Healthcare – Memorial Campus

Worcester, Massachusetts 01605

Department of Radiology<sup>4</sup>

University of Massachusetts Medical School

Worcester, Massachusetts 01605

*Manuscript in Progress*



## Abstract

Manganese ( $Mn^{2+}$ ) has proven to be a useful MR contrast agent for functional imaging and neuronal tract tracing. The paramagnetic properties of  $Mn^{2+}$  provide local contrast on  $T_1$ -weighted ( $T_1W$ ) MRI after cellular sequestration via voltage-gated calcium channels. Researchers have used the MRI contrast agent Gd-DTPA to show  $T_1$ -contrast in MR images near regions of blood-brain barrier (BBB) disruption after stroke. Gd-DTPA is an extracellular MRI contrast agent and, therefore, is not expected to provide information regarding the state of cells local to a stroke-related BBB injury. The results of this study show BBB injury after ischemic insult allows simultaneous passage of  $Mn^{2+}$  and Evans Blue (EB) dye into the brain parenchyma, resulting in localized  $T_1W$ -MRI-signal increase (MEMRI signal-enhancement). MEMRI signal-enhancement in these experiments corresponds to the degree of BBB disruption and is apparent in areas of tissue damage as verified by 2,3,5-triphenyltetrazolium hydrochloride (TTC) staining and diffusion-weighted MRI (DWI). These findings suggest that  $Mn^{2+}$ , used in conjunction with a rat embolic stroke model, can produce MEMRI signal-enhancement in areas peripheral to and/or in the stroke core with a compromised BBB. MEMRI signal-enhancement using an embolic stroke model with  $Mn^{2+}$  as the MRI contrast agent can show regions of injured BBB and may provide insight into the state of brain cells local to BBB injury. This method may prove useful for future studies using MEMRI to monitor brain response to ischemia.

**Key words:** manganese-enhanced MRI, blood-brain barrier, stroke, rat brain

## 6.1 Introduction

In Chapter 4 it was suggested that neuronal damage in the brain following osmotic blood-brain barrier (BBB) disruption was primarily responsible for uptake of manganese ( $Mn^{2+}$ ) in brain cells, resulting in so-called nonspecific MEMRI signal-enhancement. In Chapter 5 it was suggested that cell-volume regulatory mechanisms following osmotic BBB disruption may also play a role in the uptake of  $Mn^{2+}$  into the cell leading to nonspecific MEMRI signal-enhancement. These ideas are in conflict with the generally accepted theory which suggests that MEMRI signal-enhancement in the brain is a result of cell-membrane-depolarization-dependent mechanisms only (1-3). This chapter builds upon the work presented in the previous two chapters by testing the hypothesis that MEMRI can be used to monitor BBB disruption and neuronal injury following embolic stroke. This study is designed to determine if  $Mn^{2+}$  can cross a pathologically-injured BBB and subsequently enter stroke-injured brain cells; thus generating localized contrast on  $T_1W$  MRI that is specific to stroke-related BBB disruption and underlying neuronal injury.

### *Cell Volume Changes Following Stroke Detected by Diffusion-Weighted (DW) MRI (DWI)*

As described in Chapter 1, DWI is sensitive to changes in the mobility of water protons that accompanies cell-volume changes in the brain. Following an ischemic insult to the brain, the depletion of cellular energy reserves (e.g., adenosine triphosphate – ATP) results in cell-membrane depolarization (i.e., anoxic depolarization) and subsequent cellular swelling (cytotoxic edema). These cell-volume changes restrict the translational motion of tissue water molecules relative to that of normal tissue. The water molecules with reduced mobility are detected as a signal-intensity increase on DWI; reflecting a decrease of the apparent diffusion coefficient (ADC) of water in that region of the brain. The temporal dynamics of cell-volume changes (cytotoxic edema) and water ADC reductions following experimental stroke has been well documented. de Crespigny *et al.* showed that global cerebral ischemia in the rat results in a rapid decline in brain-water ADC during the first two hours following stroke onset (4). Using an embolic stroke model in the rat brain, Jiang *et al.* (3) also found that tissue-water ADC decline was most

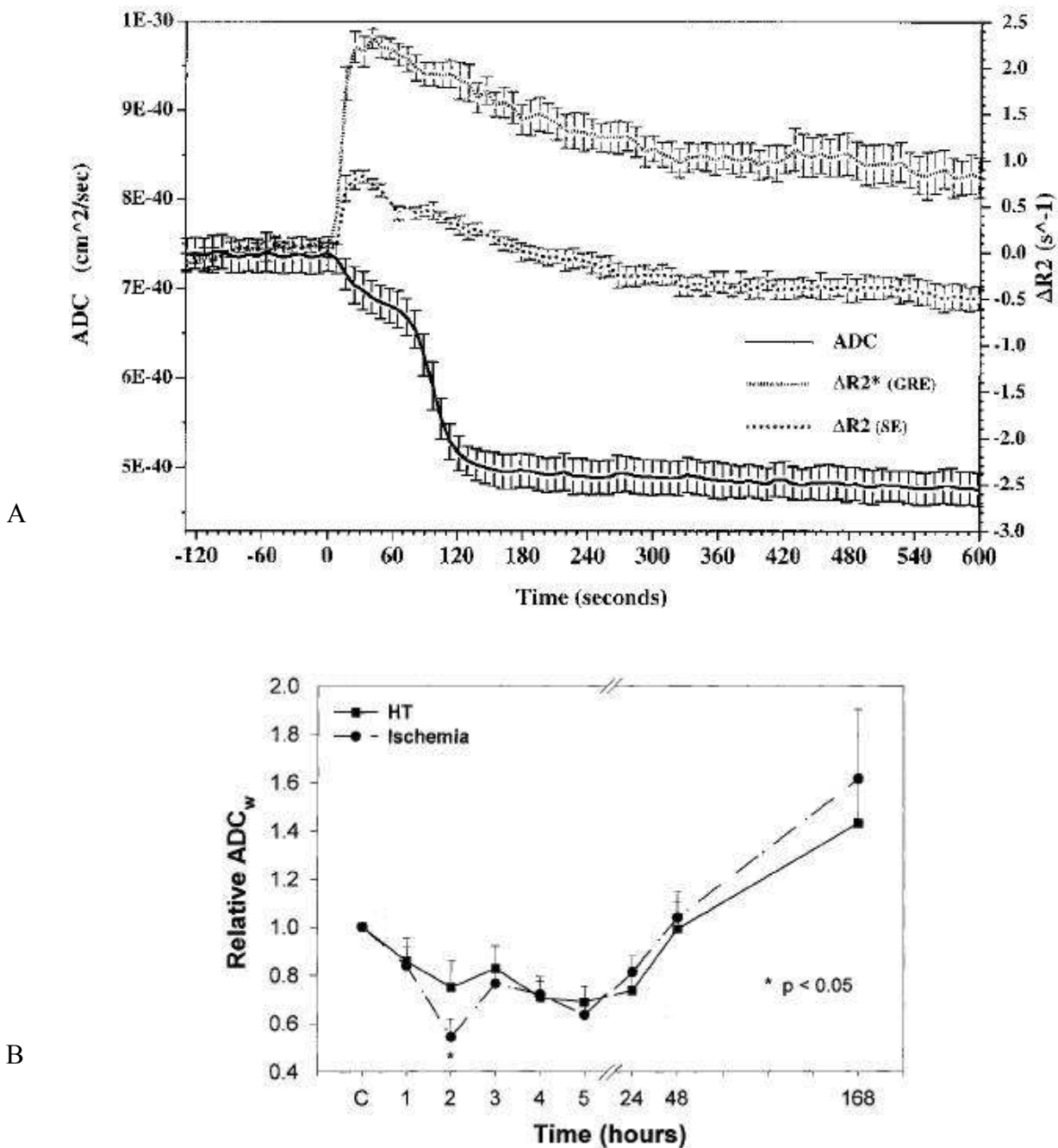


Fig. 6-1: A) Plot of water ADC (and  $\Delta R2^*$  and  $\Delta R2$ ) in the rat brain following cardiac arrest. Reproduced from de Crespigny *et al.* (4). Note how the abrupt ADC decline following cardiac arrest (at time 0) levels off starting at 120 minutes. B) Plot of water ADC in brain regions with hemorrhagic transformation (“HT”) and ischemic (“Ischemia”) injury. Note the slight increase in ADC from 2-3 h and only a modes change in ADC from 3-4 h following infusion of an embolus to block blood flow to one brain hemisphere (infusion started at point “C”). Reproduced from Jiang *et al.* (5)

abrupt in the first two hours and then plateaued after three hours. Data from de Crespigny *et al.* and Jiang *et al.* are shown in Figures 6-1a and 6-1b, respectively, for reference. The data presented in

Figure 6-1 indicate that the ADC changes in the brain related to stroke injury stabilize in the first 2-3 h after stroke onset. Therefore, if  $Mn^{2+}$  is infused i.v. during the time period that the BBB is permeable due to stroke-related damage, and at a time point after which cell-volume changes have stabilized (~4 h after stroke), then any ensuing MEMRI signal-enhancement would not likely be due to dynamic cell-volume changes but rather increase permeability of the BBB.

### 6.1.1 Stroke Background

A stroke occurs when a blood vessel that delivers oxygen and nutrients (e.g., glucose) to the brain bursts (1) or is obstructed by a blood clot or other types of emboli. Brain injury can occur within minutes if blood flow is not restored to normal. There are two main forms of stroke: ischemic and hemorrhagic. An ischemic stroke is caused by occlusion of blood vessels by a blood clot or other emboli. A hemorrhagic stroke is caused by bleeding from a burst blood vessel, which diverts blood flow away from the brain tissue that is served by the ruptured vessel. Ischemic stroke occurs more often (~80%) than hemorrhagic stroke. With modest reductions in cerebral blood flow (CBF), disturbances of brain tissue metabolism and function are mitigated by CBF autoregulation in brain (6). As a result, the onset of cerebral ischemia does not occur until the CBF is reduced below a certain threshold. Below that threshold, the CBF range is subdivided into regimes that constitute mild, moderate, and severe ischemia as depicted in Figure 6-2.

CBF

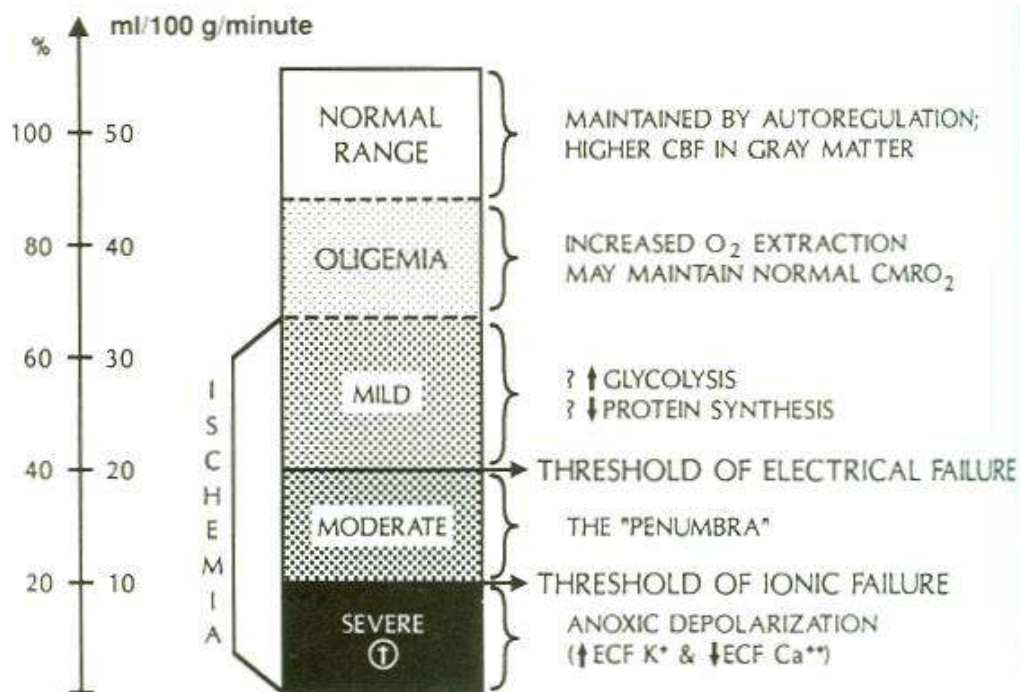


Figure 6-2: Ischemic brain injury can be characterized as a contiguous series of thresholds which define ranges of CBF values that are correlated to particular pathological events.  $CMRO_2$  = cerebral metabolic rate of oxygen,  $ECF K^+$  = extracellular fluid potassium,  $ECF Ca^{++}$  = extracellular fluid calcium. The ischemic 'penumbra' is defined as tissue with a clinical CBF deficit but that can be responsive to therapeutic intervention. Reproduced from Ref. (6).

### 6.1.2 Stroke and the BBB

Evaluation of BBB integrity following stroke has been accomplished by detection and quantification of extravasated EB dye and protein tracers into the brain parenchyma. Sadoshima and coworkers evaluated the permeability of the BBB to  $^{131}I$ -albumin and EB following global cerebral ischemia by clamping both common carotid arteries in the rat (7). Sadoshima *et al.* reported exudation of EB dye from blood into brain in 18 of 23 rats following 3 h of ischemia followed by reperfusion. Albayrak *et al.* showed exudation of normally BBB-impermeable albumin into brain after 2 h of stroke followed by 6 h of reperfusion. Based on findings of Albayrak *et al.*, longer transient ischemic events result in BBB disruption at earlier time points (as compared to shorter-duration ischemic insults) and neuronal damage precedes BBB disruption under these conditions (8). Data from a study by Petito *et al.* confirmed that neuronal necrosis alone was not sufficient to increase BBB permeability (to horseradish peroxidase) (9). Therefore, the effects of stroke on blood

vessels must be considered to understand the mechanisms that lead to BBB damage following severe CBF deficits.

### *Stroke and Brain Microvessel Damage*

The reduction in CBF and oxygen delivery following stroke has several consequences for the BBB that lead to a loss of barrier function and uncontrolled entry of blood (hemorrhagic transformation), water, and ions into the brain parenchyma: 1) microvascular permeability barriers are lost; 2) the basal lamina and extracellular matrix undergo progressive loss of antigens; and 3) cell-matrix adhesion interactions within microvessels are altered (10). These steps are depicted in Figure 6-3.

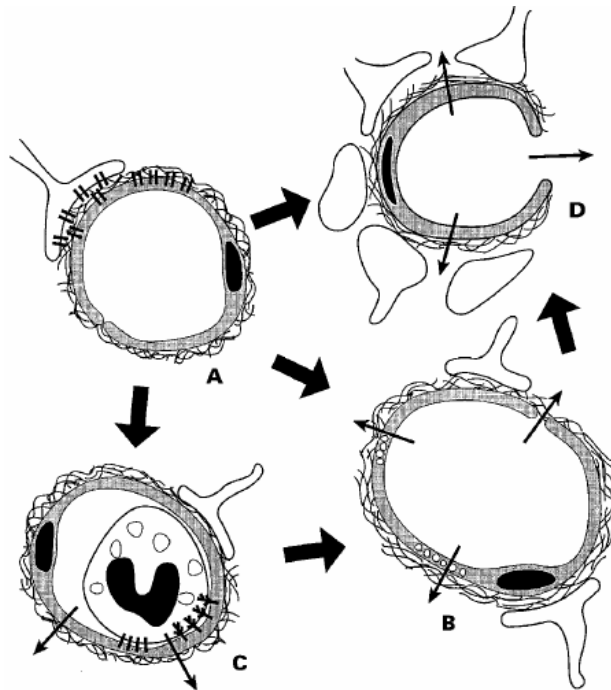


Figure 6-3: Schematic diagram of the effect of ischemia on microvascular permeability and integrity. (A) Normal cerebral microvessel. Endothelial cells and astrocytes bound to basal lamina by integrin adhesion receptors. The BBB is intact. (B) Breakdown of the BBB. (C) Leucocyte adhesion by receptors on endothelium and granulocytes; increased permeability caused by granule release. (D) Breakdown of basal lamina with loss of astrocyte and endothelial cell contacts. Reproduced from Ref. (10).

In the brain, astrocytic end-feet are adjacent to the extracellular matrix or the basal lamina in capillaries and provide a connection between the microvascular endothelium and the neuropil

(11,12). During brain development, astrocytes, in conjunction with endothelial cells, contribute laminin to the extracellular matrix and stimulate formation of the BBB (13). Integrins (heterodimeric adhesion receptors) function as structural connections between endothelial cells and underlying basal lamina. Laminins serve as a major component of the basal lamina and extracellular matrix and are ligands for the integrin heterodimers  $\alpha_1\beta_1$ ,  $\alpha_2\beta_1$ ,  $\alpha_3\beta_1$ ,  $\alpha_6\beta_1$ ,  $\alpha_7\beta_1$  (14), and  $\alpha_6\beta_4$  (15). The basal lamina is uniquely sensitive to focal cerebral ischemia (16) and it has been shown that the expression of integrin  $\beta_4$  and the heterodimer  $\alpha_6\beta_4$  are rapidly and significantly reduced following stroke (MCAO in nonhuman primate model) (12). Since astrocytes are anchored to the cerebral microvascular wall by  $\alpha_6\beta_4$ , and play a role in structural support of the BBB, the lack of  $\alpha_6\beta_4$  expression following stroke may contribute to pathological disruption of the BBB.

### 6.1.3 The Embolic Stroke Model and Associated BBB Injury

There are several methods available to induce experimental stroke in animals. These include: 1) global ischemia by cardiac arrest; 2) permanent (or temporary) occlusion of the middle cerebral artery using an intraluminal suture (suture occlusion model); and 3) occlusion of the middle cerebral artery by infusion of emboli (embolic stroke model). Since thrombosis and embolism are responsible for 80% of human stroke (17), an experimental model of stroke was designed to mimic the large middle cerebral artery thromboembolic stroke in human. The rat model of embolic focal cerebral ischemia developed by Zhang *et al.* results in selective occlusion of the middle cerebral artery and a highly reproducible CBF reduction and infarct volume (18). Figure 6-5 shows a schematic diagram of the catheter placement for infusion of an embolus in the embolic stroke model.

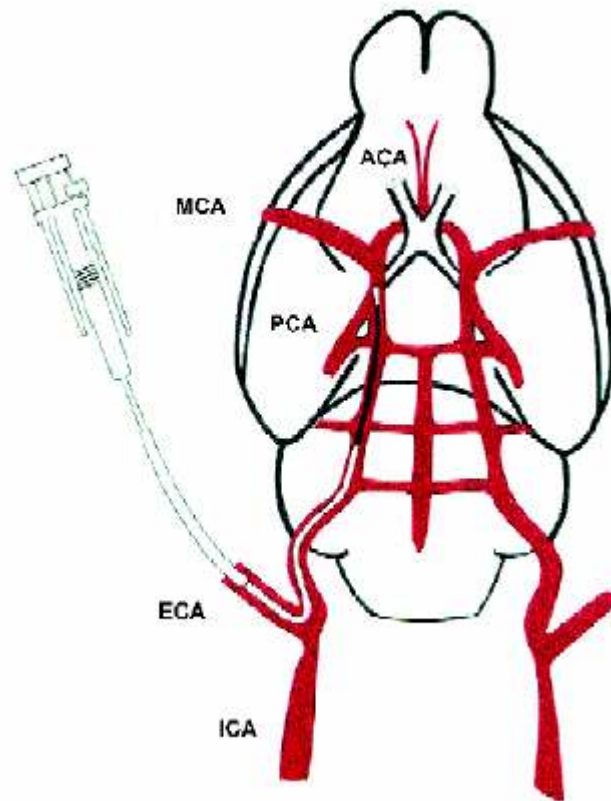


Figure 6-4: Schematic drawing of catheter placement into external carotid artery (ECA) and the internal carotid artery (ICA) of the rat, with its tip 2 mm from the origin of the middle cerebral artery (MCA). The catheter contains a clot (black), which can be injected to occlude the MCA. Reproduced from Ref. (18)

#### *Time Frame of BBB Injury Following Embolic Stroke*

Following experimental stroke by the intraluminal suture occlusion model, Belayev *et al.* showed injury to the BBB as verified by Evans Blue (EB) staining. According to their data, the BBB becomes permeable to molecules similar in size to the EB-albumin complex (MW = 68,500) within 3-5 hours after stroke (and also at 48-50 h, but not 24 h after stroke). Data from Belayev *et al.* is shown in Figure 6-5:



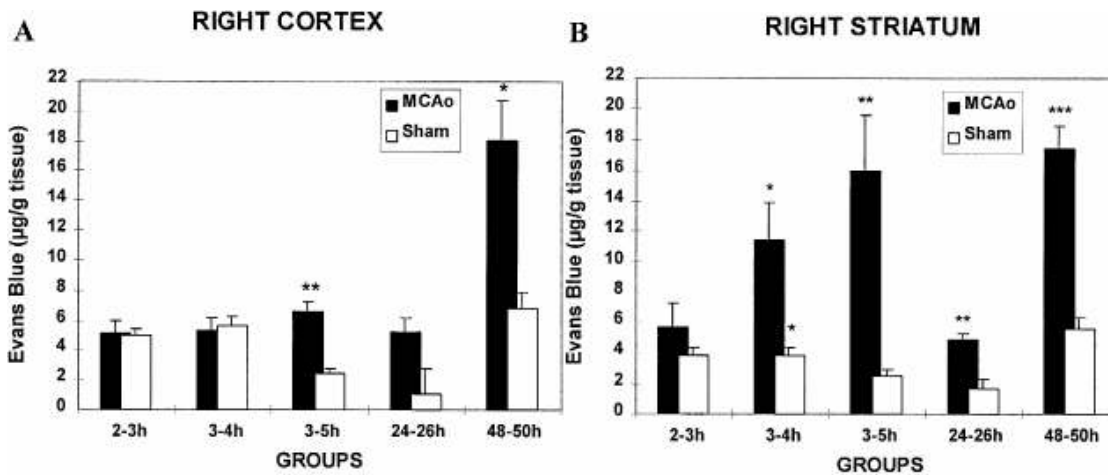


Figure 6-5: Concentration of Evans Blue (EB) dye measured in right cortex (A) and right striatum (B) of an MCA-occlusion group and sham group at different times after intraluminal-suture occlusion of the MCA. Note the biphasic character of BBB opening to EB (3-5 h and 48-50 h groups). Reproduced from Ref Belayev et al.

Using the embolic stroke model, Ding *et al.* show stroke-related BBB opening 3 h following infusion of emboli in the rat brain. In their study, passage of a gadolinium-based MRI contrast agent from the blood into the brain induced contrast changes in T<sub>1</sub>W images local to sites of BBB injury at 3 h after stroke onset. Data from the study of Ding *et al.* are shown in Figure 6-6.

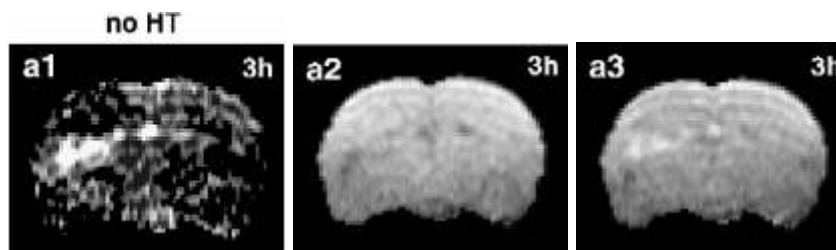


Figure 6-6: The T<sub>1</sub>W subtraction image (a1) from pre- (a2) and post-contrast (a3) T<sub>1</sub>W images of the rat brain following embolic stroke; but without embolic-stroke-induced hemorrhage ('no HT', as confirmed histologically at 48 h after stroke onset). The animal presented with BBB disruption and evidence of gadolinium-MRI-contrast-agent (Gd-DTPA) leakage at 3 h after ischemia. Reproduced from Ref. (19).

#### 6.1.4 Intracellular Calcium Level Increase During Stroke – Implications for MEMRI

##### *Intracellular Accumulation of Ca<sup>2+</sup> Occurs In Concert with BBB Injury*

Cerebral ischemia initiates many different cellular processes that lead to cell death, including generation of reactive oxygen species, intercellular release of glutamate, depressed energy

metabolism, translocation of protein kinase C, increased production of polyamine and nitric oxide, and increased intracellular calcium ( $\text{Ca}^{2+}$ ) (20). Ionic activity of extracellular calcium in the ischemic brain decreases as verified using ion-selective microelectrodes (21,22). In a study by Rappaport *et al.*, a significant accumulation of  $\text{Ca}^{2+}$  in the ischemic MCA territory was measured (via tissue calcium analysis) within 4 h after MCA occlusion. The time frame of calcium accumulation coincided with the development of abnormal BBB permeability. In addition, the data of Rappaport *et al.* showed that the concentration of the accumulated intracellular  $\text{Ca}^{2+}$  exceeded all of the available extracellular  $\text{Ca}^{2+}$  in the adjacent brain tissue. Therefore, Rappaport *et al.* postulated that  $\text{Ca}^{2+}$  lost from adjacent brain during ischemia was replenished by external sources such as blood or CSF. The intracellular accumulation of  $\text{Ca}^{2+}$  has been shown by others to occur at the site of the stroke core (20). In summary, stroke-related intracellular  $\text{Ca}^{2+}$  accumulation 1) occurs at the site of ischemic injury; 2) occurs within the same time frame that the BBB is damaged by stroke (3-4 h after stroke onset); and 3) is exacerbated by delivery of  $\text{Ca}^{2+}$  to the ischemic region by residual blood flow or CSF.

#### *Detection of Stroke Core by MEMRI*

As described previously (Chapter 3), manganese ( $\text{Mn}^{2+}$ ) is handled similarly to calcium by biological systems and does not cross a healthy intact BBB. Therefore, because high concentrations of intracellular  $\text{Ca}^{2+}$  and local BBB injury are associated with the core of the stroke lesion, it is hypothesized that  $\text{Mn}^{2+}$  delivered i.v. following stroke should result in a large accumulation of  $\text{Mn}^{2+}$  within damaged cells and localized MEMRI signal-enhancement on  $T_1W$  MRI; indicative of the stroke core.

## 6.2 Methods

### 6.2.1 Animal Preparation

This study was approved by the Institute Animal Care and Use Committee (IACUC) of the University of Massachusetts Medical School (IACUC Protocol A-1756). Five male Sprague-Dawley rats, weighing 280-350 g, were initially anesthetized with 5% isoflurane and maintained at 2% isoflurane, mixed with breathing-quality air, during surgery. PE-50 polyethylene tubing was inserted into the left femoral vein for drug administration and the left femoral artery for blood pressure and blood gas monitoring. Rectal temperature was continuously monitored with a rectal probe and

maintained at  $37.0 \pm 0.5$  °C using a thermostatically-controlled heat lamp (Model 73ATD, YSI Inc., Yellow Spring, OH) during preparation.

### 6.2.2 Embolic Middle Cerebral Artery Occlusion (eMCAO)

For eMCAO, a blood clot was infused via an i.v. catheter into the right external carotid artery (ECA), allowing the left hemisphere to serve as a control. For catheterization of the right ECA, a ventral midline incision was made in the neck. The omohyoid muscle was separated longitudinally and retracted laterally to isolate and expose the right common carotid artery (CCA), ECA, internal carotid artery (ICA) and pterygopalatine artery (PPA). The PPA was permanently ligated. Following temporary clamping of the CCA, the ECA was ligated and a small incision was made in the vessel for placement of the catheter (PE-10 tubing). PE-10 tubing was inserted into the ECA proximal to its ligation, and one red blood clot was injected – with a volume of  $\sim 50$   $\mu\text{L}$  of saline – into the ICA over approximately one second. The clot was delivered one millimeter distal from the bifurcation of the PPA and ICA. eMCAO was verified by Laser Doppler Flowmetry (Perimed PF 5010 LDPM Unit, Sweden) as a reduction of the blood flow signal by 70% (data not shown). Three hours after eMCAO, animals were transferred to the MR magnet bore for imaging.

#### *Embolus Preparation*

The embolus-preparation protocol was originally described by Toomey *et al.* (23) and modified based on a protocol originally described by Henninger *et al.* (24). The modification was limited to reducing the size of the embolus from 36 mm to 18 mm. Briefly, whole blood (200  $\mu\text{L}$ ) was withdrawn from the rat, 24 h before surgery, into an Eppendorf tube. The blood was promptly mixed with 1.0 National Institutes of Health (NIH) unit (10  $\mu\text{L}$ ) of human thrombin and 4.5  $\mu\text{L}$  of 1 mol/L (M)  $\text{CaCl}_2$  for a final concentration of 20 mM. Within 5 s, a small amount of this mixture was drawn into a 30-cm-long polyethylene catheter (PE-50) and allowed to clot at 37 °C. After 2 h, the clot was extruded from the catheter into a saline-filled Petri dish and stored at 4 °C for 22 h. Before infusing the clot into the rat ECA, a 5- to 10-cm section of clot was placed into a separate Petri dish containing deionized water, incubated for 5 min at room temperature, transferred into a solution of isotonic saline, and then dissected into a single 18-mm section. This clot section was collected into a PE-10 catheter in a volume of  $\sim 50$   $\mu\text{L}$  of saline. The interval between this final step and embolization of the rat was less than 5 min.

### 6.2.3 MR Imaging

All MR images were acquired using a Bruker Biospin 2.0T/45 cm imaging spectrometer operating at 85.56 MHz for  $^1\text{H}$  and equipped with  $\pm 20$  G/cm self-shielded gradients. Diffusion-weighted MRIs (DWIs) were acquired with six b-values (23, 92, 207, 828, 1126, and 1471  $\text{s}/\text{mm}^2$ ), a  $64 \times 64$  data matrix zero-filled to  $128 \times 128$  before Fourier transformation, FOV = 3 cm x 3cm, six 2-mm-thick slices, TR/TE = 2000/51.0 ms,  $\Delta = 6.0$  ms,  $\delta = 24.31$  ms, and NEX = 8.  $T_1\text{W}$  MRI was performed with the following parameters: TR/TE = 500/10.8 ms, FOV = 3 cm x 3 cm, data matrix =  $128 \times 128$ , six 2-mm-thick slices, and NEX = 8. The slice positions of DW images and  $T_1\text{W}$  images were co-registered. The imaging plane was referenced to the rhinal fissure at the boundary of the olfactory bulb. Acquisition time for one set of images was 8.5 minutes for  $T_1\text{W}$  and 4.8 minutes for DW imaging. During imaging, animals were placed prone within a home-built animal holder. The head of the animal was fixed within a home-built 8-element, 4.3-cm-diameter  $^1\text{H}$  birdcage coil. Animals were anesthetized with 2% isoflurane delivered at 1.0-1.5 L/min in breathing-quality air. Body temperature was maintained at  $37.0 \pm 1^\circ\text{C}$  by circulated warm air using a T-type thermocouple and a double-point feedback control system.  $T_1\text{W}$  and DW imaging continued sequentially for at least one full scan after the end of  $\text{MnCl}_2 + \text{EB}$  infusion.

### 6.2.4 $\text{MnCl}_2 + \text{EB}$ Infusion Protocol

Manganese chloride ( $\text{MnCl}_2 \cdot 4\text{H}_2\text{O}$ , MW = 198; Sigma, St. Louis, MO), dissolved to 74.5 mM in isotonic saline, and Evans Blue (EB; Sigma, St. Louis, MO), dissolved to 2% in  $\text{MnCl}_2$  solution, was infused into the left femoral vein at 3.2 ml/h for 30 min using a syringe pump (Model PHD 2000; Harvard Apparatus, Holliston, MA). Figure 6-1 shows the timing of image acquisition relative to eMCAO.

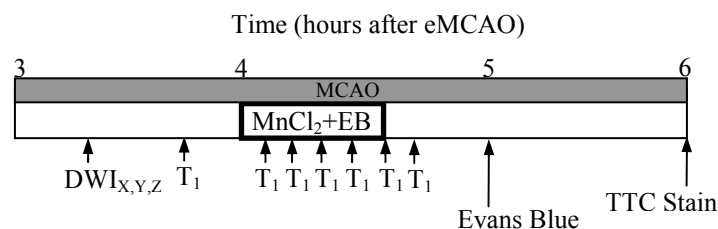


Figure 6-7. Timing of MR imaging (DWI = DW MRI and  $T_1 = T_1\text{W}$  MRI), EB and TTC staining relative to eMCAO and  $\text{MnCl}_2 + \text{EB}$  solution infusion.  $\text{MnCl}_2 + \text{EB}$  solution infusion was started 4 h after initiation of eMCAO.  $T_1\text{W}$  MRI continued for at least 25 min after cessation of the  $\text{MnCl}_2 + \text{EB}$  infusion.

### 6.2.5 EB and 2,3,5 TriphenylTetrazolium Chloride (TTC) Histology

Immediately following imaging, isoflurane anesthetic was increased to 5% and shortly thereafter the animals were decapitated. The brain was quickly removed, placed on a square section of parafilm and subsequently cooled for 30 min to facilitate handling. Brains were then dissected into six 2-mm slices that corresponded spatially to the slice positions of the MRIs (first slice at 1 mm ventral to the rhinal fissure of olfactory bulb). After dissection, brain slices were placed in saline and scanned using a Hewlett-Packard Scanner (Model #3970) at a resolution of 1200 dpi for indications of EB staining. After scanning, brain slices were placed in a 2% solution of TTC and warmed to 37 °C in a lab oven (Fisher Isotemp 500 Series). The time from eMCAO to TTC staining was approximately 6 h in each animal. After 10 min in the lab oven, all slices were placed in zinc formalin for fixation overnight. The next day, brain slices were scanned using a Hewlett-Packard Scanner (Model #3970) at a resolution of 1200 dpi.

### 6.2.6 Data Analysis

Region of interest (ROI) definitions and calculations in T<sub>1</sub>W images were made using NIH ImageJ software (Rasband, W.S., ImageJ, U. S. National Institutes of Health, Bethesda, Maryland, USA, <http://rsb.info.nih.gov/ij/>, 1997-2006). ROIs were drawn freehand to distinguish between MEMRI signal-enhanced regions, ADC-deficit regions, and normal brain tissue. MEMRI signal-enhancement increase, MEMRI signal-enhancement area, ADC deficit, and ADC-deficit area (DA) were all calculated using ROIs drawn freehand by observer visualization. Data are reported as mean ± SEM.

#### *MEMRI Enhancement*

MEMRI signal-enhancement on T<sub>1</sub>W images was calculated by comparing the MR signal intensity in visually evident MEMRI signal-enhanced regions of the ipsilateral hemisphere with homologous control regions in contralateral hemisphere, on a slice-by-slice basis:

$$\text{MEMRI Signal - Enhancement (\%)} = \frac{S_{IH} - SI_{CH}}{SI_{CH}} \times 100 \quad 6.1$$

where  $SI_{IH}$  is the mean signal intensity for an ROI in the ipsilateral hemisphere and  $SI_{CH}$  is the mean signal intensity for the equivalent ROI in the homologous control region in contralateral hemisphere. Percent-area of MEMRI signal-enhancement in the T<sub>1</sub>W images was calculated on a slice-by-slice

basis by comparing the area of MEMRI signal-enhancement to that of the entire ipsilateral hemisphere, as shown in Eq. 6.2.

$$\text{MEMRI Signal - Enhanced Area (\%)} = \frac{\text{MEMRI Signal - Enhanced Area}}{\text{Total Ipsi Hem Area}} \times 100 \quad 6.2$$

#### *Apparent Diffusion Coefficient (ADC) Parameter Mapping*

ADC mapping was performed on DW images on a pixel-by-pixel basis using in-house-written Interactive Data Language (v5.3 Research Systems, Boulder, CO) software based on the relationship between the natural log of the signal intensity in DW images and b-value as shown by equation 5.4.

$$M(t) = M_0 e^{-bD} \quad 6.3$$

where  $M(t)/M_0$  is the signal intensity at a particular b-value and D is the water apparent diffusion coefficient (ADC) along a single gradient direction (x, y, or z). Maps of the average ADC were calculated from separate DWIs acquired along the x-, y-, and z-gradient directions.

#### *Percent ADC Deficit and Percent Deficit Area (DA)*

Percent ADC deficit in ADC maps was calculated through comparison of the ADC mean in regions with visually evident ADC deficit in ipsilateral hemisphere and ADC mean in homologous control regions in the contralateral hemisphere on a slice-by-slice basis:

$$\text{ADC Deficit (\%)} = \frac{-(ADC_{IH} - ADC_{CH})}{ADC_{CH}} \times 100 \quad 6.4$$

where  $ADC_{IH}$  is the mean ADC in the ADC deficit region in ipsilateral hemisphere and  $ADC_{CH}$  is the mean ADC in the homologous control region in the contralateral hemisphere. Percent ADC deficit area in ADC maps was calculated on a slice-by-slice basis by comparison of ADC deficit area in ipsilateral hemisphere to the area of the entire ipsilateral hemisphere.

$$\text{ADC Deficit Area (\%)} = \frac{\text{Ipsilateral ADC Deficit Area}}{\text{Total Ipsi Hem Area}} \times 100 \quad 6.5$$

*MEMRI-DWI Mismatch & Match*

MEMRI-DWI mismatch area was calculated as the area of ADC deficit in the ipsilateral hemisphere exclusive of MEMRI signal-enhancing regions in the ipsilateral hemisphere. ADC-deficit ROIs were transferred to T<sub>1</sub>W images with MEMRI signal-enhancement. Regions of ADC deficit that did not contain MEMRI signal-enhancement were outlined and defined as MEMRI-DWI mismatch. DW and T<sub>1</sub>W images were registered in every animal. Percent MEMRI-DWI mismatch in T<sub>1</sub>W images was calculated on a slice-by-slice basis by comparison of MEMRI-DWI mismatch area to the area of the entire ipsilateral hemisphere.

$$\% \text{ MEMRI - DWI Mismatch Area} = \frac{\text{MEMRI - DWI Mismatch Area}}{\text{Total Ipsi Hem Area}} \times 100.6$$

Similarly, MEMRI-DWI match (overlap) area was calculated as the area of ADC deficit in the ipsilateral hemisphere inclusive of MEMRI-signal-enhancing regions. ADC deficit ROIs were transferred to T<sub>1</sub>W images with MEMRI signal-enhancement. Regions of ADC deficit that contained MEMRI signal-enhancement were outlined and defined as MEMRI-DWI match. MEMRI-DWI match area was calculated as a percentage of the ipsilateral hemisphere area.

$$\% \text{ MEMRI - DWI Match Area} = \frac{\text{MEMRI - DWI Match Area}}{\text{Total Ipsi Hem Area}} \times 100 \quad 6.7$$

The calculation of a MEMRI-DWI mismatch and match was considered necessary in order to determine if MEMRI-enhanced regions had a significantly different ADC deficit as compared to non-MEMRI-enhanced regions. A larger ADC deficit in the MEMRI-enhanced regions was expected if these regions are truly indicative of the stroke core.

*TTC Stain Deconvolution and Saturation Transform*

For technical reasons, TTC staining was performed with EB dye present in the brain. Therefore, in regions with deep EB staining, it was not visually clear if the underlying brain did or did not stain by TTC. For best results, therefore, a method was employed to separate the two colors (red by TTC and blue by EB) from the histological images, based on image deconvolution and Saturation transformation (as previously discussed in Chapter 5). Based on the work of Ruifrok and

Johnston, histological images (in RGB format) were deconvolved into images that represented the independent contributions of the TTC stain (red) and the EB stain (blue) (25). This method is based on an orthonormal transformation of the optical density values found in RGB images of each stain separately (i.e., a RGB histological image of red stain only and a RGB image of blue stain only). Since we were not able to experimentally determine the optical density (OD) values for TTC and EB, previously determined OD values for Fast Red and Alcian Blue stains were used instead. Fast Red and Alcian Blue absorb light at wavelengths similar to those of EB and TTC, respectively (wavelengths of light absorption are: Fast Red: 266 nm; TTC: 247 nm; Alcian Blue: 615 nm; EB: 611 nm; from Ref (26)). All histological-stain deconvolution calculations were performed by ImageJ (algorithm written by G. Landini and downloaded from <http://www.dentistry.bham.ac.uk/landinig/software/software.html>). Deconvolved TTC stain images were transformed into Hue, Saturation, and Intensity format using ImageJ software. Hue refers to the dominant wavelength in the color image, Saturation represents the degree to which white is mixed with the dominant wavelength, and Intensity represents the intrinsic reflectivity of the object viewed (27).

## 6.3 Results

### 6.3.1 MEMRI signal-enhancement

MEMRI signal-enhancement was determined from  $T_1W$  MRIs acquired 5-10 min following cessation of  $MnCl_2+EB$  infusion. The average percent increase in signal intensity in MEMRI signal-enhanced regions of the ipsilateral hemisphere was  $22\% \pm 5\%$  and the average percent area of the ipsilateral hemisphere with MEMRI signal-enhanced regions was  $17\% \pm 5\%$ . One animal did not show MEMRI signal-enhancement in any brain slice. Table 6-1 summarizes MEMRI signal-enhancement data.



Table 6-1: Average Percent MEMRI signal-enhancement and Percent MEMRI Signal-Enhancement Area (as a percentage of the ipsilateral-hemisphere area) from T<sub>1</sub>W MRI Following eMCAO and Infusion of the MnCl<sub>2</sub>+EB solution.

MEMRI Signal-Enhancement (using Eq. 6.1)		% Area of Ipsilateral Cortex w/ MEMRI Signal-Enhancement (using Eq. 6.2)	
Mean ± SEM (%)	ISSD <sup>a</sup> (%)	Mean ± SEM (%)	ISSD <sup>a</sup> (%)
22 ± 5	5	17 ± 5	6

<sup>a</sup>To account for intra-animal variability, the inter-slice standard deviation (ISSD) was calculated from values for average MEMRI Signal-Enhancement and average MEMRI Signal-Enhancement area (%) across slices.

### 6.3.2 ADC Deficit

Because the majority of stroke-related decrease in ADC occurs within the first 2-3 h following stroke (28) and, as shown in Chapter 5, the paramagnetic properties of intracellular Mn<sup>2+</sup> can lead to large susceptibility artifacts in DW images, ADC deficit in the ipsilateral hemisphere was determined from DW images acquired 30 min before MnCl<sub>2</sub>+EB-solution infusion and 3.5 h after embolic-stroke onset (Fig. 6-1). The average percent ADC decrease in the ipsilateral-hemisphere regions with ADC deficit was 18% ± 2% and the average percent area of the ipsilateral hemisphere with ADC deficit was 48% ± 8%. Table 6-2 summarizes ADC deficit data.

Table 6-2: Average Percent ADC Deficit and Percent Deficit Area (as a percentage of ipsilateral hemisphere area) from DW Imaging (and corresponding ADC Maps) 3.5 Hours Following eMCAO and 30 Minutes Before Infusion of MnCl<sub>2</sub>+EB Mixture Solution.

Average % ADC Deficit (using Eq. 6.4)		% Area of Ipsilateral Hemisphere w/ ADC Deficit (using Eq. 6.5)	
Mean ± SEM (%)	ISSD <sup>a</sup> (%)	Mean ± SEM (%)	ISSD <sup>a</sup> (%)
18 ± 2	4	48 ± 8	17

<sup>a</sup>To account for intra-animal variability, the inter-slice standard deviation (ISSD) was calculated from values for average ADC Deficit and average ADC Deficit area (%) across slices.

### 6.3.3 MEMRI-DWI Mismatch & Match

MEMRI-DWI mismatch area was calculated as the area of ADC deficit in the ipsilateral hemisphere that exceeded the boundaries of the MEMRI signal-enhancing regions in the ipsilateral hemisphere. In most instances, MEMRI signal-enhancement was confined to the region with ADC deficit. For the few cases where MEMRI signal-enhancement extended beyond the boundaries of the ADC-deficit region, MEMRI-DWI mismatch remained consistently defined as the region of ADC deficit outside the border of MEMRI signal-enhancement. Regions in the ipsilateral hemisphere with ADC deficit that were within the boundaries of MEMRI signal-enhancement were defined as regions with MEMRI-DWI match (overlap). Percent-area of the ipsilateral hemisphere with a MEMRI-DWI mismatch and match was  $35\% \pm 6\%$  and  $18\% \pm 7\%$ , respectively. It is noteworthy that the MEMRI-DWI match regions always coincided almost exactly with the regions of MEMRI signal-enhancement ( $86\% \pm 12\%$  of the area of MEMRI-DWI match regions was contained within MEMRI-enhanced regions in all animals). In other words, regions with MEMRI signal-enhancement were almost always within regions with ADC deficit, suggesting accumulation of  $Mn^{2+}$  in brain regions with BBB and neuronal injury. Regions of brain MEMRI-DWI mismatch and match were not confined to particular brain regions. Table 6-3 summarizes MEMRI-DWI mismatch and match percent-area data.

Table 6-3: Average Area of MEMRI-DWI Mismatch and Match As a Percentage of the Ipsilateral Hemisphere Area.

Average % Area of MEMRI-DWI Mismatch (using Eq. 6.6)		Average % Area of MEMRI-DWI Match (using Eq. 6.7)	
Mean $\pm$ SEM (%)	ISSD <sup>a</sup> (%)	Mean $\pm$ SEM (%)	ISSD <sup>a</sup> (%)
$35 \pm 6$	8	$18 \pm 7$	6

<sup>a</sup>To account for intra-animal variability, the inter-slice standard deviation (ISSD) was calculated from values for average % area of MEMRI-DWI Mismatch and Match across slices.

#### *Percent ADC Deficit in MEMRI-DWI Mismatch and Match Regions*

To determine if brain injury was more severe in MEMRI-DWI mismatch vs. MEMRI-DWI match regions, the ADC deficit was summarized and compared in these regions. ADC deficit in MEMRI-DWI mismatch and match regions was  $19\% \pm 2\%$  and  $20\% \pm 2\%$ , respectively. The difference in ADC deficit between MEMRI-DWI mismatch and match regions was not significant (P

> 0.05, Student's t-test). Table 6-4 summarizes MEMRI-DWI mismatch and match percent ADC deficit data.

Table 6-4: Average Percent ADC Deficit in MEMRI-DWI Mismatch and Match Regions.

% ADC Deficit in MEMRI-DWI Mismatch Regions (using Eq. 6.4)		% ADC Deficit in MEMRI-DWI Match Regions (using Eq. 6.4)	
Mean $\pm$ SEM (%)	ISSD <sup>a</sup> (%)	Mean $\pm$ SEM (%)	ISSD <sup>a</sup> (%)
19 $\pm$ 2	2	20 $\pm$ 2	3

<sup>a</sup>To account for intra-animal variability, the inter-slice standard deviation (ISSD) was calculated from values for average % ADC Deficit in MEMRI-DWI Mismatch and Match regions across slices.

### 6.3.4 MEMRI Signal-Enhancement and ADC Correlation With Evans Blue and TTC Histology

Figure 6-2 shows images from one animal that includes the average signal intensity of DW images acquired prior to MnCl<sub>2</sub>+EB infusion, the corresponding ADC maps, T<sub>1</sub>W images, EB-stained and TTC-stained images. Images were acquired according to the timing protocol shown in Figure 6-1.

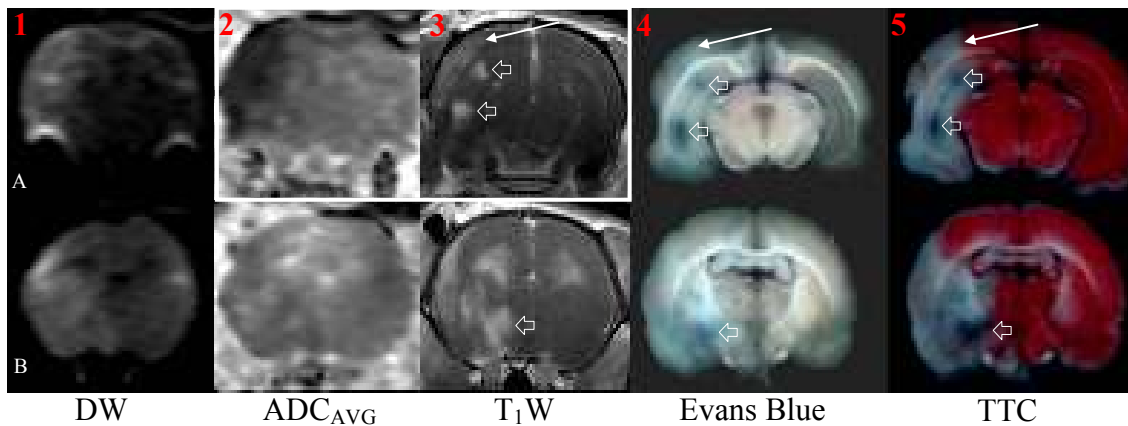


Figure 6-8: DW, Average ADC, T<sub>1</sub>W, EB-stained, and TTC-stained images from one animal. DW images were acquired prior to starting MnCl<sub>2</sub>+EB infusion. TTC staining (performed 1 h after T<sub>1</sub>W image shown here) shows a correlation between infarcted tissue and areas with T<sub>1</sub> enhancement. The images enclosed in white outlined region are shown enlarged in Fig. 6-3.

T<sub>1</sub>W images in Figure 6-2 (A3 and B3) were the last acquired among all of the T<sub>1</sub>W scans. Figure 6-2 (A3 and B3) shows regions of bright MEMRI signal-enhancement corresponding to regions with dark EB staining (small arrows) in the hippocampus (Fig. 6-2-A4) and caudoputamen (Fig. 6-2-B4). Regions of relatively weak MEMRI signal-enhancement in cortex (large arrows, Fig. 6-2-A3) do not show correlated (gross) EB staining (A4) but do correspond to areas of tissue infarct as verified by TTC staining (A5). Figure 6-3 shows an enlarged view of images from Figure 6-2 (outlined images) with regions of interest drawn corresponding to MEMRI signal-enhanced regions. The table in Figure 6-3 shows an inverse correlation between percent-increase in signal intensity in the T<sub>1</sub>W image and percent-decrease in ADC values compared to the contralateral hemisphere. The heterogeneity of the ADC map in Figure 6-3 clearly shows the correlation between ADC deficit and low percent MEMRI signal-enhancement. The correlation between high ADC deficit and low percent MEMRI signal-enhancement may be a consequence of severe perfusion deficits in these regions.

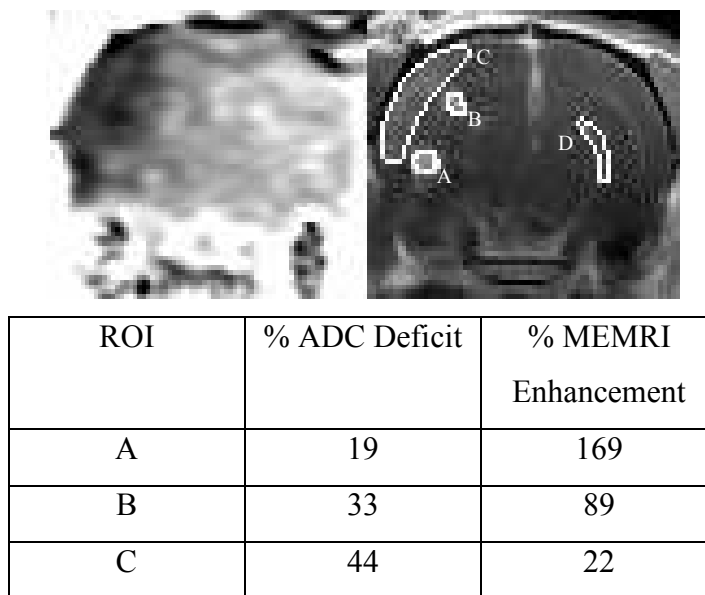


Figure 6-9: Enlarged view of calculated average ADC map and T<sub>1</sub>W image shown in Fig. 6-2 (boxed region outlined in white; ADC map is windowed here to enhance contrast). ROIs are drawn for reference. The adjoining table provides data suggesting that the ADC decrease is inversely correlates with percent MEMRI signal-enhancement. Values are mean of ROI compared to mean of homologous contralateral control region.

*TTC Stain Deconvolution*

For clarity in identifying TTC- and EB-stained regions in an independent fashion, TTC-stained images were deconvolved and transformed into the Saturation format. The deconvolved and

Saturation-transformed TTC-stained image from the animal in Figure 6-2 is shown in Figure 6-4. EB- and TTC-stained (healthy) regions appear hyperintense in the deconvolved and Saturation transformed images. From the deconvolved and Saturation transformed images it is clear that non-TTC stained regions correlate with regions of gross EB staining. This confirms that the  $\text{MnCl}_2$ +EB solution passes across the stroke-damaged BBB.

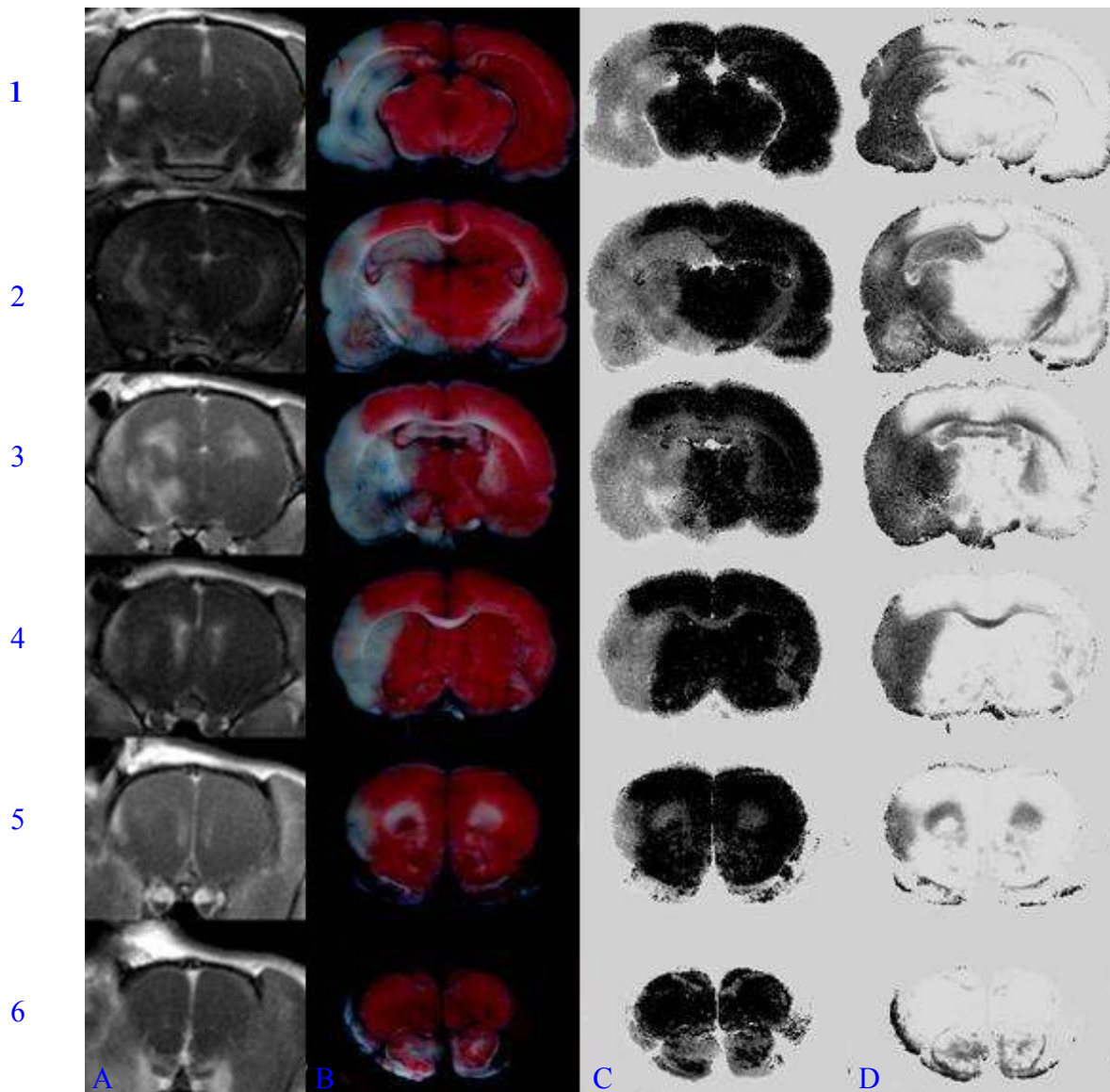


Figure 6-10: T<sub>1</sub>W MRI (A), EB+TTC histology (B), deconvolved and Saturation transformed representations (C and D) of the EB+TTC histological image shown in (B). (C) Independent representation of “EB-stain-only” image from (B). Hyperintense regions in Column (C) correspond to regions with significant EB staining and, in turn, BBB disruption. (D) Independent representation of “TTC- stain-only” image from (B). Hyperintense regions correspond to regions with positive TTC staining. Therefore, dark regions correspond to regions without stain and are considered regions of ischemic brain damage. The grayscale format of images in (C) and (D) is a result of Saturation transformation of the deconvolved images from (B). Saturation transform images exhibit better contrast between stained (EB in (C)) and non-stained (TTC in (D)) brain regions compared to the images generated by deconvolution alone.

#### *MEMRI signal-enhancement During and After MnCl<sub>2</sub>+EB Infusion*

T<sub>1</sub>W signal intensity over time relative to MnCl<sub>2</sub>+EB infusion is shown in Figure 6-5. The signal intensity in strongly-enhancing brain regions (Fig. 6-3, ROIs A and B)

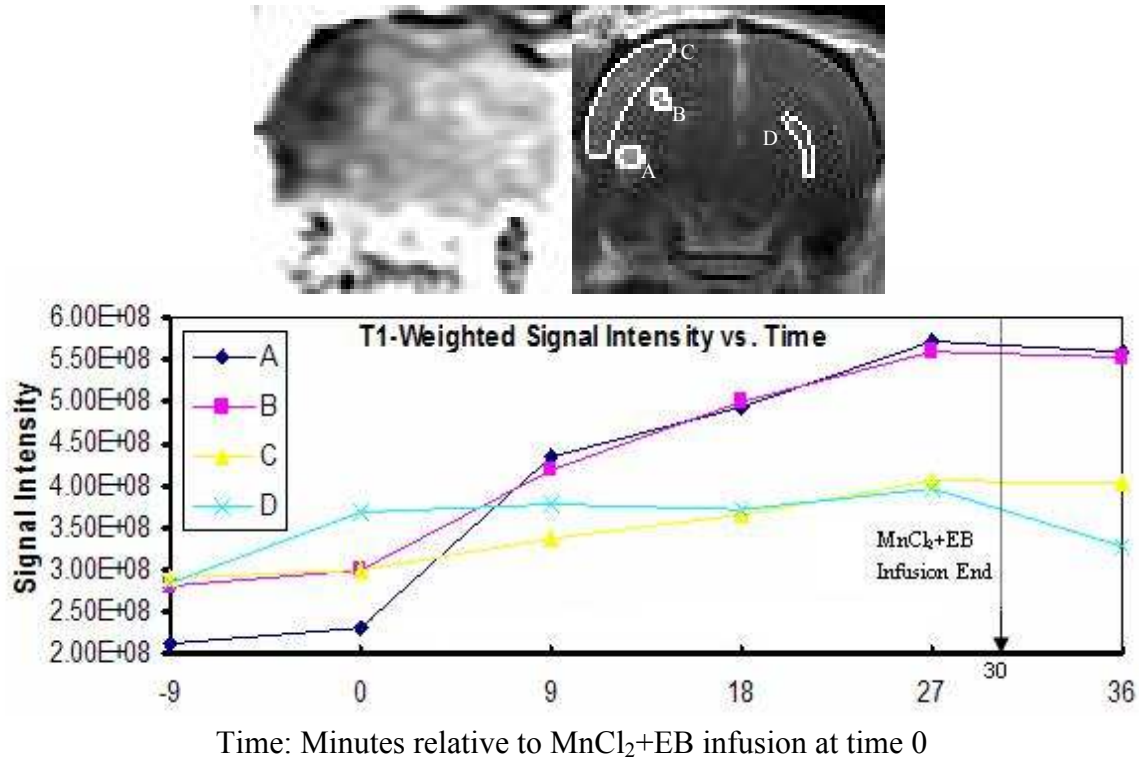


Figure 6-11: Time course of T<sub>1</sub>W signal intensity relative to the initiation (Time 0) of MnCl<sub>2</sub>+EB infusion. The data are from ROIs A, B, C, and D as shown in Figure 6-3. ROIs A and B show rapid signal increase compared to ROIs C and D. A decline or leveling off in signal intensity was detected in all ROIs following cessation of the MnCl<sub>2</sub>+EB infusion.

increases more rapidly than the signal intensity in more weakly-enhancing brain regions (Fig. 6-3, ROIs C and D) over the time course of the MnCl<sub>2</sub>+EB infusion. Differences in MEMRI signal-enhancement kinetics among different brain regions may be due to differences in BBB disruption, blood flow, and/or cellular activity local to these regions. MEMRI signal-enhancement in the ventricle (Fig. 6-3, ROI D) is detected earlier than MEMRI signal-enhancement in the brain parenchyma. This is likely due to differences in the transport pathways available for Mn<sup>2+</sup> to access the respective spaces (i.e., via the choroids plexus in the case of CSF as compared to the compromised BBB in the case of the brain parenchyma).

## 6.4 Discussion

### 6.4.1 MEMRI Signal-Enhancement: Detection of Hemorrhagic Transformation During Acute Stages of Embolic Stroke?

In this chapter we have shown that MEMRI can be used to detect regions of pathological BBB disruption. More importantly, our data show MEMRI signal-enhanced regions local to regions with spatially-correlated BBB injury and neuronal damage (Fig. 6-2 and 6-4). MEMRI signal-enhancement detected in these experiments was similar to that seen in experiments summarized in Chapters 4 and 5 in that MEMRI signal-enhancement here was correlated to regions with BBB injury as verified by EB staining.

Brain regions with a MEMRI-DWI mismatch and a MEMRI-DWI match were analyzed to determine if a significant difference was present between the ADC deficits in both regions. If the ADC deficit was lower in the region with MEMRI-DWI match, then this observation would support the concept that MEMRI signal-enhanced brain regions in these experiments are indicative of the stroke core. However, the data in this study showed that the ADC deficit in MEMRI-DWI mismatch regions was not significantly different from the ADC deficit in regions with MEMRI-DWI match (Table 6-4). Therefore, it is difficult to confirm that MEMRI signal-enhanced regions are specific to the stroke core.

On the other hand, images shown in Fig. 6-2 and 6-4 confirm that MEMRI signal-enhancement is local to regions of stroke-related brain damage, as evidenced by EB staining. In addition, our use of image deconvolution to independently separate EB stain color from TTC stain color in TTC-stained digital images (Fig. 6-4) indicate that in certain instances tissue stained with EB dye was local to regions of tissue injury (tissue not stained by TTC). In these cases, dark EB-stained regions with underlying tissue damage may represent regions undergoing hemorrhagic transformation or regions that are destined for hemorrhagic transformation (HT).

Indeed, Ding *et al.* using an embolic stroke model in rat and contrast-enhanced MRI (Gd-DTPA contrast agent), detected ‘microscopic’ HT 3 hours after stroke (19). In their case, HT was confirmed by hematoxylin and eosin (H&E) histology. An important observation by Ding *et al.* was “enhancement in  $[T_1W]$  images, or increase in  $K_i$  and  $V_p$  maps, may not directly reflect HT because the size of the Gd-DTPA molecule is smaller than that of the erythrocyte.” This observation is relevant to this study because the  $MnCl_2$  molecule (MW=198) is smaller than the Gd-DTPA molecule (MW=570, (29)); making MEMRI signal-enhancement in these experiments more sensitive to tissue destined for HT, if HT is present.

It is informative to compare the data from Ding *et al.* to the MR and histological data from the experiments in this study. As shown in Figure 6-6, one animal in our study showed similar



contrast (MEMRI signal-) enhancement and regions of tissue damage confirmed histologically as compared to the findings of Ding *et al.* Ding *et al.* did not note the location within the brain where

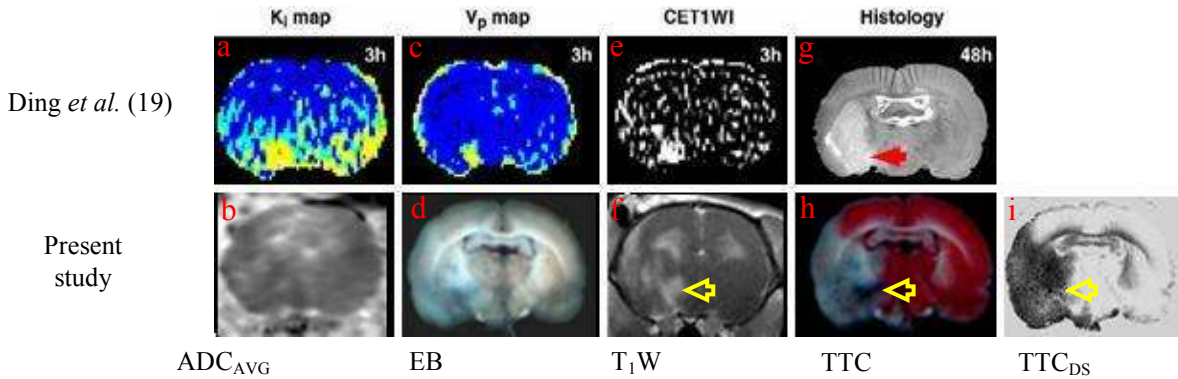


Figure 6-12: Top row: K<sub>i</sub> map (a), V<sub>p</sub> map (c), subtraction T<sub>1</sub>W image (e), and histology (g) in a representative case of microscopic HT from Ding *et al.* (18). Bottom row: ADC<sub>AVG</sub> map (b), EB-stained histological section (d), T<sub>1</sub>W image (f), TTC-stained histological section (h), and the deconvolved and Saturation-transformed version of the TTC-stained image (i), in a representative animal from the present study (same images as presented in bottom row of Fig. 6-2 with the exception of the TTC<sub>DS</sub> image). Images in the bottom row are from the same slice in this animal (ADC<sub>AVG</sub> and T<sub>1</sub>W images are registered exactly; EB, TTC, and TTC<sub>DS</sub> images are co-registered exactly; MR and histological images were registered to the extent possible). Red arrow in (g) represents region of HT as determined by microscopic examination of a histological slide in the study of Ding *et al.* Yellow arrow in (h) indicates the region of dark EB staining that correlates to the region of HT in the case of Ding *et al.* (g). Yellow arrows in (f) and (i) show MEMRI signal-enhanced and tissue-damaged regions in the T<sub>1</sub>W and TTC<sub>DS</sub> image, respectively, that correspond to the region of dark EB staining in the TTC image (h).

the images shown in the top row of Fig. 6-6 were obtained. However, it appears that the brain region shown by Ding *et al.* is closely co-registered to the brain region shown in this study (i.e., the bottom row of Fig. 6-6) based on visual comparison of the histological information. The region of contrast enhancement as indicated by Ding *et al.* (Fig. 6-6e) closely matches the region of MEMRI signal-enhancement as shown in the T<sub>1</sub>W image from this study (Fig. 6-6f). Also, the region of HT shown in the histological section of Ding *et al.* (Fig. 6-6g) closely matches the region of dark EB staining shown in the TTC-stained image in this study (Fig. 6-6h). These regions, therefore, may represent regions of HT detected by MEMRI signal-enhancement 3 hours after embolic stroke.

#### 6.4.2 MEMRI Signal-Enhancement in Stroke: Mechanisms Related to Cell Calcium Uptake

Although HT may indeed be the primary factor governing the MEMRI signal-enhancement observed in this study, it is important to consider the complicated nature of MEMRI signal-enhancement in brain. Gd-DTPA is an extracellular contrast agent and does not accumulate within cells.  $Mn^{2+}$ , on the other hand, has been shown to produce contrast in  $T_1W$  images only after cell-membrane-depolarization events(1). Aoki *et al.* have also shown that MEMRI signal-enhancement in brain may be sensitive to anoxic depolarization following experimental stroke in the rat brain, but not sensitive to disruption of the BBB (30). Other investigators have shown that  $Mn^{2+}$  infused i.v. following osmotic disruption of the BBB does not result in MEMRI signal-enhancement (31,32). Therefore, in interpreting our findings it is important to discuss other mechanisms related to stroke that may be responsible in part or completely for the MEMRI signal-enhancement detected in our experiments.

*MEMRI Signal-Enhancement After Stroke: Specific to Cell Calcium Uptake or Periinfarct Depolarization?*

Data presented here are in agreement with a study showing multifocal BBB leakage (by albumin extravasation and EB staining) in the caudoputamen after experimental stroke (33) and another study showing  $T_1W$  image contrast enhancement in the caudoputamen by gadolinium-based contrast-enhanced MRI after embolic stroke (19). As intended, the permanent occlusion model of stroke results in severe perfusion deficits to certain brain regions (in particular the stroke core) and may not allow for a significant dose of contrast agent (gadolinium or manganese) to permeate the stroke-injured BBB. Therefore, the ability of contrast-enhanced MRI to detect areas of BBB injury local to the stroke core is limited when using the embolic stroke model.

In fact, the data in this study shows a correlation between areas of dark EB staining and near-normal ADC as shown in Figure 6-2A (compare images in Fig. 6-2A2, A3, and A4); suggestive of higher cerebral blood flow (at the time of DW image acquisition) in these regions compared to regions with a low ADC and no grossly-visible EB staining. In addition, 1 of 5 animals did not show MEMRI signal-enhancement but did show a correlation between ADC deficit and lack of TTC staining; typical of stroke-induced tissue injury (data not shown). However, for animals in which MEMRI signal-enhancement was observed, stroke-induced BBB injury was severe enough, and blood flow levels were high enough, to allow delivery of  $MnCl_2+EB$  into the brain extracellular space. Ensuing MEMRI signal-enhancement may reflect cellular uptake of  $Mn^{2+}$  via transient periinfarct depolarizations and/or cells with permanently damaged calcium channels. This

hypothesis is supported by reports that show BBB injury in areas peripheral to and central to the stroke core (34), periinfarct depolarizations persisting for 6 h beyond the initial ischemic insult (35), and calcium accumulation in the rat hippocampus following cerebral ischemia (36). However, the possibility that MEMRI signal-enhancement – in the cases presented here – is the result of  $Mn^{2+}$  accumulation within BBB endothelial cells or within swollen or damaged astrocytes cannot be ruled out.

#### *MEMRI Signal-Enhancement After Stroke: Specific to Cells with Damaged Membranes?*

As suggested in Chapter 5 of this dissertation, osmotic BBB disruption has been shown to result in damaged and/or swollen astrocytes and glia. Therefore, in the case of stroke, if infusions of  $Mn^{2+}$  coincide temporally with stroke-related BBB injury and the time point at which astrocytes and glia are damaged and swollen,  $Mn^{2+}$  may have unregulated (i.e., not only through voltage-gated calcium channels) access to the intracellular space resulting in localized signal increase in T<sub>1</sub>W brain images.

Using the embolic stroke model in rat, Jiang *et al.* used fibrinogen leakage into brain parenchyma as a marker for BBB disruption. Fibrinogen is a large-molecular-weight molecule (MW=300,000) that is known to be impermeable to a healthy intact BBB (37,38). In the study of Jiang *et al.*, fibrinogen leakage into the brain parenchyma was apparent at 2 h after stroke and levels of fibrinogen in brain were increased at 5 h after stroke as compared to the 2-h time point. Other models of stroke show similar results. For example, in a study by Albayrak *et al.*, focal ischemia was induced in rats by the intraluminal-suture-occlusion method to investigate the correlation between stroke-related BBB-permeability changes and cell injury (39).

In the study by Albayrak *et al.*, albumin, which does not cross the healthy intact BBB, was found within cells local to the ischemic focus. In addition, the data of Albayrak *et al.* shows that the BBB is permeable to molecules with sizes similar to albumin (MW=68,500) at a time when neuronal damage is already manifest. The findings in this study show a spatial correlation of MEMRI signal-enhancement to EB staining in brain (Figs. 6-2 and 6-4), consistent with the data of Albayrak *et al.* Indeed, a correlation of MEMRI signal-enhancement with EB staining at a time point after stroke, when the BBB and underlying brain cells are damaged, suggests uncontrolled entry of EB-albumin and  $Mn^{2+}$  into the cell. In addition, EB dye has been shown to stain the brain after embolic stroke in rat.

Belayev *et al.* used the EB-albumin complex to determine the dynamics of BBB permeability changes following transient stroke (2 h of intraluminal-suture occlusion followed by various periods of reperfusion) in rats (33). In their work, Belayev *et al.* infused EB i.v. at 2, 3, 24 or 48 h after stroke onset (and, therefore, 0, 1, 22 or 46 hours after removal of the suture to re-establish perfusion). Rats infused with EB 3 h after stroke onset showed gross EB staining, predominantly in caudoputamen. The caudoputamen is frequently within the region of ischemic core in MCA-occlusion models of experimental stroke (39). The findings in this study are consistent with those of Belayev *et al.*, based on the observed ADC deficit, tissue damage verified by TTC staining, and MEMRI signal-enhancement in the caudoputamen-region in certain animals as shown in Figure 6-6 f and h (and Fig. 6-4-A3 and -B3).

In conclusion, the data in this study provide evidence of MEMRI signal-enhancement in areas of BBB disruption local to areas of stroke-induced tissue injury as verified by gross comparison of T<sub>1</sub>W images and histology. This method may provide insight into the state of tissue local to embolic stroke-induced BBB injury and an opportunity for longer retention of MEMRI signal-enhancement in areas of BBB injury as compared to Gd-DTPA contrast-enhanced MRI. In addition, the data in this study suggest that detection of MEMRI signal-enhanced regions shortly after stroke (4 h) may be a more sensitive indicator of tissue destined for HT as compared to traditional contrast-enhanced MRI during the acute stages of embolic stroke.

## REFERENCES

1. Lin Y. J., Koretsky A. P. Manganese ion enhances T1-weighted MRI during brain activation: an approach to direct imaging of brain function. *Magn Reson Med* 1997;38:378-388.
2. Duong T.Q., Silva A.C., Lee S.P., Kim S.G. Functional MRI of calcium-dependent synaptic activity: cross correlation with CBF and BOLD measurements. *Magn Reson Med* 2002;43:383-392.
3. Silva A.C., Lee J.H., Aoki I., Koretsky A.P. Manganese-enhanced magnetic resonance imaging (MEMRI): methodological and practical considerations. *NMR In Biomed* 2004;17:532-543.
4. de Crespigny A.J., Rother J., Beaulieu C., Neumann-Haefelin T., Moseley M.E. Comparison of Diffusion, Blood Oxygenation, and Blood Volume Changes During Global Ischemia in Rats. *Magn Reson Med* 2001;45:10-16.
5. Jiang Q., Ewing J. R., Ding G. L., Zhang L., Zhang Z. G., Li L., Whitton P., Lu M., Hu J., Li Q. J., Knight R. A., Chopp M. Quantitative evaluation of BBB permeability after embolic stroke in rat using MRI. *J Cereb Blood Flow Metab* 2005;25:583-592.
6. Paczynski R., Hsu C.Y., Diringer M.N. Pathophysiology of Ischemic Injury. In: Fisher M., editor. *Stroke Therapy*. Boston: Butterworth-Heinemann; 1995.

7. Sadoshima S., Fujishima M., Ogata J., Ibayashi S., Shiokawa O., Omae T. Disruption of Blood-Brain Barrier Following Bilateral Carotid Artery Occlusion in Spontaneously Hypertensive Rats. A Quantitative Study. *Stroke* 1983;14:876-882.
8. Albayrak S., Zhao Q., Siesjo B.K., Smith M.L. Effect of transient focal ischemia on blood-brain barrier permeability in the rat: correlation to cell injury. *Acta Neuropathol* 1997;94:158-163.
9. Petito C.K., Pulsinelli W.A., Jacobson G., Plum F. Edema and Vascular Permeability in Cerebral Ischemia: Comparison Between Ischemic Neuronal Damage and Infarction. *J Neuropathol Exp Neurol* 1982;41:423-436.
10. Del Zoppo G.J., Von Kummer R., Hamann G.F. Ischemic damage of brain microvessels: inherent risks for thrombolytic treatment in stroke. *J Neurol Neurosurg Psychiatry* 1998;65:1-9.
11. Nedergaard M. Direct signaling from astrocytes to neurons in cultures of mammalian brain cells. *Science* 1994;263:1768-1771.
12. Wagner S., Tagaya M., Koziol J.A., Quaranta V., del Zoppo G.J. Rapid Disruption of an Astrocyte Interaction With the Extracellular Matrix Mediated by Integrin alpha6 beta4 During Focal Cerebral Ischemia/Reperfusion. *Stroke* 1997;28:858-865.
13. Hurwitz A.A., Berman J.W., Rashbaum W.K., Lyman W.D. Human fetal astrocytes induce the expression of blood-brain barrier specific proteins by autologous endothelial cells. *Brain Res* 1993;625:238-243.
14. Albeda S.M., Buck C.A. Integrins and other cell adhesion molecules. *FASEB J* 1990;4:2868-2880.
15. Niessen C.M., Hogervorst F., Jaspars L.H., de Melker A.A., Delwel G.O., Hulsman E.H.M., Kuikman I., Sonnenberg A. The alpha6 beta4 integrin is a receptor for both laminin and kalinin. *Exp Cell Res* 1994;211:360-367.
16. Hamaan G.F., Okada Y., Fitridge R., del Zoppo G.J. Microvascular basal lamina antigens disappear during cerebral ischemia and reperfusion. *Stroke* 1995;26:2120-2126.
17. Sloan M.A. Thrombolysis and stroke: past and future. *Arch Neurol* 1987;44:748-768.
18. Zhang R.L., Chopp M., Zhang Z.G., Jiang Q., Ewing J.R. A rat model of focal embolic cerebral ischemia. *Brain Res* 1997;766:83-92.
19. Ding G., Jiang Q., Li L., Zhang L., Gang Zhang Z., Ledbetter K. A., Ewing J. R., Li Q., Chopp M. Detection of BBB disruption and hemorrhage by Gd-DTPA enhanced MRI after embolic stroke in rat. *Brain Res* 2006;1114:195-203.
20. Kim H.Y., Vaughan D.K., Ghosh S. Pathways of cerebral calcium accumulation in a model of focal ischemia in rats. *Neurol Res* 1998;20:169-177.
21. Harris R.J., Symon L., Branston N.M., Bayhan M. Changes in extracellular calcium activity in cerebral ischaemia. *J Cereb Blood Flow Metab* 1981;1:203-209.
22. Siemkowicz E., Hansen A.J. Brain extracellular ion composition and EEG activity following 10 minutes ischemia in normo- and hyperglycemic rats. *Stroke* 1981;12:236-240.
23. Toomey J. R., Valocik R. E., Koster P. F., Gabriel M. A., McVey M., Hart T. K., Ohlstein E. H., Parsons A. A., Barone F. C. Inhibition of factor IX(a) is protective in a rat model of thromboembolic stroke. *Stroke* 2002;33:578-585.
24. Henninger N., Sicard K. M., Schmidt K. F., Bardutzky J., Fisher M. Comparison of ischemic lesion evolution in embolic versus mechanical middle cerebral artery occlusion in Sprague Dawley rats using diffusion and perfusion imaging. *Stroke* 2006;37:1283-1287.
25. Ruifrok A.C., Johnston D.A. Quantification of Histological Staining by Color Deconvolution. *Analyt Quant Cytol Histol* 2001;23:291-299.

26. Horobin R.W., Kiernan J.A. *Conn's Biological Stains*. Oxford: BIOS Scientific Publishers Ltd; 2002.
27. Fermin C.D., Degraw S. Colour thresholding in video imaging. *J Anat* 1995;186:469-481
28. Sotak C. H. Nuclear magnetic resonance (NMR) measurement of the apparent diffusion coefficient (ADC) of tissue water and its relationship to cell volume changes in pathological states. *Neurochem Int* 2004;45:569-582.
29. Vexler V. S., Clement O., Schmitt-Willich H., Brasch R. C. Effect of varying the molecular weight of the MR contrast agent Gd-DTPA-polylysine on blood pharmacokinetics and enhancement patterns. *J Magn Reson Imaging* 1994;4:381-388.
30. Aoki I., Ebisu T., Tanaka C., Katsuta K., Fujikawa A., Umeda M., Fukunaga M., Takegami T., Shapiro E.M., Naruse S. Detection of the anoxic depolarization of focal ischemia using manganese-enhanced MRI. *Magn Reson Med* 2003;50:7-12.
31. Duong T. Q., Silva A. C., Lee S. P., Kim S. G. Functional MRI of calcium-dependent synaptic activity: cross correlation with CBF and BOLD measurements. *Magn Reson Med* 2000;43:383-392.
32. Henning E. C., Meng X., Fisher M., Sotak C. H. Visualization of cortical spreading depression using manganese-enhanced magnetic resonance imaging. *Magn Reson Med* 2005;53:851-857.
33. Belayev L., Busto R., Zhao W., Ginsberg M. D. Quantitative evaluation of blood-brain barrier permeability following middle cerebral artery occlusion in rats. *Brain Res* 1996;739:88-96.
34. Menzies S. A., Betz A. L., Hoff J. T. Contributions of ions and albumin to the formation and resolution of ischemic brain edema. *J Neurosurg* 1993;78:257-266.
35. Back T., Kohno K., Hossmann K. A. Cortical negative DC deflections following middle cerebral artery occlusion and KCl-induced spreading depression: effect on blood flow, tissue oxygenation, and electroencephalogram. *J Cereb Blood Flow Metab* 1994;14:12-19.
36. Picone C. M., Grotta J. C., Earls R., Strong R., Dedman J. Immunohistochemical determination of calcium-calmodulin binding predicts neuronal damage after global ischemia. *J Cereb Blood Flow Metab* 1989;9:805-811.
37. Willis C. L., Leach L., Clarke G. J., Nolan C. C., Ray D. E. Reversible disruption of tight junction complexes in the rat blood-brain barrier, following transitory focal astrocyte loss. *Glia* 2004;48:1-13.
38. Haring H. P., Berg E. L., Tsurushita N., Tagaya M., del Zoppo G. J. E-selectin appears in nonischemic tissue during experimental focal cerebral ischemia. *Stroke* 1996;27:1386-1391; discussion 1391-1382.
39. Albayrak S., Zhao Q., Siesjo B. K., Smith M. L. Effect of transient focal ischemia on blood-brain barrier permeability in the rat: correlation to cell injury. *Acta Neuropathol (Berl)* 1997;94:158-163.

# CHAPTER 7

## Summary

The research presented in this dissertation focused on methods to advance the state of the art in a relatively new area of research; manganese-enhanced MRI (MEMRI) in the brain. The divalent manganese ion ( $\text{Mn}^{2+}$ ) is handled similarly to calcium ( $\text{Ca}^{2+}$ ) in biological systems. Therefore,  $\text{Mn}^{2+}$  in brain has been shown to act as a cell-membrane-dependent contrast agent useful for direct mapping of brain function. Many MEMRI experiments rely on osmotic BBB disruption for delivery of  $\text{Mn}^{2+}$  to brain parenchyma prior to a specific neuronal stimulus. To date, the MEMRI literature is lacking histological (or other) evidence to show the extent of BBB disruption and/or the distribution of  $\text{Mn}^{2+}$  in brain prior to specific neuronal activity. Therefore, to remedy this, we developed a simple but novel method to histologically monitor the degree of BBB disruption and associated passage of  $\text{Mn}^{2+}$  into brain parenchyma.

Because Evans Blue (EB) dye is a well-known marker for monitoring the permeability of the BBB, we mixed EB with  $\text{MnCl}_2$  and infused the resulting solution i.v. following osmotic BBB disruption. As Chapter 4 makes clear, a co-infusion of  $\text{MnCl}_2$  and EB allows for the quantification of BBB permeability changes and an inference as to the extent of  $\text{Mn}^{2+}$  distribution in the brain. In addition, we show that using a particular infusion protocol of  $\text{MnCl}_2$ +EB and 1.6 M arabinose (to osmotically disrupt the BBB) consistently results in nonspecific MEMRI signal-enhancement. This portion of the dissertation shows that another mechanism of  $\text{Mn}^{2+}$  influx into cells (other than by voltage-gated calcium channels) may be responsible for unwanted signal changes in MEMR images.

In Chapter 5, the mechanism responsible for unwanted signal changes in MEMR images and the potential associated effects on brain structure and function was investigated further by testing the effects of two osmotic BBB disruption protocols on brain tissue, apparent diffusion coefficient (ADC), MEMRI signal-enhancement, and differences in area of ADC deficit and nonspecific MEMRI signal-enhancement (MEMRI-DWI mismatch) in the rat brain following infusion of  $\text{MnCl}_2$ +EB solution. Significant nonspecific MEMRI signal-enhancement and brain damage were detected using the experimental protocols described in Chapter 5. These findings are important for the MEMRI research field in general because many MEMRI experiments rely on normal brain function and structure following osmotic BBB disruption. This research makes clear the need for an optimal BBB protocol for MEMRI studies.

Because brain regions with nonspecific MEMRI signal-enhancement were consistently spatially correlated with EB-stained regions (and therefore regions with BBB disruption) an experiment was designed to test the efficacy of  $\text{Mn}^{2+}$  to detect regions of pathological (vs. experimental) BBB disruption. The research in Chapter 6 provides evidence of MEMRI signal-



enhancement in areas of BBB disruption local to areas of stroke-induced tissue injury as verified by gross comparison of  $T_1W$  images and histology (TTC staining). Results from experiments in Chapter 6 are useful because it was shown that  $Mn^{2+}$  can be used to track BBB injury following stroke and shows strong potential for tracking stroke-related nerve damage in brain. Because  $Mn^{2+}$  acts as an intracellular contrast agent, the methods described in Chapter 6 may provide insight into the state of tissue local to embolic stroke-induced BBB injury.

A parallel can be drawn from data summarized in Chapters 4, 5, and 6: nonspecific MEMRI signal-enhancement in brain is very likely a result of a mechanism related to BBB disruption and/or cell volume regulation in response to osmotic challenge. This idea is important because it obviates the need for future work that will determine; 1) the exact mechanism related to osmotic and pathological BBB disruption that causes nonspecific MEMRI signal enhancement; 2) the optimal experimental protocol (in terms of osmotic BBB disruption and anesthetic regimen) for MEMRI experiments that rely on specific neuronal stimulus in a healthy brain; and 3) methods other than osmotic BBB disruption that will reliably allow delivery of  $Mn^{2+}$  into brain such that time-efficient MEMRI experiments are possible.

## Future Considerations

### *MEMRI Experiments and Osmotic BBB Disruption*

The use of osmotic agents to disrupt the blood-brain barrier (BBB) has several drawbacks, such as brain damage and swelling and barrier opening that is inhomogeneous, as outlined in this dissertation. MEMRI experiments that utilize osmotic BBB disruption should, therefore, provide evidence of healthy brain tissue and the degree of BBB disruption following osmotic challenge. The methods of TTC and Evans Blue staining presented in this dissertation provide qualitative evidence of brain tissue health and the homogeneity of BBB disruption following infusions of hyperosmotic arabinose or mannitol.

### *MEMRI Experiments and Baseline MR Imaging*

Results of MEMRI experiments that include osmotic BBB disruption performed on the benchtop are susceptible to misinterpretation because MRI scans acquired before neuronal stimulus and after osmotic BBB disruption are not possible. To monitor possible changes in  $T_1$ -weighted ( $T_1W$ ) or diffusion-weighted (DW) contrast following osmotic BBB disruption and  $MnCl_2$  infusion,

a control group of animals can be used in which neuronal stimulus is not performed. Although use of a control group may be sufficient to rule out unwanted changes in T<sub>1</sub>W or DW contrast following a specific infusion protocol of arabinose (or mannitol) and MnCl<sub>2</sub>, this group increases the number of animals needed to complete the study. In fact, the control group in many studies uses the same number of animals as the treatment group, thus doubling the number of animals in the study if treatment animals cannot also be used as controls. When MEMRI experiments are moved from the benchtop to the bore of the MR scanner each animal can be scanned prior to neuronal stimulus allowing 1) each animal to serve as its own control; and 2) more accurate determination of nonspecific changes in T<sub>1</sub>W and DW contrast in the treatment group.

## Future Experiments

Several MEMRI experiments have been carried out that do not rely on osmotic BBB disruption (1-3). These experiments were not, however, designed to detect the presence or absence of clinically-relevant disease in brain. The methods described in these works may be useful for future experiments that can utilize the unique contrast agent properties of Mn<sup>2+</sup> to provide new information regarding a particular brain disease.

### *MEMRI and Multiple Sclerosis*

Multiple sclerosis (MS) is an autoimmune disease of the central nervous system which results in demyelination of axons (4). Current MRI techniques to monitor MS include image contrast that is dependent upon the proportion of water protons that are bound to macromolecules (i.e., magnetization transfer contrast) (5). From magnetization transfer (MT) contrast the degree of tissue structure (and, therefore, axonal loss) can be inferred but cannot be measured directly. Other MRI techniques to measure the degree of axonal loss include MR spectroscopy and conventional T<sub>1</sub>W imaging (5). MR spectroscopy suffers from low spatial resolution and conventional T<sub>1</sub>W imaging does not provide a direct measure of axon structure or function. MEMRI offers an advantage to MR spectroscopy and conventional T<sub>1</sub>W imaging for detection of axonal loss in experimental models of MS. The unique mechanism by which normal cells sequester Mn<sup>2+</sup> and generate localized contrast in T<sub>1</sub>W images makes MEMRI an attractive alternative to other MRI techniques of neuronal loss detection in experimental MS.

### *MEMRI and Parkinson's Disease*

Parkinson's disease is a neurodegenerative disorder with symptoms that include body tremors, alterations in personality, impaired color vision discrimination, and decreased autonomic function (6). One of the distinct pathological features of Parkinson's disease is progressive loss of dopamine (DA) neurons in the pars compacta of the substantia nigra. Although the causes of DA neuron loss are not well known, evidence points to oxidative stress, mitochondria dysfunction, protein mishandling, and inflammation as possible pathological contributors (7). In addition, Li *et al.* have offered evidence that calcium ( $\text{Ca}^{2+}$ ) homeostasis disturbance under conditions of proteasome inhibition may be a novel pathological mechanism leading to DA neuronal injury (7). Because  $\text{Mn}^{2+}$  is treated similarly to  $\text{Ca}^{2+}$  *in vivo*, MEMRI may be a useful tool to follow up on Li's work in *in vivo* experiments. Current *in vivo* imaging strategies rely, in part, on correlating single photon emission tomography (SPECT) and  $T_2$ -weighted MR images of Parkinson's disease patients (8). SPECT imaging can be used for the noninvasive determination of dopamine concentration *in vivo* but cannot be used to detect DA neuronal injury directly. MEMRI may therefore be a novel method for detection of DA neuron injury in animal models of Parkinson's disease. Because lower levels of intracellular calcium are expected with DA neuronal injury under conditions of proteasome inhibition (7), lower levels of intracellular  $\text{Mn}^{2+}$  are also expected during proteasome inhibition in the presence of consistent extracellular  $[\text{Mn}^{2+}]$ . Lower levels of intracellular  $\text{Mn}^{2+}$  will lead to lower MEMRI signal-enhancement on high resolution (78  $\mu\text{m}$  in rat) MR scans providing 1) accurate localization of regions of brain with DA neuronal injury and 2) additional evidence that DA neuronal injury is associated with disturbed calcium homeostasis.

### MEMRI in the Clinic

As described in Chapter 3 of this dissertation,  $\text{Mn}^{2+}$  is toxic and is not currently applicable for human brain imaging. In addition, although previous studies have suggested the usefulness of osmotic blood-brain barrier (BBB) disruption to allow entry of  $\text{Mn}^{2+}$  into brain following intravenous infusion, Chapters 4 and 5 of this dissertation outlined the serious side effects of osmotic BBB disruption under certain experimental conditions. Therefore, to bring MEMRI to the clinic there is a clear need to reduce or eliminate the toxic effects of  $\text{Mn}^{2+}$  and to eliminate the need for osmotic disruption of the BBB in order to introduce  $\text{Mn}^{2+}$  to the extracellular space of the brain

without causing brain injury and confounding changes in diffusion-weighted (DW) and T<sub>1</sub>-weighted (T<sub>1</sub>W) image contrast.

*Chelation for Mn<sup>2+</sup> For Reduced Toxicity and Efficient Transport Across the Intact BBB*

The design of a chelate for the Mn<sup>2+</sup> ion that allows for efficient (in time and space) transport across the BBB and reduced (or eliminated) toxicity in brain while maintaining the unique Ca<sup>2+</sup> channel dependent contrast agent characteristics of Mn<sup>2+</sup> would be a major research effort. As a first step towards this goal, different chelates for Mn<sup>2+</sup> could be tested that allow for efficient transport of Mn<sup>2+</sup> across the BBB in such a way that sufficient quantities of free Mn<sup>2+</sup> are available for cellular sequestration (via voltage-gated calcium channels) once the chelated molecule has passed from the vasculature into the brain parenchyma. As the next and necessary step for getting MEMRI into the clinic, a chelate must be found for Mn<sup>2+</sup> that reduces or eliminates toxicity in the brain. To reduce the toxicity of Mn<sup>2+</sup> in brain and to maintain the unique characteristics of MEMRI it would be important to find a chelating molecule that would; 1) allow entry of Mn<sup>2+</sup> to the intracellular space via voltage-gated calcium channels; 2) prevent excessive (i.e., more than 4 hours) long-term accumulation in the cell (and mitochondria); and 3) allow efficient excretion of Mn<sup>2+</sup> via kidneys or bile.

A chelate that combines the efficient transport of Mn<sup>2+</sup> across the BBB (thus eliminating the need for osmotic BBB disruption) and reduces or eliminates toxicity in brain is not likely to be found soon. In the meantime, therefore, newer MRI techniques (i.e., pulse sequences) may be developed and more research at higher magnetic fields may be undertaken that will make very low doses of Mn<sup>2+</sup> in brain apparent after systemic administration and entry of Mn<sup>2+</sup> into brain via the blood-CSF barrier. In addition, future MEMRI experiments of brain pathology (stroke, multiple sclerosis, Parkinson's disease) in animals with brain structure similar to humans should be performed in order for better translation of MEMRI results in animals to clinical situations.

## REFERENCES

1. Aoki I., Lin Wu Y.J., Silva A.C., Lynch R.M., Koretsky A.P. In vivo detection of neuroarchitecture in the rodent brain using manganese-enhanced MRI. *Neuroimage* 2004;22:1046-1059.
2. London R.E., Toney G., Gabel S.A., Funk A. Magnetic Resonance Imaging Studies of the Brains of Anesthetized Rats Treated With Manganese Chloride. *Brain Res Bull* 1989;23:229-235.

3. Lee J.H., Silva A.C., Merkle H., Koretsky A.P. Manganese-Enhanced Magnetic Resonance Imaging of Mouse Brain after Systemic Administration of  $MnCl_2$ : Dose-Dependent and Temporal Evolution of  $T_1$  Contrast. *Magn Reson Med* 2004;53:640-648.
4. Kutzelnigg A., Faber-Rod J. C., Bauer J., Lucchinetti C. F., Sorensen P. S., Laursen H., Stadelmann C., Bruck W., Rauschka H., Schmidbauer M., Lassmann H. Widespread demyelination in the cerebellar cortex in multiple sclerosis. *Brain Pathol* 2007;17:38-44.
5. Dehmeshki J., Chard D. T., Leary S. M., Watt H. C., Silver N. C., Tofts P. S., Thompson A. J., Miller D. H. The normal appearing grey matter in primary progressive multiple sclerosis: a magnetisation transfer imaging study. *J Neurol* 2003;250:67-74.
6. Postuma R. B., Lang A. E., Massicotte-Marquez J., Montplaisir J. Potential early markers of Parkinson disease in idiopathic REM sleep behavior disorder. *Neurology* 2006;66:845-851.
7. Li X., Yang D., Li L., Peng C., Chen S., Le W. Proteasome inhibitor lactacystin disturbs the intracellular calcium homeostasis of dopamine neurons in ventral mesencephalic cultures. *Neurochem Int* 2007.
8. Lee J. D., Huang C. H., Weng Y. H., Lin K. J., Chen C. T. An automatic MRI/SPECT registration algorithm using image intensity and anatomical feature as matching characters: application on the evaluation of Parkinson's disease. *Nucl Med Biol* 2007;34:447-457.

# APPENDIX

## David G. Bennett

Worcester Polytechnic Institute  
Department of Biomedical Engineering  
100 Institute Road, SL121  
Worcester, MA 01609  
Lab: 508-752-3110

36 Eunice Avenue  
Worcester, MA 01606  
Cell: 508-736-3164  
dgbenn@gmail.com

**OBJECTIVE** Research & Development and/or supportive role in a laboratory setting with the goal of improvement and enhancement of magnetic resonance imaging and/or spectroscopy technology and its application to clinical and/or animal disease detection.

### EDUCATION

Worcester Polytechnic Institute, Worcester, MA

**Ph.D., Biomedical Engineering** June, 2007

Dissertation Title: "Osmotic- and Stroke-Induced Blood-Brain Barrier Disruption Detected by Manganese-Enhanced Magnetic Resonance Imaging (MEMRI)"

**University of Massachusetts Lowell, Lowell, MA**

M.S., Electrical Engineering May, 2003

Research Topic: "Time-Dependent 3D Object Classification Using Hidden Markov Models"

**B.S., Electrical Engineering** June, 1997

Senior Projects: • Autonomous Maze-Solving Robot (1997 IEEE Micromouse competition)  
• "Chaotic Analysis of Electromyographic Signals"

### PROFESSIONAL EXPERIENCE

**NMR Laboratory Research Assistant**, Worcester Polytechnic Institute, Worcester, MA Sept. 2002 – present

- Design and execution of experiments for original manganese-enhanced MRI research and dynamic contrast-enhanced mouse tumor MRI.
- MR imaging using Bruker Avance Spectrometer (Paravision 2.1 software).
- Design of RF surface and volume coils for MRI experiments.
- Writing custom Interactive Data Language (IDL) software for MR image analysis.
- Assisting in maintenance and upkeep of GE 2T research magnet.
- Developed and tested benchtop NMR spectrometer hardware and software (Labview).
- Operated GE Signa LX 1.5T clinical scanner during clinical functional magnetic resonance imaging (fMRI) trials.
- Wrote C shell scripts on Linux 9.0 platform to control fMRI data analysis using AFNI.

**Graduate Teaching Assistant**, Worcester Polytechnic Institute, Worcester, MA Fall 2005  
BE 582. Principles of *In Vivo* Nuclear Magnetic Resonance Imaging.

- Assist students performing laboratories using the Bruker Avance Spectrometer.
- Correct student homework assignments.
- Demonstrate NMR theory using benchtop NMR spectrometer controlled by in-house Labview software.

- Software Engineer**, Goodrich Corp, Lexington, MA Aug., 2001 – Sept. 2002
- Developed and maintained control algorithms for aircraft-mounted digital camera.
  - Enhanced camera's ability to monitor speed, altitude, latitude and longitude in acquiring images according to pre-determined areas of interest.
  - Wrote algorithms using MATLAB and subsequently translated them to the C programming language on a VxWorks platform.

- Software Engineer** (*Secret Clearance Required*), MITRE Corp. Bedford, MA Jan., 1999 – Aug., 2001
- Developed code for various systems using software packages and languages such as C, Perl, Assembly, Lex, and Expect.
  - Member of team responsible for code enhancements and reviews.

- Assistant Staff, Electrical Engineer** MIT Lincoln Laboratory, Lexington, MA June, 1997 – Jan., 1999
- Supported an engineering development and sensor technology group comprised of 30 technical personnel.
  - Assisted in the design and development of an embedded communication system using the 8751 microcontroller.
  - Wrote communication system-specific C code.
  - Tested, debugged and wrote a user's manual for a wireless communication system controlled by Labview.

## FELLOWSHIPS AND GRANTS

GAANN Fellowship, 08/15/03-08/15/05. Worcester Polytechnic Institute, Worcester, MA

Stedman Smith Fellowship, 08/15/05 – Present. Worcester Polytechnic Institute, Worcester, MA

## HONORS AND AWARDS

WPI Crimson and Gray Award, 04/13/04. Recognizes exceptional and sustained involvement in campus life and service to WPI.

Educational Stipend Award for Students, Postdoctoral and Clinical Trainees: ISMRM 2005, 2006, and ISMRM/ESMRMB 2007.

## PUBLICATIONS

Detection of Blood-Brain Barrier Disruption Using Manganese-Enhanced Magnetic Resonance Imaging. D.G. Bennett, N. Henninger, M.Fisher, C.H. Sotak, *In Preparation*.

A paramagnetic contrast agent for detecting tyrosinase activity. M. Querol, D.G. Bennett, C.H. Sotak, A.A. Bogdanov, Jr. *The Royal Society of Chemistry, submitted*.



Tumor-targeted enzyme mediated MR signal amplification using paramagnetic substrates. A.A. Bogdanov, H-W. Kang, D.G. Bennett, M.Querol, A.Y. Yudina, I. Verel, C.H. Sotak, *In Preparation*.

## CONFERENCE PROCEEDINGS

Manganese-Enhanced MRI (MEMRI) and Diffusion-Weighted MRI Mismatch in the Absence of a Specific Neuronal Stimulus. D. Bennett, N. Henninger, M. Fisher, C.H. Sotak. Abstract, Poster Presented at the Joint Annual Meeting of ISMRM-ESMRMB in Berlin, Germany, May 2007.

EGF receptor expression imaging using antibody-conjugated enzymes and a paramagnetic substrate. A.A. Bogdanov, M. Querol, H-W. Kang, D.G. Bennett, C. Sotak. Abstract, Oral Presentation at the Joint Annual Meeting of ISMRM-ESMRMB in Berlin, Germany, May 2007.

Detection of Blood-Brain Barrier Disruption Using Manganese-Enhanced Magnetic Resonance Imaging (MEMRI). D. Bennett, N. Henninger, M. Fisher, C. Sotak. Abstract, Poster Presented at the 14<sup>th</sup> Scientific Meeting of the International Society of Magnetic Resonance in Medicine, Seattle, Washington, May 2006.

Tumor-targeted enzyme mediated MR signal amplification using paramagnetic substrates. A.A. Bogdanov, H-W. Kang, D.G. Bennett, M.Querol, A.Y. Yudina, I. Verel, C.H. Sotak. Abstract, Oral Presentation at the 14<sup>th</sup> Scientific Meeting of the International Society of Magnetic Resonance in Medicine, Seattle, Washington, May 2006.

Characterizing Intra- and Extracellular Spaces of Skeletal Muscle In Vivo Using MEMRI. J.G. Seland, K.G. Helmer, G. Nair, D.G. Bennett, C.H. Sotak. Abstract, Poster Presented at the 14<sup>th</sup> Scientific Meeting of the International Society of Magnetic Resonance in Medicine, Seattle, Washington, May 2006.

## MEMBERSHIPS

2005 – Present	International Society of Magnetic Resonance in Medicine (ISMRM)
2004-2005	Graduate Student Representative for WPI's Provost Search Committee
2004-2005	Graduate Student Representative for WPI Community Council
2003-2005	WPI Social Awareness Committee
1997-2000	Institute of Electrical and Electronics Engineers (IEEE)
1997	Tau Beta Pi National Engineering Honor Society
1997	Eta Kappa Nu National Electrical Engineering Honor Society

## Detection of Blood-Brain Barrier Disruption in Rat Brain After Osmotic Shock Using Manganese-Enhanced Magnetic Resonance Imaging (MEMRI)

D. Bennett<sup>1</sup>, N. Henninger<sup>3,5</sup>, M. Fisher<sup>4,5</sup>, C. Sotak<sup>1,2,4</sup>

Departments of <sup>1</sup>Biomedical Engineering and <sup>2</sup>Chemistry & Biochemistry, Worcester Polytechnic Institute, Worcester, MA, USA, Departments of <sup>3</sup>Neurology and <sup>4</sup>Radiology, University of Massachusetts Medical School, Worcester, MA, USA, <sup>5</sup>Department of Neurology, University of Massachusetts Memorial Healthcare, Worcester, MA, USA

**Synopsis.** Infusion of manganese two minutes after osmotic disruption of the blood-brain barrier (BBB) resulted in areas of signal enhancement closely correlated with areas of Evans Blue histological staining. For MEMRI experiments using applied neuronal stimulus to generate T<sub>1</sub>-contrast, this infusion protocol may obscure intended results. This infusion protocol may, however, be a useful alternative for imaging experimental BBB disruption.

**Introduction.** MEMRI experiments<sup>1-3</sup> employ the intracellular uptake of Mn<sup>2+</sup> through voltage-gated calcium channels to shorten the T<sub>1</sub> relaxation time of intracellular water resulting in localized increases in T<sub>1</sub>-weighted MRI signal intensity which correspond to regions of neuronal activation.<sup>1</sup> These experiments rely on disruption of the blood brain barrier (BBB) by osmotic shock to deliver a significant concentration of Mn<sup>2+</sup> into the extracellular space prior to the neuronal stimulus. In order to optimize the contrast, the distribution of extracellular Mn<sup>2+</sup> should be homogeneous across the region of interest with little or no initial MR signal enhancement prior to the neuronal stimulus. Here we show that the timing of Mn<sup>2+</sup> administration relative to BBB opening, as well as the method of Mn<sup>2+</sup> delivery, are important factors in achieving this goal. Regions of T<sub>1</sub>-contrast enhancement were spatially correlated with areas of Evans Blue (EB) dye uptake after hyperosmotic BBB disruption. A significant increase in T<sub>1</sub>-weighted signal enhancement was observed following internal-carotid-artery infusion of Mn<sup>2+</sup> two minutes after hyperosmotic BBB opening; indicating a significant role for MEMRI in visualizing BBB disruption under these circumstances. However, this enhancement would also obscure T<sub>1</sub>-weighted signal increases arising from subsequent neuronal stimuli; thus mitigating against using this particular administration protocol for such studies.

**Methods.** Four male Sprague-Dawley rats weighing 280-350 g were anesthetized with 2.0 % isoflurane mixed with breathing-quality air. 25% D-mannitol solution (5 ml/kg; Sigma) was injected into the internal carotid artery over 50 seconds. Prior to each injection, the common carotid, external carotid and pterygopalatine artery were ligated. Two minutes after the mannitol injection was completed manganese chloride (MnCl<sub>2</sub>, MW = 198; Sigma), dissolved to 30 mM in isotonic saline, and EB (Sigma), dissolved to 2% in manganese chloride solution (2 ml/kg), was infused into the internal carotid artery at 4.5 ml/hr. MR images were acquired using a Bruker Biospin 2.0T/45 cm imaging spectrometer operating at 85.56 MHz for <sup>1</sup>H and equipped with  $\pm$ 20G/cm self-shielded gradients. T<sub>1</sub>-weighted MRI was performed with the following acquisition parameters: TR/TE = 300/7 msec, FOV = 3 cm x 3 cm, matrix = 128x128, six 2-mm slices with NEX = 8.

**Results.** Figure 1A shows signal enhancement from T<sub>1</sub>-weighted MEMRIs following administration of 30 mM MnCl<sub>2</sub>. Figure 1B shows EB staining in the corresponding histological brain slices. The average regional enhancement was ~250% of that in the homologous contralateral region (e.g., see ROIs in the top MRI slice of Fig. 1A). As seen in Fig. 1 EB histological staining correlates well with areas of increased T<sub>1</sub>-contrast in the corresponding MRI slices. For this particular animal, the effect of Mn<sup>2+</sup> on T<sub>2</sub> relaxation shows the importance of T<sub>1</sub>-weighted imaging with a short TE to minimize signal loss due to T<sub>2</sub> and T<sub>2</sub><sup>\*</sup> as Figure 2 demonstrates.<sup>4</sup> Figure 2 shows images acquired with TE = 7 ms (Fig. 2A and Fig. 1A top row) and 20 ms (Fig. 2B). The negative contrast shown in Fig. 2B is likely due to higher concentrations of Mn<sup>2+</sup> in the respective brain regions. Also, as seen in Fig. 1, EB histological staining is darker in the regions corresponding to higher [Mn<sup>2+</sup>] suggesting more extensive BBB opening. Figure 2C shows the MR signal decline as a function of TE in the cortical ROI shown in Fig. 1A.

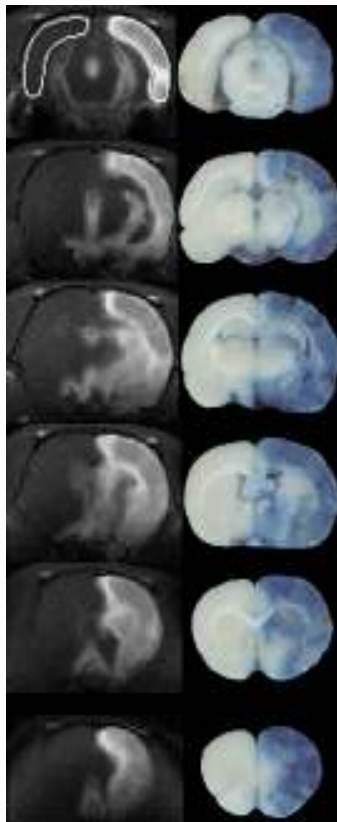


Figure 1: T<sub>1</sub>-weighted MRIs (A) and corresponding EB-stained histological slices (B). 30 mM MnCl<sub>2</sub>/2% EB was administered 2 min after osmotically-induced BBB opening. Areas of MRI signal enhancement correlate well with regions of BBB opening on EB-stained slices. Top MRI slice in (A) shows the ROIs used for enhancement calculations.

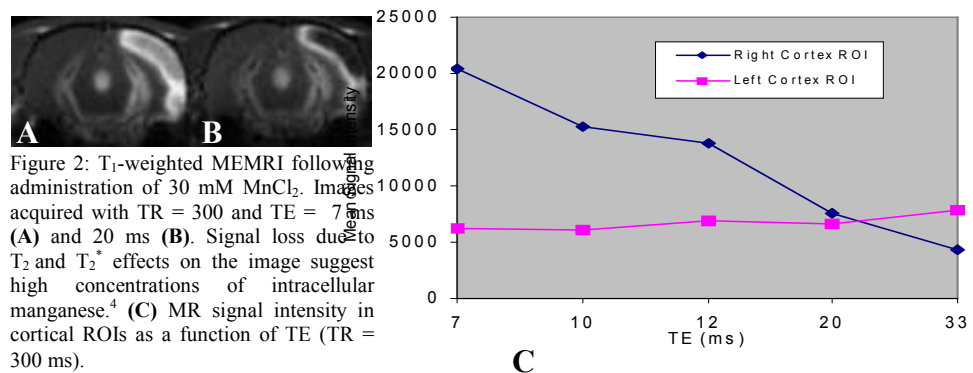


Figure 2: T<sub>1</sub>-weighted MEMRI following administration of 30 mM MnCl<sub>2</sub>. Images acquired with TR = 300 and TE = 7 ms (A) and 20 ms (B). Signal loss due to T<sub>2</sub> and T<sub>2</sub><sup>\*</sup> effects on the image suggest high concentrations of intracellular manganese.<sup>4</sup> (C) MR signal intensity in cortical ROIs as a function of TE (TR = 300 ms).

**Discussion.** MEMRI experiments for visualizing the brain response to neuronal stimulation rely on disruption of the blood brain barrier (BBB) by osmotic shock to deliver a significant concentration of Mn<sup>2+</sup> into the extracellular space prior to the neuronal stimulus. However, there should be little or no initial MR signal enhancement prior to the neuronal stimulus in order to achieve optimal T<sub>1</sub>-contrast enhancement. Although the administration protocol used in this study has been employed by others,<sup>3</sup> the time period between BBB opening and Mn<sup>2+</sup> administration was longer (approximately 15 minutes) than that used in this study (two minutes). Using the current administration protocol, significant initial T<sub>1</sub>-enhancement would obscure T<sub>1</sub>-contrast changes arising from any subsequent neuronal stimulus; thus precluding the use of this particular dosing regimen for such studies. However, this Mn<sup>2+</sup> administration method is quite effective in visualizing the region of BBB opening under these circumstances. The strong T<sub>1</sub>-contrast enhancement observed in these experiments suggests a large accumulation of intracellular Mn<sup>2+</sup> immediately following osmotically-induced BBB opening; assuming that the mechanism of contrast change is similar to that observed following neuronal stimulation or for white-matter-tract tracing. However, because of the dramatic changes in cell volume that occur under these circumstances, Mn<sup>2+</sup> sequestered in the extracellular space may also be a contributing factor. In spite of this uncertainty, we observed (data not shown) that regions of T<sub>1</sub> contrast did not change significantly over time (3 hours) with respect to 1) spatial position, 2) region size, or 3) level of enhancement. These observations are consistent with the intracellular uptake of Mn<sup>2+</sup>, where signal-enhancement levels have been shown to be maintained for several hours because of intracellular Mn<sup>2+</sup> sequestration following neuronal stimulation.<sup>1</sup> However, an extracellular contribution to the T<sub>1</sub>-contrast enhancement cannot be ruled out, since closure of the BBB following osmotic shock could also trap a significant concentration of Mn<sup>2+</sup> in the extracellular space, preventing its subsequent washout over time. Finally, this administration protocol may be a useful alternative for imaging experimental BBB disruption.

**References.** [1] Lin et al. *Mag. Reson. Med.* **38**: 378-88 (1997). [2] Henning et al. *Mag. Reson. Med.* **53**: 851-857 (2005). [3] Aoki et al. *Mag. Reson. Med.* **50**:7-12 (2003). [4] Silva et al. *NMR in Biomed.* **17**: 532-543 (2004).

# Manganese-Enhanced MRI (MEMRI) and Diffusion-Weighted MRI Mismatch in the Absence of a Specific Neuronal Stimulus

D. Bennett<sup>1</sup>, N. Henninger<sup>3,5</sup>, M. Fisher<sup>4,5</sup>, C. Sotak<sup>1,2,4</sup>

**Introduction:** Manganese ( $Mn^{2+}$ ) has proven to be a useful MR contrast agent for functional imaging<sup>1</sup> and neuronal tract tracing<sup>2</sup>. The paramagnetic properties of  $Mn^{2+}$  provide localized contrast on a T<sub>1</sub>-weighted (T<sub>1</sub>W) MR image after cellular sequestration via voltage-gated calcium channels<sup>1</sup>. Many MEMRI experiments rely on the delivery of a significant volume of  $Mn^{2+}$  to the brain parenchyma via an osmotically-disrupted blood-brain barrier (BBB). Neuronal activity associated with stroke<sup>3</sup> and cortical spreading depression<sup>4</sup> can also result in localized T<sub>1</sub>-enhancement. For example, in an effort to detect ischemic brain regions using MEMRI Aoki et al.<sup>3</sup> coined the term “MEMRI-DWI mismatch” to categorize the difference between T<sub>1</sub>-enhanced brain regions and regions with an ADC below  $0.5 \times 10^{-3} \text{ mm}^2/\text{s}$  after permanent occlusion of the middle cerebral artery in the rat. The T<sub>1</sub>-enhanced regions in Aoki’s study were suggested to represent stroke core. However, mechanisms other than stroke, such as brain edema and the paramagnetic effects of manganese, were not discussed with respect to ADC deficits in the hemisphere of interest. Here, using an experimental protocol similar to that of Aoki et al.<sup>3</sup>, we show significant ADC reductions in brain regions infused with hyperosmotic solution, manganese chloride, and Evans Blue as well as non-specific T<sub>1</sub>-enhancement and DWI contrast due to  $Mn^{2+}$  accumulation. Additionally, 2,3,5-triphenyltetrazolium hydrochloride (TTC) staining showed signs of tissue injury in areas with significant ADC deficit. These studies suggest that when  $MnCl_2$  is delivered via an osmotically-disrupted BBB, careful assessment of baseline MEMRI-DWI mismatch regions should be performed prior to any subsequent neuronal stimulus or ischemic intervention.

**Methods:** Eight male Sprague-Dawley rats (280-350 g) were anesthetized with 2.0% isoflurane mixed with breathing-quality air during surgery. Five minutes prior to hyperosmotic BBB-opening, rats were switched to 2% isoflurane mixed with 100% O<sub>2</sub>. Prior to each injection, the external carotid (ECA) and pterygopalatine artery were ligated and the common carotid (CCA) was temporarily clamped (~10 minutes) during catheterization of the ECA with PE-10 tubing. 1.6M arabinose solution (5 ml/kg; Sigma) was infused into the internal carotid artery over 55 seconds using an infusion pump (Harvard Apparatus, Model PHD2000). The CCA was immediately unclamped after securing the ECA catheter. During the arabinose infusion, the CCA was clamped to ensure flow towards the brain. Immediately after arabinose infusion the CCA clamp was removed and the rat was switched back to 2% isoflurane mixed with breathing quality air. Two (N=3) and ten (N=4) minutes after arabinose infusion manganese chloride ( $MnCl_2 \cdot 4H_2O$ , MW = 198; Sigma), dissolved to 10 mM in isotonic saline, and Evans Blue (EB, Sigma), dissolved to 2% in  $MnCl_2$  solution ( $MnCl_2+EB = 2 \text{ ml/kg}$ ), was infused into the internal carotid artery at 4.5 ml/hr.  $MnCl_2+EB$  and arabinose solutions were filtered with 0.45  $\mu\text{m}$  syringe filters (Nalgene). MR images were acquired using a Bruker Biospin 2.0T/45 cm imaging spectrometer operating at 85.56 MHz for <sup>1</sup>H and equipped with  $\pm 20\text{G/cm}$  self-shielded gradients. DW images were acquired with six b-values (23, 92, 207, 828, 1126, and 1471 s/mm<sup>2</sup>), 64x64 matrix zero-filled to 128x128 before Fourier transformation, FOV=3x3cm, six 2-mm slices, TR/TE = 2000/51.0ms,  $\Delta = 6.0\text{ms}$ ,  $\delta = 24.31\text{ms}$ , and NEX=8. T<sub>1</sub>W MRI was performed as follows: TR/TE = 500/10.8ms, FOV = 3x3cm, matrix = 128x128, six 2-mm slices with 0.1mm gap and NEX = 8. Slice profiles of DW- and T<sub>1</sub>W images were commonly referenced to the rhinal fissure at the olfactory bulb boundary.

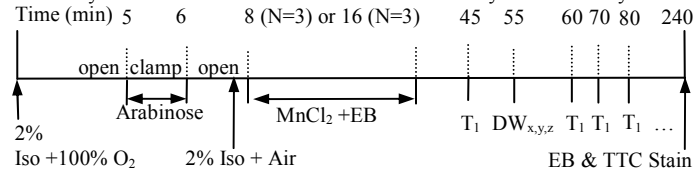


Figure 1: Timeline of infusions, imaging and histological staining.

**Results:** Animals infused with  $MnCl_2+EB$  2 minutes after arabinose showed a T<sub>1</sub>W signal increase of  $38.7 \pm 7.9\%$  covering  $43.1 \pm 7.2\%$  of each infused hemisphere. Animals infused with  $MnCl_2+EB$  10 minutes after arabinose showed a T<sub>1</sub>W signal increase of  $40 \pm 4\%$  covering  $50 \pm 19\%$  of each infused hemisphere. Figure 2 shows images from three animals that include the average signal intensity of DW images, corresponding ADC maps, T<sub>1</sub>W images, EB and TTC stains. Images were acquired according to Figure 1. Figure 2A and 2B show regions of bright T<sub>1</sub>-enhancement corresponding to regions with dark EB staining (white arrows). Figure 2A and 2B also show regions of DW hypointensity due to  $Mn^{2+}$  accumulation (white arrow 2A, center of hemisphere in DW image 2B). Regions of MEMRI-DWI mismatch (red arrows in 2A,2B, whole hemisphere in 2C) do not show correlated (gross) EB staining but do correspond to areas of tissue injury as verified by TTC stains (2A,2B). Data shown in Figure 2C are from an animal infused with 1.6M arabinose at 50 ml/hr ( $MnCl_2+EB$  10 minutes after arabinose) to control for brain edema and non-specific T<sub>1</sub>-enhancement due to infusion rate of arabinose. For the slice shown, brain water changes are apparent and may reflect severe edema due to hyperosmotic shock. Brain edema may be responsible for reducing blood flow and delivery of  $MnCl_2+EB$  to this region. Figure 3 shows percent area of non-T<sub>1</sub>-enhanced regions with ADC deficit, percentage ADC deficit in non-T<sub>1</sub>-enhanced regions and percent area of the  $MnCl_2+EB$ -infused hemisphere with a MEMRI-DWI mismatch. T<sub>1</sub>-enhancement was defined as voxels in infused hemisphere whose signal intensity exceeded the mean +2 SDs in the non-infused hemisphere. ADC deficit was defined as voxels in the infused hemisphere with ADC values less than the mean plus 2 SDs in the non-infused hemisphere.

MEMRI-DWI mismatch size was defined as the area of ADC deficit within regions without T<sub>1</sub>-enhancement compared to the area of the entire hemisphere. Calculations and regions of interest were made using imageJ (NIH).

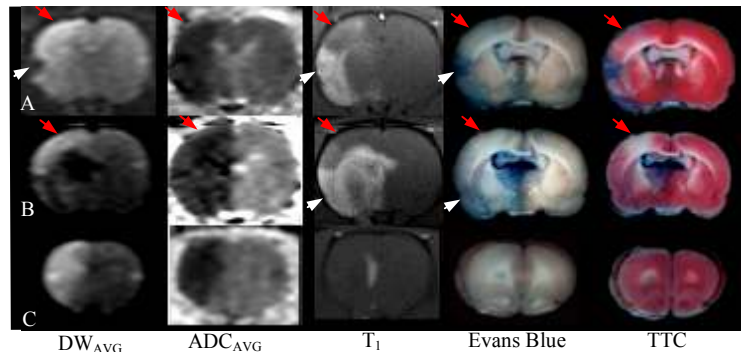
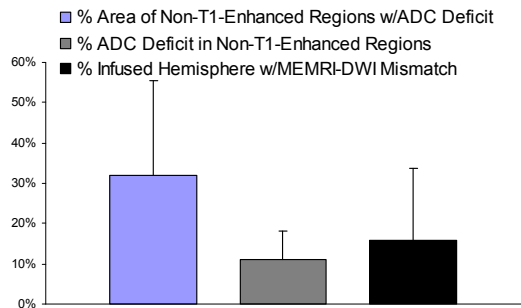


Figure 2: Averaged signal intensity of DW images acquired in x,y, and z directions ( $b=1126 \text{ s/mm}^2$ ), average ADC map, T<sub>1</sub>W, EB, and TTC images from three animals. MR images are from animals infused with  $MnCl_2+EB$  A) 2 minutes and B), C) 10 minutes after arabinose bolus. Red arrows in A) and B) point to regions of MEMRI-DWI mismatch and EB staining and tissue damage suggestive of low blood flow to these regions possibly due to severe edema. C) One animal infused with 5ml/kg 1.6M arabinose at 50 ml/hr shows an almost complete MEMRI-DWI mismatch in this slice. MR slice in C) is 4mm ventral to MR slices in A) and B). ADC deficit and apparent hemispheric volume changes (EB and TTC slices) in C) suggests severe edema which may explain lack of T<sub>1</sub>-enhancement and EB stain in this slice.



**Discussion:** Many MEMRI experiments rely on the delivery of  $Mn^{2+}$  to the brain parenchyma via an osmotically-disrupted BBB prior to specific neuronal stimulus<sup>1,3,4</sup>. For these studies, non-specific T<sub>1</sub>-enhancement and DWI contrast is undesirable and may obscure the expected T<sub>1</sub>-contrast and ADC changes. Although ischemic conditions were not intentionally induced in these experiments, our data suggests that hyperosmotic shock itself can give rise to non-specific brain T<sub>1</sub> and ADC changes (permanent, Figure 2B) under these conditions. These observations are consistent with previous studies that provided evidence for brain cell and endothelial cell injury after hyperosmotic shock<sup>5,6,7</sup> and for ADC changes as a result of brain edema<sup>8,9</sup>. Our data does not, however, permit us to rule out T<sub>1</sub>-enhancement, DWI contrast and edema formation by an anesthetic effect. Isoflurane, specifically, has been shown to increase blood plasma glutamate levels in humans<sup>10</sup> and exacerbate brain edema in brain-injured rats<sup>11</sup>. Although we did not use a combined non-volatile and volatile anesthetic regimen as described by Aoki et al.<sup>3</sup>, this approach may be helpful in reducing or eliminating any non-specific T<sub>1</sub>-enhancement under these conditions. While insufficient anesthetic depth may contribute to non-specific T<sub>1</sub>-enhancement, the MEMRI-DWI mismatched regions shown here may also reflect a brain response (functional, volumetric, or both) to the hyperosmotic disruption of the BBB alone. The results of these experiments stress the need for careful assessment of baseline MEMRI-DWI mismatch prior to any subsequent neuronal stimulus or ischemic intervention; in order to ensure that the osmotic disruption of the BBB itself does not contribute significantly to any non-specific brain T<sub>1</sub> or ADC changes.

**References:** [1] Lin et al. *Mag. Reson. Med.* **38**:378-88 (1997). [2] Aoki et al. *Neuroimage* **22**:1046-59 (2004). [3] Aoki et al. *Mag. Reson. Med.* **50**:7-12 (2003). [4] Henning et al. *Mag. Reson. Med.* **53**:851-857 (2005). [5] Suzuki et al. *J Neurosurg* **69**:421-428 (1988). [6] Lossinsky et al. *J Neurocytology* **24**:795-806 (1995). [7] Richmon et al. *Brain Research* **780**:108-118 (1998). [8] Baird et al. *JCBFM* **18**: 583-609 (1998). [9] Barzo et al. *J Neurosurg* **87**:900-907 (1997). [10] Stover et al. *Acta Neurochir (Wien)* **147**:847-853 (2005). [11] Stover et al. *Acta Neurochir Suppl.* **76**:375-378 (2000).

## Separating Signals from Intra- and Extracellular Water Compartments in Rat Skeletal Muscle *In Vivo* Using MEMRI

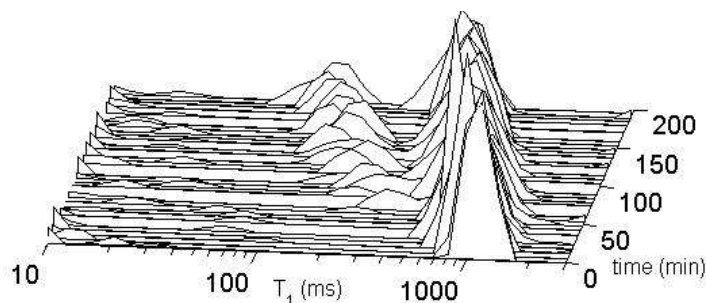
J. G. Seland<sup>1</sup>, K. G. Helmer<sup>2</sup>, G. Nair<sup>2</sup>, D. G. Bennett<sup>2</sup>, C. H. Sotak<sup>2,4</sup>

<sup>1</sup>Department of Circulation and Medical Imaging, Norwegian University of Science and Technology, N-7489 Trondheim, Norway  
<sup>2</sup>Departments of Biomedical Engineering and <sup>3</sup>Chemistry & Biochemistry, Worcester Polytechnic Institute, Worcester, Massachusetts 01609  
<sup>4</sup>Department of Radiology, University of Massachusetts Medical School, Worcester, MA 01655

**Introduction.** Tissue inter-compartmental equilibrium water exchange can significantly affect the quantitative analysis of various *in vivo* MR parameters. One method for investigating equilibrium-water-exchange effects is NMR Relaxography,<sup>1</sup> which can employ an MR contrast agent to selectively modify the  $T_1$  relaxation time of one tissue compartment relative to the other. In the absence of a contrast agent, the inter-compartmental water exchange rate is significantly faster than the difference in longitudinal relaxation rates ( $R_1 = 1/T_1$ ) in each compartment. In this case, a mono-exponential  $T_1$  relaxation time would be measured. However, selective addition of an MR contrast agent (of sufficient concentration) to one compartment can increase the  $T_1$ -relaxation-rate difference between the two compartments (relative to the inter-compartmental exchange rate, which remains constant); potentially moving the system into an intermediate- or slow-exchange regime. If the slow-exchange regime can be achieved, then the MR signal contributions from each compartment can be separated on the basis of their  $T_1$  relaxation time differences. In the simplest case, a bi-exponential  $T_1$  relaxation time would be measured. One impediment to achieving the slow-exchange regime *in vivo* has been the difficulty in attaining the necessary contrast-agent concentration in one of the tissue compartments. In previous *in vivo* attempts in rat skeletal muscle using Gd-DTPA, only the intermediate-exchange regime could be achieved.<sup>2</sup> In this study, manganese-enhanced MRI (MEMRI) has been investigated as a method for separating and identifying the MR signals from intra- and extracellular water compartment in rat skeletal muscle *in vivo*.

**Materials and Methods.** The experiments were performed on a GE CSI-II 2.0T/45-cm imaging spectrometer operating at a <sup>1</sup>H frequency of 85.56 MHz. A 22 mm (ID), 4-turn solenoid RF coil was placed around the right thigh of male Sprague-Dawley rats. In order to prevent the RF field from extending outside the longitudinal edges of the coil, a doughnut-shaped piece of copper foil was placed at each end. This made it possible to perform localized spectroscopy using only the RF-field profile of the coil itself. MnCl<sub>2</sub> was infused through a catheter inserted in the femoral vein. Five rats, with an average weight of 320 g, were studied at six different [Mn<sup>2+</sup>] (20, 30, 40, 50, 60 and 70 mM); each infused successively over periods of 32 min at a flow rate of 0.0266mL/min. The total accumulated dose was 0.715 mmol/kg Mn<sup>2+</sup> after 192 min. During infusion,  $T_1$  was measured over 6-min intervals using a standard Inversion Recovery (IR) pulse sequence with an adiabatic inversion pulse. The data were analyzed by Inverse Laplace Transform (ILT); which, when performed on the IR data, yields the distribution of  $T_1$  relaxation times in the sample.<sup>1</sup>

**Results.** A typical series of  $T_1$  distributions, as a function of infused [Mn<sup>2+</sup>], over time is shown in the Figure (Exp. No 5). At low [Mn<sup>2+</sup>] only one peak (located around 1170 ms) is observed. This is indicative of the fast-exchange regime, where the difference in the  $T_1$  relaxation rates ( $\Delta R_1$ ) between the two compartments is small relative to the inter-compartmental equilibrium water exchange rate. However, as the administered [Mn<sup>2+</sup>] increases over time, the mean of the single distribution shifts to lower  $T_1$  values. At a certain [Mn<sup>2+</sup>] in this case, a second distribution appears. If there is no significant transport of Mn<sup>2+</sup> into the skeletal-muscle intracellular (IC) space over the experimental time course, then the fast  $T_1$  component can be assumed to arise from water in contact with Mn<sup>2+</sup> in the extracellular (EC) space (as well as in equilibrium with the vascular water). The appearance of two  $T_1$  distributions also heralds the onset of the slow-exchange regime. The means of the  $T_1$  distributions (and the fractional population, p1, of the short- $T_1$  component; p2 = 1.0 - p1) at the highest (final) infused [Mn<sup>2+</sup>] are given in the Table and were similar for all experiments. The fraction of the shortest component (p1) corresponds well to values for the skeletal muscle EC fraction reported in the literature.<sup>3</sup>



**Discussion and Conclusions.** A similar study using Gd(DTPA) was not able to separate the water signals from the two compartments in rat skeletal muscle.<sup>2</sup> A shoulder was observed at highest [Gd(DTPA)]; perhaps indicating the approach of the slow-exchange regime. In the Gd(DTPA) study, the shortest  $T_1$  value attained was ~600 ms at the highest dose. In our study, a value of ~350 ms was observed at the onset of peak separation, indicating a significantly higher [Mn<sup>2+</sup>] and/or relaxivity for Mn<sup>2+</sup> the EC space. Mn<sup>2+</sup> bound to macromolecules in the plasma and interstitial space can result in a 5-fold increase in relaxivity vs. Mn<sup>2+</sup> in water.<sup>4</sup> The enhanced relaxivity, in combination with [Mn<sup>2+</sup>], appears to be sufficient to achieve the slow-exchange regime; allowing separation of the EC and IC water signals. By contrast, the relaxivity of Gd(DTPA) is the same in water and plasma,<sup>3</sup> which may explain why only the intermediate-exchange regime was attained in (2), even at plasma [Gd(DTPA)] as high as 10 mmol/L. The ability to differentiate between IC and EC water compartments *in vivo* using MEMRI would have important implications for studying inter-compartmental equilibrium water exchange in skeletal muscle under a variety of circumstances as well as other applications.

**References.** 1. Labadie C, *et al*, J. Magn. Reson. Ser B, 1994;105: 99-112. 2. Landis CS, *et al*, Magn. Reson. Med., 1999; 42: 467-478. 3. Donahue, KM, *et al*, Magn. Reson. Med., 1995; 34: 423-432. 4. Wendland, MF, NMR Biomed., 2004; 71: 581-594.

Exp. no	$T_1$ initial	$T_{1-1}$ final	$T_{1-2}$ final	p1 final
1	1197	134	539	0.25
2	1175	155	616	0.24
3	1230	138	530	0.27
4	1152	130	480	0.26
5	1170	95	473	0.24
Overall (SD)	1185 (30)	130 (22)	528 (57)	0.25 (0.01)